C|D|T

TRUXENE BASED MATERIALS FOR ORGANIC ELECTRONICS

Submitted by

ROISIN ELIZABETH BROWN

A thesis submitted to the Department of Pure and Applied Chemistry, University of Strathclyde, in fulfilment of the regulations for the Degree of Doctor of Philosophy.

2018

This thesis is the result of the author's original research. It has been composed by the author and has not been previously submitted for examination which has led to the award of a degree.

Signed:

Date:

Contributions from others

The work presented in Section 3.2 was carried out by Mr Hangyang Ye at the University of Oxford. Dr Jean-Benoit Giguere of CDT carried out the electrochemistry in Chapter 3; the OLED in Figure 3.15 was fabricated at CDT. Crystal structures were acquired at the National Crystallographic Centre by Dr Claire Wilson, Dr Mateusz Pitak and Dr Wim Klooster.

Acknowledgements

Firstly, thanks to Pete for giving me the opportunity to work in his group, the mentoring and help over the years, plus some good days in the Scottish countryside!

Thanks to CDT for funding this work, and also for all the useful meetings and insight into the project. Special thanks to Dr Jeremy Burroughes, Dr Richard Wilson, and Dr Thomas Kugler for their input; also to Dr Jean-Benoit Giguere for the electrochemistry work.

I would like to thank Dr Moritz Reide and his group for their collaboration, particularly Ivan and Hangyang for all of their work on the OPVs and very helpful chats. Thanks also to Dr Claire Wilson, Dr Mateusz Pitak and Dr Wim Klooster at the National Crystallographic Centre for the crystallography work.

I would also like to acknowledge the help that Craig Irvine, Patricia Keating and Alexander Clunie have given me in the areas of NMR, mass spectroscopy and elemental analysis respectively. Thanks to Gavin Bain for his help with the Karl Fischer titrations and fixing random pieces of equipment. Thanks to Lindsay McCulloch and Kate Reid for their assistance with the TGA, and also to John Liggat for informative discussions about TGA and DSC.

Neil, Joe, Rupert and Alex you guys have taught me just about everything I know. You put up with me constantly pestering you with questions and ranting, yet somehow haven't lost your sanity, thanks.

The rest of the Skabara group, present and past (especially Neil T and Clara), cheers for all the help and the pub visits. We've had a lot of good times, some stress, and way too much cake! I wish you all the best for the future.

Thanks to Polly, Dave and Gary. You guys have been a great support network for complaining when things don't work in the lab, and celebrating when they do.

To the rest of my friends, thank you for understanding my antisocial behaviour and nodding along when I talk about chemistry.

Mum and Dad, I wouldn’t be here without you. Thanks for always believing in me and supporting me no matter what.

Last but definitely not least, Andy I could not have done this without you. You keep me sane and always make me smile. Thank you, TDGLOYL.

Abstract

Organic electronics has become a major area of research interest over the last 20–30 years. As society moves away from a reliance on fossil fuels, “cleaner energy” sources are being developed to complement existing avenues for energy, with one such source being organic photovoltaics. Additionally, as technology becomes more ubiquitous in everyday life, consumer expectations have driven advancements to improve the resolution and lifetime of devices while reducing their energy consumption. One way this has manifested itself is with the advent of organic light emitting diode (OLED) displays. In both of these examples, conjugated organic molecules can provide the fundamental function of these organic semiconductor based devices.

This thesis describes the synthesis and characterisation of several truxene based materials, which have potential application as interlayers within these devices. Initially, the influence of alkyl chain length was examined on a series of tricarboxylic acids. No significant change was observed in the optical and electrochemical properties; however the thermal properties and crystallographic packing were affected. While these molecules were found to be unsuitable for vacuum deposition, one of the intermediate materials (**2.3**) demonstrated templating ability. When included in organic photovoltaic devices, the performance was improved by the presence of this truxene interlayer.

Following a short screen of reaction conditions, a hexaester (**4.4**) was prepared in high yields on a multigram scale. As a result of the extended conjugation present, this material exhibited a high PLQY in addition to strong π-π stacking in the crystal structure. Finally, two molecules with cyano containing functionalities were synthesised. These materials both exhibited pseudo-reversible oxidations, and one (**5.2**) a pseudo-reversible reduction. Additionally, solvatochromism was observed for compound **5.3**.

Outline

An overview of organic semiconducting materials is given in **Chapter 1**, including methods for band gap engineering. This is followed by a brief introduction to the structure, fabrication and operation of OLEDs and OPVs, along with some examples of materials used in these devices. There is also a focus on the development of materials based on the truxene core.

Chapter 2 presents the synthesis of tricarboxylic acid functionalised truxene molecules with alkyl chain lengths varying from C_1 to C_4. The length of alkyl chain was found to have an insignificant effect on the optical and electrochemical properties of the materials. However, the thermal properties and crystallographic packing of these materials were impacted as the alkyl chain length increased.

The vacuum deposition of an intermediate material (**2.3**) is examined in **Chapter 3**. This small molecule displayed templating ability, so was included as an interlayer in organic photovoltaic devices. The device characteristics were improved by inclusion of this layer due to morphology changes within the device. Additionally, evaporation of a representative tricarboxylic acid (**2.11**) is explored. Further electrochemical studies are presented in this chapter. Salts of the tricarboxylic acid (**2.13**) were synthesised to temper the undesirable electrochemical properties of the tricarboxylic acid series. Although the electrochemical properties of the salts were not improved, they were applied as an interlayer in an OLED which did produce light.

Chapter 4 builds on the results presented in Chapter 3, by incorporating ester functionalities onto phenyl arms which are then linked to the truxene core. The synthesis and characterisation of this material is described; due to the extended conjugation it was found to have a high PLQY. Additionally, strong π-π stacking was observed in the crystal structure.

Chapter 5 describes attempts to synthesise more electron-deficient materials by including electron-withdrawing cyano-containing functionalities. A pseudo-

reversible reduction was obtained for compound **5.2**, though the HOMO-LUMO gap remains very similar to the tricarboxylic acids. Due to the more electron withdrawing dicyanovinyl group, the properties of compound **5.3** are more significantly altered, with a reduced HOMO-LUMO gap in addition to a positive solvatochromic effect being observed.

The results presented in Chapters 2 to 5 are then summarised in **Chapter 6**, while the experimental procedures used for the synthesis of these materials are contained within **Chapter 7**. Further experimental data is given in the appendices (**Chapter 9**).

Abbreviations

°C	degrees Celcius
Å	angstrom
AFM	atomic force microscopy
AO	atomic orbitals
aq	aqueous
arb. unit	arbitrary units
BPhen	bathophenanthroline
br	broad
Bu	butyl
calcd	calculated
CCT	correlated colour temperature
CDT	Cambridge Display Technology Ltd
CIE	Commission Internationale d'Eclairage
CRI	colour rendering index
CV	cyclic voltammetry
d	doublet
Da	Dalton(s)
dd	double doublet

DMF	*N*,*N*-dimethylformamide
DMSO	dimethylsulfoxide
DSC	differential scanning calorimetry
dt	double triplet
E_g	energy gap
EQE	external quantum efficiency
Et	ethyl
eV	electron volt
Fc	ferrocene
Fc^+	ferrocenium
FF	fill factor
HOMO	highest occupied molecular orbital
IQE	internal quantum efficiency
ITO	indium tin oxide
J_{SC}	short circuit current
K	Kelvin
LUMO	lowest unoccupied molecular orbital
M	molar
m	multiplet
MALDI-TOF	matrix assisted laser desorption ionisation-time of flight

Me	methyl
MO	molecular orbital
mol	mole
m.p.	melting point
MS	mass spectrometry
NMR	nuclear magnetic resonance
OLED	organic light emitting diode
OPV	organic photovoltaic
ox	oxidation
PCE	power conversion efficiency
PEDOT	poly(3,4-ethylenedioxythiophene)
PL	photoluminescence
PLQY	photoluminescence quantum yield
Pr	propyl
PSS	poly(styrenesulfonic acid)
q	quartet
red	reduction
rpm	revolutions per minute
s	singlet/second
STM	scanning tunnel microscopy

SubPc	boron subphthalocyanine chloride
SWV	square wave voltammetry
t	triplet
TCBD	tetracyanobutadiene
TCNE	tetracyanoethylene
T_g	glass transition temperature
TGA	thermogravimetric analysis
THF	tetrahydrofuran
TLC	thin layer chromatography
TMS	trimethylsilyl
TTF	tetrathiafulvalene
UV	ultraviolet
vis	visible
V_{OC}	open circuit voltage

Table of Contents

1 INTRODUCTION

1.1 Band theory

Electrons on a single atom are located in atomic orbitals (AOs), regions around the atom where there is a high probability of finding an electron. When atoms join together molecular orbitals (MOs) are formed by the linear combination of atomic orbitals, as shown in Figure 1.1.[1] One of the molecular orbitals will be higher in energy (in this example an antibonding orbital denoted with an *) and one lower (a bonding orbital in this case).

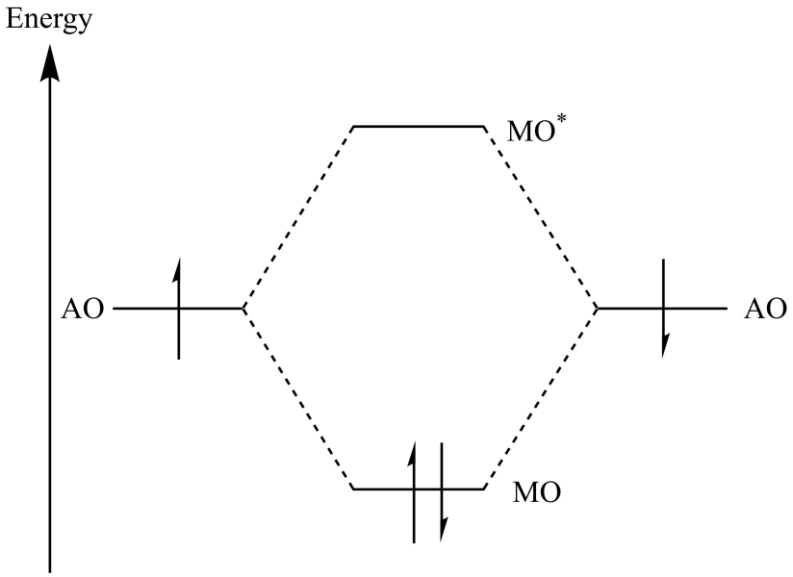

Figure 1.1 - Formation of molecular orbitals

As a result of the Aufbau principle, when more electrons are introduced, the electrons fill the orbital with the lowest energy first. In this example the electrons fill only the bonding MO, thus this is a stabilising interaction which provides a driving force for the orbital overlap.[2] The frontier orbitals are commonly referred to as the highest occupied molecular orbital (HOMO, the highest energy orbital filled with electrons) and the lowest unoccupied molecular orbital (LUMO). The energy of the LUMO represents the electron affinity, while the energy of the HOMO represents the ionisation potential of the molecule.[3]

As the number of overlapping atomic orbitals increases, the spacing between the energy levels becomes infinitely small and a continuous energy band is formed. The distance between the top of the occupied (valence) band and bottom of the unoccupied (conduction) band is known as the band or transport gap, and this determines the electrical conductivity of the material.[3] Figure 1.2 shows the band structures of a metal, an insulator and a semiconductor.[4]

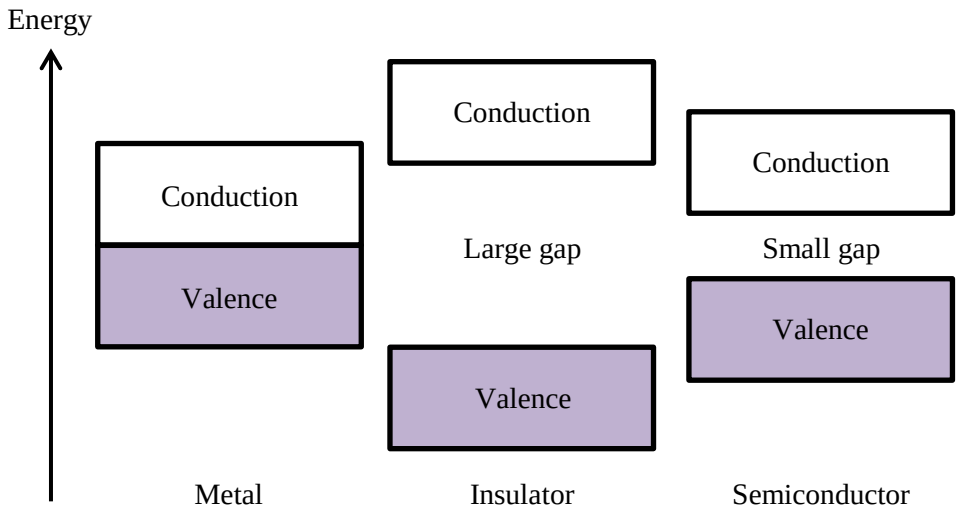

Figure 1.2 - Band diagram of a metal, insulator and semiconductor

In a metal there is a good overlap of the conduction and valence bands; above 0 K there is enough energy to populate the conduction band, leaving behind holes (positively charged vacancies) in the valence band. The movement of these electrons and holes confers conductivity to the material.[4]

The band gap of an insulator is so large that electrons cannot be promoted to the conduction band; hence the material conducts no current.

A semiconductor has a small band gap, thus some electrons can be promoted to the conduction band by thermal or photo excitation. This gives rise to an electron-hole pair which can travel through the material, a fundamental process in the operation of some organic electronic devices.[4,5]

1.2 Organic semiconductors

Carbon has the electronic structure $1s^2$ $2s^2$ $2p^2$ and can form up to four bonds, as a result of orbital hybridisation. For example, sp^2 hybridisation results in three sp^2 orbitals with a trigonal arrangement, and an unhybridised p_z orbital situated perpendicular to the trigonal plane. Figure 1.3 shows the formation of carbon-carbon double bonds by the overlap of one sp^2 orbital (represented in blue) from each carbon, and the unhybridised p_z orbital (represented in red).[1,6]

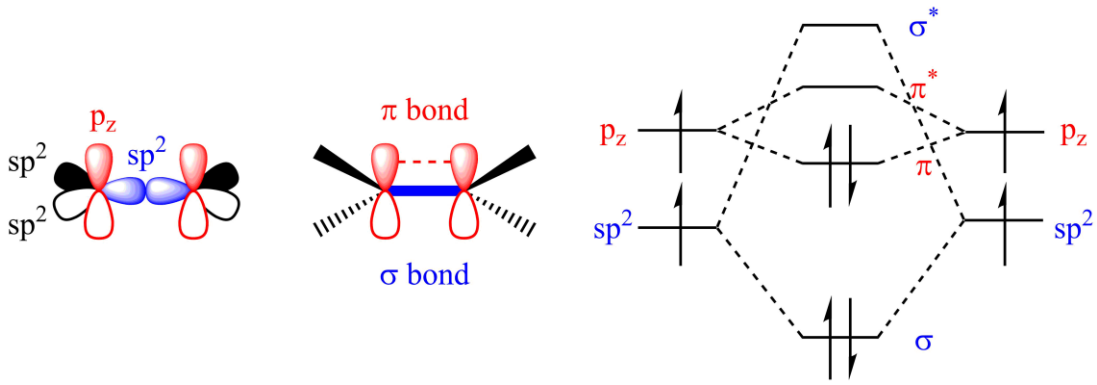

Figure 1.3 - C=C bond formation, showing orbitals of sp^2 hybridised carbon (left and middle) and molecular orbitals (right)

The σ-bond formed from the end-on overlap of the sp^2 orbitals is strong, therefore the energy gap between the σ and σ* orbitals is large. Conversely, the side-on overlap between the p_z orbitals is weaker, and thus there is a smaller energy difference between the HOMO (π) and LUMO (π*).[6]

Conjugated organic molecules contain alternating single and multiple bonds along the carbon chain. Since π-bonds are relatively weak, resonance structures such as those shown in Figure 1.4 are possible. As a result of this resonance, conjugated molecules such as 1,3-butadiene (**1.1**) allow for delocalisation of charge.

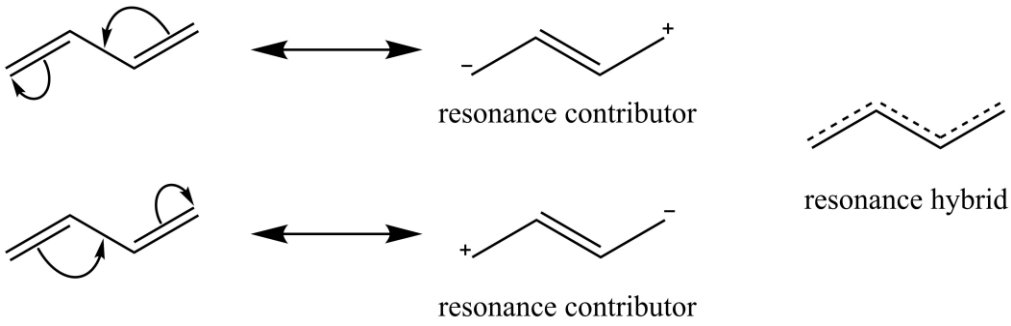

Figure 1.4 - Resonance strucutres of 1,3-butadiene **1.1**

In general the HOMO-LUMO gap is smaller when the conjugated network is larger, the conjugation can be extended indefinitely, giving rise to conjugated polymers.[3] Poly(acetylene) (both cis-, **1.2**, and trans-, **1.3**, Figure 1.5) is one of the simplest, and in 1977 doping of poly(acetylene) led to the first conductive polymers.[7,8] The significance of this work was recognised in 2000 with the Nobel prize in Chemistry.[9,10]

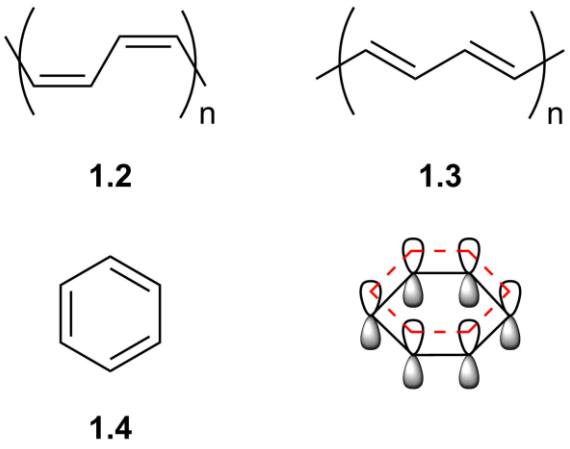

Figure 1.5 - Structure of cis-poly(acetylene) **1.2**, trans-poly(acetylene) **1.3**, and benzene **1.4**

Aromatic molecules are also conjugated and so allow for charge delocalisation. A compound is classed as aromatic if it is planar, cyclic and conjugated, and has (4n +2) π electrons (Hückel's rule, where n = 0 or any positive integer).[1] The simplest

aromatic molecule is benzene (**1.4**, Figure 1.5), where the electrons are situated in p orbitals that overlap above and below the plane of the σ-bond.

1.2.1 Band gap engineering

There are five factors which influence the band gap (E_g) of organic semiconductors; these are shown in Equation 1.1. Individually addressing these aspects of the molecular design allows the band gap to be tailored for the desired application.[11,12] Figure 1.6 shows how these components apply to molecular design. Each is discussed below in turn.

$$E_g = E^{\delta r} + E^{\theta} + E^{Res} + E^{Sub} + E^{Int}$$

Equation 1.1 - Factors which influence band gap

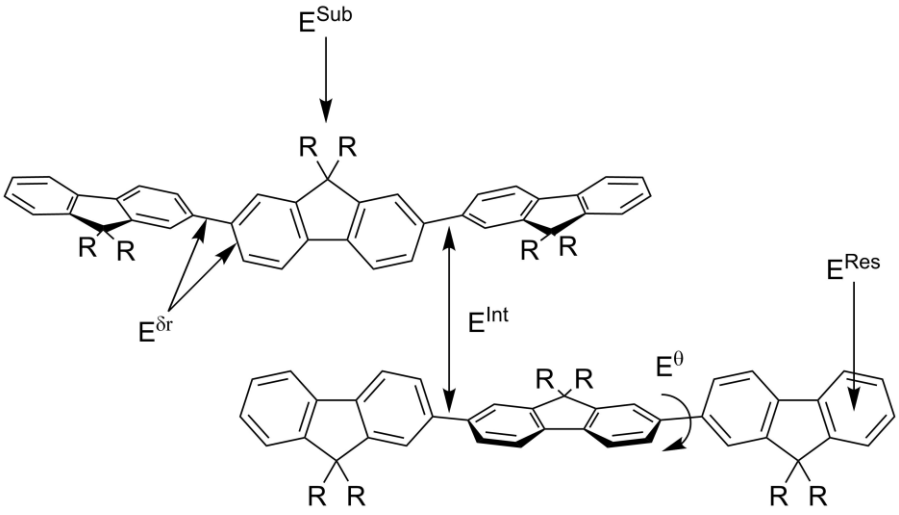

Figure 1.6 - Effects contributing to band gap

1. Bond length alteration, or $E^{\delta r}$, is often the major contribution to the band gap energy. This term arises from the fact that C-C bonds are not all equal in length, thus the π electrons are slightly localised.

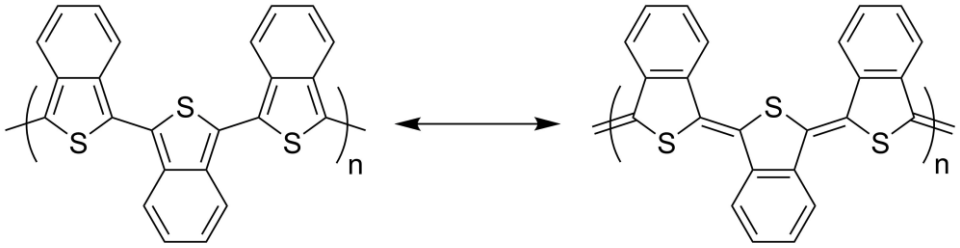

1.5 **1.6**

Figure 1.7 - Two resonance structures of poly(isothianaphthene), aromatic form **1.5** and quinoidal form **1.6**

2. E^{θ}, the dihedral angle, is the angle between repeating units. As this angle increases the overlap of the p orbitals decreases, breaking the conjugation pathway and widening the energy gap.
3. Unlike polyenes, aromatic systems such as poly(isothianaphthene) (Figure 1.7) have non-degenerate mesomeric forms, the term E^{Res} is derived from the energy difference between aromatic states. For example, in Figure 1.7 the stabilisation energy of benzene is greater than that of thiophene, meaning that the quinodal form **1.6** is favoured. In general the quinoidal form reduces the contribution of the $E^{\delta r}$ term, thus the band gap decreases as the quinoid character of the backbone increases.[13] Therefore the band gap of poly(isothianaphthene) is lower compared to poly(thiophene) which favours the aromatic form.
4. Electronic effects from substituents (E^{Sub}) are important when the conjugated backbone contains electron withdrawing or donating groups. This is the most direct way to modulate HOMO and LUMO levels, as changing the strength of the donor or acceptor will change the electron distribution along the backbone.
5. Finally, E^{Int} is a bulk property of the solid state. Referring to the interaction energy between molecules, this term can have a significant impact on the band gap.

Experimentally the band gap can be measured in several different ways including: cyclic voltammetry (CV), changes in conductivity with heat, and ultraviolet-visible (UV-vis) light absorption.

Solution state CV gives values of the oxidation and reduction potentials which can be approximated to the ionisation potential and electron affinity, respectively. Using this approximation the band gap can be calculated according to Equation 1.2. This represents the minimum energy needed to create a positive charge carrier minus the gain in energy from the addition of a negative charge carrier elsewhere in the material. This method is based on a number of conversion factors so the results should be taken with caution.[3,14,15]

$$E_g{}^{CV} = ionisation\ potential - electron\ affinity$$

Equation 1.2 - Calculation of electrochemical band gap

UV-vis spectroscopy can also be used as the optical band gap corresponds to the lowest optical transition. This differs from the band gap discussed above as excitation results in a bound electron-hole pair (or exciton) rather than complete ionisation; therefore the optical band gap does not include the exciton binding energy.[3] The optical band gap can be calculated from the onset of the longest wavelength of absorbance (in nm) as shown in Equation 1.3 below.

$$E_g{}^{UV} = \left(\frac{h \times c}{\lambda}\right)/(1.6 \times 10^{-19}) \cong \frac{1240}{onset}$$

Equation 1.3 - Calculation of optical band gap (in eV), where h = Planck's constant (J s), c = the speed of light (m s^{-1}), λ = wavelength (nm), and 1.6×10^{-19} is the conversion from J to eV

1.2.2 Light absorption and emission

As mentioned above, optical transitions can be measured using UV-vis spectroscopy. A UV-vis spectrophotometer has two light beams which pass through a sample and a 'blank' simultaneously. The intensity of the beam is measured at each wavelength before and after passing through the sample, allowing the unitless absorbance (A) of the sample to be calculated over a range of wavelengths, Equation 1.4.

$$A = \log_{10}\left(\frac{I_0}{I}\right)$$

Equation 1.4 - Calculation of absorbance from the intensity of incident (I_0) and transmitted light (I)

The absorbance of a material can be influenced by several factors, as shown in the Beer-Lambert law in Equation 1.5. In this equation *l* is the path length of the cell (in cm), *c* is the concentration of analyte (in mol L^{-1}), and ε is the wavelength dependent molar absorptivity (expressed in mol L^{-1} cm^{-1}). This final term is characteristic of each material and signifies the magnitude of the absorbance, which depends on the nature of the electronic transition. Due to their larger absorbances, molar absorptivities for allowed transitions are larger than those of forbidden transitions.[1,16]

$$A = \varepsilon \times l \times c$$

Equation 1.5 - Beer-Lambert law, where ε = wavelength dependent molar absorptivity (mol L^{-1} cm^{-1}), *l* = path length (cm), and *c* = concentration (mol L^{-1})

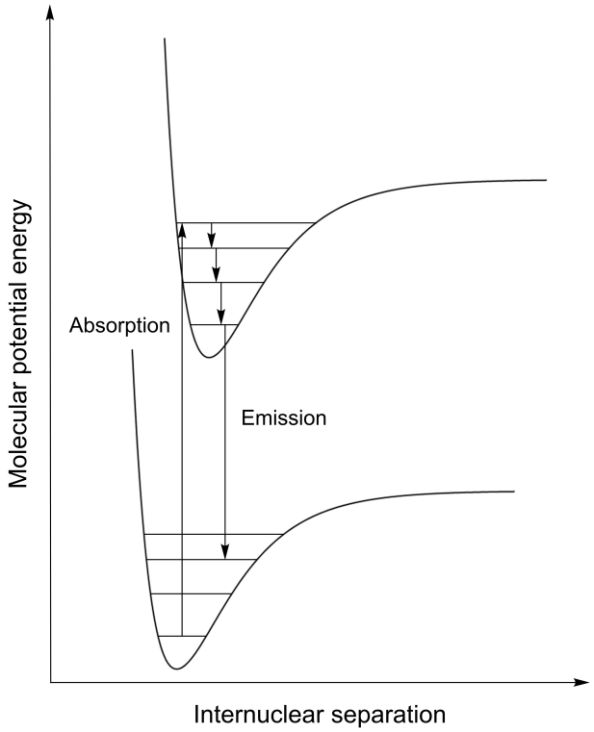

Figure 1.8 - Morse curve diagram showing absorption and emission

When a molecule absorbs a photon of sufficient energy (*i.e.* greater than the band gap) an electron is promoted to a higher orbital, meaning the molecule is now in an electronically excited state. Within these electronic states there are also vibrational states, as shown in Figure 1.8. The electron which has been promoted may undergo vibrational relaxation, a rapid radiationless decay process often resulting from collisions with other molecules.[2] When the molecule is in the lowest vibrational level of the excited state, the energy the molecule requires to lose to reach the ground state may be too great to be accepted by surrounding molecules. Therefore, the molecule must emit a photon in order to relax to the ground state, this is known as fluorescence. The wavelength of the photon emitted will be longer than that absorbed, as energy has been expelled in the vibrational transitions. This difference in wavelength is known as the Stokes shift.[2]

When an electron is promoted to the excited state it retains its spin, however as it undergoes vibrational relaxation the electron spin may change under certain conditions such as spin-orbit coupling. This spin forbidden transition is known as intersystem crossing, and leads to a triplet state as shown in Figure 1.9. The triplet state also loses some energy *via* vibrational relaxation, but to relax to the ground state intersystem crossing must occur once more. This can be facilitated by the same spin-orbit coupling. Emission from the triplet state is known as phosphorescence and occurs over longer time frames than fluorescence. Due to the requirement for intersystem crossing it is normally much less intense than fluorescence.[2]

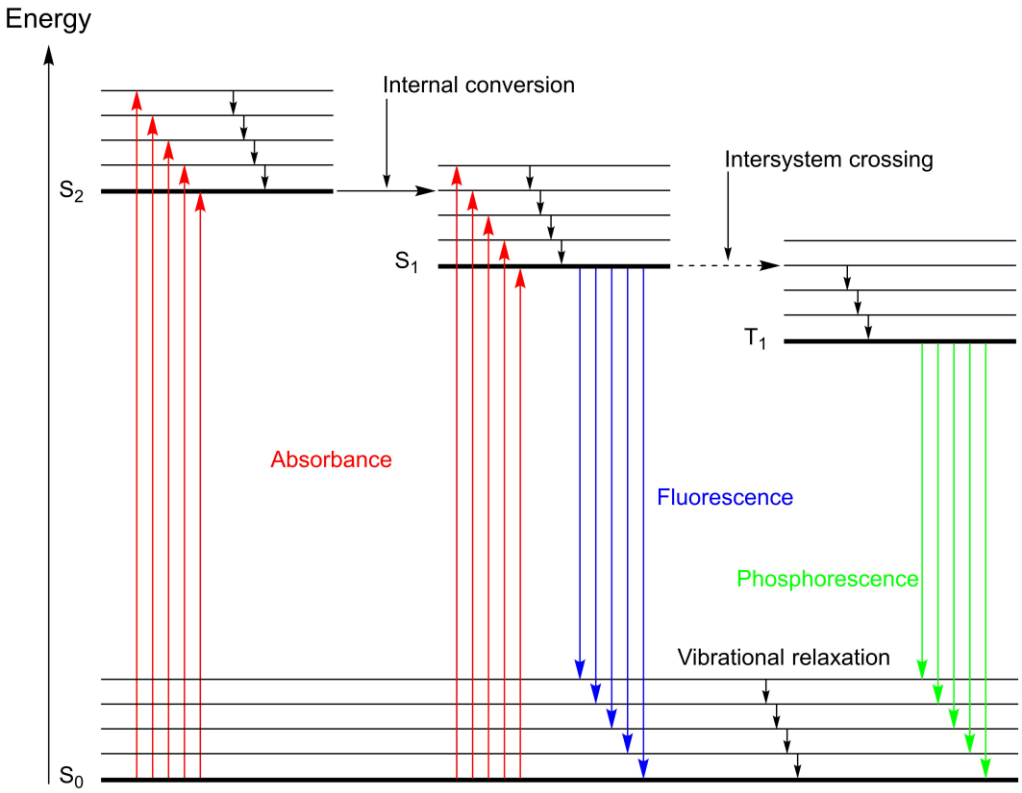

Figure 1.9 - Jablonski energy level diagram. Red lines indicate absorbance, blue lines fluorescence and green lines phosphorescence. Radiationless processes are represented with black lines. S_0 is the ground electronic state, S_1 and S_2 are excited singlet states and T_1 is the excited triplet state. Each electronic level is divided into vibronic sublevels

The efficiency of these optical processes can be quantified through the quantum yield, which is the number of events divided by the number of photons absorbed by the molecule.[2] For example the photoluminescence quantum yield (PLQY) determines how many of the absorbed photons are re-emitted through fluorescence or phosphorescence. The PLQY gives an indication of the probability of the excited state being deactivated by a radiative mechanism.

The absolute PLQY can be measured using an integrating sphere.[17] Alternatively, the relative PLQY can be measured be comparing the compound of interest to a standard with a known PLQY. The standard used should have a similar emission range to the compound of interest.[18]

To measure the relative PLQY the absorption and emission of both the standard and the compound of interest are measured at a range of concentrations. These concentrations should be selected to give an absorbance below 0.1 arb. unit to minimise re-absorption effects. The area under the emission spectra is then plotted against the absorbance at the wavelength of maximum absorbance. The gradient of these lines can then be used to calculate the relative PLQY according to Equation 1.6.[19]

$$QY_x = QY_s \times \left[{A_x}/{A_s}\right] \times \left[{F_s}/{F_x}\right] \times \left[{n_x}/{n_s}\right]^2$$

Equation 1.6- Calculation of relative PLQY, where QY = quantum yield, A = absorbance, F = fluorescence, and n = refractive index of the solvent. The subscript *x* denotes the compound of interest, while *s* denotes the standard

1.3 Organic electronic devices

There are many applications for organic semiconducting materials including: organic field effect transistors, organic lasers, sensors, organic light emitting diodes (OLEDs) and organic photovoltaics (OPVs). OLEDs and OPVs will be examined in more detail below.

1.3.1 OLEDs

The main applications of OLEDs are digital displays and solid-state lighting. Due to their potential flexibility, fast response time, range of colours, wide viewing angles, and high resolution they have been adopted in many consumer displays.[20] However, it is in lighting that OLEDs will have a real impact, and demand is increasing globally. Currently lighting is the second largest user of energy in buildings. This is mainly due to the inefficiencies of current technologies, with much of the energy being lost as heat.[21,22]

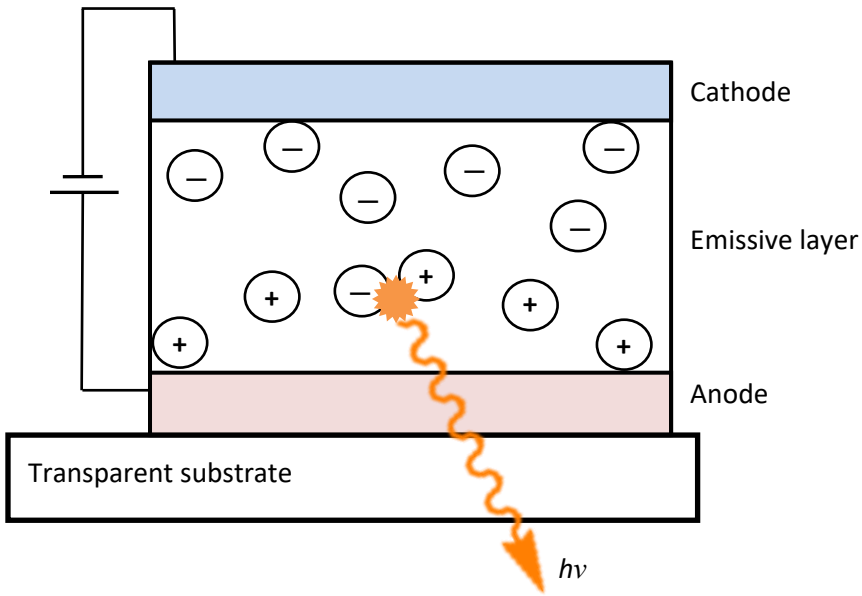

Figure 1.10 - Schematic of a basic OLED device

The basic structure of an OLED, shown in Figure 1.10, consists of two electrodes, and an emissive layer. When a current is applied electrons migrate from the cathode into the emissive layer, and meet holes migrating from the anode. When they combine within a single molecule an excited state is produced and, as the excited state returns to the ground state, a photon is emitted. The wavelength of this photon depends on the band gap of the material, thus the colour of light produced can be tuned by changing the structure of the emissive material, as discussed previously.[23,24]

For the light to be observed one of the electrodes must be semi-transparent, ordinarily the anode is made of indium tin oxide (ITO) which allows light to pass through. The cathode is made from low work function (the minimum energy needed to remove an electron from the surface to a point in free space),[25] electropositive metals such as aluminium, calcium or magnesium.

The colour produced by an OLED is evaluated in several ways:

- Commission Internationale d'Eclairage (CIE) coordinates. A representation of the colour of emission as perceived by the human eye.
- Correlated colour temperature (CCT). The temperature of a blackbody radiator emitting the same colour as the light source.
- Colour rendering index (CRI). How closely the light source can reproduce the true colour of an object.[26]

Some other key parameters used for comparing OLEDs include:

- Device lifetime. The time taken for the light intensity to fall to half that of the initial value.
- Internal quantum efficiency. The ratio of electrons injected to photons generated in the device.
- External quantum efficiency. The ratio of electrons injected to photons emitted from the device.
- Luminous power efficiency. The ratio of light emitted to power consumed, taking into consideration the sensitivity of the human eye.[26]

Efficient capture of charge carriers depends on the electrons and holes being injected and transported at the same rate. However, most emissive materials will favour the transport of one charge carrier over the other, resulting in the favoured charge carrier becoming the majority charge carrier. This leads to a reduction in device efficiency due to losses of the majority charge carriers through the opposite electrode.[27]

Device efficiencies and lifetimes can be improved by the addition of a thin interlayer, which can be either electron transport/hole blocking or hole transport/electron blocking. By using an interlayer the exciton is most likely to form at the interface between the emissive layer and the interlayer, far away from either electrode, reducing exciton quenching by the electrodes.[23]

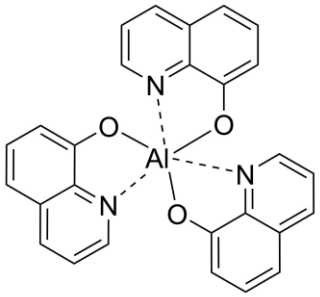

1.7

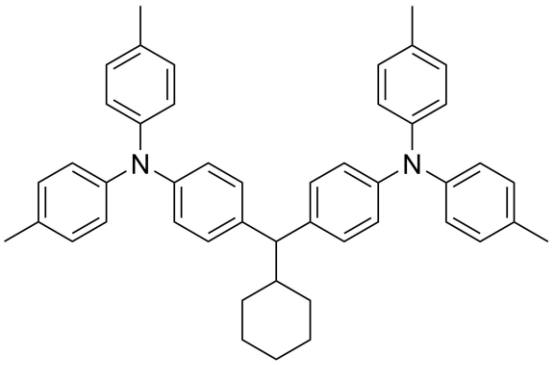

1.8

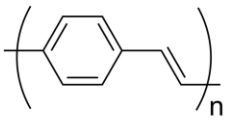

1.9

Figure 1.11 - Structure of OLED materials **1.7**–**1.9**

The first working OLED was reported in 1987 by Tang and Van Slyke. Their device used Alq_3 (tris-(8-hydroxyquinoline) aluminium, **1.7**, Figure 1.11) as the emissive layer, and an interlayer layer of the aromatic diamine **1.8** (Figure 1.11) which acts as a hole transport layer to alleviate shorting in the device.[28]

The first polymer based OLED was reported in 1990 by Burroughes *et al.*, based on poly(*p*-phenylene vinylene) (PPV, **1.9**, Figure 1.11).[29] This single layer device produced green-yellow light with a PLQY of around 8%.

Since these initial devices many different organic structures have been applied as the emissive layer in OLEDs, one family of which are fluorene based materials. Due to their blue emission polymers such as poly(9,9'-dioctylfluorene) (**1.10**, Figure 1.12) have been widely in OLEDs.[30–32] The alkyl chains provide solubility and hinder the formation of excimers. Furthermore, substituted polyfluorenes have been shown to be more stable to oxidative degradation than PPV materials such as **1.9**.[33]

The colour of their emission can be tuned. For example Pu *et al.* synthesised a series of small molecules with two bifluorene units attached to different central dyes (**1.11**, Figure 1.12). The properties and colour vary with **1.11a** being sky blue, **1.11b** blue-green, and **1.11c** yellow while **1.11d** displays deep red fluorescence.[34] By including a low amount of 4,7-dithienyl-2,1,3-benzothiadiazole in the polymer chain, white emission from a single polymer was achieved (**1.12**, where m = 0.0005, Figure 1.12).[35]

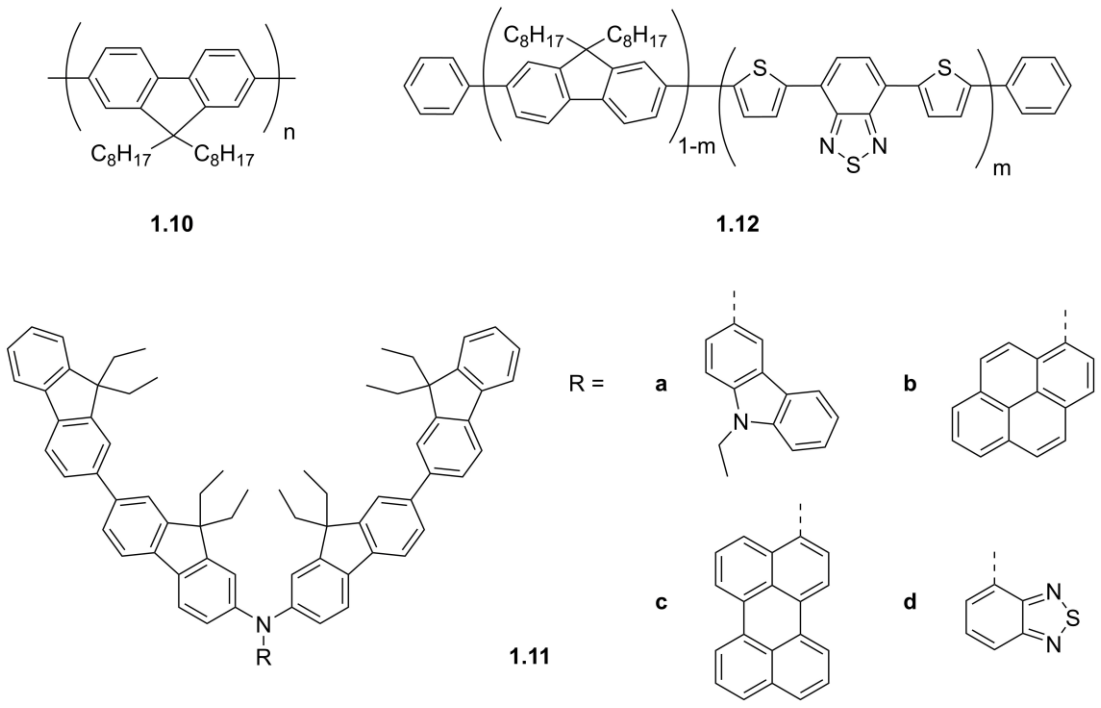

Figure 1.12 - Examples of emissive materials used in OLEDs. Fluorene based polymer **1.10**, small molecule **1.11a**–**d**, and copolymer **1.12** where m = 0.0005

1.3.2 OPVs

Organic solar cells, or OPVs, rely on the photoelectric effect. Similar to OLEDs, these devices consist of an active layer sandwiched between two electrodes. Once again ITO is commonly used as the anode due to its transparency. The active layer is comprised of an electron accepting material and a material which acts as an electron donor.[36] This layer can be biphasic or blended as a bulk heterojunction, the latter is shown in Figure 1.13. The ratio of donor:acceptor must be optimised to achieve the best device performance.[37]

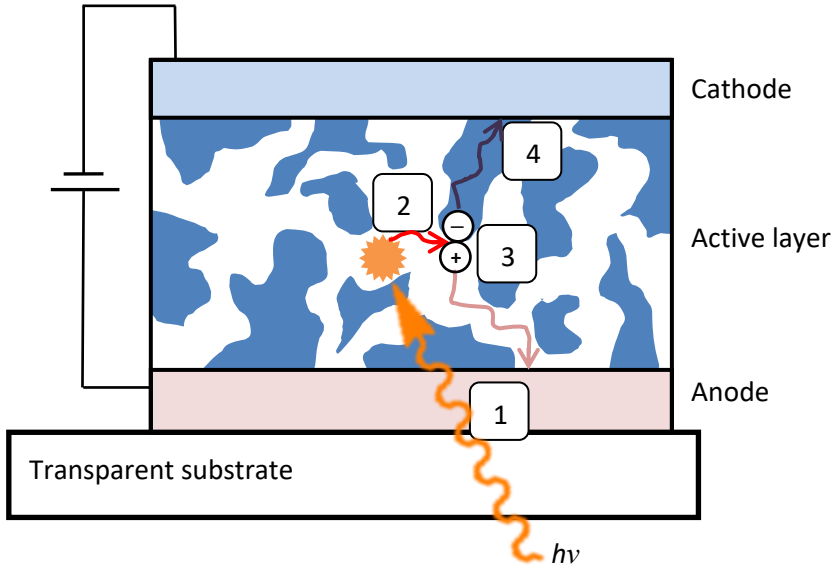

Figure 1.13 - Schematic of a basic OPV device showing the steps of charge generation

When the device is irradiated with light, photons are absorbed by the donor. An electron is promoted to the conductance band, leaving behind a hole. The generation of this excited state is represented by step 1 in Figure 1.13.

Following the photoabsorption, the electron-hole pair (exciton) diffuses through the active layer, represented by step 2.

Once it reaches the donor:acceptor interface a charge transfer complex is formed; the excited electron is transferred to the acceptor material, step 3. This results in the formation of a radical cation and radical anion.

After the free charge carriers are generated, they are subsequently transported to the respective electrodes, thereby producing a current. These four steps are further illustrated in Figure 1.14.[38–40]

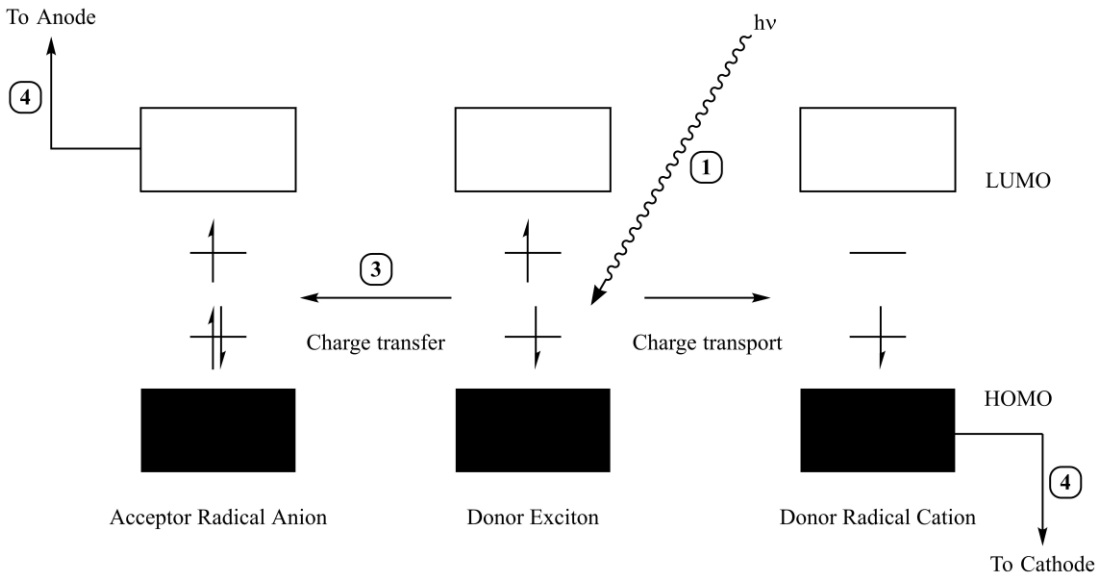

Figure 1.14 - OPV charge generation

The pathlength of diffusion must be short, otherwise the hole and electron can recombine; this annihilation of the exciton leads to a decrease in device efficiency. For this reason bulk heterojunction devices often outperform bilayer devices.[41] However, as both materials are in contact with each electrode careful selection of the electrode material is necessary to ensure that charge transport occurs in the desired direction.[39]

There are four key parameters for evaluating OPV performance:[37]

1. Short circuit current, J_{SC}. The maximum current density while illuminated and no reverse bias is applied.
2. Open circuit voltage, V_{OC}. The maximum voltage of the cell while illuminated and no current is flowing.
3. Fill factor, FF. The percentage of power generated relative to the maximum possible, given by Equation 1.7 where P_{max} (the maximum power point) is the location on the J-V curve which gives the maximum product of current density and voltage.
4. Power conversion efficiency, PCE or η. The ratio of the maximum electrical power generated to the total incident optical power (P_{in}), calculated using the above terms, as shown in Equation 1.8.

$$FF = \frac{P_{max}}{J_{SC} \times V_{OC}}$$

Equation 1.7 - Calculation of fill factor in a solar cell

$$PCE\ (\eta) = \frac{V_{OC} \times J_{SC} \times FF}{P_{in}}$$

Equation 1.8 - Calculation of power conversion efficiency for a solar cell

The acceptor material in OPVs is often based around buckminsterfullerenes, for example C_{60} exhibits excellent charge transport characteristics, but has limited solubility.[42] This can be improved by functionalising the material to give the widely used $PC_{61}BM$ ([6,6]-phenyl C_{61} butyric acid methyl ester, **1.13**, Figure 1.15).[43,44]

The larger $PC_{71}BM$ is also widely used as it maintains the same advantageous properties while improving device performances, in one example the PCE increased from 6.1% with $PC_{61}BM$ to over 9% with $PC_{71}BM$. Park *et al*. suggest that $PC_{71}BM$ leads to enhanced exciton dissociation at the donor:acceptor interface.[45–48]

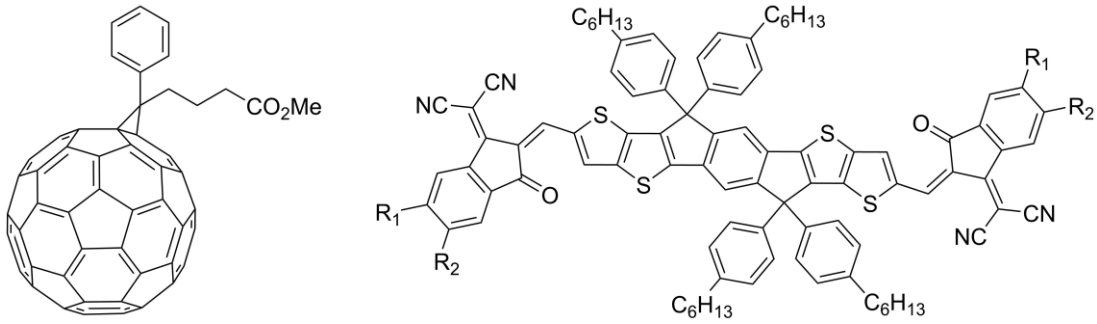

1.13

1.14 **a** : $R_1 = R_2 = H$
b : R_1 or R_2 = Me, R_2 or R_1 = H
c : $R_1 = R_2$ = Me

Figure 1.15 - Fullerene (**1.13**) and non-fullerene (**1.14**) based acceptor materials used in OPVs

There is much research into non-fullerene acceptors, both polymers and small molecules.[49,50] The energy levels of these materials are more easily altered than fullerenes, the addition of methyl substituents gradually increases the HOMO and LUMO levels of **1.14a**–**c** (Figure 1.15). These small molecules show promise as acceptor materials, with **1.14b** exhibiting the highest PCE of 11.6% (certified).[51–53]

P3HT (poly(3-hexylthiophene)) is often used as a donor in OPVs and has been reported in cells with PCEs greater than 4%.[44,54,55] Although it is used as somewhat of a benchmark material there are donor materials which give better device performances, for example the PTB family of alternating copolymers (**1.15**, Figure 1.16).[56]

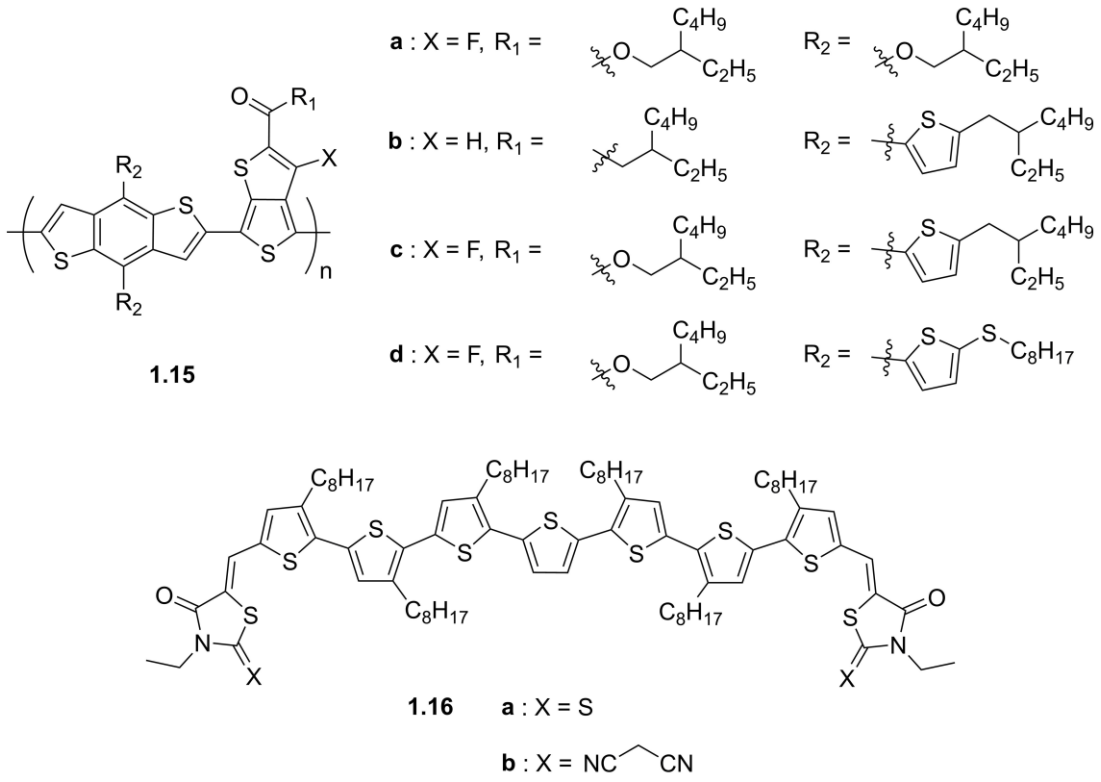

Figure 1.16 - Polymer (**1.15**) and small molecule (**1.16**) donor materials used in OPVs

The copolymer **1.15a** (PTB7) was initially reported with a PCE of 7.4%, but through the use of additives this has since been increased to 7.74%.[48,57,58] Slight structural modifications lead to copolymer **1.15b** (PBDTTT-C-T) which has a PCE of 7.59%; **1.15c** (PTBT-Th) combines the features of these two materials and leads to an increased PCE of 9.00%.[59,60] By fabricating the active layer as a gradient, a further enhanced PCE of 10.95% has been reported for **1.15c**.[61] Finally, by changing to a linear thioalkyl chain in **1.15d** (PBDT-TS1) the properties were further altered while maintaining a high PCE of 9.65%.[56,58,62,63]

Small molecules also perform well in OPVs, for example the oligothiophene based material **1.16a** (Figure 1.16) was reported with a PCE of 6.10%.[64] The addition of the dicyanomethylene group to form **1.16b** (Figure 1.16) vastly improved the PCE to 9.3% (certified at 8.995%). The authors suggest that this is due to increased light absorption and high internal quantum efficiency, the latter as a result of the crystalline structure as domains of the donor material were found to be close in size to the exciton diffusion length.[46]

1.3.3 Charge transport materials

As discussed previously, the inclusion of interlayers can improve device efficiencies by providing a balance of charge carriers. Adjusting the thickness of these interlayers allows for further optimisation of device performance.

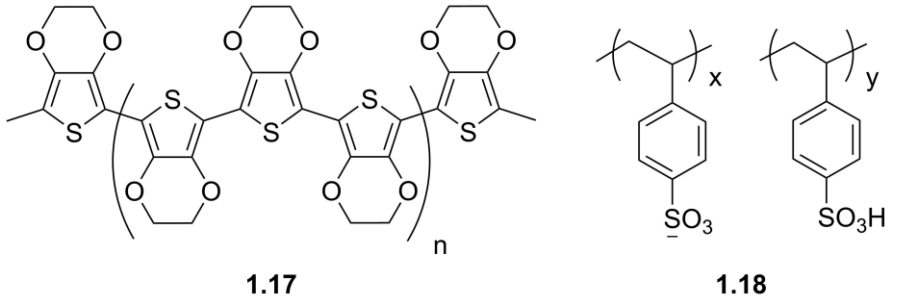

Figure 1.17 - Structure of PEDOT **1.17** and PSS **1.18**

The polymer PEDOT (poly(3,4-ethylenedioxythiophene), **1.17**, Figure 1.17) can be dispersed with PSS (poly(styrenesulfonic acid), **1.18**, Figure 1.17). The resulting water soluble material, known as PEDOT:PSS, is often used as a hole transporting interfacial layer to modify ITO electrodes in devices.[39,65]

The conductivity of this material can be tuned by changing the ratio of PEDOT and PSS. Furthermore, doping with additives such as ethylene glycol or treatment with H_2SO_4 also increases the conductivity, with values of over 3000 S cm^{-1} reported.[66–68]

Due to their high hole mobilities, the majority of materials used as hole transport layers include an electron rich arylamine component. For example, the inclusion of TPD (*N*,*N*'-di(3-methylphenyl)-*N*,*N*'-diphenyl(1,1'-biphenyl)-4,4'-diamine, **1.19**, Figure 1.18) increased the emission efficiency 100 fold, compared to the device with no hole transport layer.[69]

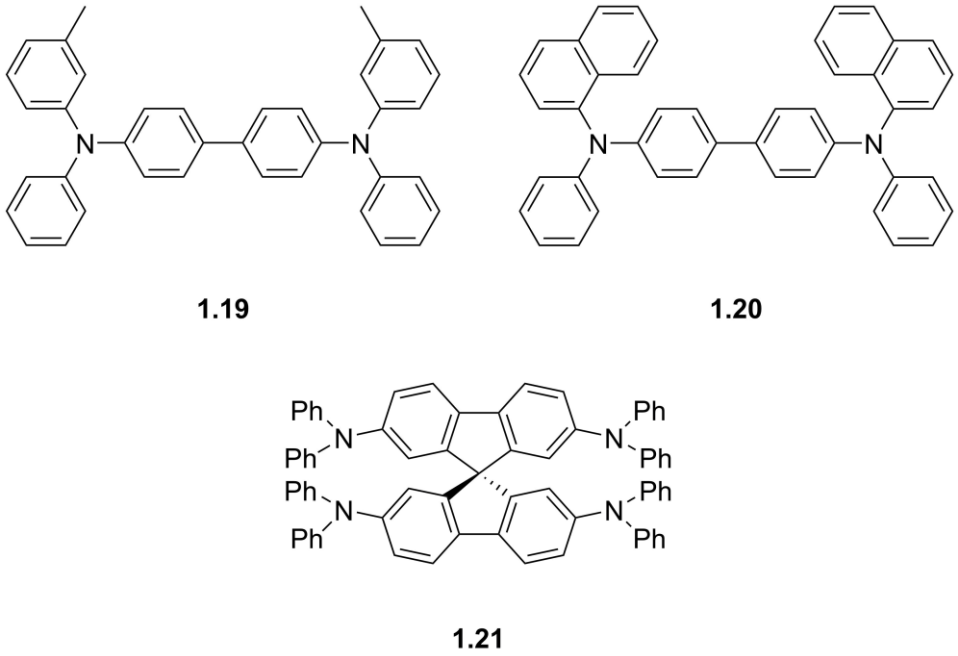

Figure 1.18 - Structure of hole transporting materials **1.19**–**1.21**

The closely related material NPB (*N*,*N*'-di(1-naphthyl)-*N*,*N*'diphenyl-(1,1'-biphenyl)-4,4'-diamine, **1.20**, Figure 1.18) is also used as an interlayer.[70] Though both are solution processable, the bulkier naphthyl substituents in the later result in a higher glass transition temperature (96 °C versus 65 °C). The result of this is that films of **1.20** will have longer term morphological stability, making it more practical in devices.[71] Derivatives of both which can be cross-linked have also been reported; this improves the thermal stability and allows subsequent layers to be solution deposited.[72]

Starburst materials featuring a triphenylamine core and three, often identical, branches have also been used as hole transport layers.[73,74] Though these have slightly higher glass transition temperatures than the linear arylamines, by including a spiro centre the glass transition is further increased. For example spiro-TAD (2,2',7,7'-tetrakis-(diphenylamino)-9,9'-spirobi-fluorene, **1.21**, Figure 1.18) has a reported glass transition of 133 °C, giving it a significantly higher morphological stability than the equivalent linear compound.[75]

Electron withdrawing groups such as aromatic heterocycles are often included in materials for electron transport layers. Alq_3 (**1.7**) provided the dual function of emissive layer and electron transport layer in the device produced by Tang and Van Slyke.[28] Alq_3 is still used in devices today due to its favourable thermal stability and film forming properties.[71,76]

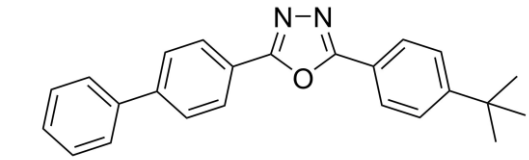

1.22

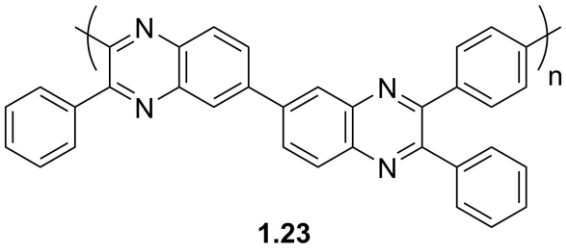

1.23

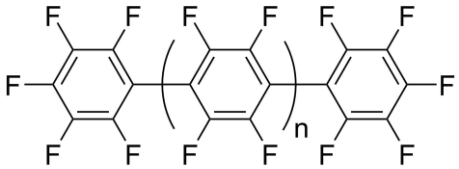

1.24

Figure 1.19 - Structure of electron transporting materials **1.22**–**1.24**

Due to their electron deficient nature oxadiazoles are another widely studied class of electron transport materials, a typical example is butyl PBD (2-(biphenyl-4-yl)-5-(4-tert-butylphenyl)-1,3,4-oxadiazole, **1.22**, Figure 1.19).[77] Inclusion of a butyl PBD layer results in significant improvement in LED performance, up to 1000 times over the equivalent device. However due to the low T_g (~60 °C), films of this material can crystallize even at room temperature, having a detrimental effect on device lifetimes.[77,78] As with the hole transporting materials mentioned previously, starburst and spiro oxadiazole derivatives have been made to improve the thermal properties of the linear material while maintaining the electron transport properties.[71,77,79]

In addition to small molecules, polymers such as PPQ (poly(phenyl quinoxaline), **1.23**, Figure 1.19) have also been used.[79,80] Here the electron deficient quinoxaline units along the backbone aid the transport characteristics. This led to improved device performances with a more uniform and brighter emissive layer than when the interlayer was not present.

Perfluorinated materials such as the perfluorinated oligo(p-phenylene)s (**1.24**, Figure 1.19, n = 3–6) also make good electron transport materials.[77,81] They have good thermal stability with no glass transitions, and tend to be soluble in fluorinated solvents enabling orthogonal processing.[82]

Overall, the selection of a material for an effective transport layer is based on many factors. Most importantly the material should have high mobility of the desired charge carrier, suitable LUMO and HOMO energy levels and high thermal stability.[77]

1.3.4 Device fabrication

The fabrication of the devices discussed above requires the inclusion of a thin film of organic material. Broadly speaking these layers can be constructed using evaporative techniques or solution processed techniques. Both may be involved in the fabrication of a device.[5]

Evaporative deposition is normally applied to small molecules, the most common methods being organic vapour phase deposition and vacuum thermal evaporation. As the name suggests, vacuum thermal evaporation requires the material to be heated while under high vacuum. With a controllable sublimation, multiple layers may be deposited with great control allowing complex device architectures to be constructed. This technique is typically only applicable with molecular weights below 1000 Da, and the wastage can be very high.

Organic vapour phase deposition uses an inert carrier gas in a hot walled vessel, without the need for high vacuum. It allows production of a highly uniform layer with effective control of the morphology.[83]

Solution processed techniques include inkjet printing, spin-coating and drop casting.

During spin-coating the solution is dropped onto the substrate which then rotates at a pre-set speed. The solution spreads and flies off the edges of the substrate, simultaneously the solvent will be evaporating leaving behind a film. The thickness can be influenced by varying the solution concentration or rotational speed. Solvent properties can affect the film formation, so choice of solvent is crucial.[84]

Inkjet printing can be used effectively to deposit materials over a large area with a great degree of precision. There is less wastage then with spin-coating, and the film thickness is also easily controlled. However, materials must be highly soluble and the formulations used are more complex than the simple solutions used in spin-coating. The resolution is significantly limited by the droplet size, but may be improved by using non-wetting regions to repel the ink, directing the organic semiconductor into a narrow channel, while also promoting alignment.[5,85] This technique is very suited to

roll-to-roll processing, a continuous manufacturing process which would lead to lower production costs.[86]

Care must be taken when fabricating multilayer devices by solution processing, as any solvents used can re-dissolve the underlying layers. This can lead to mixing of layers at the surface rather than the desired well defined interface. One way to circumvent this problem is through orthogonal processing, whereby each material is dissolved in a solvent that the other components are insoluble in. In some cases this can be achieved with careful choice of solvents, however many materials used in organic electronic devices have similar solubility. Another solution is to include functional units which can be cross-linked after deposition as this reduces the solubility of the material allowing further layers to be added by solution processing.[71,87]

There are problems with organic electronic devices that still need to be addressed, such as sensitivity to oxygen and water. To improve the device lifetimes they are normally encapsulated; while glass can be used, this adds both weight and cost. There is research into developing lightweight, flexible, encapsulation layers which are normally thin films. For example an Al_2O_3/polymer film prevented the ingress of water leading to a lifetime of 3800 hours.[88–92]

1.4 Truxenes

Truxene (10,15-dihydro-5*H*-diindeno[1,2-*a*;1′,2′-*c*]-fluorene, **1.25**, Figure 1.20) is a planar heptacyclic polyarene which possesses C_{3h} symmetry, and a rigid π conjugated structure. Truxene may be viewed as three overlapping fluorene units, thus it might be expected that this compound will have similar reactivity and properties. However, the star-shaped architecture can impart truxene and its derivatives with some different electronic properties such as degeneracy of the HOMO and LUMO.[93–95] These molecules have been investigated as intermediates in the synthesis of fullerenes, liquid crystalline compounds, sensors, and OLEDs.[96–100]

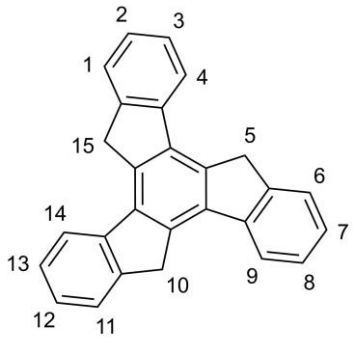

1.25

Figure 1.20 - Structure of truxene (**1.25**) showing numbering

Easily synthesised by an acid catalysed cyclotrimerisation, truxene is formed from an aldol condensation reaction of 1-indanone.[101] Truxene is often functionalized in the 5, 10 and 15 positions, as numbered in Figure 1.20, for a number of reasons.

The first is to aid solubility, as ‘bare’ truxene is very sparingly soluble in organic solvents. These positions are also susceptible to photo-oxidation, so by blocking them the stability of the material is improved. Another fundamental reason is to hinder π-π stacking interactions, as aggregation reduces the PLQY of fluorescent conjugated systems.

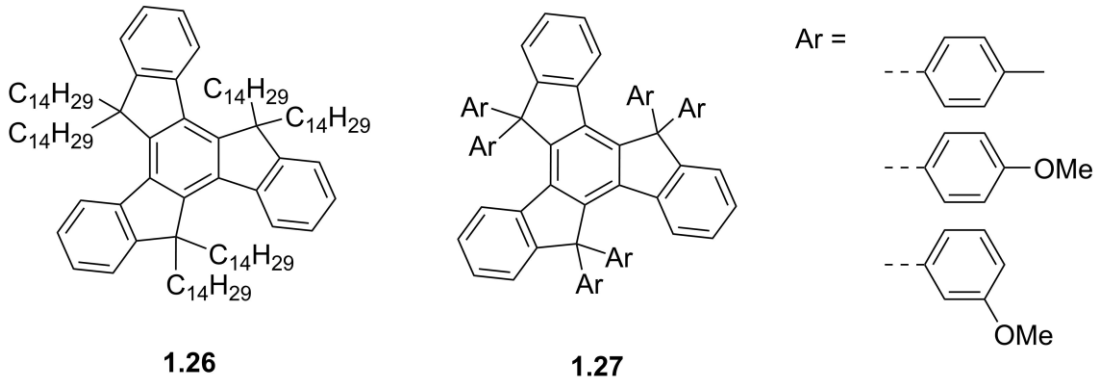

Figure 1.21 - Structure of truxenes functionalised with alkyl chains (**1.26**) and aryl groups (**1.27**)

The simplest truxene derivatives involve alkyl chains in these positions, for example compound **1.26** shown in Figure 1.21.[102] Aryl groups can also be added, for example **1.27** in Figure 1.21.[103] In this case the aryl groups modified the properties of the core, whereas the alkyl analogue did not.

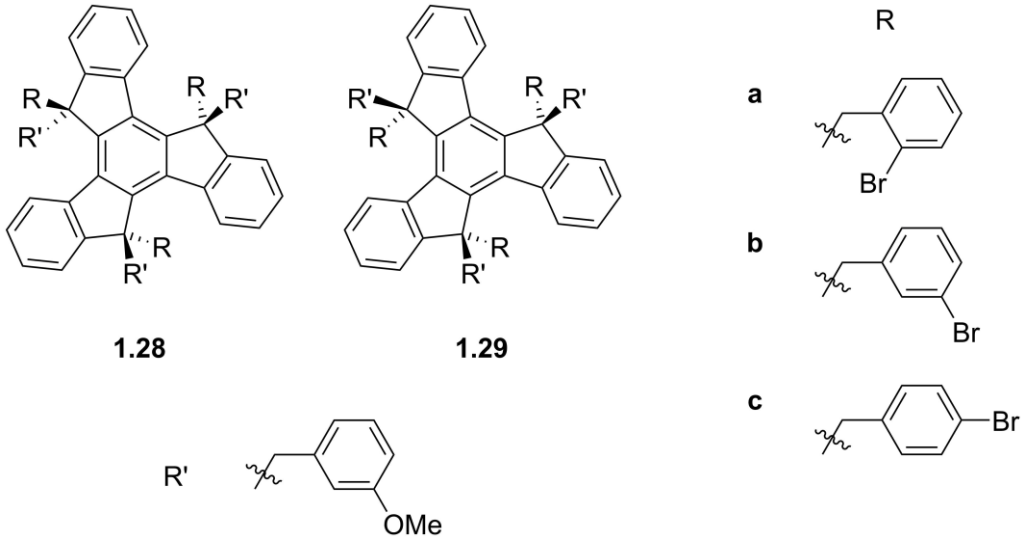

Figure 1.22 - Structure of *anti*- and *syn*-hexaalkylated truxenes, **1.28** and **1.29**

Though the six substituents are normally identical, unsymmetrical alkylation is possible by varying the amount of base used during the synthesis.[104] The authors report that this gave a mixture of *anti*- and *syn*-hexaalkylated compounds (**1.28** and **1.29** respectively, Figure 1.22), which could be separated by column chromatography. They propose that these materials could be used as the building blocks for larger structures.

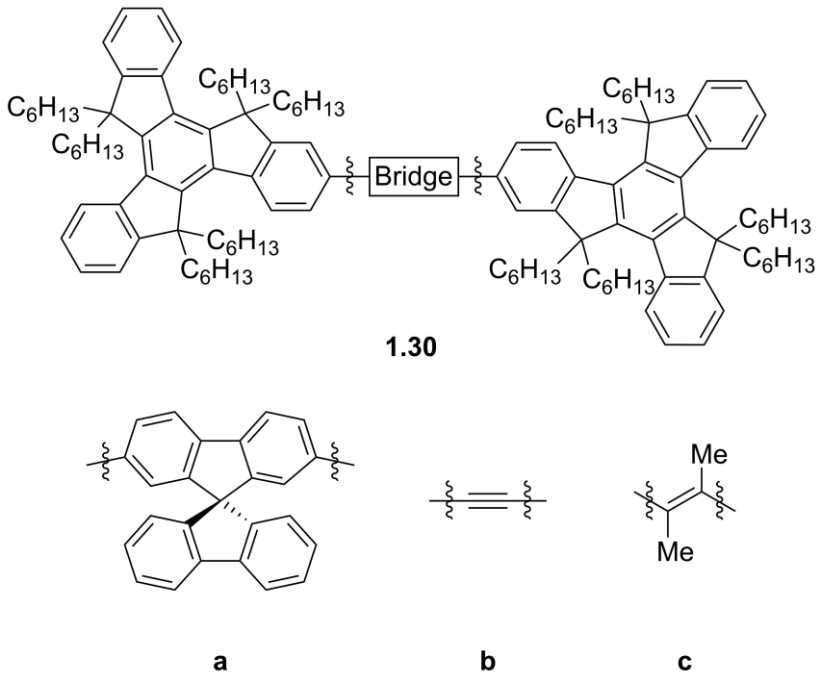

Figure 1.23 - Structure of bridged truxene **1.30**

Bridged molecules (**1.30**, Figure 1.23), where two molecules of hexahexyl truxene are connected by either spirobifluorene, ethynylene, or vinylene, were synthesised by Pei *et al.*.[105] The optical properties of these molecules are dependent on the π-linkage used: the spirofluorene bridged **1.30a** reduced π-π aggregation, whereas the emission of **1.30b** and **1.30c** were red shifted. The latter showed no vibronic structure, suggesting that the vinylene bridge does not allow extended conjugation between the cores. The authors propose that the conjugated materials **1.30a** and **1.30b** be applied as blue emitting materials.

In addition to small molecules, a great deal of research has been reported on truxene based oligomers. Almost all of these reports involve cross coupling reactions to functionalise the 2, 7 and 12 positions. These star shaped molecules have good thermal properties and the optical properties are tuneable. For example, by varying the length of oligothiophene arms in compounds **1.31a**–**d** (Figure 1.24) Pei *et al.* found that the π-π* absorption band of the oligothiophene was progressively red shifted. The authors note that compounds **1.31a**–**d** were also red shifted relative to their poly(thiophene) analogue, and suggest that this is a result of conjugation through the truxene core.[106]

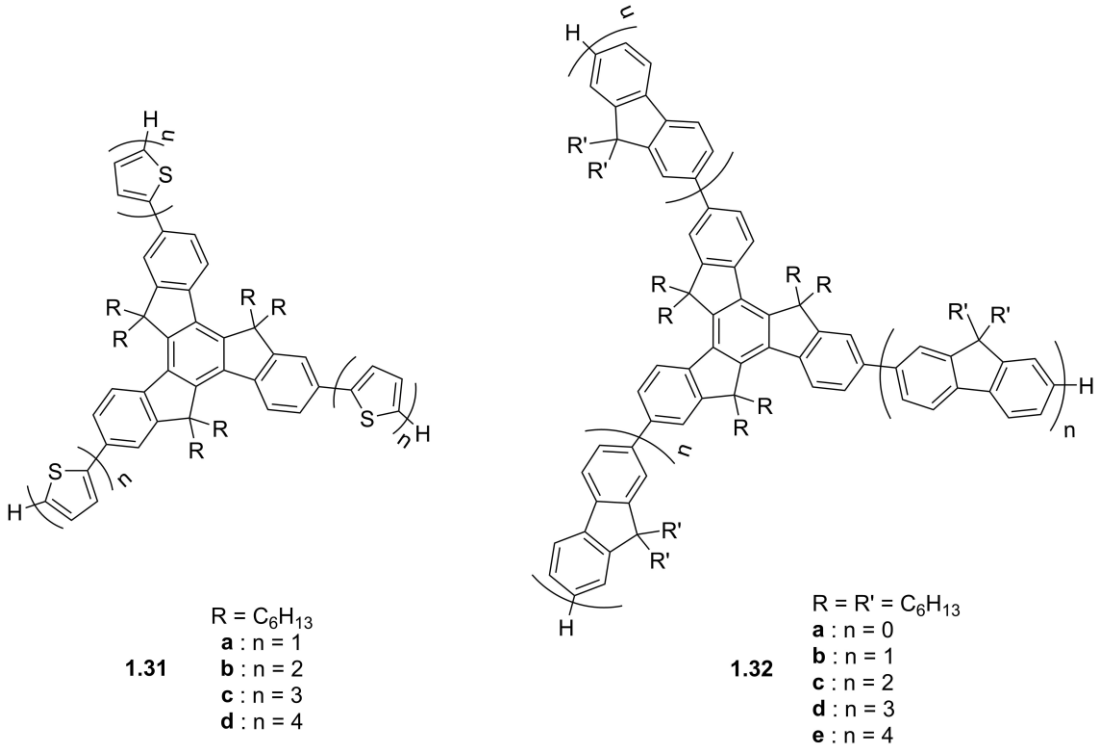

Figure 1.24 - Structure of truxene based oligomers **1.31** and **1.32**

Compounds **1.31a**–**c** were applied in organic field effect transistors where they demonstrated a reduction in mobility on increasing conjugating length, this is attributed to a transition from a polycrystalline state to an amorphous state.[107]

Skabara *et al*. attached oligofluorene arms of various lengths to a central truxene, **1.32b**–**e** in Figure 1.24, and found that these materials had high thermal and electrochemical stability.[108] These oligofluorene arms act as antennae, and dominate the electronic spectra of molecules **1.32c** to **1.32e**.[94] Increasing the chain length increases the conjugation length and results in a red shifted absorption spectra.

Through density functional theory calculations of their methyl analogues, molecules **1.32a** and **1.32b** were found to have degenerate frontier MO's. This orbital degeneracy is also present in the electronic structure of the star shaped system with truxene core and bithiophene arms **1.31b**, which is a π-isoelectronic analogue of **1.32b**. When compared to the corresponding energy levels of **1.32b**, the degenerate HOMO's of **1.31b** are destabilised by 0.12 eV due to the more electron rich thiophene units, whereas the LUMO's of this bithiophene system are significantly stabilised by 0.24 eV as a result of the less aromatic nature of the thiophene π-electronic system and its greater contribution to a quinoid resonance structure.[94]

The two-dimensional architecture provided by the truxene core has been shown to enhance the lasing properties relative to other fluorene based emitters. For example, polyfluorene based lasers have a reported threshold intensity of 58 kW cm^{-2} while **1.32d** and **1.32e** lasers have much lower thresholds of 2.1 kW cm^{-2} and 4 kW cm^{-2}, respectively. Compound **1.32d** exhibits a large tuning range of 51 nm, an improvement on 39 nm of polyfluorene.[109–112] Lately **1.32d** has been applied as a laser for biosensing applications, where it has been shown to selectively detect the binding of a small molecule to a protein.[113]

Skabara *et al.* also synthesised a series of oligomers based on compound **1.32e** with a 2,1,3-benzothiadiazole unit sequentially inserted in each position along the arms.[114] These soluble, green-yellow emitting compounds displayed varying absorption and photoluminescent properties depending on the position of the benzothiadiazole.

As with the oligomers previously discussed, in most instances the arms attached to the 2, 7 and 12 positions are identical. However, there are some examples where this is not the case: Ziessel *et al*. attached three different dyes (which absorbed in the yellow, green and blue regions of the visible spectrum, Figure 1.25) to a central truxene. The resultant supermolecular structure absorbs light from across the visible spectrum, while the emission spectrum is dominated by the green dye. This intramolecular quenching occurs irrespective of the excitation wavelength.[115,116]

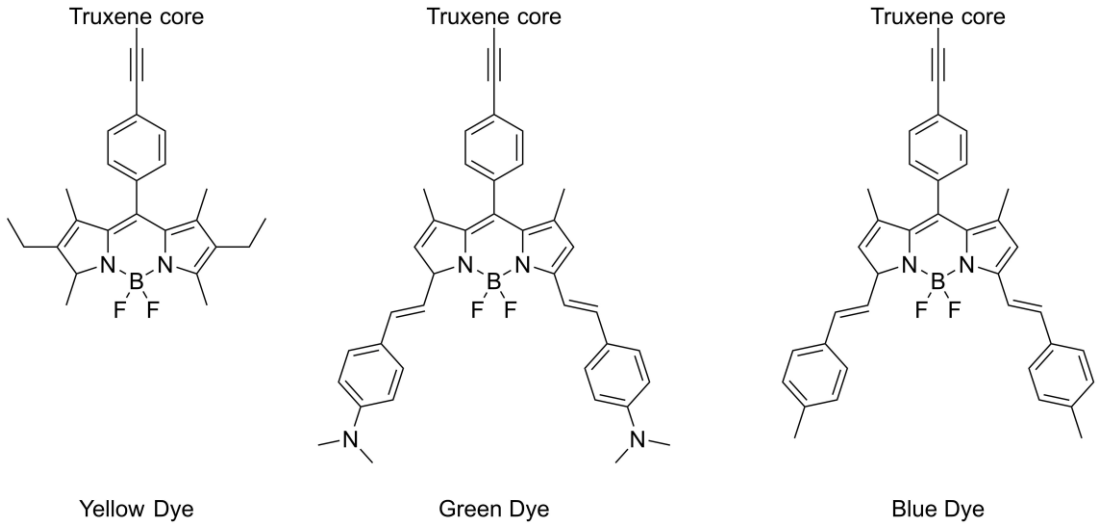

Figure 1.25 - Structure of dyes

Another application of truxene based materials is as a hole transport layer in devices, with examples shown in Figure 1.26. Huang *et al*. used molecule **1.33** as an interlayer in a perovskite solar cell and found that the molecule increased the surface contact angle and improved the density of the adjacent perovskite film compared to PEDOT:PSS. The nearly transparent films absorbed UV light, which can degrade perovskites, and increased the PCE to 18.6% from 8.61% without a hole transport layer.[117,118]

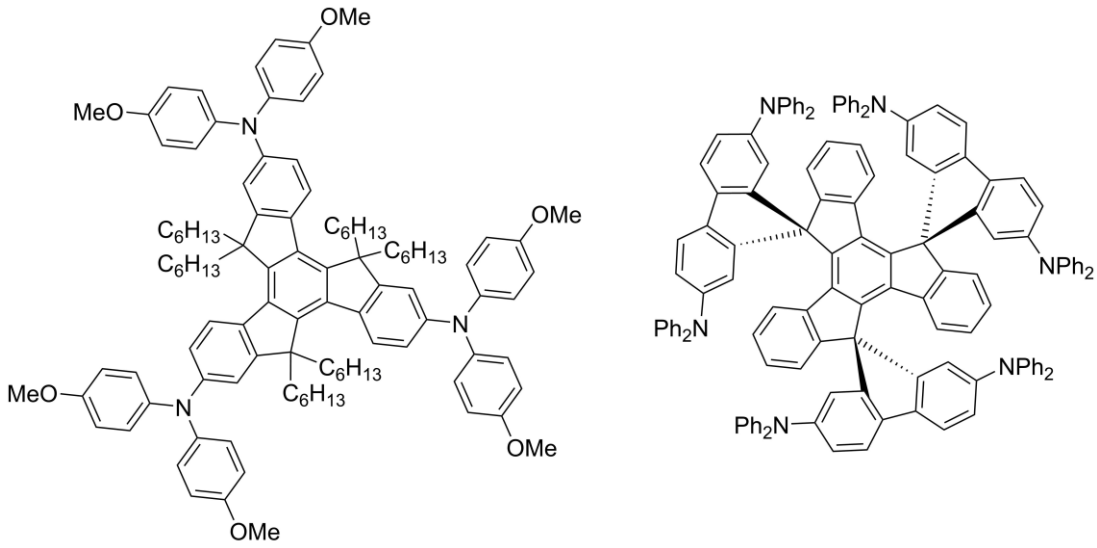

1.33 **1.34**

Figure 1.26 - Structure of truxene based hole transport materials **1.33** and **1.34**

A similar material with propyl chains at the X, X'-positions was reported in the same year. This propyl derivative demonstrated excellent thermal stability and a more modest increase in PCE.[119]

The spiro compound **1.34** (Figure 1.26) forms an amorphous film with a high T_g of 170 °C. The material showed three reversible waves in cyclic voltammetry, and when applied in an OLED the device lifetime was substantially increased compared to those with other non-truxene hole transport layers.[120]

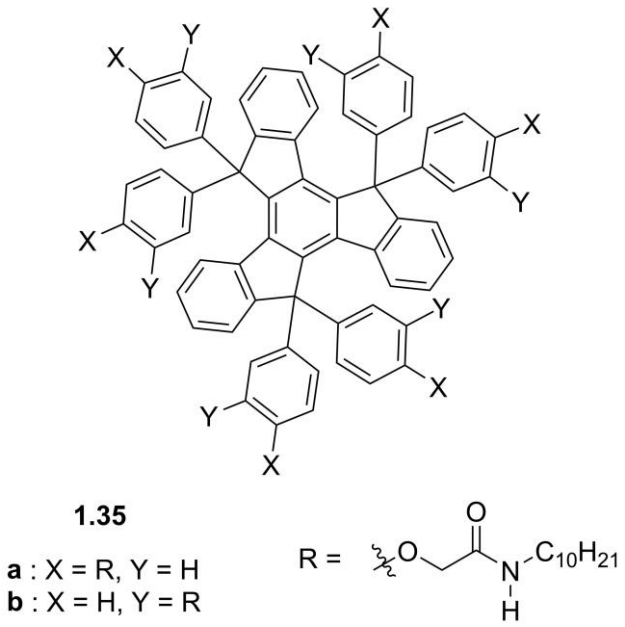

Figure 1.27 - Structure of truxene based gelator **1.35**

Truxenes have been shown to self-assemble, for example compound **1.26** forms an ordered layer on a surface of highly oriented pyrolyted graphite due to the interdigitation of the long alkyl chains.[102] In non-polar solvents compound **1.35** (Figure 1.27) reversibly forms a gel. The different substitution pattern led to the formation of different nanostructures: the *para* substituted **1.35a** formed into hollow spheres that aggregate into clusters with a pearl-necklace-like morphology, whereas the *meta* substituted **1.35b** formed filaments and sheet like morphologies, which were found to consist of thin filaments twisted into helical bundles.[121]

Self-assembly of truxene materials in solution has been demonstrated by Echavarren *et al*., who have synthesised a series of *syn*-trialkylated truxenes **1.36** (Figure 1.28). These molecules show varying levels of association, poor solubility hampers some, while the tribenzyl derivatives demonstrate the strongest association. No corresponding effect was observed for the less stable *anti*-derivatives.[122–124]

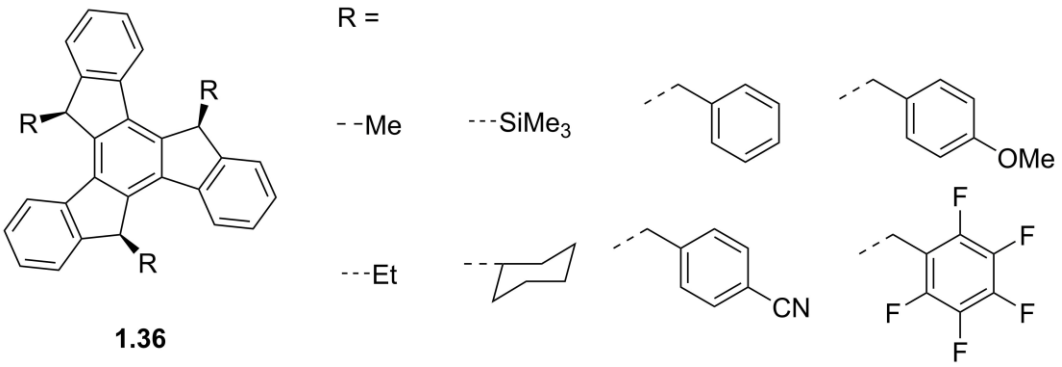

Figure 1.28 - Structure of *syn*-trialkylated truxenes **1.36**

Furthermore, nanofibres were formed from **1.37** (Figure 1.29), where the hydrogen bonds provide a strong tendency to self-assembly in the vertical direction. This rigid structure reduces self-quenching in the solid state, allowing the material to retain its fluorescence. When functional groups were added to the side chains their photophysical properties were not altered by the self-assembly in the solid state.[95,125,126]

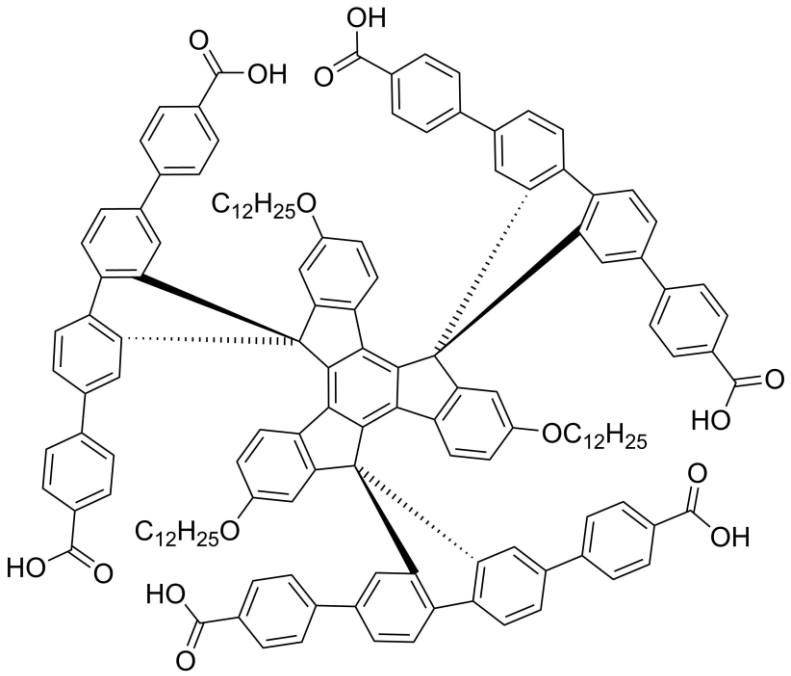

1.37

Figure 1.29 - Structure of spirotruxene hexaacid **1.37**

2 TRUXENE TRICARBOXYLIC ACIDS

2.1 Introduction

As discussed in the previous chapter, device performances can be improved through the inclusion of interlayers. The performance of these interlayers, and thus the whole device will be improved if the morphology can be controlled; this can be achieved through the use of templating layers.[127–130] Templating layers are normally included in vacuum deposited devices as it is easier to build complex device architectures, see Section 1.3.4.

Due to its planar structure, truxene is a promising scaffold to develop a self-assembled monolayer which can act as a templating layer in devices. Materials based on truxene have outstanding thermal stability, which is an important factor for vacuum deposited materials. Furthermore, the self-assembly of truxene based molecules has been reported as presented in Section 1.4.

Previous work carried out within the Skabara group has shown that truxene derivatives do self-assemble on highly ordered pyrolytic graphite.[131] The scanning tunnel microscope (STM) images in Figure 2.1 shows that regular films are formed; these films have order at the molecular level.

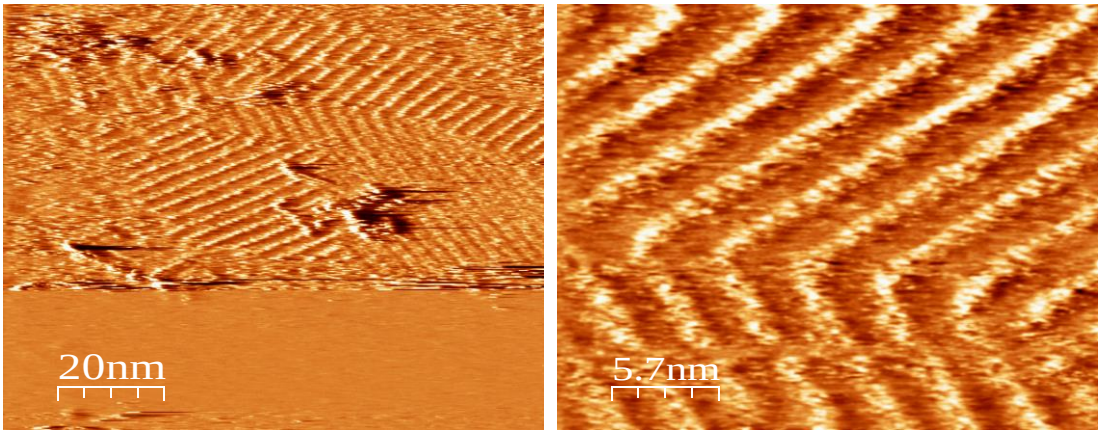

Figure 2.1 - STM images showing self-assembly of a truxene based material on highly ordered pyrolytic graphite

As with most truxene compounds discussed in Section 1.4, the compounds used in this previous work are oligomers with long alkyl chains at the 5, 10 and 15 positions. Small molecule derivatives functionalised with short alkyl chains would be expected to lay flat on the surface of the substrate, providing a molecular template to encourage subsequent layers to order in a similar fashion. Normally short chains are insufficient to prevent aggregation, however as these materials were to be used as monolayers, this was not envisaged as being a concern for this work.

The initial targets were tricarboxylic acids as this functional group exhibits strong hydrogen bonding, which can promote molecular self-assembly.[125,132] The target tricarboxylic acids have molecular weights ranging from 558 to 811 Daltons, making these materials suitable candidates for vacuum deposition.

2.2 Synthesis

The synthesis of four tribromotruxene derivatives is shown below in Scheme 2.1. Firstly the truxene core, **1.25**, is formed from the cyclisation of commercially available 1-indanone. This reaction proceeds with high yields (82%) and due to the low solubility of truxene any remaining starting material or soluble by-products are easily washed away.

To aid solubility, alkylation of this core is then carried out. Though the most acidic protons are at the 5, 10, and 15 positions, an excess of *n*-butyllithium and alkyl halide was required to drive this six-fold reaction to completion. Due to the very similar polarities of the desired hexaalkylated and the undesired lower alkylated truxenes, separation of the desired material was non-trivial in all cases. It was found that the hexaalkyl truxene derivatives could be recrystallised from boiling acetonitrile, allowing the desired products to be isolated in suitably high purities.

Formation of the hexamethyl derivative, **2.1**, was problematic due to precipitate formation. Though the truxene trianion is soluble, on reaction with iodomethane the anion is quenched and the resultant neutral species is assumed to be less soluble. This underalkylated material precipitates from solution, meaning it is not as available to react with the second portion of *n*-butyllithium added. This resulted in a yield of only 7.9%, whereas compounds **2.2**–**2.4** have improved solubility so can be prepared with yields of 79–85%.

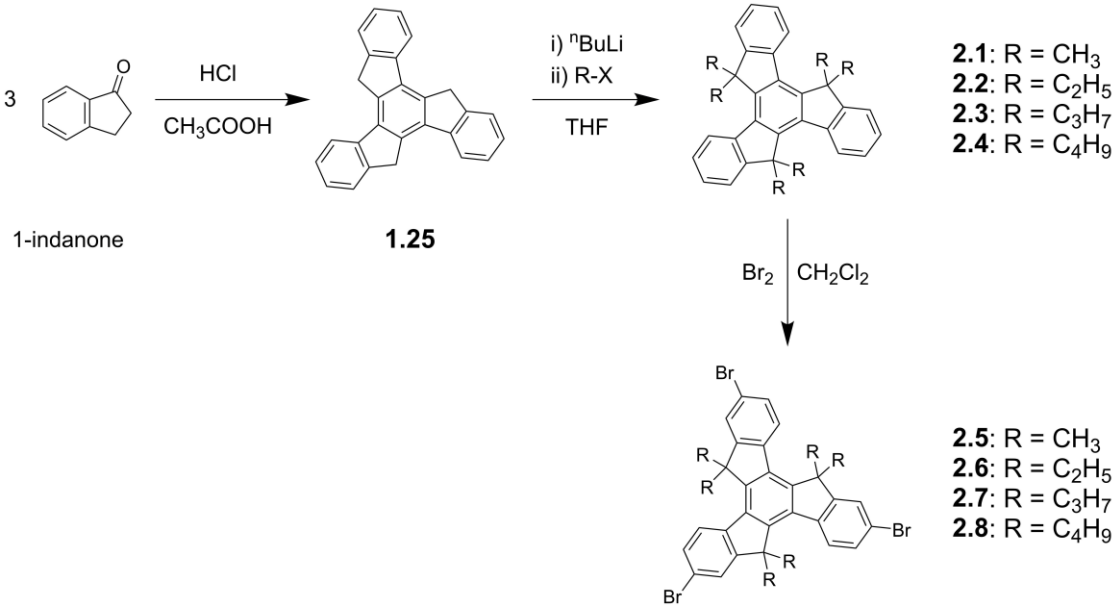

Scheme 2.1 - Synthesis of tribromotruxene derivatives **2.5**–**2.8**

These compounds were easily brominated to give the tribromotruxenes, **2.5**–**2.8**, in high yields (70–97%) following recrystallisation to remove under brominated material. The brominated derivatives may themselves be interesting as there is potential for self-assembly through Br---Br intermolecular interactions, a well-known non-covalent interaction in supramolecular chemistry.[133]

Originally the final conversion was to be achieved by lithium halogen exchange followed by addition of an alkoxycarbonyl chloride to form an ester, as shown below in Scheme 2.2. It was hoped that this ester would be easy to purify and could subsequently be cleanly converted to the desired tricarboxylic acid. Compound **2.8** was initially chosen to trial conditions as the longer alkyl chains would aid solubility.

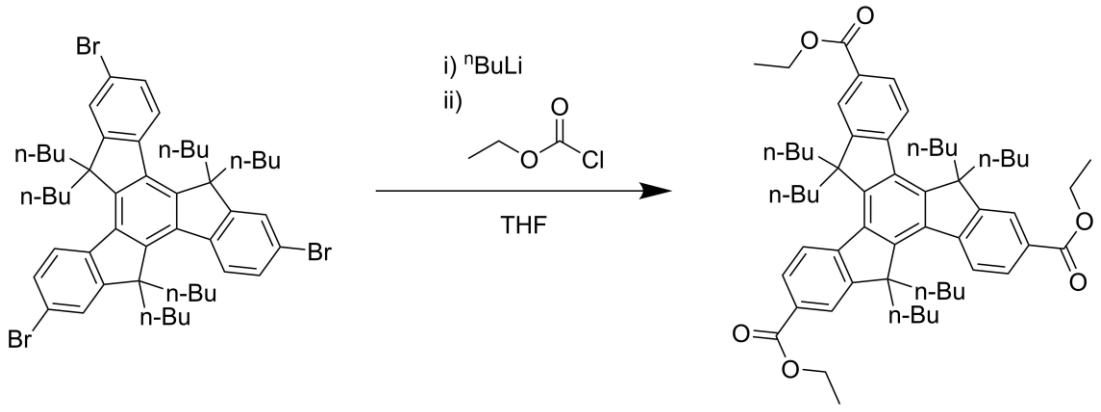

2.8 **2.9**

Scheme 2.2 - Synthesis of triester **2.9**

Initially the reaction was carried out at 0 °C, however this was lowered to −80 °C in an attempt to stop the lithium trianion being quenched before the addition of ethyl chloroformate. Though this reaction worked, it was low yielding due to the formation of a complex mixture of products which were difficult to separate. Nonetheless it was possible to isolate the hexabutyl triester, **2.9**, but in only 36% yield. In an attempt to improve this procedure, an alternative approach was investigated. Through lithium halogen exchange followed by addition of carbon dioxide, the desired products could be directly obtained as shown in Scheme 2.3.

This final step initially proved challenging as some of the corresponding mono- and dicarboxylic acid was also formed. It is expected that the trilithium species are formed quantitatively, but will react immediately with any water present to add a proton at one of the three reaction sites, as observed during the synthesis of **2.9**. Due to very similar and high polarities, the mono- and dicarboxylic acids could not be separated from the desired product by column chromatography.

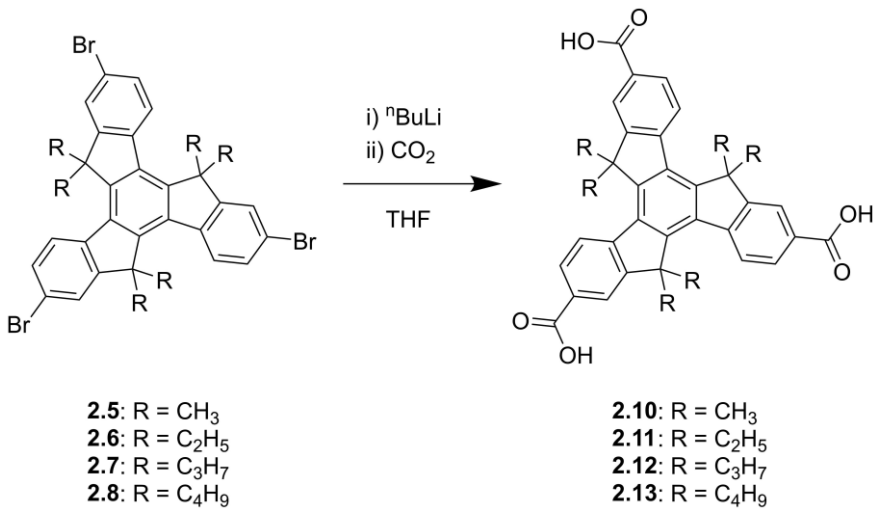

2.5: R = CH_3
2.6: R = C_2H_5
2.7: R = C_3H_7
2.8: R = C_4H_9

2.10: R = CH_3
2.11: R = C_2H_5
2.12: R = C_3H_7
2.13: R = C_4H_9

Scheme 2.3 - Synthesis of tricarboxylic acid derivatives **2.10**–**2.13**

Through stringent exclusion of moisture from the reaction mixture, including passing carbon dioxide through a dying tube, it was possible to purify the tricarboxylic acids through subsequent crystallisation. Slow diffusion of hexane into a THF solution of the acid mixture produced pure samples of compounds **2.10**–**2.13**; two of the crystals produced were of sufficient quality for x-ray diffraction, as discussed in Section 2.3.3. While yields for this step ranged from poor to good (31–80%), overall this was an improvement on the initially planned route as it also saved a synthetic step.

2.2.1 Karl Fisher titrations

There were difficulties in obtaining samples of **2.10–2.13** completely free from polar solvents, even after drying *in vacuo*. Therefore, the tricarboxylic acid was suspended in water and converted to the sodium salt by the addition of 3.3 equivalents (1.1 per acid functionality) of sodium hydroxide solution. After filtration, the solution was acidified to ~pH 2 using hydrochloric acid and the precipitate collected and dried to yield products with reduced solvent impurities for NMR analysis. Nonetheless some residual water remained, and this caused the elemental analysis to deviate from the expected results, as shown below in Table 2.1.

The water content could not be quantified from the ^{1}H NMR spectra as the solvent (DMSO-d_6) is hygroscopic; thus Karl Fisher titrations were used. This analytical technique is based on a coulometric titration as shown below in Scheme 2.4.

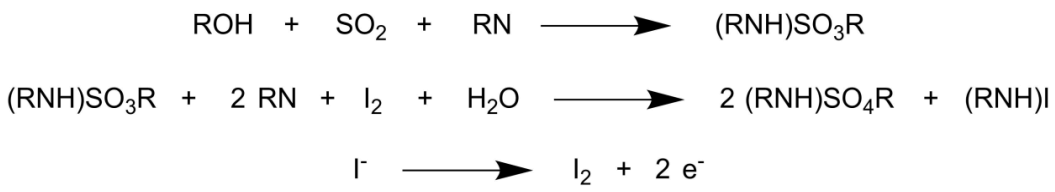

Scheme 2.4 - Karl Fischer titration

The iodine is generated electrochemically by anodic oxidation, along with electrons. Thus, when the water is depleted, I^- is no longer converted to iodine and no more electrons are produced. Therefore, the end point is evident as a rapid drop in voltage and this can be used to calculate the amount of water present.

In this case the tricarboxylic acids were dissolved in THF before titration; therefore the water content of the THF was also measured and subtracted from the final values.

The expected elemental analysis values were recalculated to account for the residual water content, however these values also deviated from those found experimentally suggesting that there is both residual water and THF present.

Table 2.1 - Water content of tricarboxylic acids **2.10**–**2.13**

Compound	Residual water		Elemental analysis					
	% w/w	$[H_2O]_x$ per molecule	Expected		Corrected		Experimental	
			C	H	C	H	C	H
2.10	11.5%	3.6	77.40	5.41	69.40	6.02	74.72	6.28
2.11	4.6%	1.6	78.48	6.59	75.01	6.81	76.83	6.67
2.12	7.2%	2.9	79.31	7.49	73.96	7.76	76.26	7.38
2.13	3.4%	1.5	79.96	8.20	77.31	8.32	80.16	8.69

Though the purity of these compounds could not be determined by elemental analysis, the identity of these compounds was confirmed by mass spectrometry. Furthermore, the ^{1}H NMR spectra showed no major impurities (spectra given as appendices in Chapter 9), thus it was decided to proceed with the characterisation.

2.3 Results and discussion

2.3.1 Optical and electrochemical properties

The optical properties of compounds **2.10**–**2.13** were measured in acetonitrile solution, with concentrations of 1×10^{-5} M and 1×10^{-6} M for absorption and emission, respectively. An excitation wavelength of 320 nm was used as this was close to the maximum absorbance of all four materials.

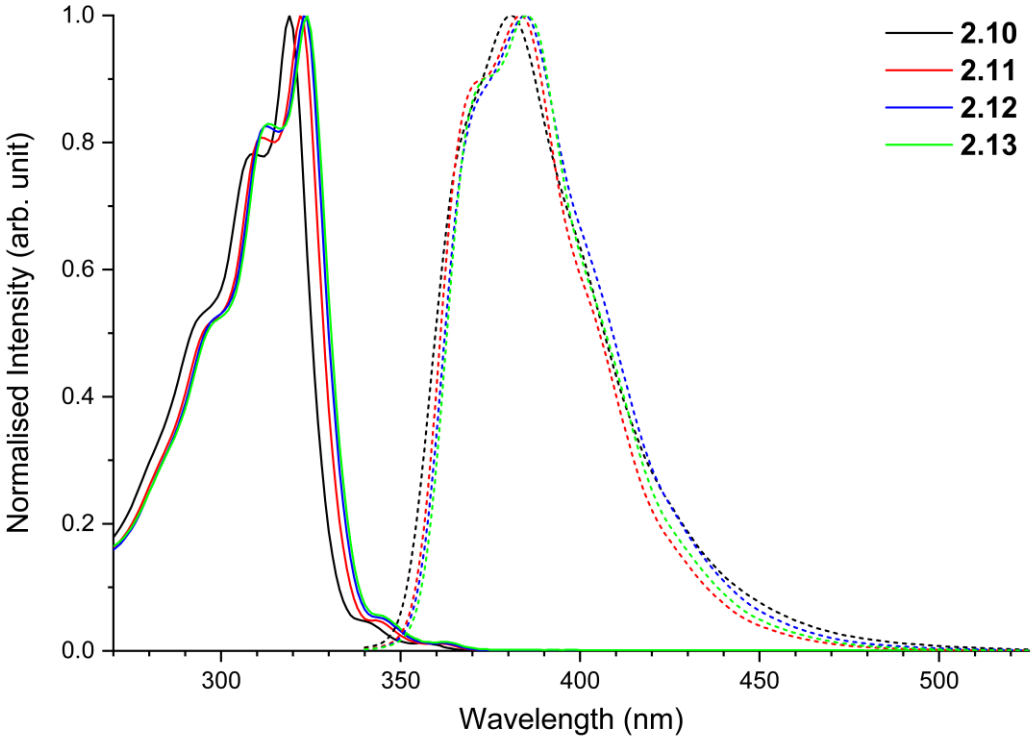

Figure 2.2 - Normalised absorption (solid lines, 1×10^{-5} M) and emission (dashed lines, 1×10^{-6} M) spectra of compounds **2.10**–**2.13** in acetonitrile

The absorbance and emission spectra showed little difference on altering the length of attached alkyl chain, with all compounds exhibiting a similar vibronic structure, as shown in Figure 2.2. The wavelengths of maximum absorption and emission vary by 5 nm and 4 nm respectively. These values are given in Table 2.2 along with the optical HOMO-LUMO gaps, which were calculated using Equation 1.3 and the onset of the longest wavelength of absorption. As the length of alkyl chain increases over the whole series, the optical HOMO-LUMO gap decreases slightly by 0.07 eV. As this is not a substantial change it can be surmised that altering the alkyl chain length does not significantly change the optical properties of these materials. The Stokes shift observed is 61–62 nm, while this is fairly large a monolayer of these materials should not alter the light output of devices.

Solutions of compounds **2.10**–**2.13** at various concentrations in THF were prepared and deposited by spin-coating onto quartz slides, the absorption and emission properties measured in the solid state and are shown in Figure 2.3. A rotational speed of 1500 rpm was used throughout, a test was conducted at 3000 rpm but this had no substantial impact on the films and spectra produced. In the absorbance spectra **2.10** shows the most intense shoulder of the four films. Due to the rigidity of this molecule it has fewer vibrational states available, therefore the observed excitation comes from discrete vibrational states. With increasing concentration there is a change in the packing, molecules are forced together and so cannot vibrate as freely, resulting in an increase in the intensity of the shoulder. As the length of the alkyl chain increases the shoulder becomes less defined; the chains interdigitate and have more room to move, therefore the absorption profile results from an average of all the vibrations.

Conversely, the emission spectrum of compound **2.13** has the most defined shoulder. The excited state of the butyl derivative will have a greater chance of vibrational relaxation, therefore can emit from various vibrational states. As the concentration is increased the denser arrangement of the molecules means that the chains will be forced to interdigitate more, suppressing some of the vibrations of the excited state which leads to the observed reduction of the shoulder.

On decreasing the alkyl chain length the molecule becomes less flexible, meaning the emission will come from a single vibrational state. Thus the shoulder is not observed for the more rigid **2.10**.

The absorbance of the films lacks the low energy shoulders observed in the solution state. This is due to the restricted degrees of freedom, meaning that the molecules in the solid state cannot access all of the vibrations possible in solution. In general the solid state absorption has a broader and slightly less defined vibronic structure. Both the absorption and emission are slightly red shifted by 5–11 nm, which is normally observed due to aggregation in the condensed state.

Table 2.2 - Optical and electrochemical properties of compounds **2.10**–**2.13**

Compound	**2.10**	**2.11**	**2.12**	**2.13**
$\lambda_{abs,\ solution}$ (nm)	294 (sh), 309, 319, 340, 357	296 (sh), 311, 322, 343, 361	297 (sh), 312, 323, 345, 362	298 (sh), 313, 324, 345, 363
$\lambda_{abs,\ film}$ (nm)	298 (sh), 315, 325	299 (sh), 316, 327	300 (sh), 317, 328	301 (sh), 317, 329
$\lambda_{PL,\ solution}$ (nm)	366 (sh), 381	370 (sh), 383	371 (sh), 384	373 (sh), 385
$\lambda_{PL,\ film}$ (nm)	390	378 (sh), 391	379 (sh), 392	379 (sh), 392
$E_{1/2}^{ox}$ (V)	1.28	1.35	1.31	1.24
E_p^{red} (V)	−2.40, −2.61	−2.48, −2.56	−2.52, −2.70	−2.53, −2.62
E_g^{UV} (eV)	3.84	3.80	3.78	3.77
E_g^{CV} (eV)	3.68	3.84	3.83	3.77

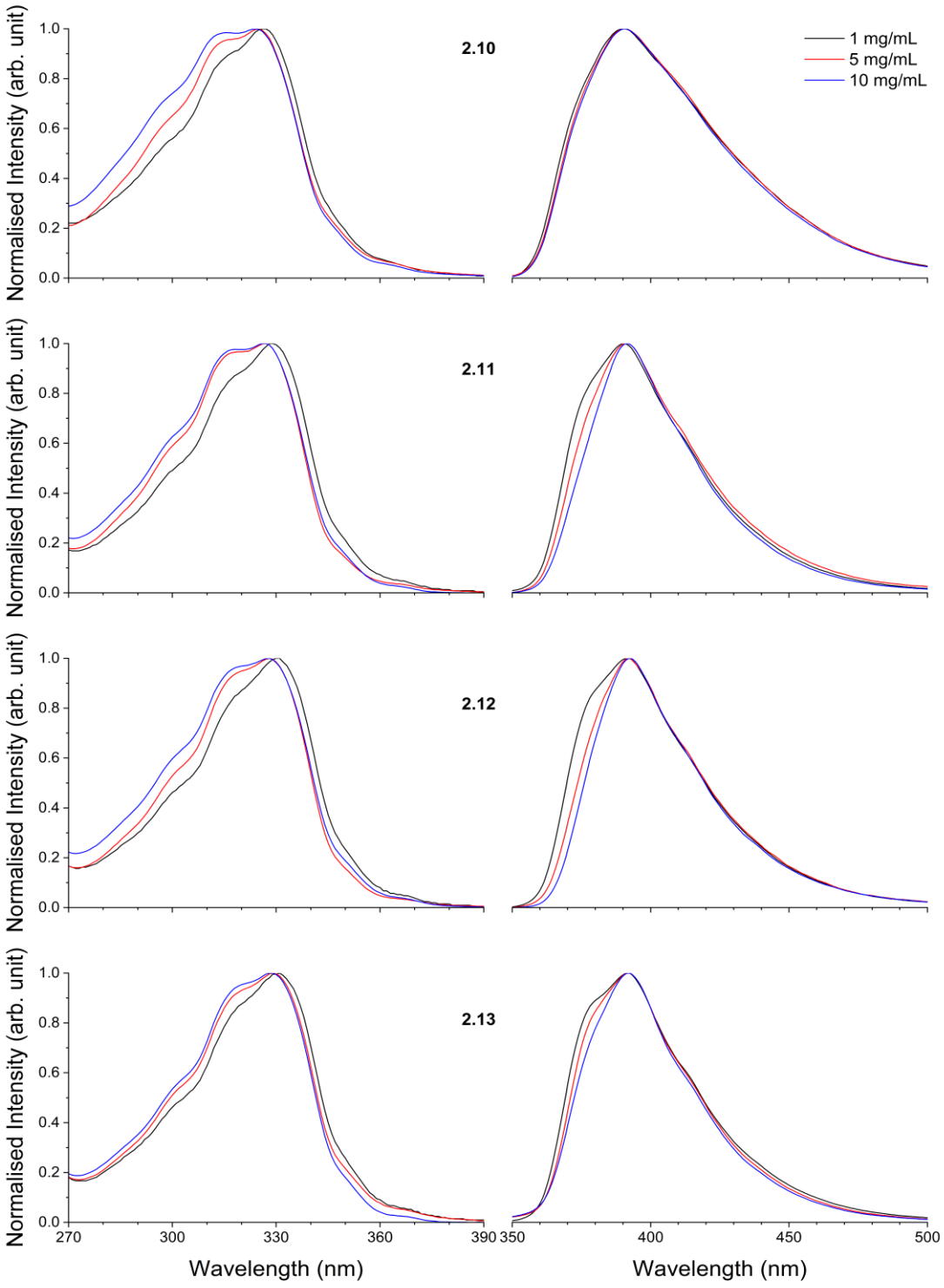

Figure 2.3 - Normalised absorption (left) and emission (right) spectra of films of compounds **2.10**–**2.13** spin-coated from THF solutions

Analogously, the alkyl chains do not appear to influence the electrochemical properties of compounds **2.10**–**2.13.** As observed in Figure 2.4 these materials have similar CV profiles, with a pseudo-reversible oxidation wave and two irreversible reduction waves. This data is referenced to the ferrocene/ferrocenium redox couple which has a known value, here taken to be −4.8 eV.[14] The positions of these waves are not significantly affected by the change in length of alkyl chain, see Table 2.2.

The optical and electrochemical HOMO-LUMO gaps do not change greatly across the series, indeed for compound **2.13** they are identical. For compounds **2.11** and **2.12** the electrochemical HOMO-LUMO gap is larger than the optical HOMO-LUMO gap, this is expected as the former includes the exciton binding energy. However, for compound **2.10** the optical HOMO-LUMO gap is 0.16 eV higher due to both the lower onset of the optical HOMO-LUMO gap and higher reduction potential.

Overall, altering the length of the alkyl chain does not greatly influence the optical and electrochemical properties; however it does have an impact on the thermal properties.

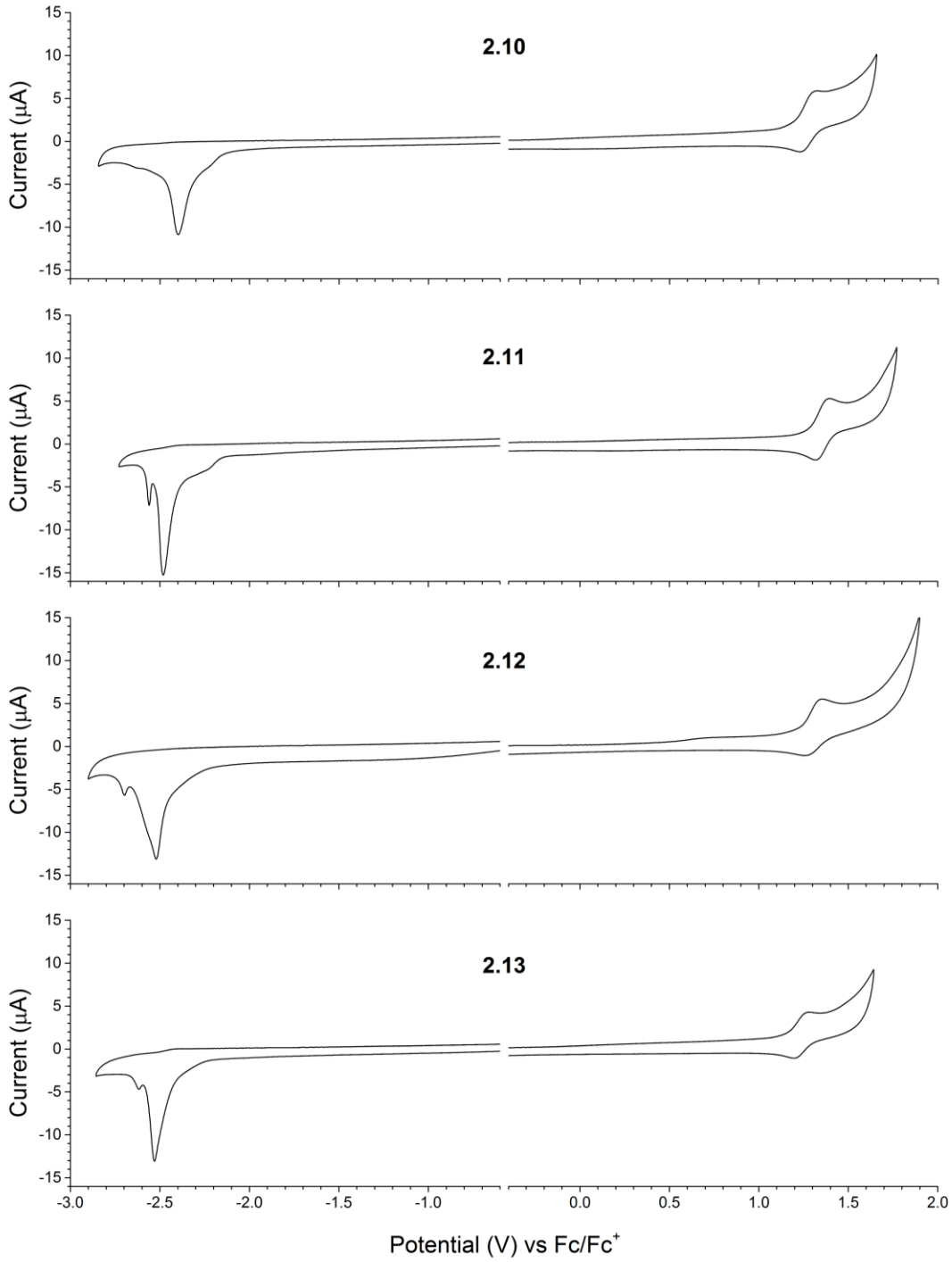

Figure 2.4 - Cyclic voltammagrams of compounds **2.10**–**2.13** in 10^{-4} M acetonitrile solutions. Obtained using a glassy carbon working electrode, platinum wire counter electrode and silver wire reference electrode, a scan rate of 100 mV s^{-1}, and 0.1 M *n*-Bu_4NPF_6 as the supporting electrolyte

2.3.2 Thermal properties

The thermal properties of the final tricarboxylic acids were assessed by thermal gravimetric analysis (TGA) and differential scanning calorimetry (DSC). The TGA graphs are shown in Figure 2.5 and summarised below in Table 2.3. No transitions were observed during DSC, Figure 2.6, and the melting points were all found to be above 350 °C.

The four compounds have similar TGA profiles, though 5% mass loss for compound **2.10** occurs at 193 °C, a much lower temperature than the longer chain analogues. Looking at the graph this appears to be due to the loss of bound water/solvent molecules as this gradual tail off then reaches a plateau. Additionally after heating to 300 °C there was no observable change in the ^{1}H NMR spectra of compound **2.10**. Using this flat region as the baseline, 5% mass loss for **2.10** is observed at 430 °C.

The onset of mass loss ranges from 348–429 °C, well above normal device operating temperatures. For all compounds there appears to be two processes occurring as the rate of mass loss decreases and then increases again. The onset of this second process is also included in the table below.

Table 2.3 - Thermal properties of compounds **2.10–2.13**

Compound	Onset of mass loss (°C)	5% mass loss (°C)	Mass remaining at 540 (%)
2.10	429, 494	430 [a]	40.3
2.11	367, 431	342	46.4
2.12	348, 413	350	41.1
2.13	378, 427	392	36.8

[a] recalculated using plateau as baseline

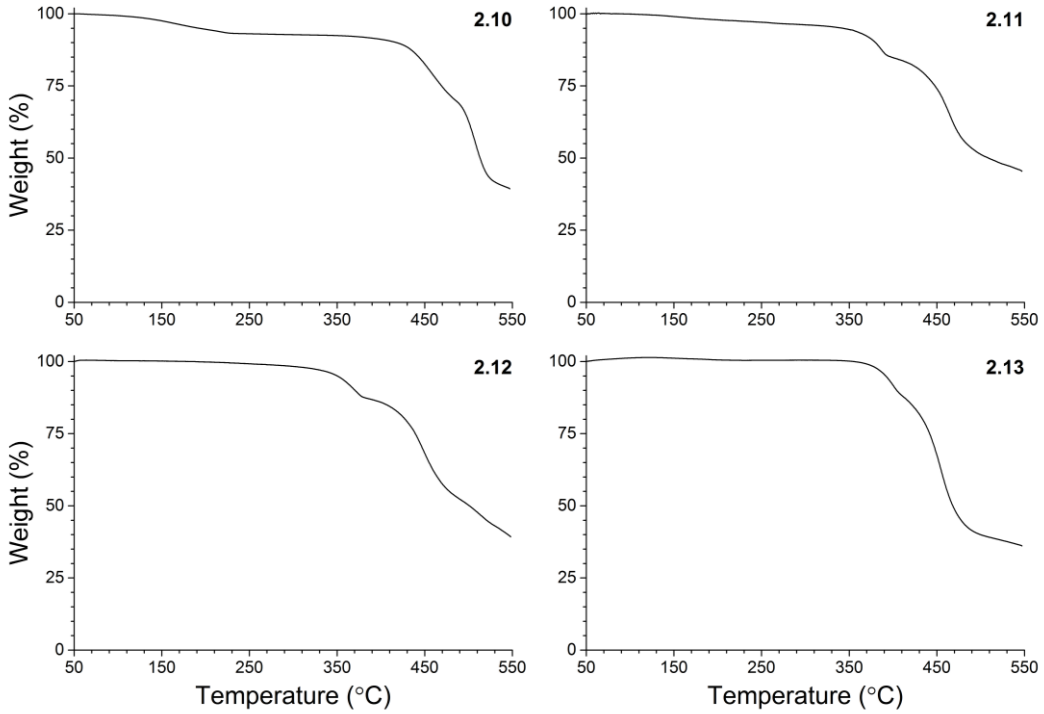

Figure 2.5 - TGA plots of compounds **2.10**–**2.13**, heating at a rate of 10 °C min^{-1} under argon

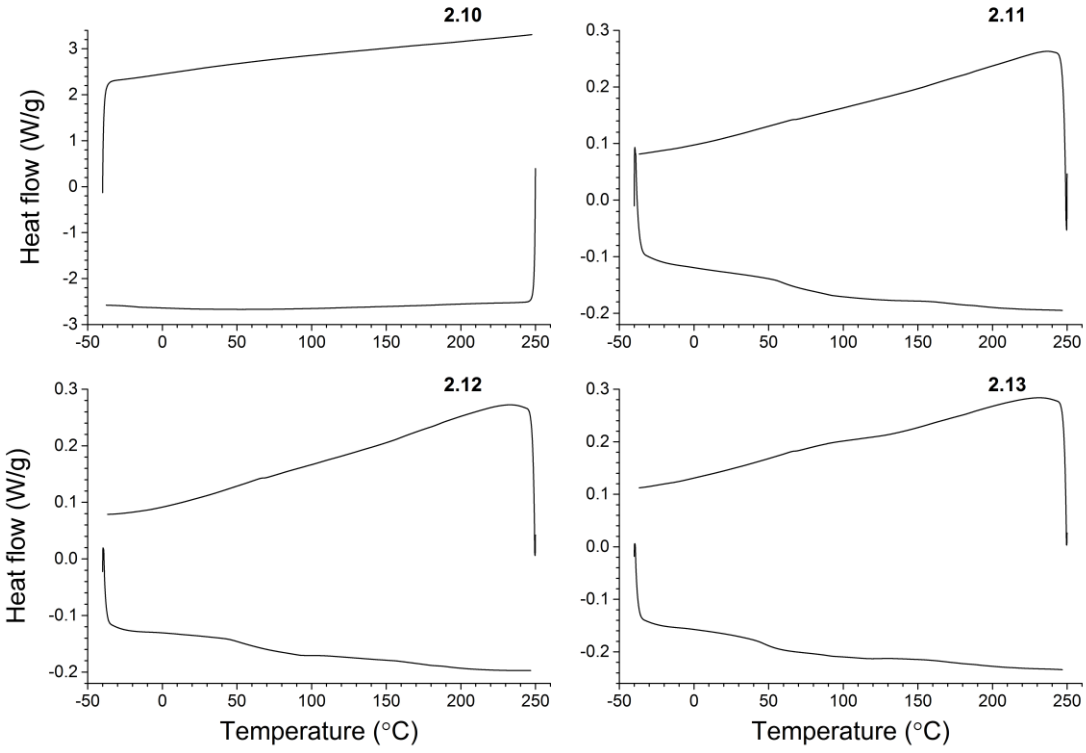

Figure 2.6 - DSC plots of compounds **2.10**–**2.13** during heat-cool-heat cycles, showing cooling from 250 °C to −40 °C, then heating from −40 °C to 250 °C at a rate of 10 °C min^{-1} under nitrogen

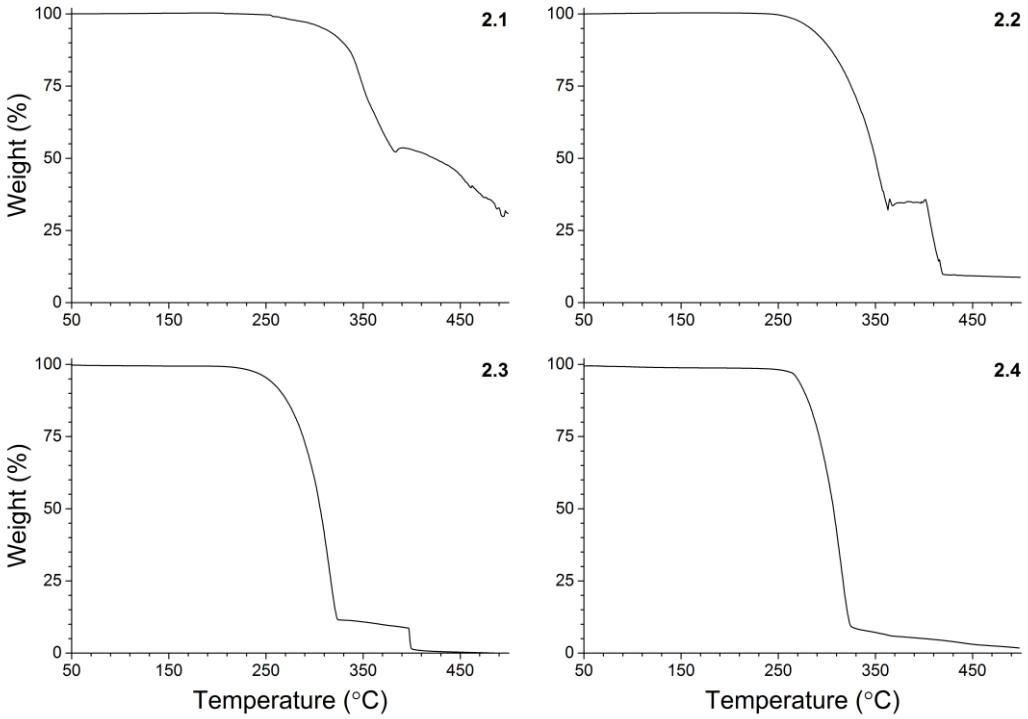

Figure 2.7 - TGA plots of compounds **2.1**–**2.4**, heating at a rate of 10 °C min^{-1} under argon

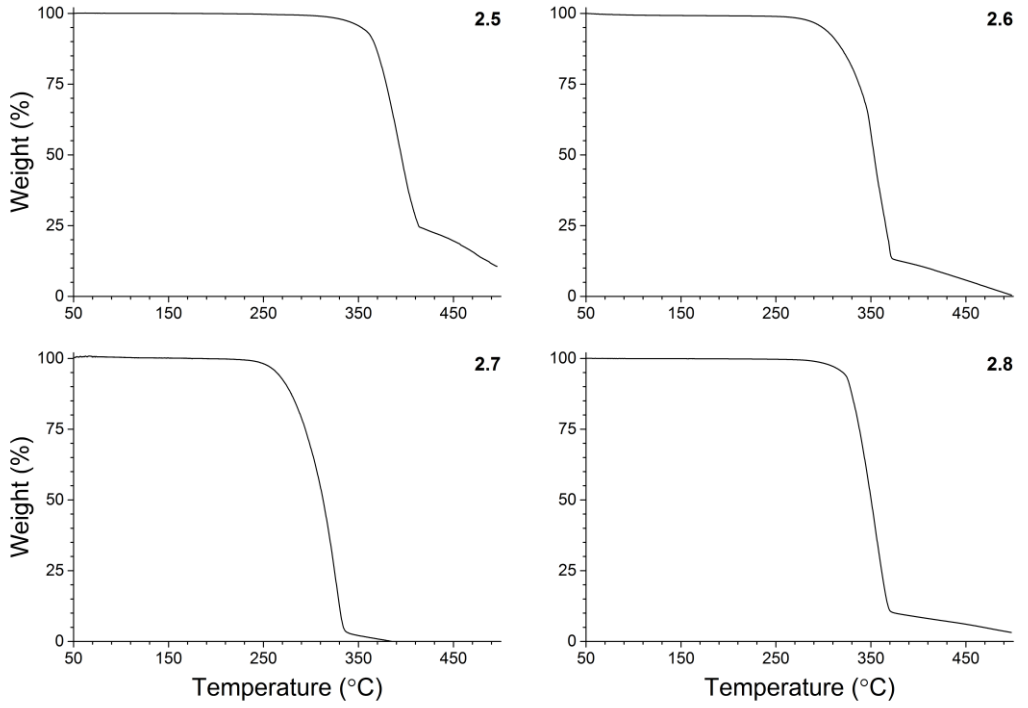

Figure 2.8 - TGA plots of compounds **2.5 –2.8**, heating at a rate of 10 °C min^{-1} under argon

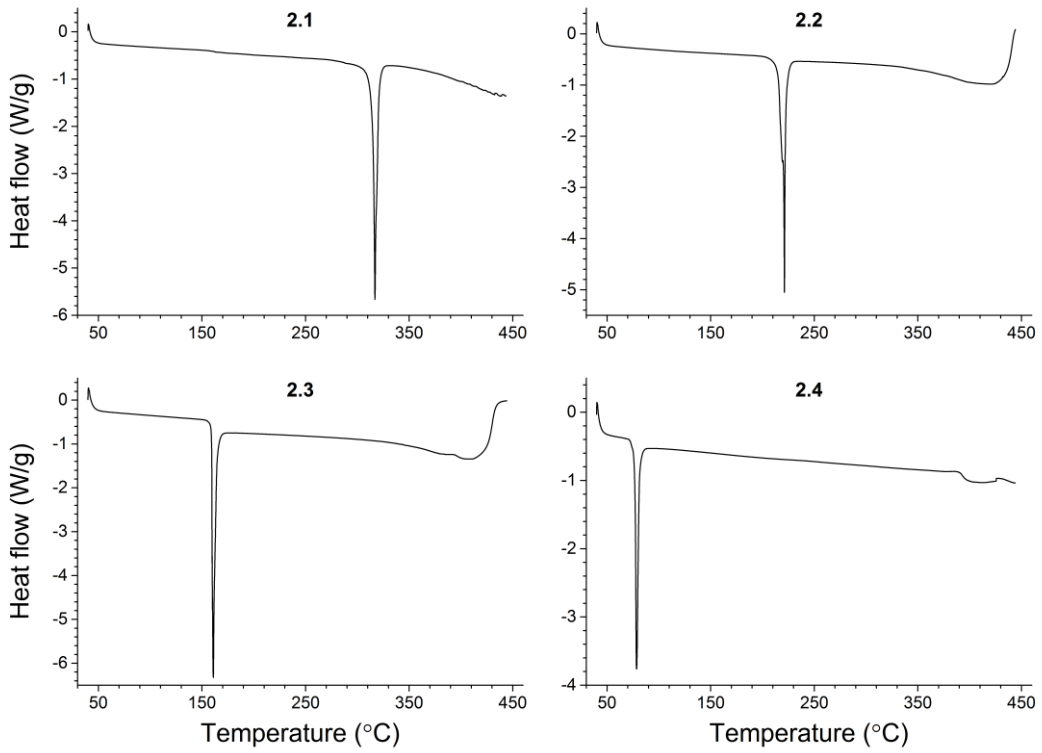

Figure 2.9 - DSC plots of compounds **2.1**–**2.4**, heating at a rate of 20 °C min^{-1} under nitrogen

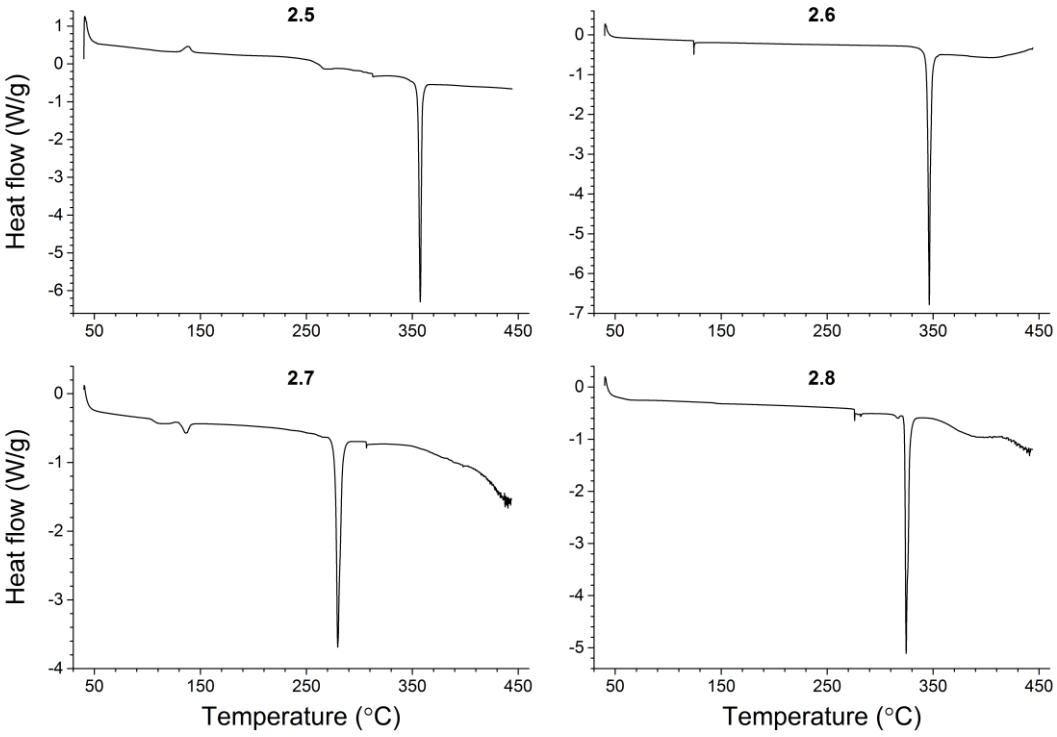

Figure 2.10 - DSC plots of compounds **2.5**–**2.8**, heating at a rate of 20 °C min^{-1} under nitrogen

Though the tricarboxylic acids all demonstrate thermal stability suitable for use in devices, the trends were not linear. The temperature at which the onset of mass loss occurred showed a drop for the propyl chain, while 5% mass loss occurred at a lower temperature for the ethyl chain.

To further examine this phenomenon the thermal properties of the intermediate compounds **2.1**–**2.8** were also examined. The TGA traces of the alkyl derivatives **2.1**–**2.4** are shown in Figure 2.7, and the traces of the tribromo derivatives **2.5**–**2.8** are in Figure 2.8. The DSC traces are shown in Figure 2.9 and Figure 2.10 for compounds **2.1**–**2.4** and **2.5**–**2.8** respectively. These results are summarised in Table 2.4 along with the melting point of each compound.

When compared to compounds **2.10**–**2.13** the TGA traces showed a more drastic drop in mass, with a much smaller mass left at the end of heating. Again two processes are observed in each TGA, which may be attributed to sublimation and decomposition. There is an obvious melting transition observed in the DSC of compounds **2.1**–**2.8**. Though other transitions are observed these may be due to other effects as this is the first heating cycle. The same dip in stability is observed in the intermediates for the melting points, the onset of mass loss, and the temperature at which 5% mass loss occurs.

The temperature at which 5% mass loss occurs is plotted against length of alkyl chain in Figure 2.11. Due to the weaker intermolecular interactions the un-functionalised molecules **2.1**–**2.4** are the least stable, while hydrogen bonding increases the thermal stability of the tricarboxylic acids **2.10**–**2.13**. All show a dip in stability.

This thermal stability dip could be due to the intersection of the sublimation and decomposition points. As the length of the alkyl chain increases, higher temperatures will be required to sublime the material, and as the temperature increases it becomes more likely that the compound will decompose.

Table 2.4 - Thermal properties of compounds **2.1**–**2.8**

Compound	Melting point [a] (°C)	Onset of mass loss (°C)	5% mass loss (°C)	Mass remaining at 490 (%)
2.1	322–324	329	307	32.2
2.2	220–222	290	282	8.9
2.3	157–159	255	251	0
2.4	236–238	269	268	2.0
2.5	>350	359	353	11.6
2.6	345–348	308	299	1.3
2.7	287–288	265	261	0
2.8	321–324	323	320	3.6

[a] Melting points determined on a melting point apparatus

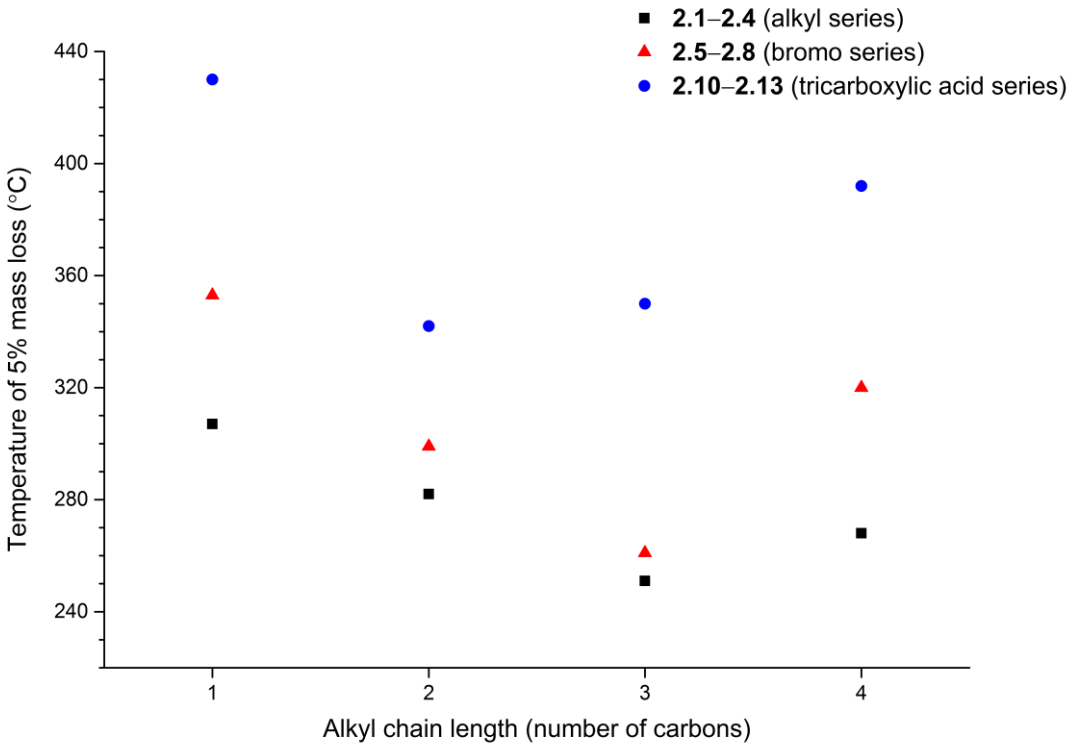

Figure 2.11 - 5% mass loss versus alkyl chain length for compounds **2.1**–**2.4** (alkyl series), **2.5**–**2.8** (bromo series) and **2.10**–**2.13** (tricarboxylic acid series)

For the tricarboxylic acids a decomposition process could be expected involving the loss of carbon dioxide.[134] However, a dip in stability is also observed for the alkyl and bromo compounds, suggesting that the mass loss is dependent on the molecular weight rather than the chemical structure. Therefore, the decomposition is presumed to be due to chain scission, which can lead to radical formation and dimerization, a process which has been observed in polyfluorenes.[135,136]

Thus it can be seen that altering the length of alkyl chain does have an impact on the thermal properties. This will be an important factor in choice of materials for any device fabricated as the thermal stability impacts the performance and lifetime. However, the main difference is in the crystal packing of these materials (*vide infra*).

2.3.3 X-ray crystallography

Single crystals of compounds **2.1**–**2.4** were obtained from acetonitrile, and the main features are shown in Table 2.5. The intramolecular twist angles were measured by plotting a plane through each of the three fluorene units and calculating the angle between each plane. It can be seen that as the length of the alkyl chain increases the truxene core becomes less planar. This is also represented in the asymmetric unit of each, shown below in Figure 2.12.

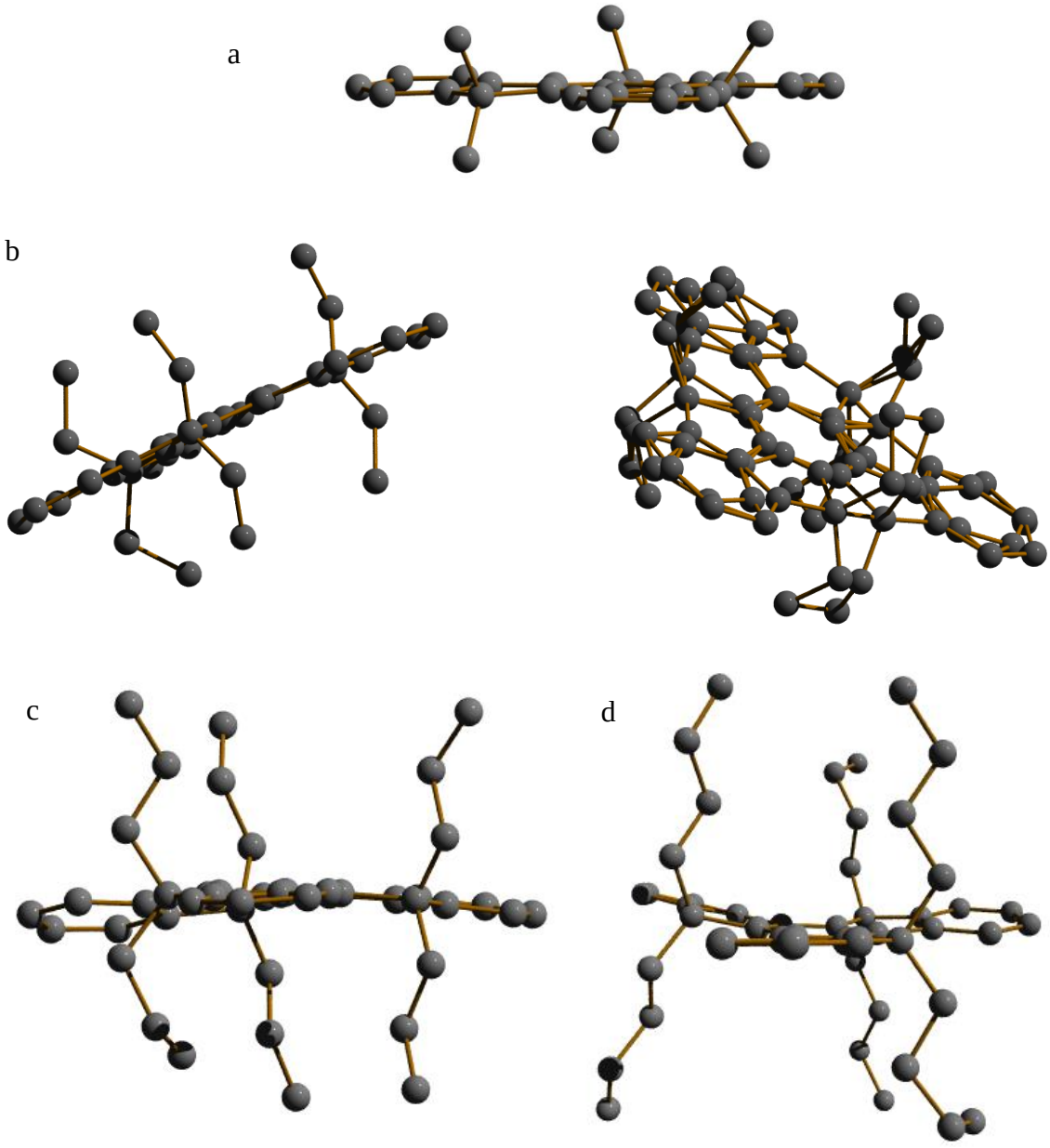

Figure 2.12 - Asymmetric units from the crystal structures of: a) compound **2.1**; b) compound **2.2**; c) compound **2.3**; and d) compound **2.4**. Hydrogen atoms omitted for clarity.

Compound **2.2** contains two molecules per asymmetric unit, as observed in Figure 2.12. One of these is disordered, leading to a lower quality structure than the others, but it is included for completeness.

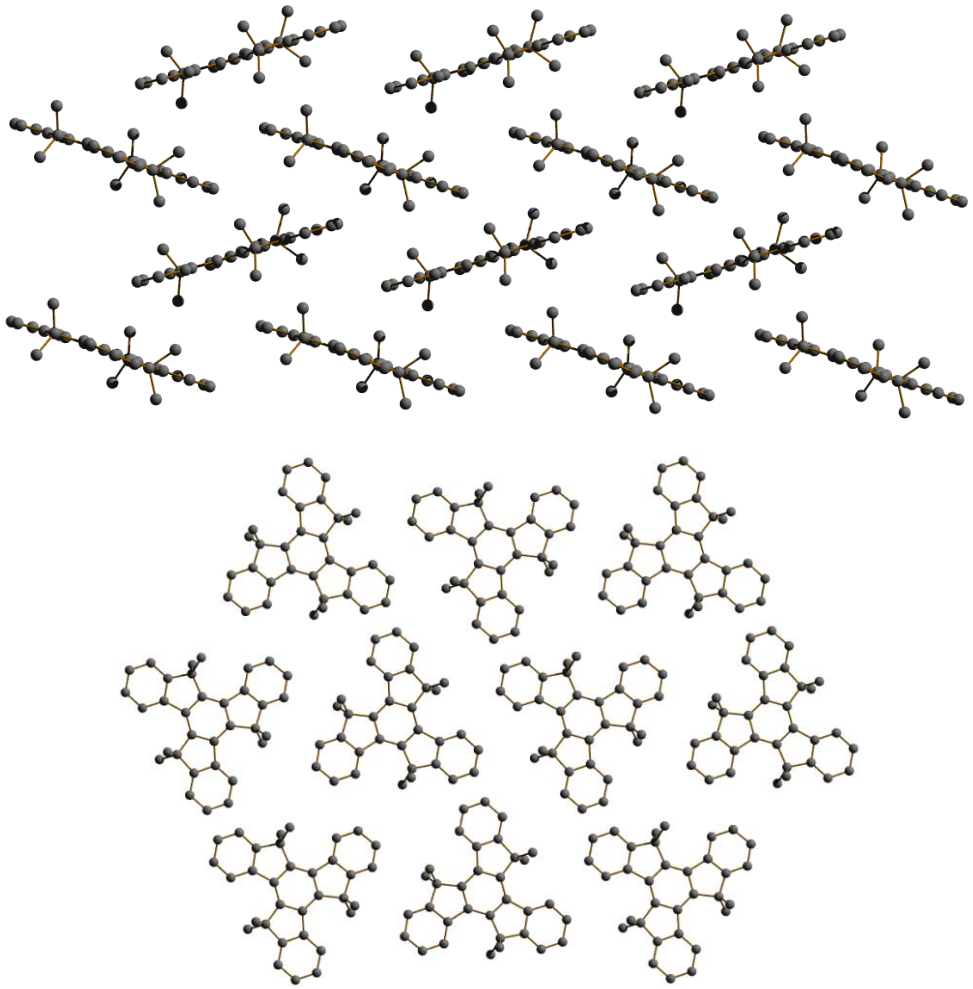

Figure 2.13 - Packing motif of compound **2.1**. Hydrogen atoms omitted for clarity.

As may be expected, the crystal structure of **2.1** shows the tightest packing, and thus the highest density. As it contains the shortest alkyl chains the molecules can pack tightly in the crystal lattice, with a distance of 3.4 Å between the closest truxene moieties. The molecules are arranged in a herringbone pattern with an intermolecular stack angle of 35.9° as shown in Figure 2.13. Within each layer of the herringbone pattern the molecules are arranged in an alternating fashion; this orientation allows for the closest packing of the truxene cores.

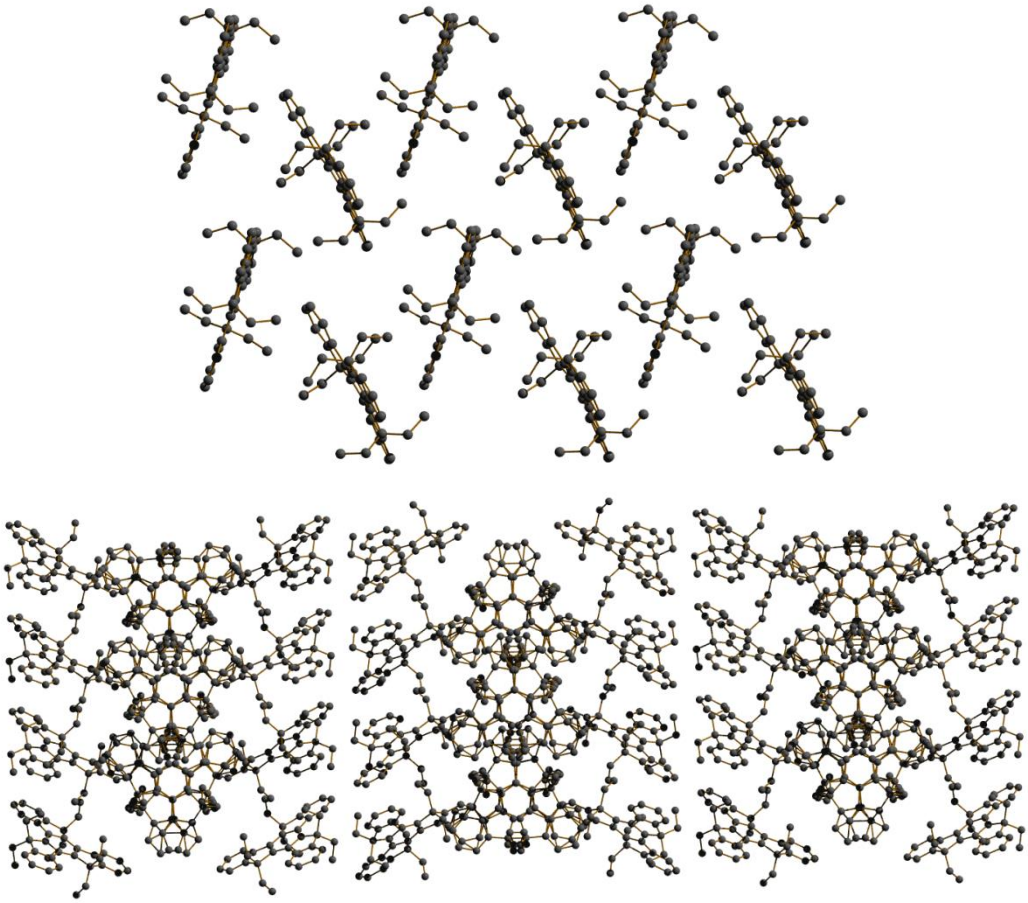

Figure 2.14 - Packing motif of compound **2.2**. Hydrogen atoms omitted for clarity.

Table 2.5 - Crystallographic features of compounds **2.1**–**2.4**

Compound	Intramolecular twist angles (°)	Calculated density (g/cm^3)
2.1	1.27–3.59	1.205
2.2	0.76–4.22	1.133
2.3	5.01–8.15	1.115
2.4	6.94–9.75	1.113

As mentioned above, compound **2.2** has a degree of disorder in the crystal lattice resulting in a more complex packing motif. Despite this, in Figure 2.14 it is possible to see the regular structure, which is very similar to that observed for the methyl analogue, though the intermolecular stack angle is reduced to 16.0°. Due to the longer alkyl chain the truxene cores are forced slightly further apart, with a distance of 3.8 Å.

As the length of the alkyl chain increases, the molecular arrangement is altered to extend the interactions between the molecules through overlap of the alkyl chains. Figure 2.15 shows the packing in compound **2.3**, which is composed of interlaced columnar stacks, the molecules within alternating columns are bent in alternate directions to maximise packing. Within each column the truxene cores are 6.4 Å apart, and between columns the closest contact between the π systems is 3.5 Å. When viewed from above each column, the molecules are arranged in interlocking zig-zags.

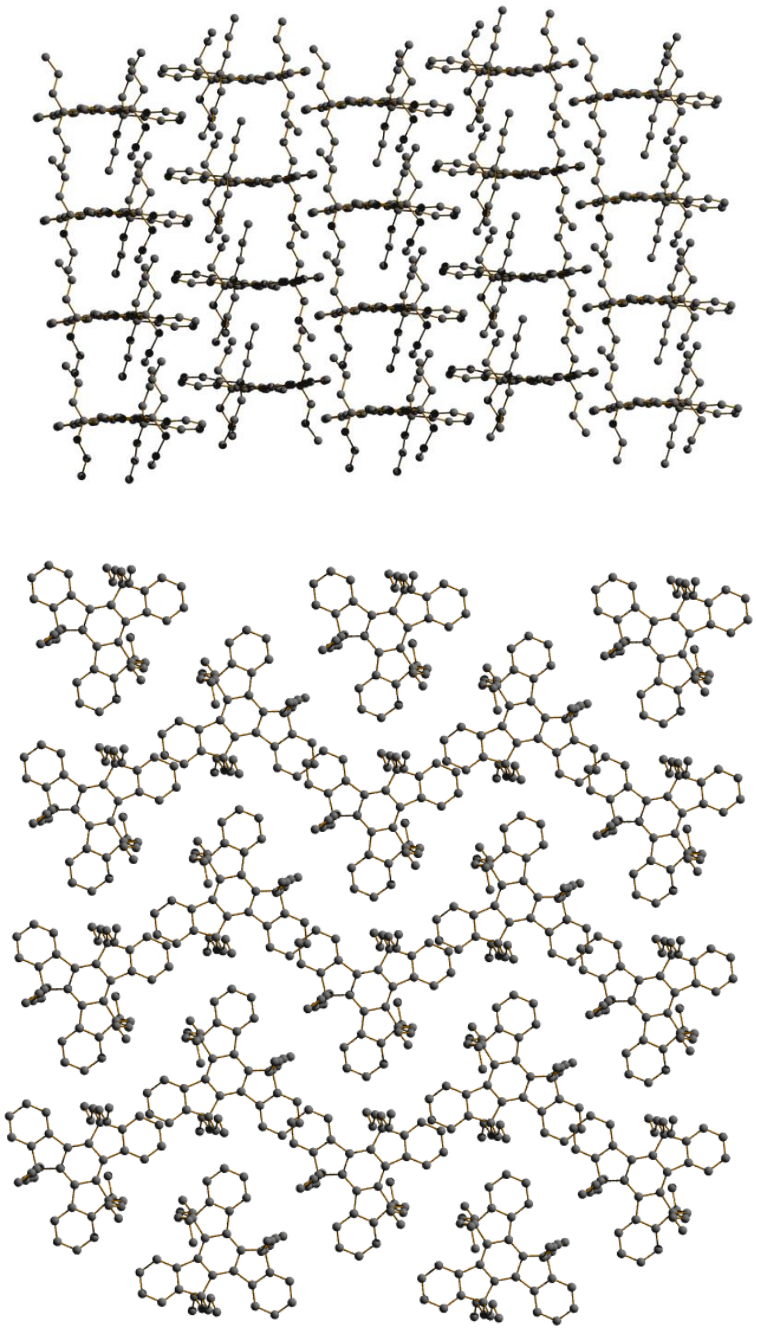

Figure 2.15 - Packing motif of compound **2.3**. Hydrogen atoms omitted for clarity.

The crystal structure of compound **2.4** is very similar to that of the propyl derivative; the slipped stacks shown in Figure 2.16 are also arranged in a zig-zag. The main difference is that the truxene molecules in **2.4** are slightly further apart, at 8.3 Å between cores within a column, with a similar shortest contact of 3.4 Å

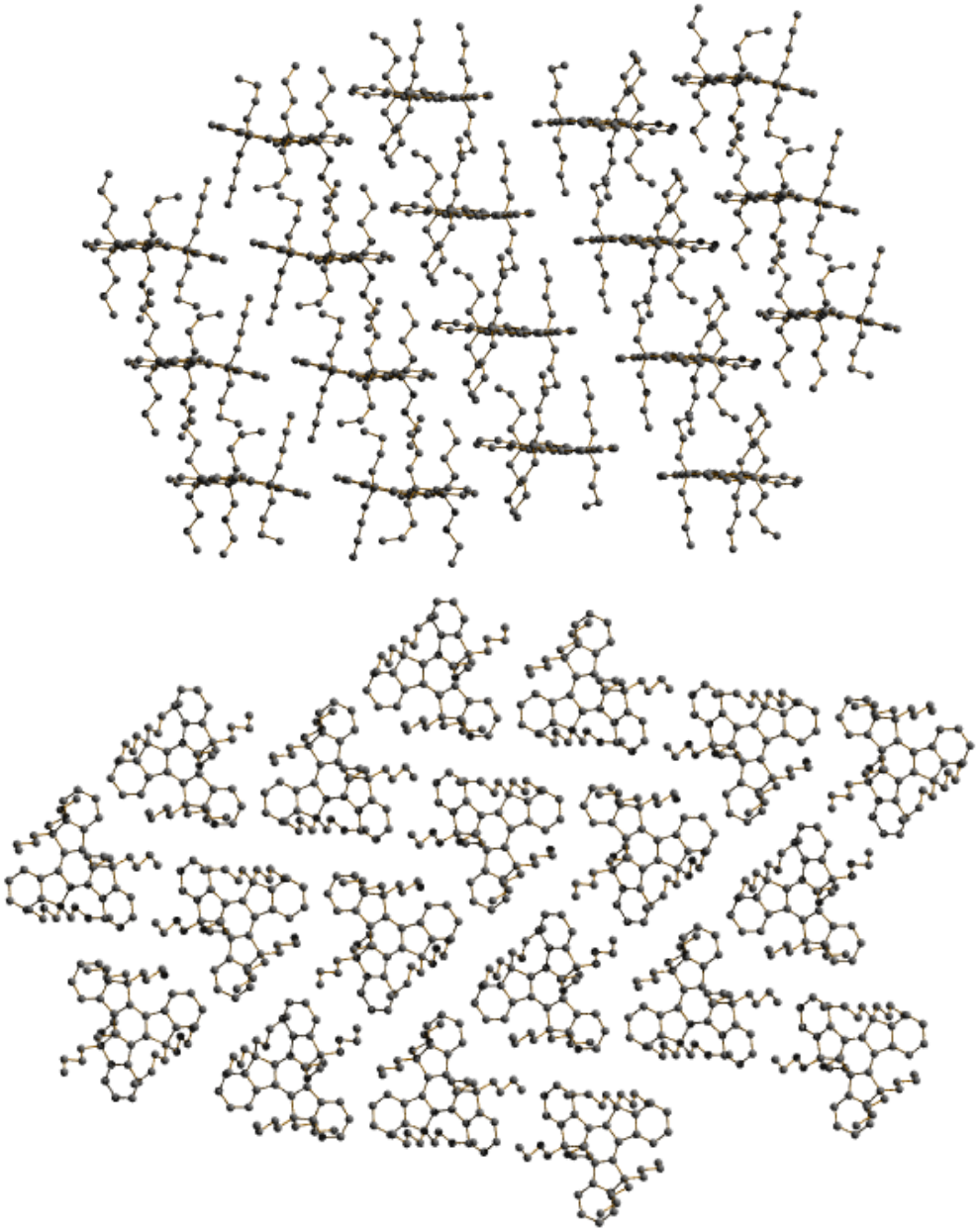

Figure 2.16 - Packing motif of compound **2.4**. Hydrogen atoms omitted for clarity.

.

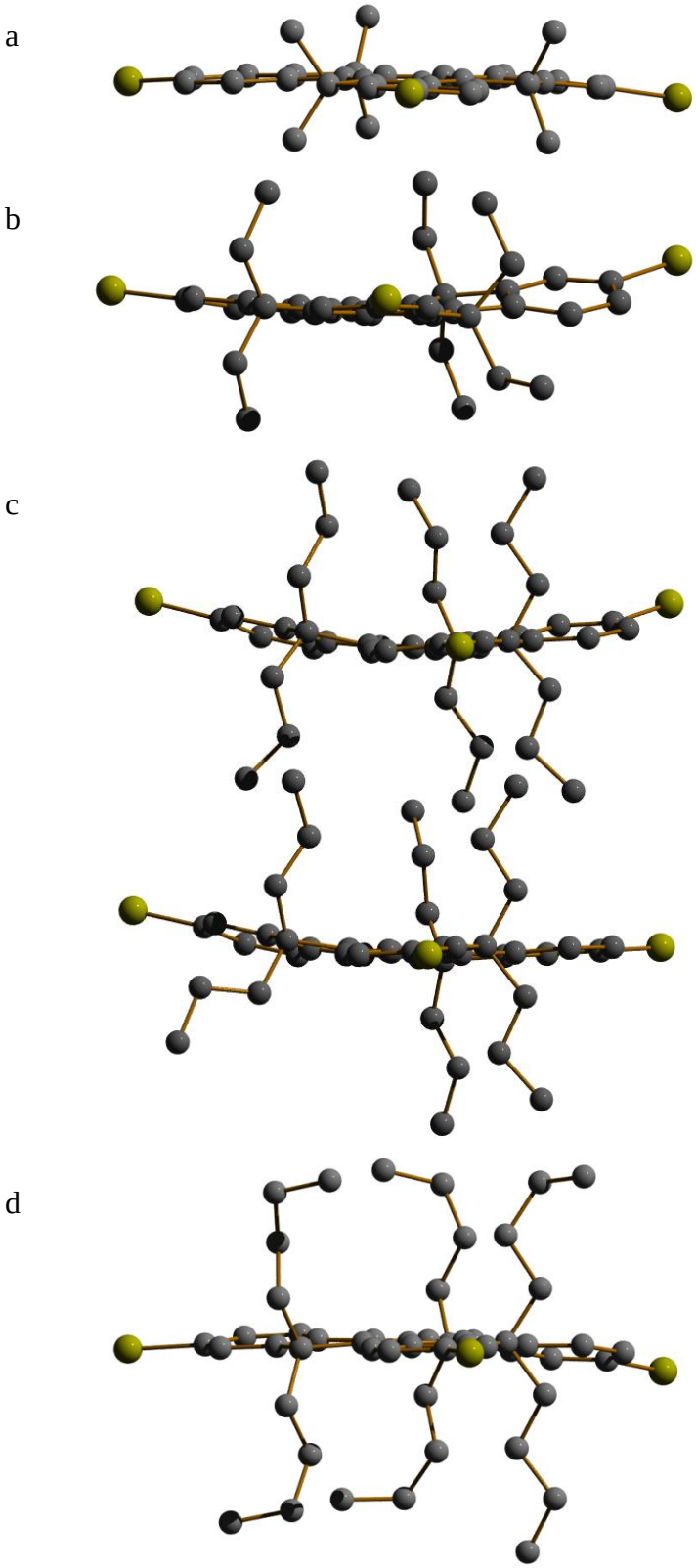

Figure 2.17 - Asymmetric units from the crystal structures of: a) compound **2.5**; b) compound **2.6**; c) compound **2.7**; and d) compound **2.8**. Hydrogen atoms omitted for clarity.

Table 2.6 shows the crystallographic features of compounds **2.5**–**2.8** which were obtained from a 1:1 mixture of dichloromethane and acetonitrile. Due to the presence of bromine the calculated densities are higher, but they show the same trend of decreasing density as the alkyl chain length is increased.

Table 2.6 - Crystallographic features of compounds **2.5**–**2.8**

Compound	Intramolecular twist angles (°)	Calculated density (g/cm^3)	C-Br bond lengths (Å)	Br---Br distances (Å)
2.5	1.50–3.85	1.626	1.88, 1.89, 1.90	3.73, 3.84, 4.02, 4.10
2.6	2.48–9.71	1.524	1.89, 1.90, 1.90	3.88, 4.29
2.7	1.70–13.14	1.358	1.87, 1.89, 1.89, 1.89, 1.91, 1.92	4.32, 4.41, 4.50, 4.78
2.8	1.72–7.50	1.356	1.91, 1.91, 1.91	3.91, 4.33, 4.59

As with the unbrominated derivatives the twist angle between fluorene units increases with length of alkyl chain, with the exception of compound **2.8**. The brominated derivatives have more of a twist, Figure 2.17, most likely due to the inclusion of the large bromine atoms and the possibility of stronger intermolecular interactions between these atoms.

In a similar way to non-functionalised analogue **2.1**, the crystal structure of compound **2.5** has a herringbone pattern, as shown in Figure 2.18. Due to the addition of large bromine atoms the intermolecular stack angle is increased to 78.6°, and the distance between truxene moieties to 4.6 Å. Within each layer there is an alternating orientation of the truxene cores, which leads to weak bromine-bromine interactions forming a quadrilateral.

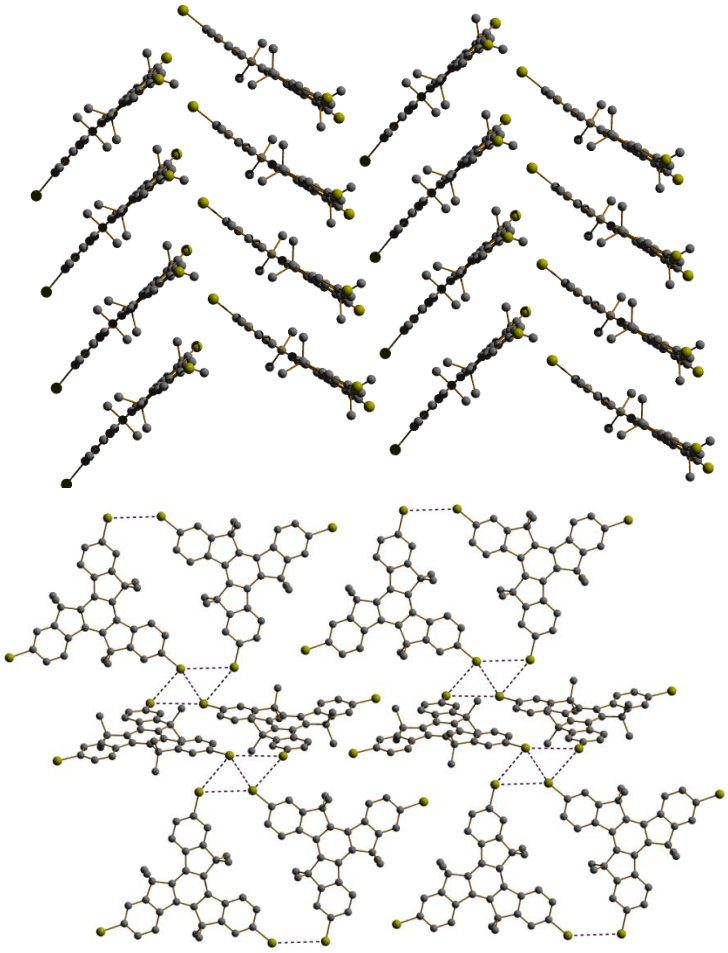

Figure 2.18 - Packing motif of compound **2.5**. Hydrogen atoms omitted for clarity.

The ethyl derivative (**2.6**) also packs in a herringbone arrangement, where the motif depicted in Figure 2.19 is composed of dimers which form zig-zag sheets that stack. The intermolecular stack angle is 61.8°, much larger than the unbrominated analogue **2.2**. There are two bromine-bromine interactions per position and 3.4 Å between the closest truxene moieties.

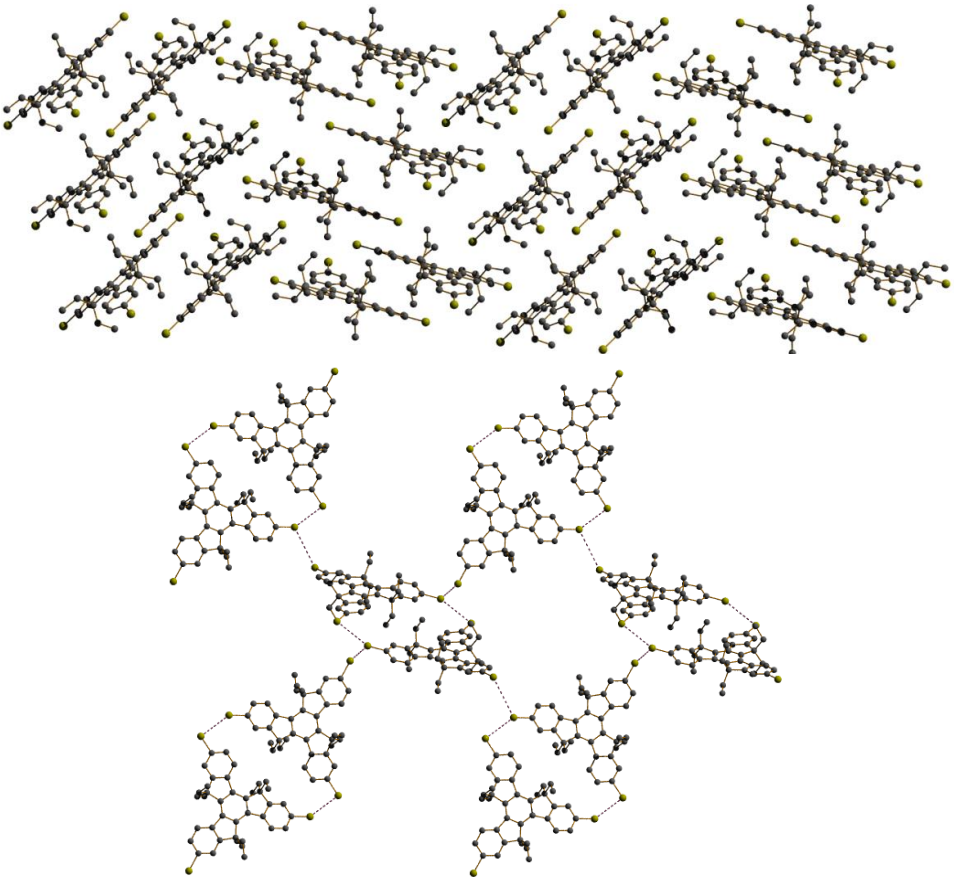

Figure 2.19 - Packing motif of compound **2.6**. Hydrogen atoms omitted for clarity.

Compound **2.7** has an asymmetric unit composed of two molecules, resulting in a very different packing motif, Figure 2.20. This may be due to slight variations in crystallisation conditions which resulted in a different polymorph crystallising. Like its unbrominated counterpart, **2.7** has a slightly slipped stack structure with a distance of 8.4 Å between the cores. The bromine-bromine interatomic distances are the longest of the series, and it also shows the largest intramolecular twist angles of all the tribromo truxene compounds discussed.

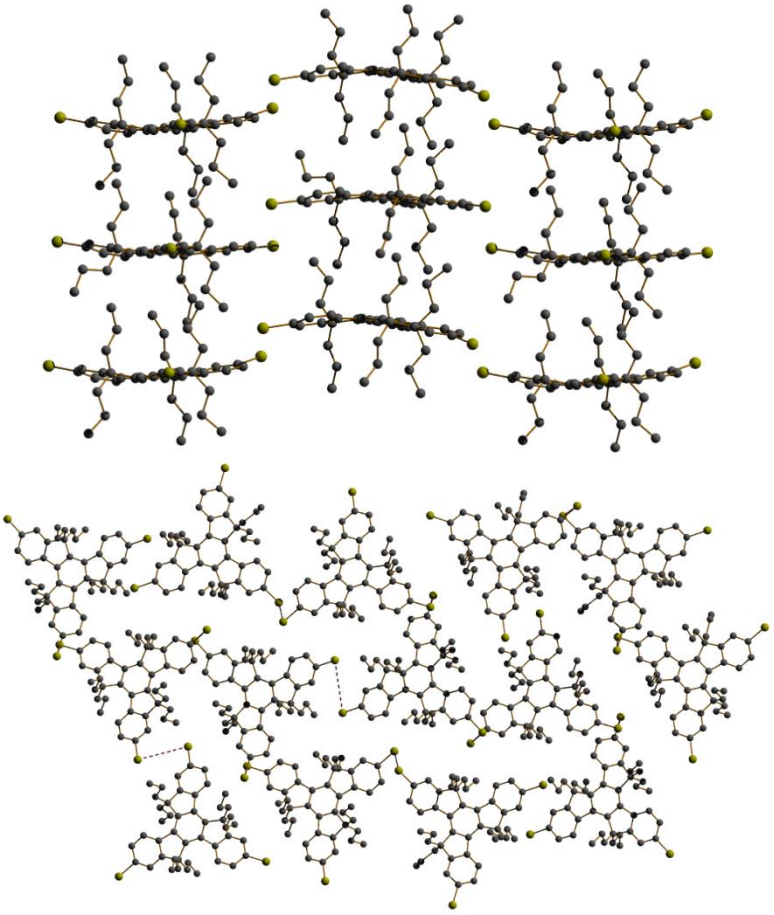

Figure 2.20 - Packing motif of compound **2.7**. Hydrogen atoms omitted for clarity.

The crystal structure of compound **2.8** also has a herringbone pattern, Figure 2.21. Though this is similar to **2.5** and **2.6**, the longer alkyl chains force the sheets flatter resulting in a much smaller intermolecular stack angle of 21.4°. These sheets are composed of columns of dimers, where the bromine-bromine interactions form a triangle. The closest contact between the truxene cores is 4.0 Å.

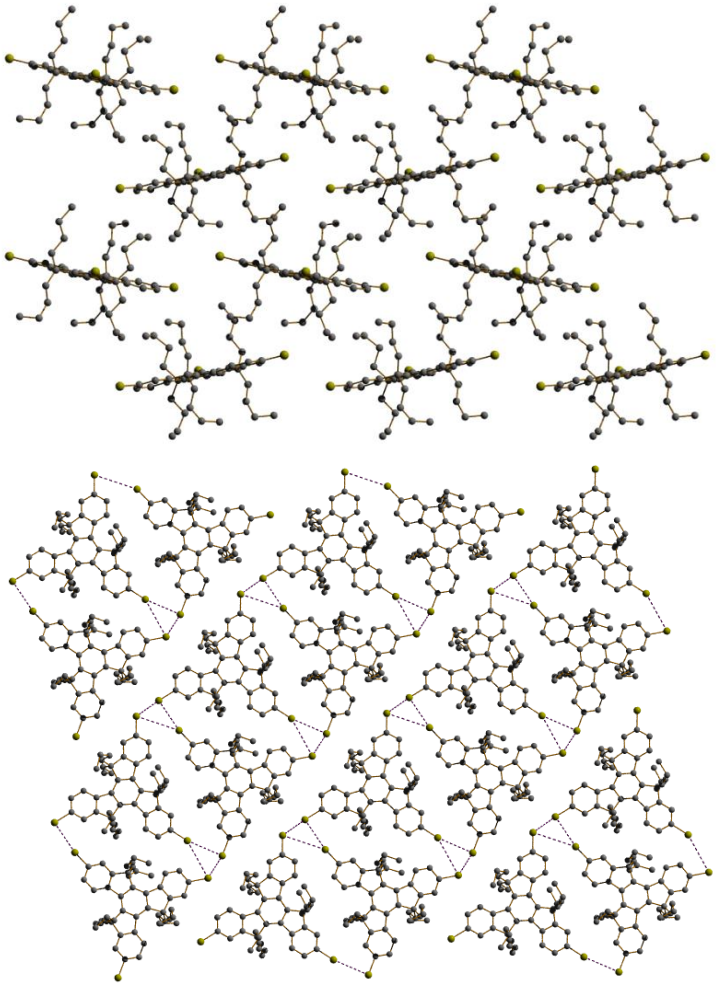

Figure 2.21 - Packing motif of compound **2.8**. Hydrogen atoms omitted for clarity.

Crystals of sufficient quality could not be obtained for compounds **2.10** and **2.11**. Compounds **2.12** and **2.13** were crystallised from a 1:1 mixture of THF and hexane and both contain THF molecules in the crystal lattice. Once again, the main features are summarised in Table 2.7.

Table 2.7 - Crystallographic features of compounds **2.12**–**2.13**

Compound	Intramolecular twist angles (°)	Calculated density (g/cm^3)	O-H---O distances (Å)	O-H---O dihedral (°)
2.12	1.92–8.09	1.185	2.49–2.67	153.9–176.5
2.13	5.42–6.12	1.182	2.58–2.68	155.4–172.5

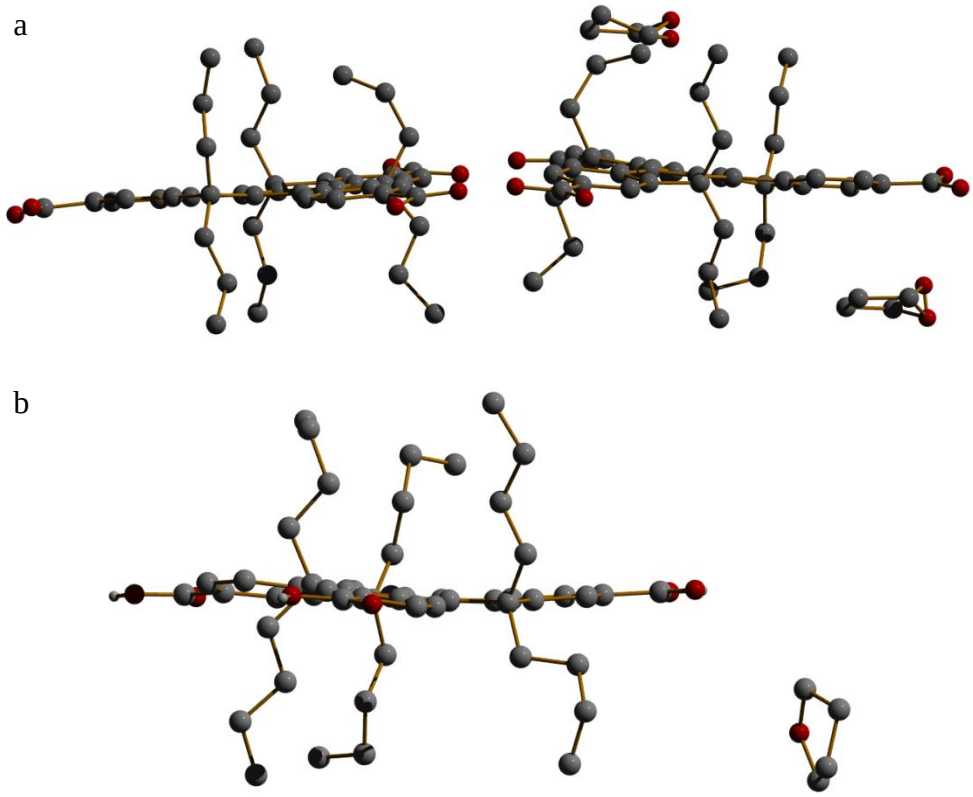

Figure 2.22 - Asymmetric units from the crystal structures of: a) compound **2.12**; and b) **2.13**. Hydrogen atoms omitted for clarity.

The asymmetric unit of each is shown in Figure 2.22. The propyl derivative, **2.12**, has two truxene molecules and a disordered molecule THF which has been modelled over two sites with a ratio of roughly 70:30. The butyl derivative has one THF molecule in the asymmetric unit, and a slightly lower calculated density. This can be attributed to the slight disorder present in **2.12** meaning the occupancy of the THF sites is overestimated.

Both structures are composed of hydrogen bonded sheets of truxene dimers with THF at the edges. In compound **2.12** the truxene molecules pack in the same slipped stack as previously observed, Figure 2.23. Within each stack the truxene cores are bent in alternating directions, with a distance of 6.40 Å between cores. Each truxene molecule within the sheet hydrogen bonds to three other truxene molecules, and one THF molecule.

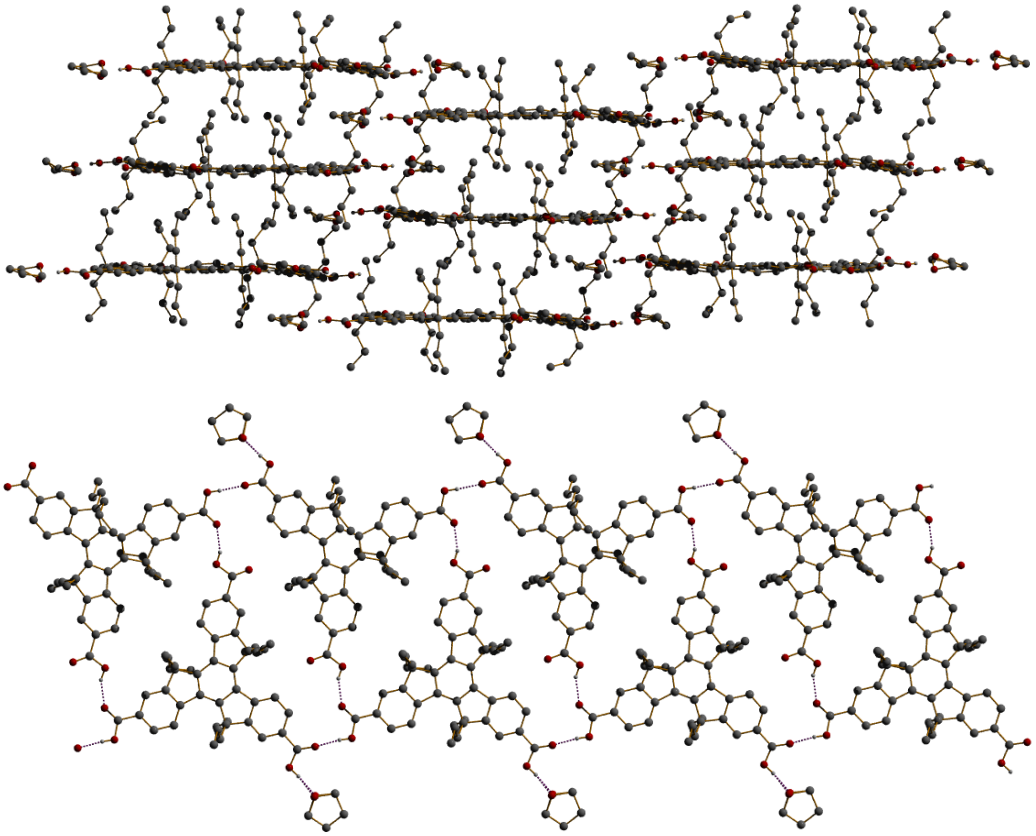

Figure 2.23 - Packing motif of compound **2.12**. Hydrogen atoms omitted for clarity.

Due to the longer alkyl chains, the truxene cores in the **2.13** are forced further apart to 7.65 Å, Figure 2.24. However, the lengths and dihedral angles of the hydrogen bonds are consistent between the two.

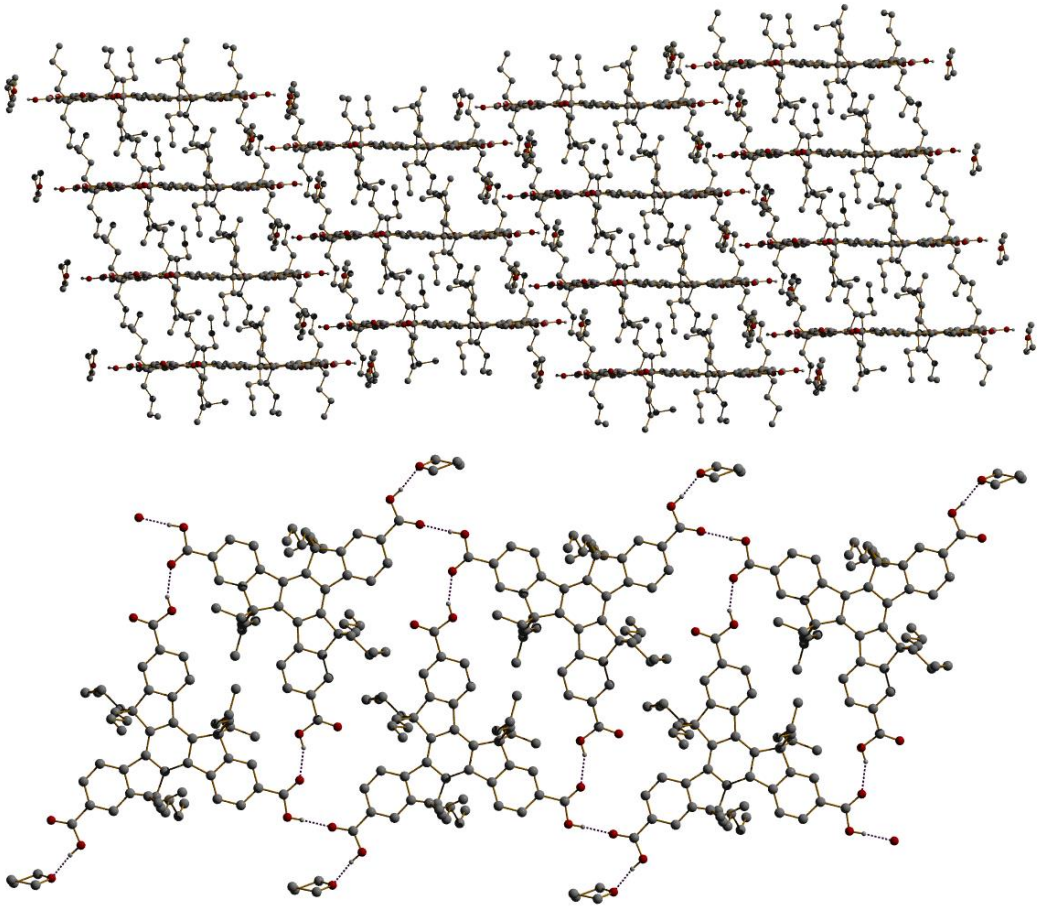

Figure 2.24 - Packing motif of compound **2.13**. Hydrogen atoms omitted for clarity.

It might be expected that **2.12** and **2.13** would show complementary hydrogen bonds between carboxylic acid functionalities on different molecules. However this synthon is not observed due to the presence of THF. Biradha *et al.* have shown that solvents can influence the hydrogen bonding network, as is likely the case here.[137]

On comparing the butyl analogues (**2.4**, **2.8** and **2.13**) the brominated derivative differs in its structure, whereas across the series of propyl derivatives (**2.3**, **2.7** and **2.12**) the crystal structures all display a slipped stack arrangement.

In general, the longer alkyl chains cannot pack as tightly leading to a slight decrease in density on increasing the length of alkyl chain. The density of the brominated derivatives is considerably higher due to the inclusion of three heavy bromine atoms. There appears to be a trend of increasing twist angle as the length of alkyl chain increases. However, there are some exceptions (**2.8** and **2.13**) which may be ascribed to the appearance of different polymorphs. Slight variations in crystallisation conditions can lead to different molecular packing, this may also be the reason for compounds **2.2**, **2.7** and **2.12** having two truxene molecules in the asymmetric unit. This polymorphism may lead to problems in reproducibly obtaining consistent morphologies in thin films.

These differences in crystal packing may translate to differences in packing in thin films, though this is not always the case. The film morphology is an important aspect of templating layers for use in organic electronic devices, therefore it is promising that simply altering the length of alkyl chain may lead to variations in film morphology. Overall, intermolecular interactions are observed which will confer some order to films. Furthermore, as the alkyl chains interdigitate between the truxene cores, this reduces π-π stacking thus no aggregation is observed in solutions of these compounds.

2.4 Conclusions and future work

In summary, the target compounds were successfully synthesised and fully characterised. The original synthetic route was altered as there were difficulties in separating the mono- and di-reacted species. Using this improved route, the desired tricarboxylic acids could be obtained through crystallisation by slow vapour diffusion, providing pure products in isolated yields of 31–80%. By this method crystal structures were obtained for 10 of the 12 molecules discussed. Changes in the packing motifs were observed due to the alteration of the length of alkyl chains. Due to the strong hydrogen bonding ability of the carboxylic acids, molecules of THF were trapped in the lattice. While these could mostly be removed by precipitation this introduced water molecules instead.

These molecules showed little change in the optical and electrochemical properties on altering the length of the alkyl chains. The optical and electrochemical HOMO-LUMO gaps were around 3.8 eV, showing minor variation with the length of alkyl chain. In the solution state the peak position and vibronic structure of the absorption and emission spectra did not significantly change. In the solid state there was a concentration dependant variation in the vibronic structure.

Cyclic voltammetry showed a pseudo-reversible oxidation and irreversible reduction for compounds **2.10**–**2.13**. This electrochemical instability may be an issue when these materials are applied in organic electronic devices; normally reversibility is desired to ensure high device lifetimes. However, if a monolayer could be deposited charges may be able to pass through and thus the electrochemical instability may not be an issue. This monolayer may alter the surface properties enough that it will confer order onto subsequently deposited layers.

The tricarboxylic acids displayed excellent thermal stability, with a slight dip observed for compounds **2.11** and **2.12**. The intermediate compounds **2.1**–**2.8** also exhibited a dip in thermal stability for the propyl derivatives, **2.3** and **2.7**. This is most likely caused by a crossing over of the decomposition and sublimation temperatures. As it occurs across all three series, this dip is not dependent on the

chemical structure but instead the molecular weight indicating that the source of the decomposition is chain scission.

These materials will be evaluated as candidates for vacuum deposition and the results of this used to select new synthetic targets. When other functional groups are investigated these will initially be examined on a core of hexabutyl truxene. The variation in alkyl chain length does not change the optical or electrochemical properties, the longer chains will give increased solubility while preventing aggregation. Thus moving forward the butyl chain should allow for higher yielding syntheses and easier purification.

Once a suitable candidate with the desired optical and electrochemical profile has been identified, it would be prudent to rescreen the alkyl chain length. This will allow the desired processability and thermal properties of the material to be obtained, and by optimising these conditions the device performance can be improved. Many variations are possible beyond the simple alkyl chains, for example branched chains could be investigated. These chains will fill the space differently, impacting the molecular packing.

Alternatively, it may be advantageous to have different chains on each face of the molecule. By incorporating different functionalities on each face, multiple interactions would be available to these materials, giving rise to the possibility of face selective binding. This would provide asymmetric functionalization of the surface, while maintaining intermolecular interactions within the layer through the 2, 7 and 12 positions.

3 EVAPORATION, DEVICE APPLICATION AND FURTHER ELECTROCHEMISTRY

3.1 Introduction

Following the synthesis presented in Chapter 2, these truxene based materials were examined for their potential to be vacuum deposited. Additional electrochemistry experiments and device work are also included.

3.2 Device work

To examine the concept of using truxenes as a templating layer, compound **2.3** was chosen as a simple starting point. The hexapropyl truxene (**2.3**) was purified by thermal gradient sublimation and then sent to Moritz Reide's group at the University of Oxford.

To test the templating ability of **2.3**, films of different thickness were evaporated onto glass substrates and studied by atomic force microscopy (AFM). This was repeated with a 20 nm layer of boron subphthalocyanine chloride (SubPc, **3.1**, Figure 3.1) deposited on top of the hexapropyl truxene layer.

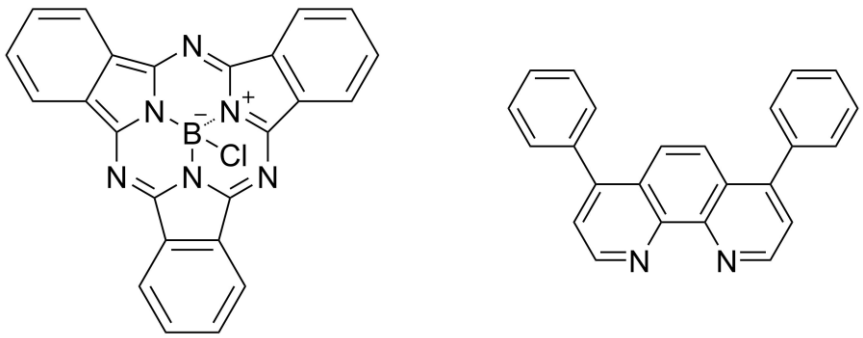

3.1 **3.2**

Figure 3.1 - Structure of SubPc **3.1** and BPhen **3.2**

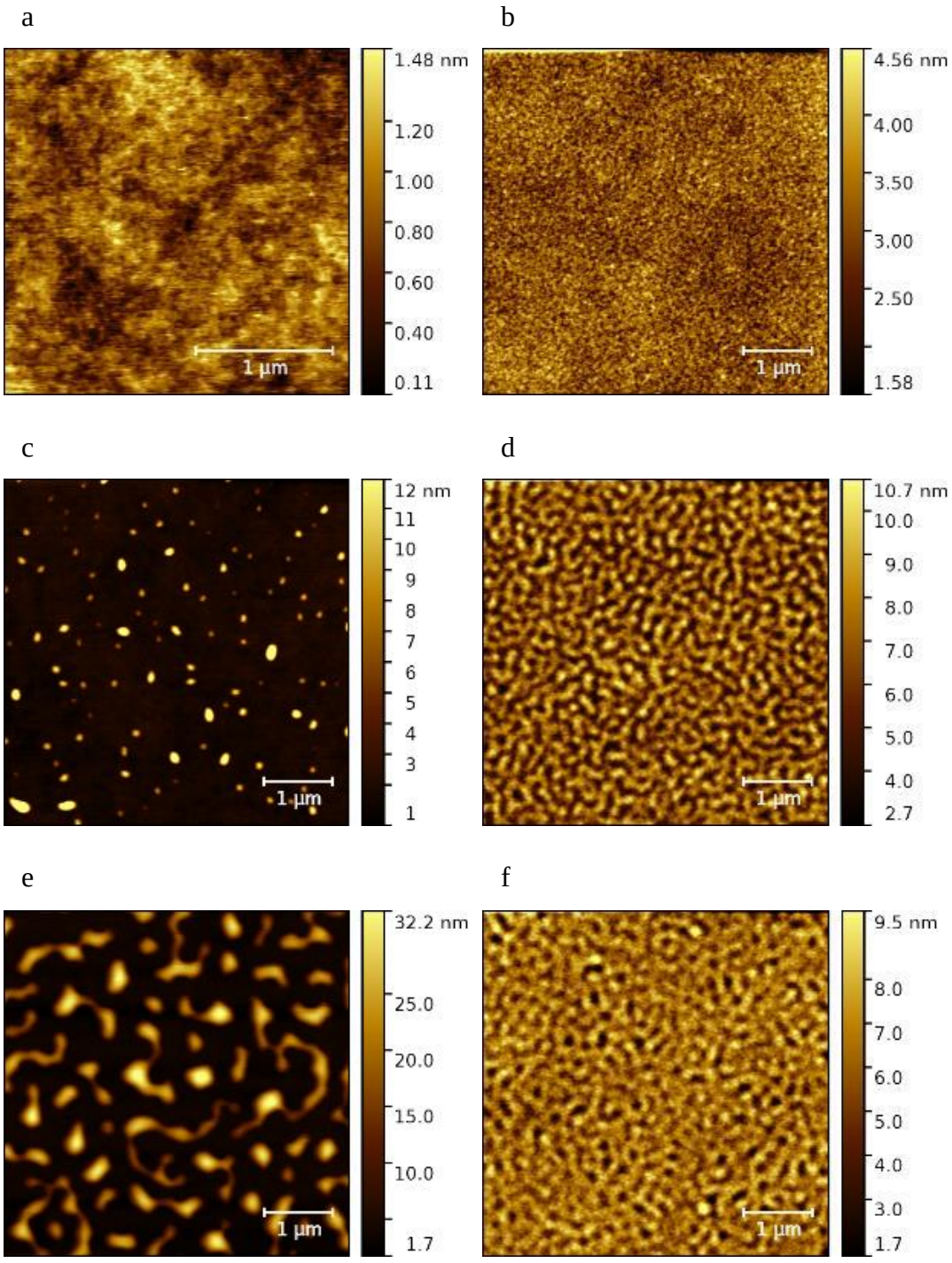

Figure 3.2 - AFM images of evaporated films: a) 1 nm of **2.3**; b) 1 nm of **2.3** then 20 nm of **3.1**; c) 5 nm of **2.3**; d) 5 nm of **2.3** then 20 nm of **3.1**; e) 10 nm of **2.3**; and f) 10 nm of **2.3** then 20 nm of **3.1**

When 1 nm of hexapropyl truxene is deposited, the substrate has a fairly uniform coverage, Figure 3.2a. As thicker films are deposited the molecules coalesce into clusters, the size of these islands increasing with the film thickness, Figure 3.2c and e. A fairly uniform film is produced when a layer of SubPc is deposited on to the thin **2.3** layer, Figure 3.2b. As the thickness of the hexapropyl truxene layer increases larger SubPc grains form, the morphology of which are influenced by the underlying layer. Larger gaps between the grains are observed on a 5 nm film of **2.3**, Figure 3.2d; this is less noticeable on a 10 nm film, Figure 3.2f. Thus the hexapropyl truxene layer strongly influences the growth behaviour of the subsequently deposited SubPc layer.

Given that the hexapropyl truxene layer displays some templating ability this material was incorporated into devices. Due to the Reide group's expertise, OPVs were fabricated rather than OLEDs but the templating concept remains the same.

A standard solar cell stack was fabricated with the following configuration: MoOx (5 nm)/**2.3** (x nm)/SubPc (13 nm, **3.1**)/C_{60} (35 nm)/BPhen (8 nm, **3.2**, bathophenanthroline, Figure 3.1)/Al (100 nm) on an ITO coated glass substrate. The energy levels of this device are shown in Figure 3.3.

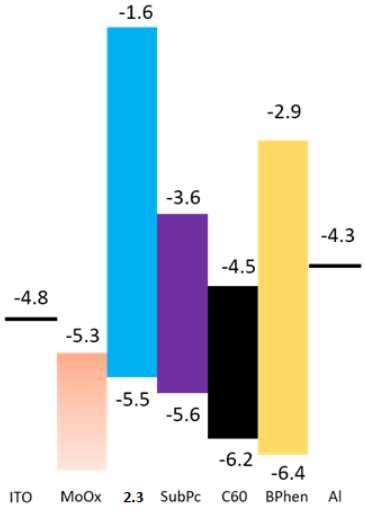

Figure 3.3 - Energy level diagram of the OPV stack, numbers correspond to eV relative to vacuum

Different thicknesses of the interlayer were included between the first two layers and the device characteristics measured, Figure 3.4, allowing the optimal thickness to be found.

As the thickness of the hexapropyl truxene layer increases from 0 to 3.8 nm the PCE also increases from 2.54% to 3.09%. This is associated with an increase in the J_{SC} which may be due to improved carrier mobility and lower resistance within the device, as a result of the inclusion of the hexapropyl truxene layer.

However as the thickness of the interlayer further increases, the PCE significantly drops to 1.26% with a 7.7 nm interlayer. This drop corresponds to a drop in the fill factor which is presumably caused by morphology changes in the device. As observed in the AFM study, the SubPc grain sizes do vary and this will affect the IV characteristics of the device.

The V_{OC} rises slightly throughout the series suggesting that there is improved overlap between the HOMO of SubPc and the LUMO of C_{60}, this is a small effect which again is presumably caused by the morphology changes in the device.

To further investigate the reason for the increased J_{SC} the external quantum efficiency (EQE) and UV-vis reflectance were measured. Figure 3.5 shows the results for the control device (with no interlayer) and the best performing device (with 3.8 nm of hexapropyl truxene).

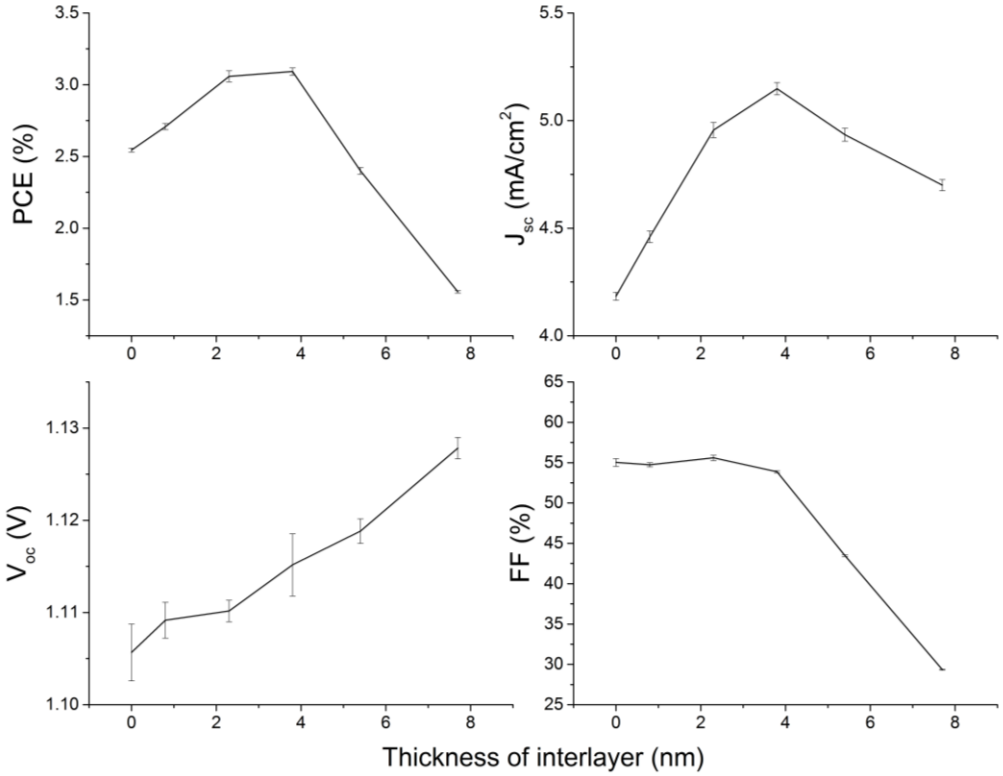

Figure 3.4 - OPV characteristics of devices with different thicknesses of hexapropyl truxene included

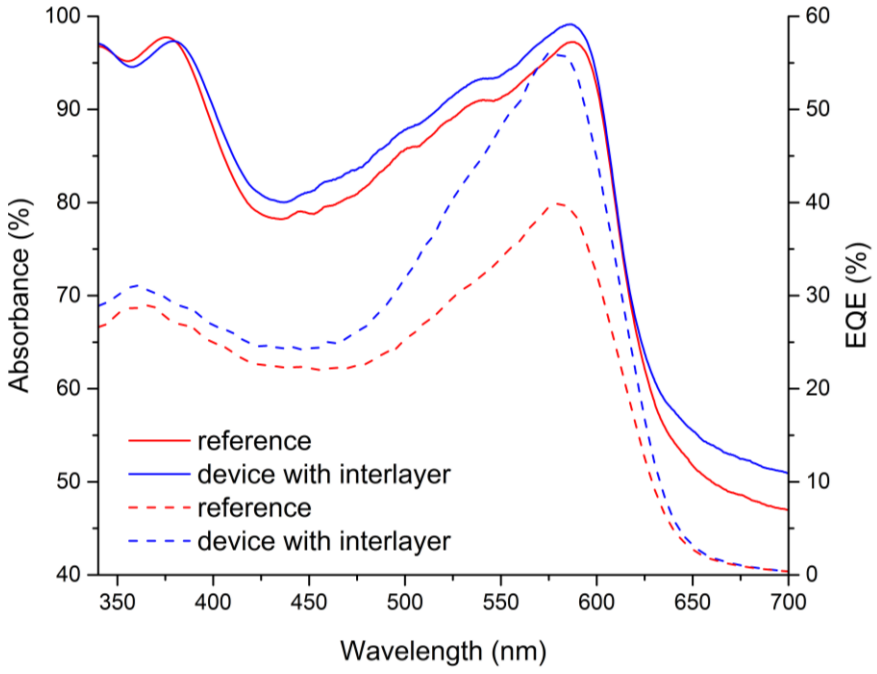

Figure 3.5 - Measurement of EQE (dotted line) and absorbance (solid line) for reference device (red) and device with 3.8 nm interlayer of hexapropyl truxene (blue)

There are two peaks in the absorbance spectra, one from 330 nm to 400 nm which corresponds to the C_{60} absorption range and the other from 520 nm to 600 nm which is the SubPc absorption range. With the inclusion of a hexapropyl truxene interlayer slightly more light is absorbed in the visible region. The EQE shows a corresponding increase across the C_{60} region. However, between 520 nm and 600 nm the inclusion of the interlayer increases the EQE from 39.8% to 56.1%. This drastic increase cannot be solely attributed to improved light absorption in the SubPc region.

To further examine this variance, the internal quantum efficiency (IQE) of the devices was calculated, Figure 3.6. Once more, the presence of the interlayer leads to an enhancement of the IQE over the wavelength range shown, with a more pronounced increase in the SubPc region. This suggests that the hexapropyl truxene interlayer alters the absorption of the active layer by changing the morphology, in addition to acting as an electron blocking layer. To test this theory the dark curve of devices with and without the interlayer were measured. It was found that the devices with the interlayer had a lower current density, which indicates that the hexapropyl truxene interlayer prevents exciton quenching. Hence, this is likely the cause of the increase in J_{sc} and the subsequent 21% increase observed in the PCE of the solar cells.

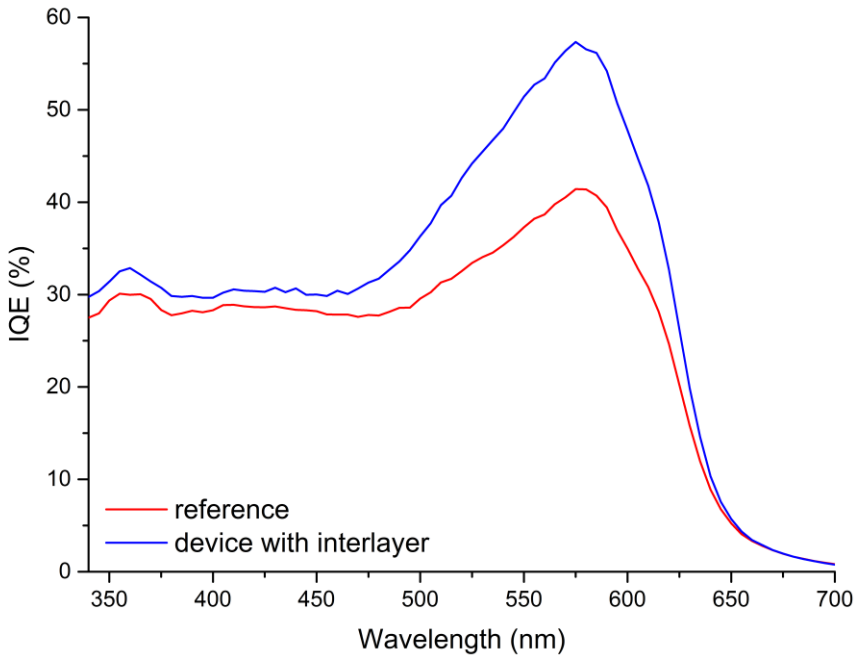

Figure 3.6 - Measurement of IQE for reference device (red) and device with 3.8 nm interlayer of hexapropyl truxene (blue)

3.3 Evaporation of ethyl tricarboxylic acid

To examine if the templating effect was observed with more complex truxene based materials, evaporation of compound **2.11** was attempted. A boron nitride crucible with a tungsten wire was used as the evaporation source, with a rate of 0.7–1.1 Å s^{-1} at a vacuum of 1×10^{-5} mbar. The initial attempt produced a thin (~150 nm) film which was examined by AFM, Figure 3.7. This showed a fairly even surface morphology with a RMS roughness of 29.1.

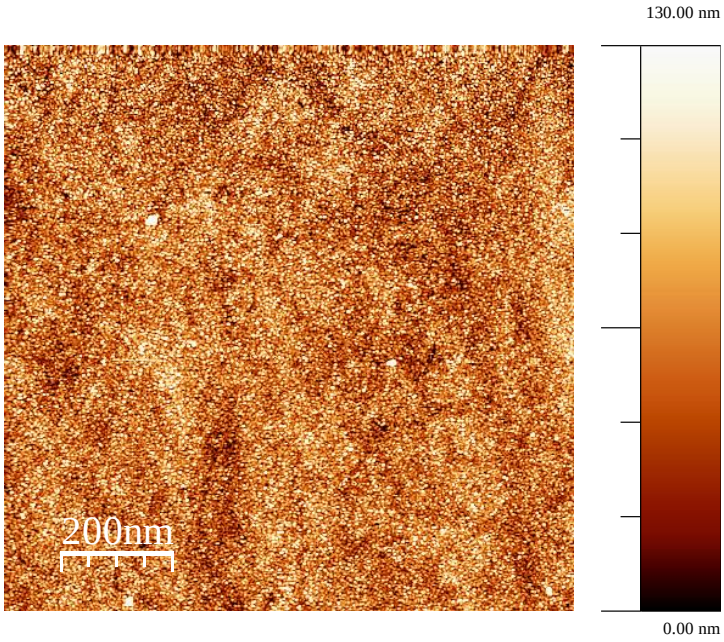

Figure 3.7 - AFM image of substrate after evaporation attempt 1

The material remaining in the crucible was then analysed by ^{1}H NMR, Figure 3.8. The appearance of new peaks indicates that decomposition occurred during the evaporation. Comparing the integrations of the aliphatic peaks before and after evaporation shows little change, but the shapes of these peaks are altered suggesting that there are some overlapping signals. However the main decomposition is related to the aromatic region. Although the relative integrations of the aromatic signals do not change, these signals are noticeably reduced with the appearance of three new aromatic signals.

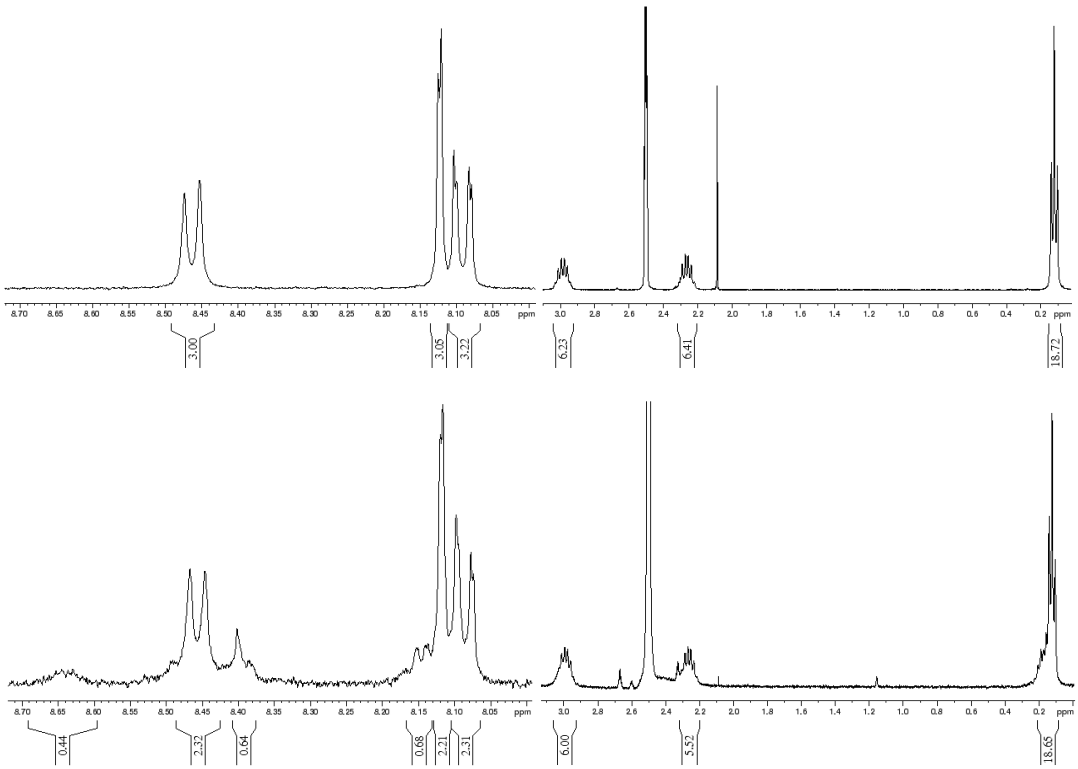

Figure 3.8 - ^{1}H NMR spectra of compound **2.11** before evaporation (top) and the material left in crucible (bottom)

This material remaining in the crucible was evaporated again using a slower rate of 0.2 Å s^{-1} instead of 1 Å s^{-1}. Though a thin film was formed, the evaporation reached a certain point after which no more material reached the substrate. It was found that the material remaining in the crucible was black and too insoluble to be analysed by NMR, Figure 3.9, attempt 2.

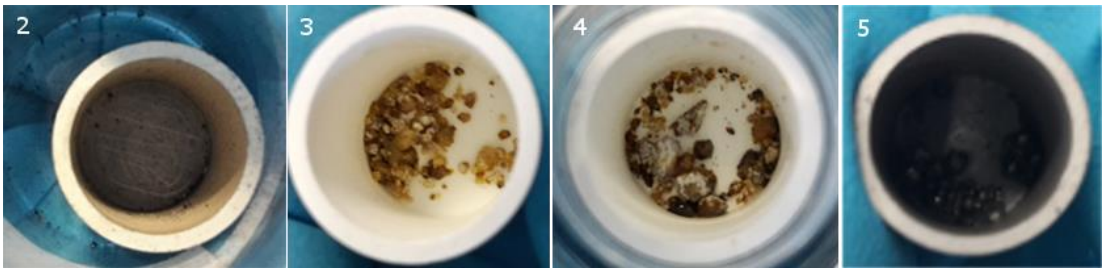

Figure 3.9 - Material remaining in crucibles after attempted evaporations 2–5

New crucibles and portions of compound **2.11** were used in further evaporations. Attempts 3 and 4 used additional liquid nitrogen cooling of the diffusion pump in a bid to maintain the vacuum during evaporation. Attempt 5 was carried out in a different evaporation chamber.

Although films were produced in each evaporation, they were much thinner than desired as in each attempt there was a limiting point, after which no more evaporation occurred. Figure 3.10, shows an AFM image of the film produced during attempt 5.

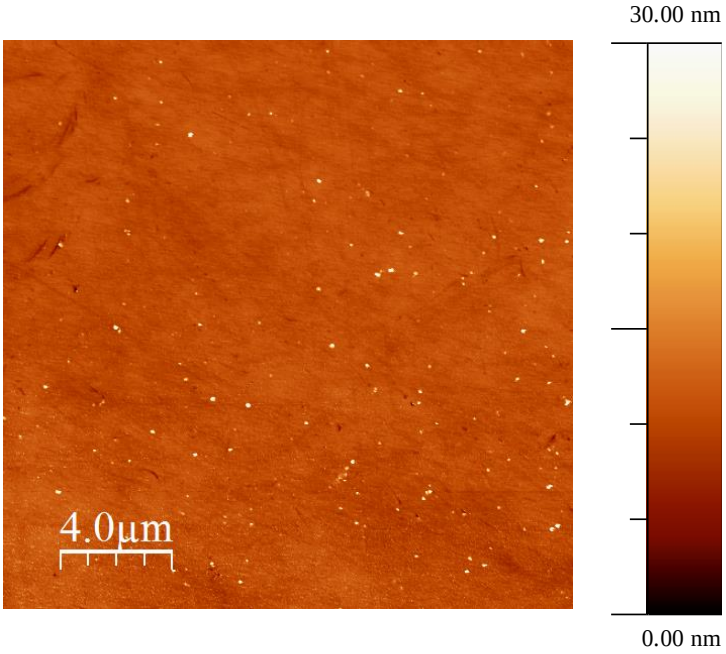

Figure 3.10 - AFM image of substrate after evaporation attempt 5

In each case, the material remaining in the crucible had visually decomposed after each attempt, Figure 3.9. As no further material is available for evaporation this decomposition will cause the limiting point. Overall this suggests that the tricarboxylic acids, **2.10–2.13**, are unsuitable for vacuum deposition.

3.4 Further experiments

3.4.1 Square wave voltammetry

To confirm the CV experiments in Section 2.3.1, square wave voltammetry (SWV) of **2.13** was carried out by Cambridge Display Technology Ltd (CDT) using a 2:1 mixture of acetonitrile:toluene. This solvent system is different to that used for the CV, meaning that in this case the oxidation was found to be outside the stability window of the electrolyte. The reduction was found to occur at −2.30 V by SWV, Figure 3.11. When referenced to ferrocene this was found to be −2.70 V which is broadly similar to the −2.53 V found by cyclic voltammetry, Section 2.3.1.

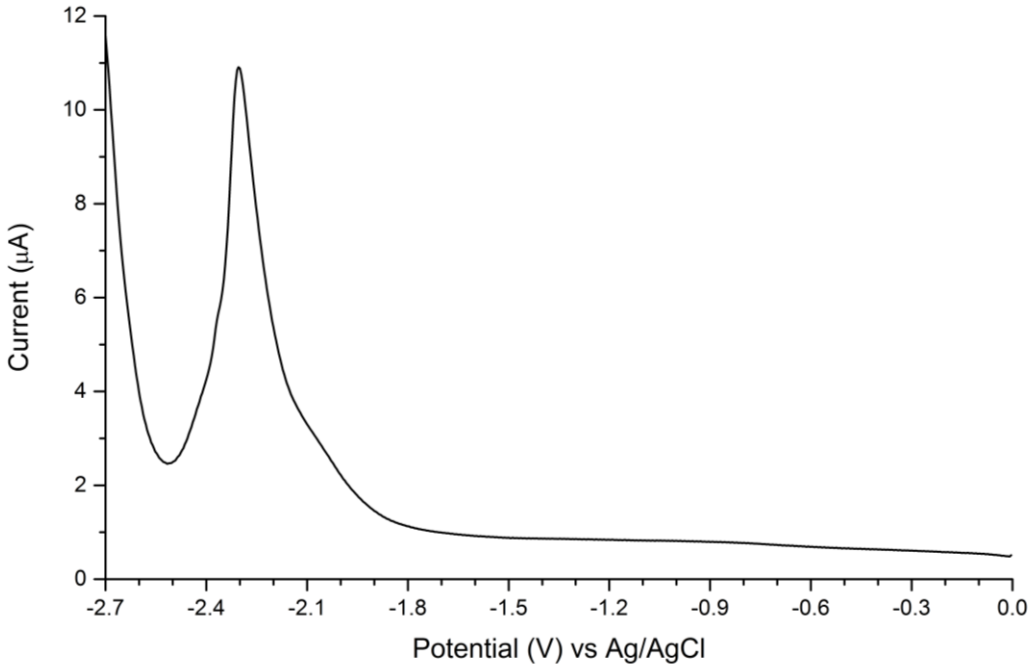

Figure 3.11 - Square wave voltammetry of compound **2.13** carried out by CDT. Obtained in a 2:1 acetonitrile:toluene solution using a glassy carbon working electrode, platinum wire counter electrode and silver/silver chloride reference electrode, with 0.1 M *n*-Bu_4NPF_6 as the supporting electrolyte

It was found that the reduction was still irreversible, and this is likely due to a high overpotential for the proton reduction using a glassy carbon working electrode. When a reference of benzoic acid was tested using a platinum working electrode the reduction occurred at a much lower voltage than that of **2.13**, suggesting that in this

case it is the truxene core which is being reduced. As this is an irreversible process this indicates that the n-doped truxene is not stable in the presence of acidic protons. The proton of the carboxylic acid would be reduced, resulting in the formation of hydrogen gas and carboxylate anions. This would cause a build-up of charge, thus stopping any electron transfer through the truxene layer. Therefore these results suggest that the tricarboxylic acid truxenes are very likely to act as deep electron traps if included in a device such as an OLED.

A small amount of the ethyl ester, **2.9**, was also tested by CDT for electrochemical stability. Again it was found that the oxidation was outside the stability window of the electrolyte in the solvent system used. However in this case the reduction was found to be reversible, Figure 3.12 shows the CV and SWV. There are two reversible peaks at −2.08 V and −2.34V, when referenced to ferrocene this corresponds to a LUMO of −2.23 eV. This is shallower than the analogous tricarboxylic acid as the protons present are not as acidic.

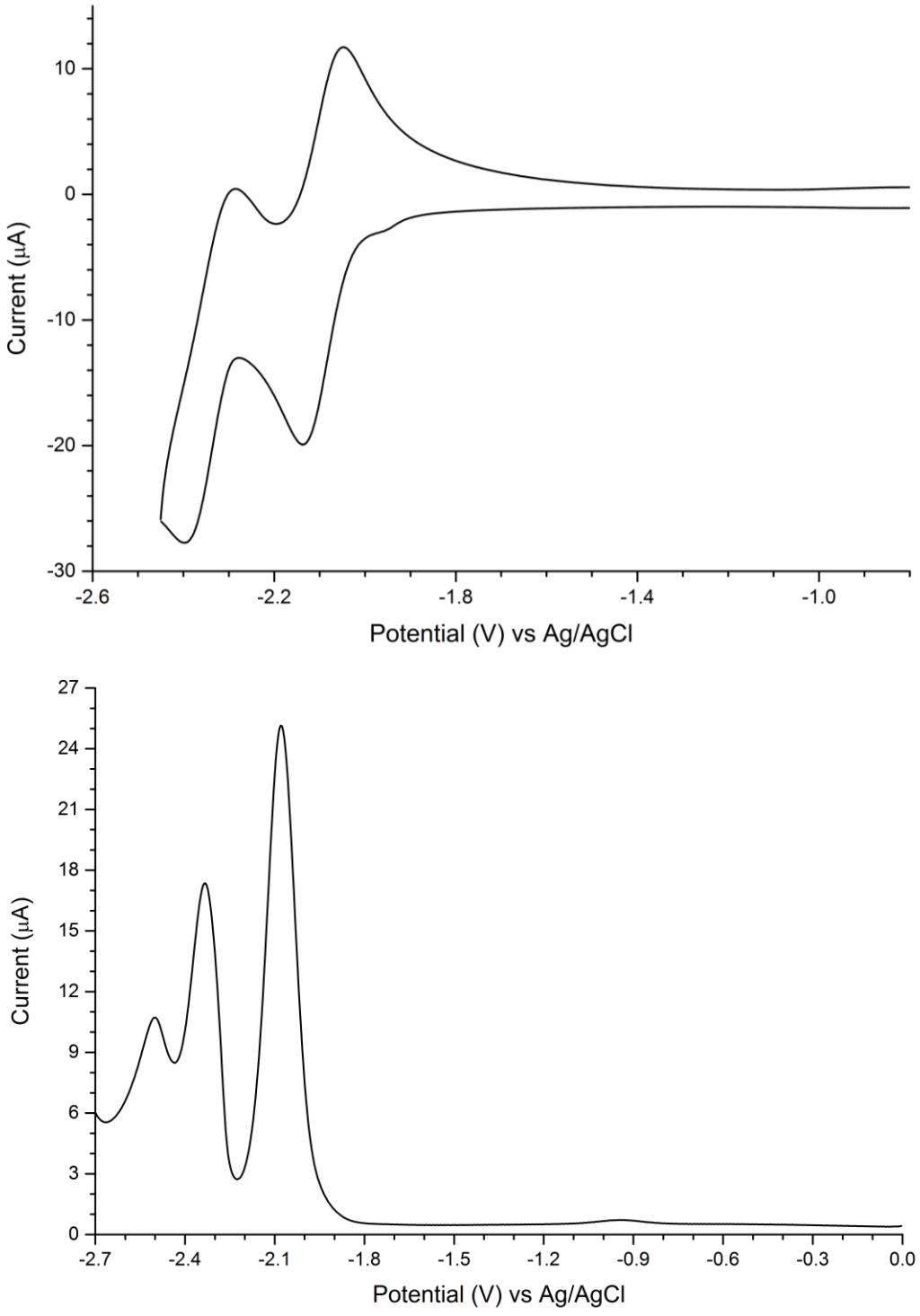

Figure 3.12 - CV (top) and SWV (bottom) of compound **2.9** carried out by CDT. Both obtained in a 2:1 acetonitrile:toluene solution using a glassy carbon working electrode, platinum wire counter electrode and silver/silver chloride reference electrode, with 0.1 M *n*-Bu_4NPF_6 as the supporting electrolyte

3.4.2 Carboxylate salts

Another way to remove the instability associated with the carboxylic acid functionality is to form salts. This should prevent the formation of electron traps in devices. The conversion, shown below in Scheme 3.1, was carried out by suspending the tricarboxylic acid in methanol. To this, 3.3 equivalents (1.1 per position) of the respective hydroxide salt were added as a methanol solution; finally diethyl ether was added to precipitate the carboxylate salt. These salts were collected by filtration, dried *in vacuo* and then used without further purification.

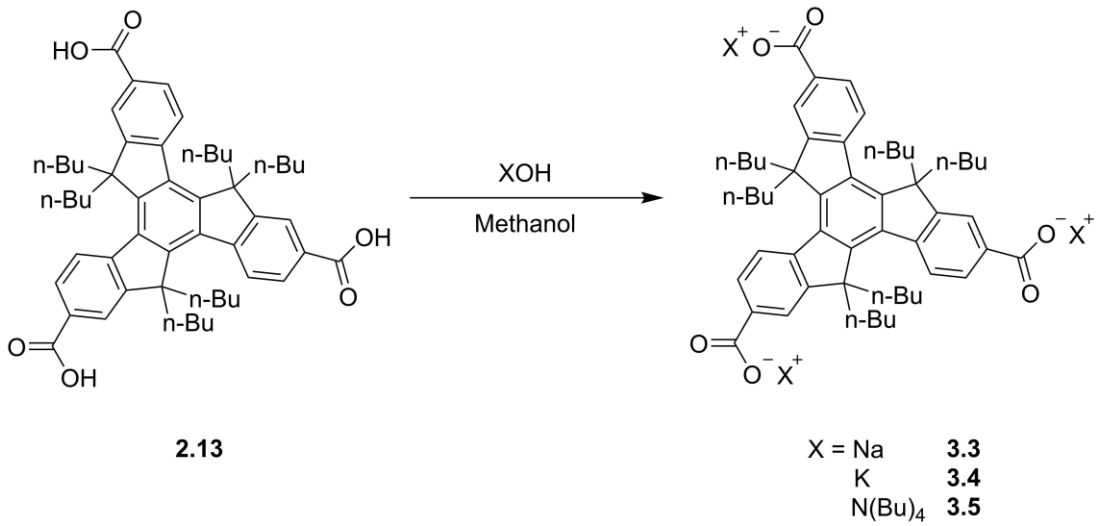

2.13

X = Na **3.3**
K **3.4**
$N(Bu)_4$ **3.5**

Scheme 3.1 - Formation of carboxylate salts **3.3**–**3.5**

The electrochemistry of salts **3.4** and **3.5** was tested by CV and SWV at CDT. The former was found to be insoluble in acetonitrile therefore was tested in a mixture of acetonitrile and ethanol, while **3.5** was tested in acetonitrile. The data is shown in Figure 3.13 and Figure 3.14, respectively. Unfortunately it was found that the carboxylate salts also have an irreversible reduction process.

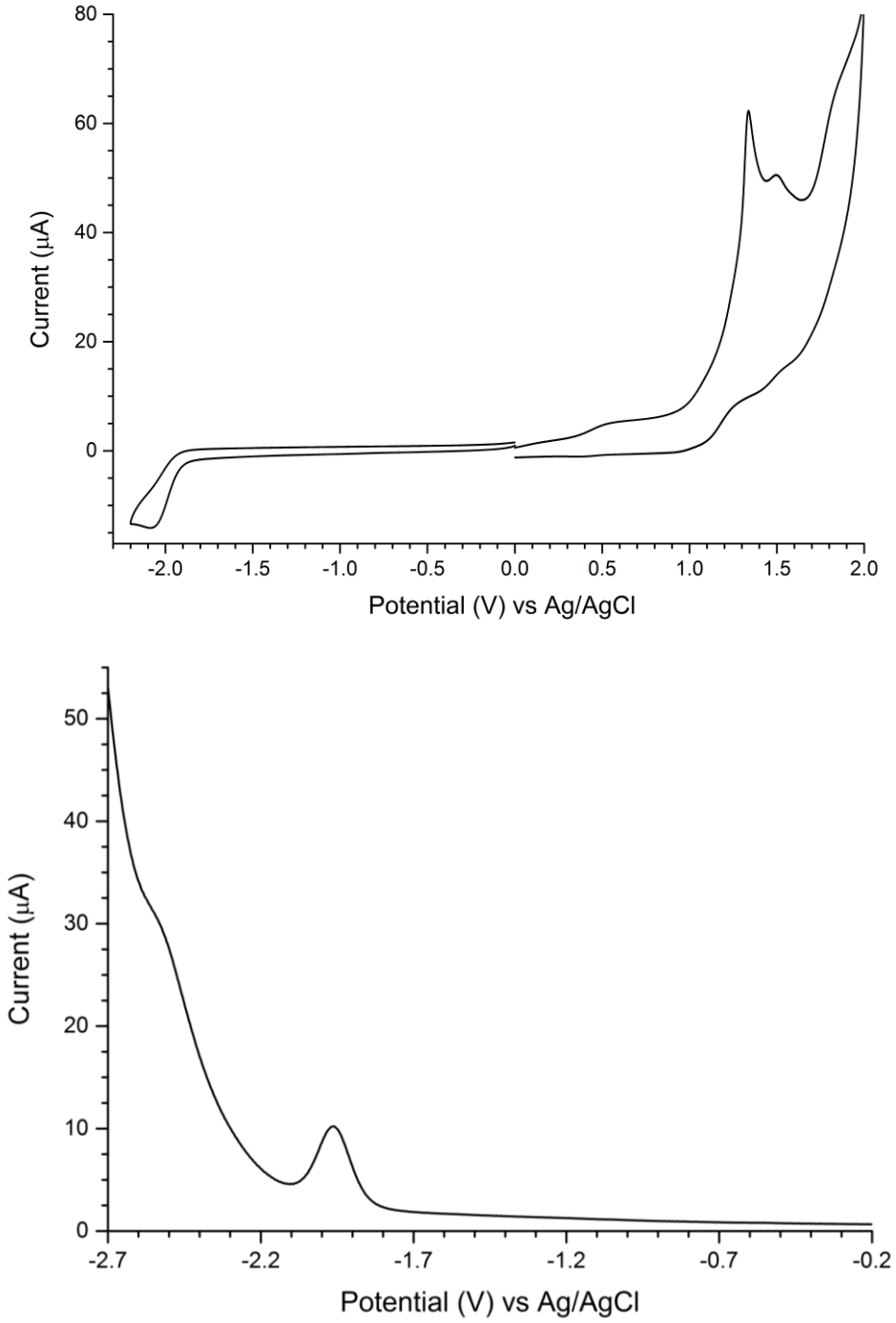

Figure 3.13 - CV (top) and SWV (bottom) of compound **3.4** carried out by CDT. Both obtained in an acetonitrile ethanol mixture using a glassy carbon working electrode, platinum wire counter electrode and silver/silver chloride reference electrode, with 0.1 M *n*-Bu_4NPF_6 as the supporting electrolyte

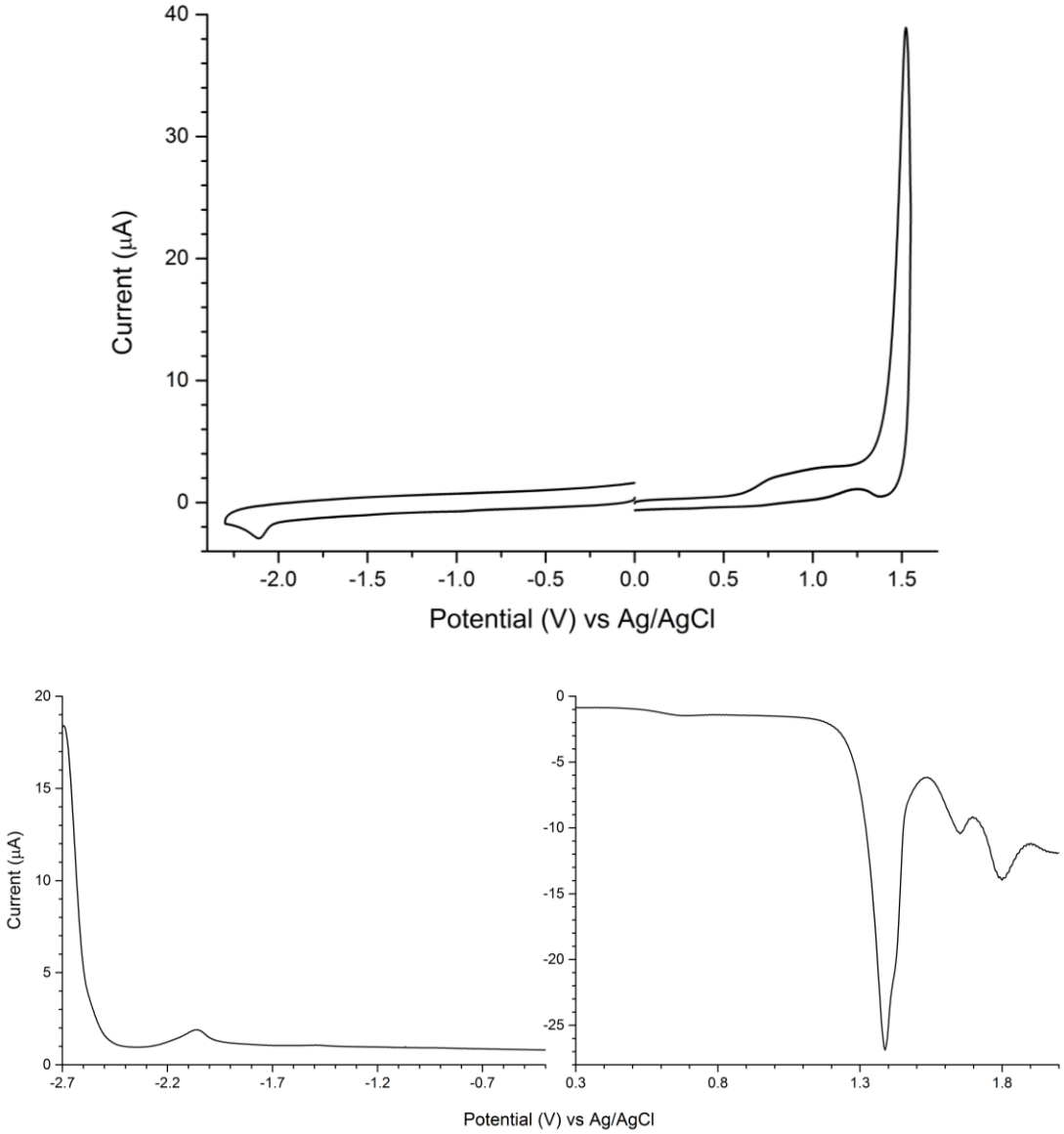

Figure 3.14 - CV (top) and SWV (bottom) of compound **3.5** carried out by CDT. Both obtained in an acetonitrile solution using a glassy carbon working electrode, platinum wire counter electrode and silver/silver chloride reference electrode, with 0.1 M *n*-Bu_4NPF_6 as the supporting electrolyte

CDT included the potassium salt **3.4** as an interlayer in a solution processed OLED to test if a functioning device could be made. This was accomplished, and the potassium salt does work as an interlayer. As shown in Figure 3.15 light was produced from the device, but only in the regions where the interlayer was present. The morphology is clearly not ideal, as the emission is not uniform across the device. It appears that as the spin-coated layer dries it forms aggregates, instead of an even film. This leads to the formation of "islands" which then produce light.

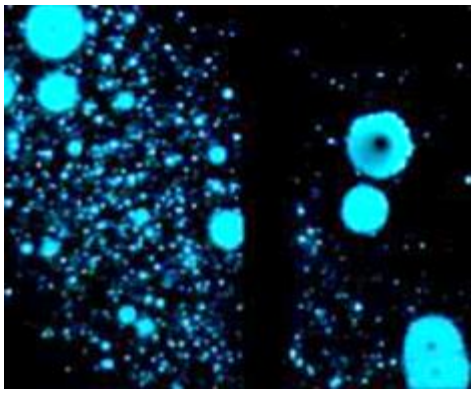

Figure 3.15 - Light produced from an OLED using salt **3.4** as an interlayer

This poor morphology was also observed when spin-coating the salts from a 10 mg/L methanol solution onto a glass substrate. Cracks in the films are visible using both optical microscopy and AFM, as seen below in Figure 3.16.

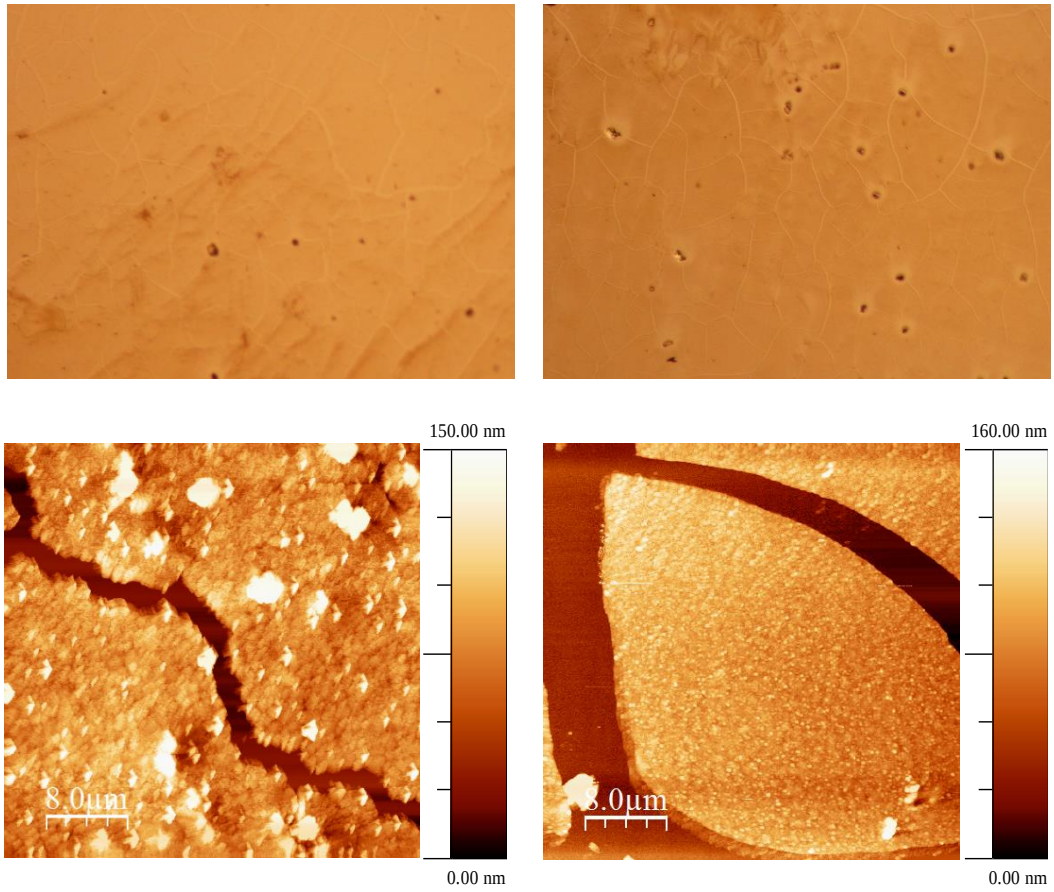

Figure 3.16 - Top: optical microscopy images of spin-coated salt solutions, **3.4** (left) and **3.5** (right). Bottom: AFM images of spin-coated salt solutions, **3.4** (left) and **3.5** (right)

It may be possible to improve the morphology of these spin-coated films by changing the counter ion or the solvent used. However, due to time constraints this was not further examined in this work.

3.5 Conclusions and future work

Based on the results discussed in this chapter, the short chain unfunctionalised truxenes do show promise as a templating layer. There is a clear change in morphology when SubPc is deposited on top of a layer of compound **2.3**.

Interlayers of **2.3** with varying thicknesses were included in a standard solar cell stack. It was found that the optimal interlayer thickness was 3.8 nm; above this the fill factor and PCE began to decline. Compared to reference devices with no interlayer, the J_{SC} and consequently the PCE increased from 2.54% to 3.09%, an improvement of 21%. The main reason for this performance enhancement is the increased absorption of the SubPc layer, most likely due to morphology changes caused by the inclusion of the interlayer. This interlayer acts as an electron blocking layer, reducing exciton quenching which also contributes to the augmented efficiency.

Unfortunately the more complex tricarboxylic acid **2.12** was unstable to vacuum deposition using the equipment available. Though some material could be evaporated, the thickness seemed to be limited due to the onset of decomposition. Overall, this instability renders these materials unsuitable for use in vacuum deposited devices. While unlikely to give the same morphology it would be worth investigating solution processed films of the tricarboxylic acids as interlayers in devices. Due to the strength of the hydrogen bonding interactions the morphology control and templating effect should be more pronounced.

Square wave voltammetry was carried out on compound **2.13**, and the results confirmed the cyclic voltammetry experiments discussed in Chapter 2. Due to the electrochemical instability of the tricarboxylic acids, carboxylate salts of compound **2.13** were formed. When spin-coated from methanol these materials showed very poor wettability leading to an uneven, cracked film. Despite this rough morphology, when the carboxylate salt **3.4** was applied in an OLED it functioned as an interlayer allowing light to be produced from the device.

Further electrochemistry experiments showed that compound **2.9** exhibits reversible reduction peaks at −2.08 V and −2.34 V. This stability arises from the tempering of the carboxylic acid.

The simple derivative **2.3** shows great promise as an interlayer, both by templating the active layer and blocking charge recombination. While the applications of this material remain to be fully explored, by tuning the energy levels of a truxene cored material, the device performance is likely to be improved. Going forward, other active layer materials should be investigated to explore the extent of templating afforded by compound **2.3**. Some commonly reported materials include anthracene, P3HT and PTB7 so these would be a logical starting point.

Future work should examine other functional groups which mitigate the instability associated with the acidic protons. For example, the ester groups show reversible reductions and should retain the hydrogen bonding ability. Similarly, intermolecular interactions will be possible with the inclusion of amides, nitrile containing groups, sulfonamides, thioamides and various heterocycles (such as oxadiazoles, thiadiazoles, thiazolidine dione and pyrrolidine dione).

Finally, the deposition of uniform films of the carboxylate salts could be achieved by exploring different cations such as calcium or anilinium. Additionally, spin-coating from a longer chained alcohol such as butanol will impact the film drying, this could prevent the cracking which was observed with methanol. Other higher boiling point solvents like DMF (*N*,*N*-dimethylformamide) or DMSO will also slow the drying time of the films. The salts have already been shown to function as a charge transport layer; therefore depositing an even film would allow full characterisation of a device.

4 TRUXENE HEXAESTER

4.1 Introduction

On completion of the synthesis and purification of the truxene tricarboxylic acids (discussed in Chapter 2) it was found that the properties of these materials were not suited for application in organic electronic devices. However, the tricarboxylic ester **2.9** exhibited more stable electrochemistry. Due to the exclusion of acidic protons electron traps should not be an issue for materials containing this functional group.

As mentioned at the end of Chapter 2, the butyl derivative will provide the most routine synthesis and purification, while giving a clear indication of the optical and electrochemical properties of the material. Therefore a molecule was designed with six carboxylic ester functionalities surrounding a hexabutyl truxene core.

4.2 Synthesis

A convergent synthetic route was imagined where the ester arm could be attached through a palladium catalysed cross-coupling with the truxene core. The yield of these coupling reactions can be improved by including a better leaving group, therefore the first target was the triiodo truxene core, **4.1**.

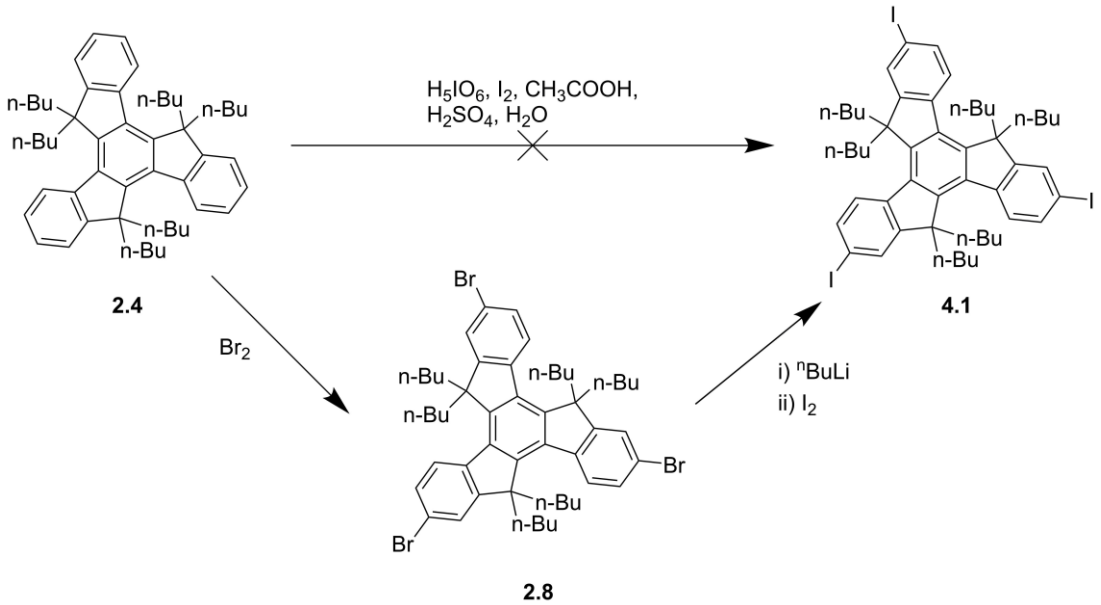

2.4 **4.1** **2.8**

Scheme 4.1 - Routes to triiodohexabutyltruxene **4.1**

The direct conversion of **2.4** to **4.1**, Scheme 4.1, has been previously reported in literature with controlled conditions allowing selective iodination to take place 1, 2, 3 or 6 times.[138] However, in this case the reaction was unsuccessful, producing only a complex mixture of products. As the tribromo derivative, **2.8**, had been previously synthesised an alternative route of halogen interconversion was carried out. Reaction with *n*-butyllithium formed the trianion which could be quenched with iodine to afford **4.1** as shown in Scheme 4.1. The purification was straightforward, allowing the triiodotruxene to be isolated in excellent yield, 92%.

To form the phenyl acetylene, **4.3**, dimethyl 5-bromoisophthalate and ethynyltrimethylsilane (TMS-acetylene) were reacted using Sonogashira conditions to give **4.2**. The desired product could then be obtained by removal of the trimethylsilyl (TMS) group, as shown below in Scheme 4.2. Following the straightforward literature procedure, **4.3** was obtained using 1.5 equivalents of tetrabutyl ammonium fluoride, in a moderate yield of 68%.[139]

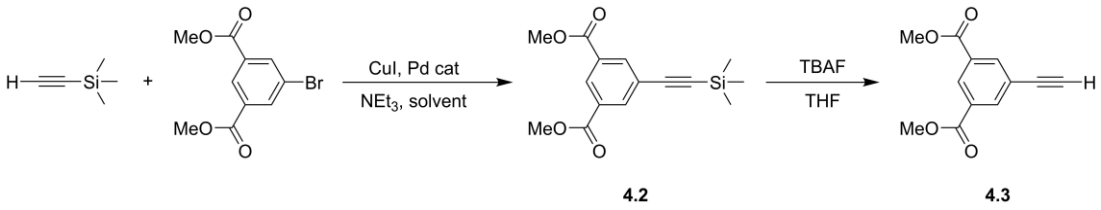

Scheme 4.2 - Formation of ester arm **4.3**. Solvent refers to DMF, THF, or neat triethylamine

The general mechanism of the Sonogashira coupling is shown in Scheme 4.3. Often initial ligand disassociation is required so that the palladium is coordinatively unsaturated, *i.e.* has a site available for substrate bonding.[6,140]

Oxidative addition (*a*) is usually the rate determining step, due to the increase in coordination number and crowding around the metal centre. This can be accelerated by using electron rich ligands and/or electron deficient RX. The X group is then replaced by the second substrate through transmetallation (*b*).

For the reaction to advance *cis/trans* isomerisation (*c*) must occur so that the substrates are *cis* to each other. Finally reductive elimination (*d*) releases the coupled product and regenerates the catalyst for another cycle. Typically this step is very fast, but is further accelerated by bulky ligands.

The copper co-catalyst is used to increase the rate of the transmetallation step, by producing the activated copper acetylide. As a weak base is generally used, the copper ion must first complex to the acetylene before deprotonation. The copper acetylide is then formed and can react with the palladium catalyst.

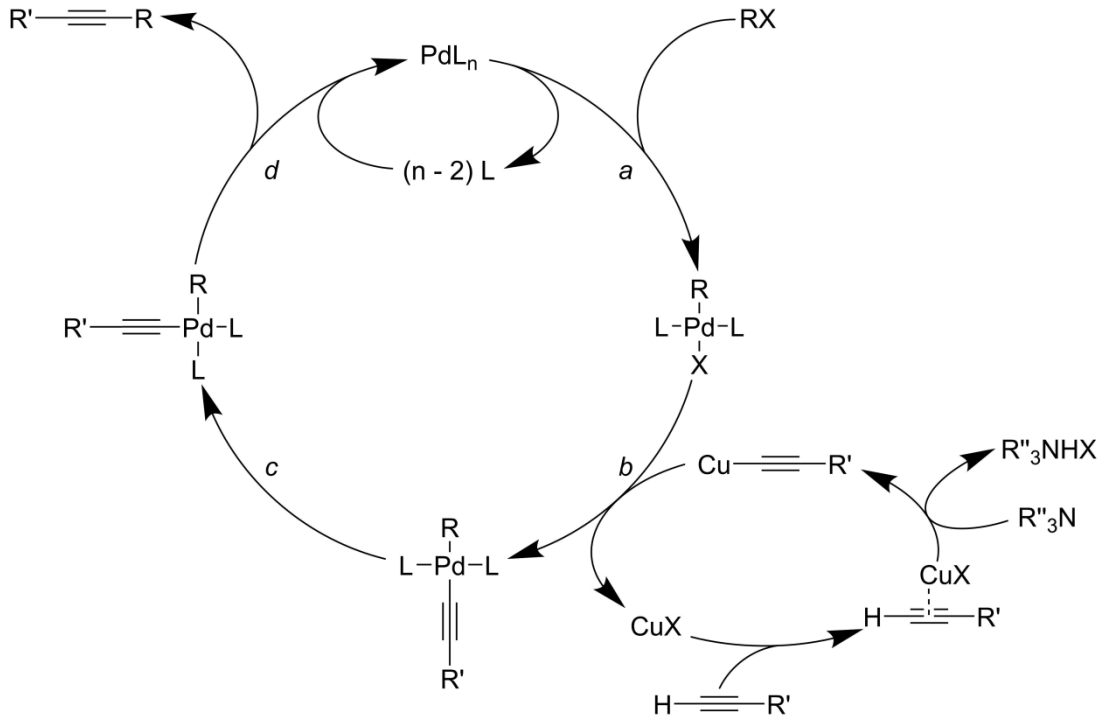

Scheme 4.3 - General mechanism of Sonogashira cross coupling reaction

The same palladium catalysed cross coupling reaction was to be carried out threefold to form the final product; therefore a short screening process was carried out to optimise conditions for the formation of **4.2**, as shown in Table 4.1.

Table 4.1 - Sonogashira condition screening

Attempt	Heating	Catalyst	CuI [a]	TMS-acetylene [a]	Base: Solvent	Conversion (Yield [b])
1	M	10 wt % $Pd(PPh_3)_4$	0.30	2.0	NEt_3:DMF (1:7)	92%
2	M	10 wt % $Pd(PPh_3)_4$	0.36	3.9	NEt_3:DMF (1:7)	50%
3	M	10 wt % $Pd(dppf)Cl_2$	0.36	3.9	NEt_3:DMF (1:7)	89%
4	C	10 mol % $Pd(PPh_3)_4$	1.0	28	NEt_3 (neat)	100%
5	C	10 mol % $Pd(PPh_3)_4$	1.0	21	NEt_3 (neat)	100% (46% [b])
6	C	5 mol % $Pd(PPh_3)_4$	1.1	20	NEt_3 (neat)	0%
7	C	10 mol % $Pd(PPh_3)_4$	1.1	7.9	NEt_3 (neat)	100% (52% [b])
8	C	10 mol % $Pd(PPh_3)_4$ [c]	1.1	3.8 [c]	NEt_3:THF (1:2)	100% (88% [b])

M = microwave heating at 160°C; C = conventional heating at reflux; [a] molar equivalents relative to dimethyl 5-bromoisophthalate; [b] isolated yield; [c] more added throughout reaction

In attempt 1 the triethylamine was used as supplied, while in attempt 2 it was freshly distilled over calcium hydride immediately prior to use. Though this decreased the yield slightly, to ensure the removal of impurities the triethylamine was also distilled in subsequent attempts.

The catalyst was changed for attempt 3 to [1,1'-bis(diphenylphosphino)ferrocene]dichloropalladium(II) ($Pd(dppf)Cl_2$), however this also lead to a decreased yield so only the less expensive tetrakis(triphenylphosphine)palladium(0) ($Pd(PPh_3)_4$) was used subsequently. In these three attempts TLC and ^1H NMR showed that the starting material was consumed, however there were many impurities formed along with some product.

The conversion of starting material was improved by changing from microwave heating to conventional heating. Though the reaction times are longer, removing the requirement for a reaction medium that absorbs microwave irradiation allowed the base to be used neat as a solvent.

When switching to conventional heating, an increased number of equivalents of TMS-acetylene were used due to concerns over the efficiency of the condenser for low boiling reagents over long reaction times. However it was found that this was not required and the relative quantity of TMS-acetylene could be lowered.

Additionally, the number of equivalents of copper iodide was increased. Though the copper should be regenerated during the reaction adding a slight excess in attempt 7 resulted in an improved yield compared to attempt 5.

Alongside the greater conversion, the formation of triphenylphosphine oxide was observed; as it can be difficult to remove this coproduct the catalyst loading was decreased. However, the reaction did not proceed as desired and mainly unreacted starting material was recovered after attempt 6.

When the reaction was scaled up, in attempt 8, it was decided that a solvent should be used to limit the amount of triethylamine required. This reaction was more closely monitored by ^{1}H NMR with more catalyst and TMS-acetylene added to increase the consumption of starting material. Anecdotally, it has been found within the Skabara group that adding the catalyst in portions rather than all at the start can improve the yields of palladium catalysed cross-couplings.

This was not an extensive reaction screen and other factors such as the base used and different catalysts could also be examined. Additionally, if dimethyl 5-iodoisophthalate was used the improved leaving group ability and reactivity should make the coupling more efficient. However these conditions were easily scalable and led to an excellent isolated yield after straightforward purification.

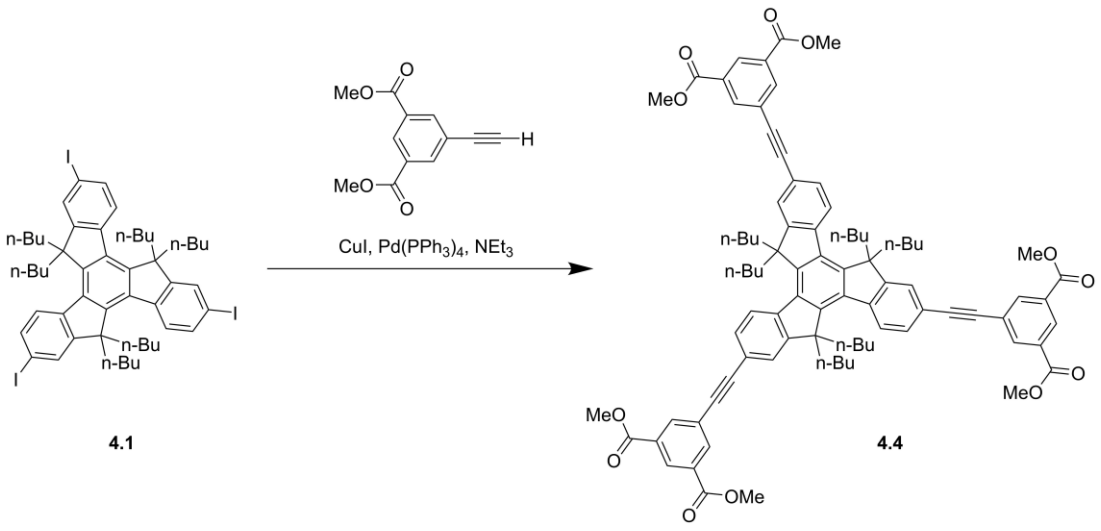

Scheme 4.4- Coupling of phenyl acetylene to truxene core to form compound **4.4**

Using the optimised conditions, compounds **4.1** and **4.3** were coupled to produce **4.4**, Scheme 4.4. The reaction proceeded well and no additional catalyst was required, most likely due to a combination of the improved leaving group ability of iodine and the increased polarisation of the acetylene. Furthermore, the purification of **4.4** was straightforward; the lower polarity of the ester functionality meant that column chromatography was feasible, unlike the tricarboxylic acids **2.10**–**2.13**. Due to the

larger differences between the mono-, di- and tri-coupled species the desired product was easily separated, and could be further purified by recrystallisation with a final yield of 87%.

4.3 Results and discussion

4.3.1 Optical and electrochemical properties

The absorbance and emission spectra of **4.4** were measured in CH_2Cl_2 at concentrations of 10^{-5} and 10^{-7} molar respectively, Figure 4.1. The main absorbance peak is at 341 nm, with another at 351 nm of almost equal intensity. The emission spectrum has one main peak at 384 nm, with a shoulder at 399 nm. Again the optical HOMO-LUMO gap was calculated from the onset of the longest wavelength of absorbance, these results are summarised in Table 4.2. Films of sufficient quality could not be formed to measure the solid state absorption and emission properties.

In comparison to the tricarboxylic acids the absorbance of compound **4.4** is red shifted, however the compounds emit around the same wavelength. Additionally, there is a greater overlap of the absorption and emission profiles suggesting that there is a smaller change in geometry between the ground and excited states. This indicates that hexaester is more rigid than the analogous tricarboxylic acid (**2.13**), the improved definition of peaks in the absorption spectra and smaller Stokes shift observed support this hypothesis.

The electrochemical properties were also measured in CH_2Cl_2 at a concentration of 10^{-3} molar. The voltammogram in Figure 4.2 shows an irreversible reduction and two irreversible oxidation peaks.

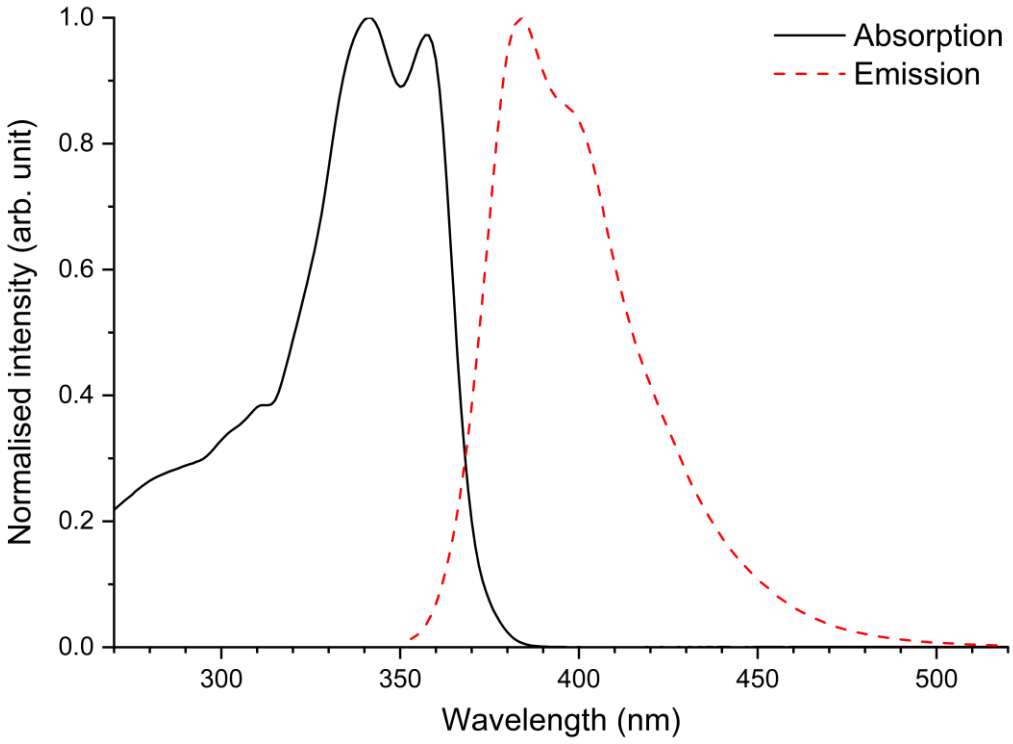

Figure 4.1 - Normalised absorption (10^{-5} M) and emission (10^{-7} M) spectra of compound **4.4** in CH_2Cl_2

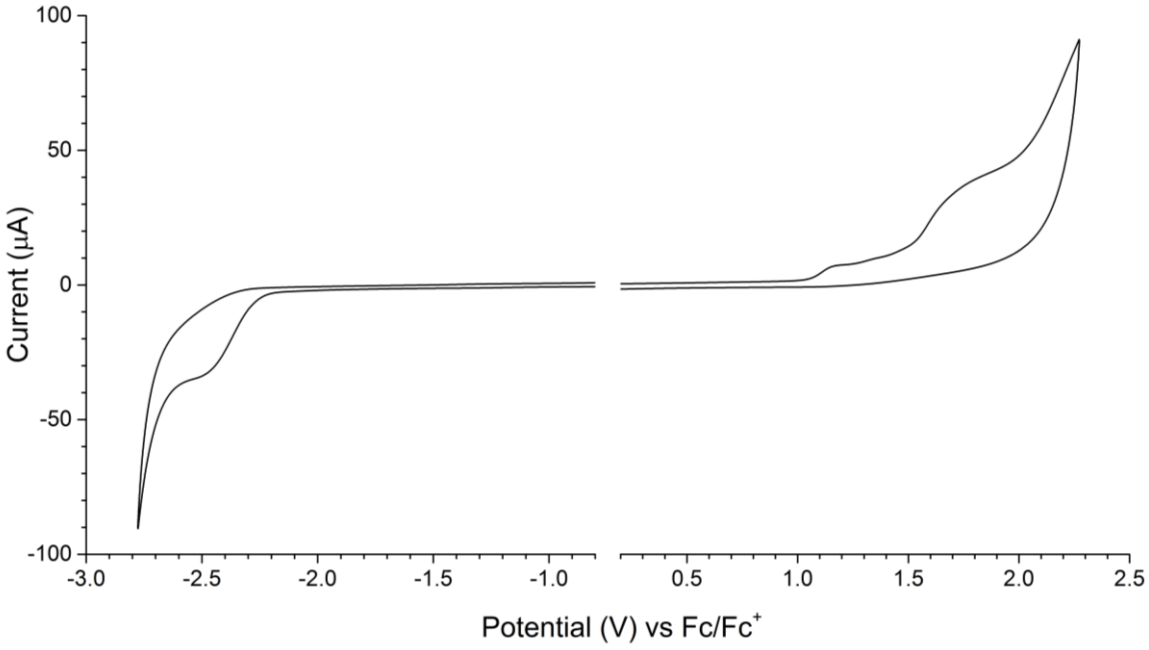

Figure 4.2 - Cyclic voltammogram of compound **4.4** in a 10^{-3} M CH_2Cl_2 solution. Obtained using a glassy carbon working electrode, platinum wire counter electrode and silver wire reference electrode, a scan rate of 100 mV s^{-1}, and 0.1 M *n*-Bu_4NPF_6 as the supporting electrolyte

When referenced to ferrocene the electrochemical HOMO-LUMO gap was found to be 3.6 eV, Table 4.2. This is higher than the optical HOMO-LUMO gap, due to the addition of the exciton binding energy. Overall, the HOMO-LUMO gap is lower than the tricarboxylic acids discussed previously, this is mainly as a result of the extended conjugation present in **4.4**. The structure of this molecule also allows for more π-π intermolecular interactions, which will influence the HOMO-LUMO gap (Section 1.2.1).

Table 4.2 - Optical and electrochemical properties of compound **4.4**

λ_{abs} (nm)	λ_{PL} (nm)	E_p^{ox} (V)	E_p^{red} (V)	E_g^{UV} (eV)	E_g^{CV} (eV)
282 (sh), 310 (sh), 341, 357	384, 399 (sh)	1.16, 1.73	−2.48	3.2	3.6

Due to the observed high fluorescence of this material, the PLQY was measured. As a result of equipment limitations, only the relative PLQY could be measured, but compound **4.4** is highly fluorescent in the solid state.

Anthracene was selected as the reference standard as its emission range of 360–480 nm is similar to that of **4.4**. To measure the relative PLQY, five solutions of each compound were prepared at different concentrations, compound **4.4** was dissolved in toluene and the anthracene reference in ethanol, then the absorbance and fluorescence of each solution was measured. Figure 4.3 shows the integrated area under the emission spectra versus the absorbance at the wavelength of maximum absorbance, 356 nm for anthracene and 341 nm for compound **4.4**.

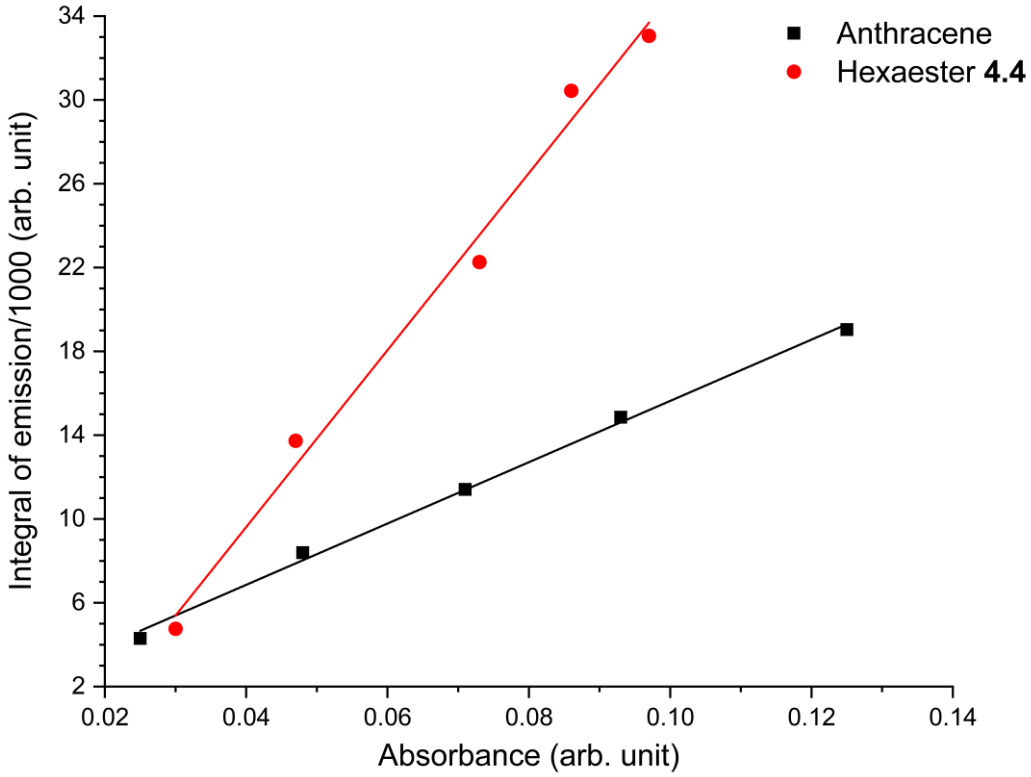

Figure 4.3 - Relative PLQY measurement of compound **4.4** against anthracene

The gradient of the trendlines in Figure 4.3 are related to the PLQY, and as the quantum yield of anthracene is known that of the hexaester can be calculated. The refractive index of each solvent much also be taken into account, thus the values in Table 4.3 are used in Equation 1.6. The calculated relative PLQY of **4.4** is 0.94, this very high value may indicate other potential uses for this small molecule, such as lasing applications.

Table 4.3 - Calculation of relative PLQY of compound **4.4**

Compound	Gradient	Solvent refractive index	PLQY
Anthracene	146300	1.36	0.27
4.4	422400	1.497	0.94

4.3.2 Thermal properties

Figure 4.4 shows the TGA trace of compound **4.4**, the material is stable up to ~350 °C at which point slow decomposition begins. 5% mass loss occurs at 427 °C, and after heating to 540 °C there is 58.9% of the original mass present.

A heat-cool-heat cycle of DSC was also run on compound **4.4**, the results of the second and third cycles are shown in Figure 4.5. No thermal event occurs within the temperature range examined meaning this compound would be suitable for device processing. With a melting point of 280–282 °C the normal annealing temperatures used for device fabrication should not negatively affect any deposited layers of compound **4.4**.

Overall, this material displayed slightly improved thermal stability when compared to compound **2.13**.

Table 4.4 - Thermal properties of compound **4.4**

Melting point [a] (°C)	280–282
5% mass loss (°C)	427
Mass remaining at 540 °C (%)	58.9

[a] Melting point determined on a melting point apparatus

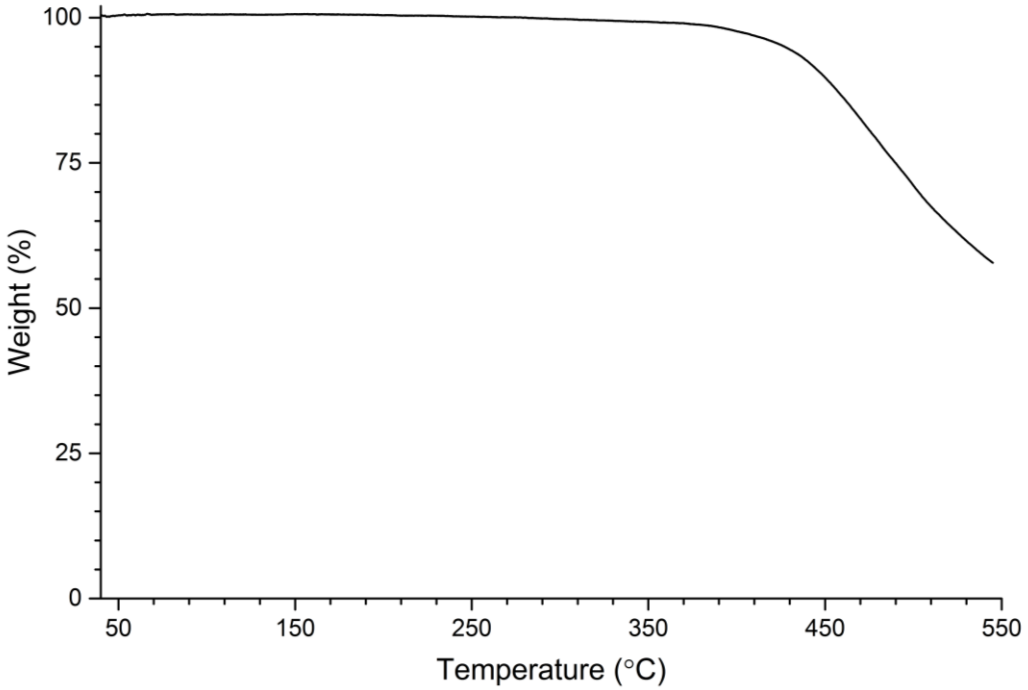

Figure 4.4 - TGA plot of compound **4.4**, heating under argon at a rate of 10 °C min^{-1}

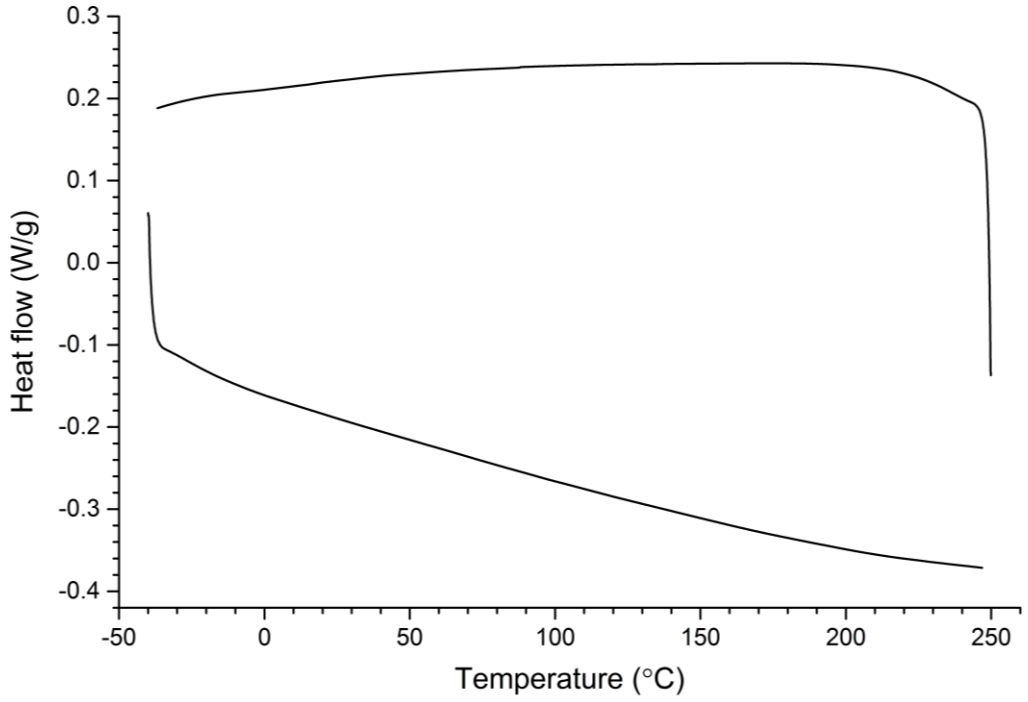

Figure 4.5 - DSC plot of compound **4.4** during a heat-cool-heat cycle, showing cooling from 250 °C to −40 °C, then heating from −40 °C to 250 °C at a rate of 10 °C min^{-1} under nitrogen

4.3.3 X-ray crystallography

Single crystals of **4.4** were obtained from a 1:1 mixture of CH_2Cl_2:MeCN, the asymmetric unit of which is shown in Figure 4.6. The truxene core has twist angles of 3.80–8.27°. One of the phenyl substituents sits in the same plane as the truxene core, with a slight bend in the alkyne bond. The other substituents are slightly twisted, allowing the dihedral angle along the alkyne bond to be closer to 180°. These angles are summarised in Table 4.5, where 1, 2 and 3 refer to the numbering in Figure 4.6.

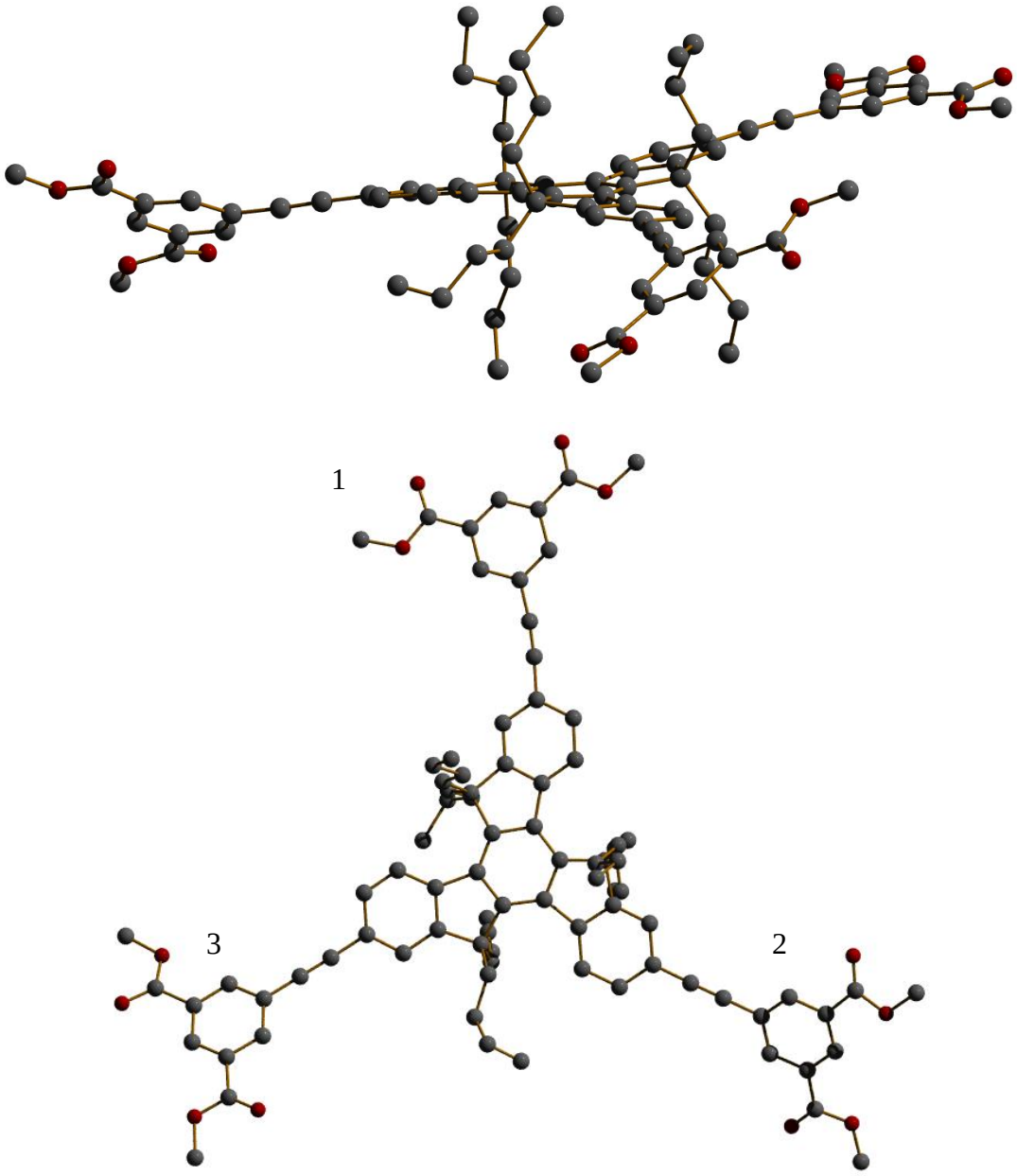

Figure 4.6 - Asymmetric unit of compound **4.4**. Hydrogen atoms omitted for clarity

Table 4.5 - Crystallographic features of compound **4.4**

	1	2	3
Substituent twist angle (°) [a]	3.09	24.37	36.61
C≡C–phenyl dihedral (°)	174.17	177.58	178.63
C≡C bond length (Å)	1.20	1.24	1.21

[a] the calculated angle between planes plotted through the aromatic ring of the phenyl substituent and the adjacent benzene ring of the truxene core

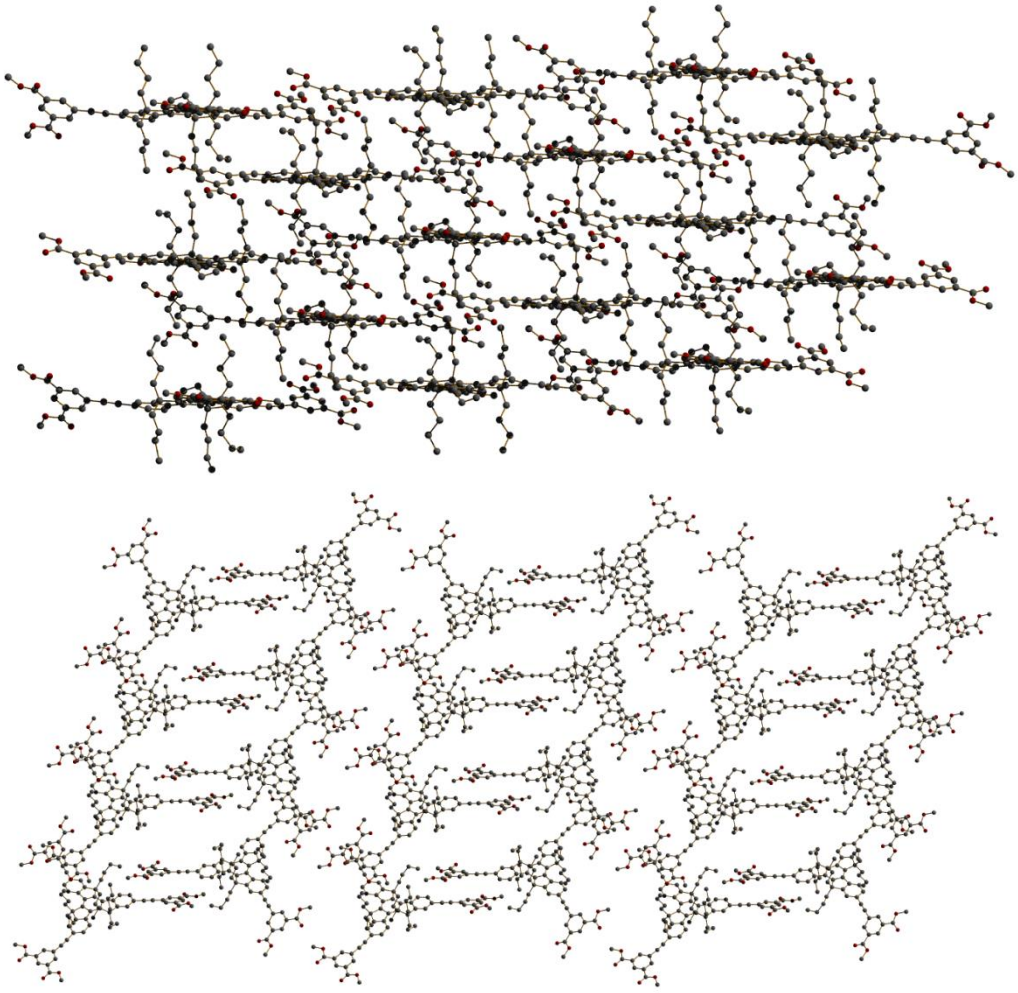

Figure 4.7 - Packing motif of compound **4.4**. Hydrogen atoms omitted for clarity

The slipped stack packing motif of this structure is shown in Figure 4.7. Looking along one axis the twisted substituents sit parallel to each other; within these sheets the closest contact between the phenyl rings is 9.96 Å. Along another axis the phenyl substituents sit closely to a neighbouring truxene core, with 3.34 Å separating the phenyl groups and 4.09 Å between the substituent and neighbouring core, forming the dimers observed in Figure 4.7. These stacks of dimers are separated by the ester groups with 3.30 Å between the methyl group of one molecule and the carbonyl functionality of another.

4.4 Conclusions and future work

The synthesis of an extended truxene derivative with six carboxylic ester functionalities was successfully completed. A small screen was carried out to find improved reaction conditions for the Sonogashira coupling of the arm, with isolated yields ranging from 46% to 88%. Applying the best conditions to the coupling between the arm and the iodinated core allowed the final compound to be prepared in excellent yields at a considerable scale.

Cyclic voltammetry showed irreversible oxidation and reduction, which may limit applicability to devices. The absorption profile shows two main peaks, while the emission profile contains one peak with a shoulder. The electrochemical HOMO-LUMO gap was found to be 3.6 eV; the optical HOMO-LUMO gap was slightly lower at 3.2 eV. Due to the extended conjugation present in **4.4** this is lower than the tricarboxylic acids presented in Chapter 2.

A crystal structure was obtained for this molecule, the core was found to be planar while two of the arms were twisted. The hexaester showed some very interesting packing with strong π-π stacking.

The most significant finding was the very high relative PLQY of 0.94 in solution. Though not quantified, this material is also very emissive in the solid state; thus could be applicable to lasing applications.[141]

If this material proved successful as an organic lasing material different substituents on the phenyl groups could be explored as way of tuning the wavelength of the laser. Furthermore, the inclusion of more electronegative substituents would produce a more reversible electrochemical profile which is desirable for electrically pumped lasers.

Although the molecular weight of **4.4** may make it unsuitable for vacuum deposition, it could still be applied to a solution processed device. Additionally, the ester could be easily converted to a carboxylate salt, as discussed in Chapter 3, and then incorporated into a solution processed device. The morphology may be improved due

to the increased aromatic character of this material. Additionally, combining the hexaanion with multivalent cations such as calcium, copper or iron could be used to create a complex intermolecular network within the thin film.

5 CYANO SUBSTITUTED TRUXENES

5.1 Introduction

With an aim of improving the electrochemical characteristics of the truxene based materials, more electron withdrawing cyano containing groups were introduced. These groups should alleviate the instability associated with the acidic protons present in the tricarboxylic acids, while retaining the ability to influence the morphology of subsequently deposited layers. Additionally, these lower molecular weight materials should be thermally stable and therefore suitable candidates for vacuum deposition.

5.2 Synthesis

To facilitate the introduction of electron withdrawing groups the trialdehyde (**5.1**) was first synthesised. As shown in Scheme 5.1, lithium-halogen exchange followed by reaction with *N*,*N*-dimethylformamide (DMF) gave the common intermediate **5.1**.

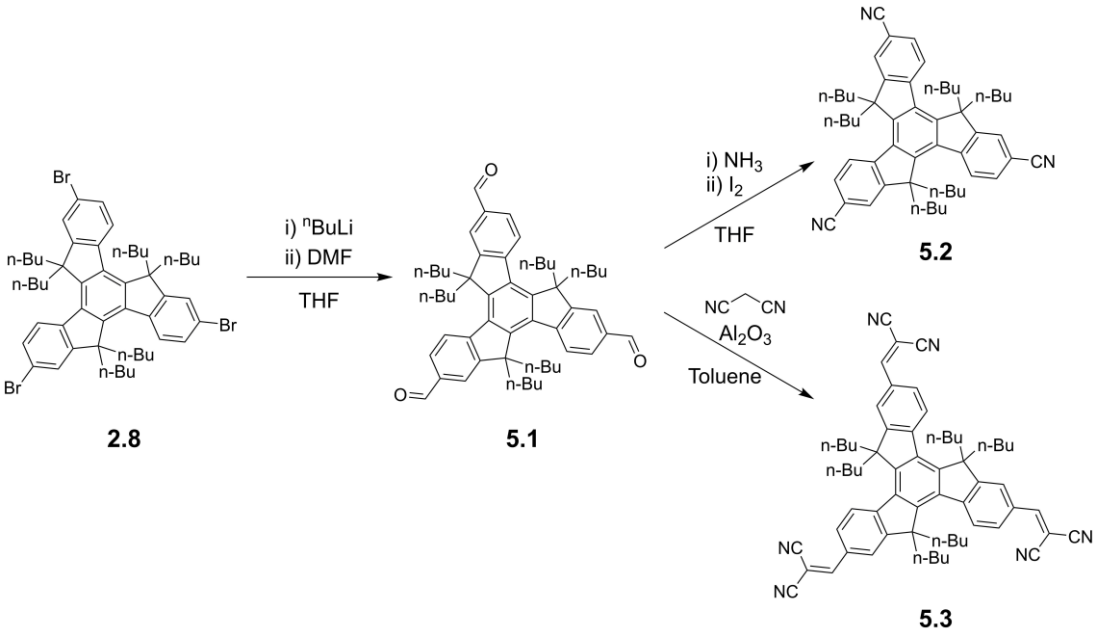

Scheme 5.1 - Synthesis of CN substituted truxenes **5.2** and **5.3**

Table 5.1 shows the conditions attempted in the synthesis of **5.1**, in all cases a slight excess of *n*-butyllithium and DMF were used. In the first attempt *n*-butyllithium was added at −78 °C and the mixture stirred at this temperature for 60 minutes. This was to ensure that the lithium halogen exchange occurred fully before the addition of DMF. Due to the low yield, the time between additions was decreased in attempt 2; this lead to a marginal increase in yield (3%). The reaction with *n*-butyllithium should be fast even at low temperature, thus the extra time between additions makes it more likely that undesirable side reactions will occur. By keeping the time between additions low and increasing the relative quantities of both *n*-butyllithium and DMF the yield was significantly increased to 80% in attempt 3.

Table 5.1 - Conditions trialled in the formation of compound **5.1**

Attempt	*n*-BuLi [a]	DMF [a]	Time at −78 °C (minutes)	Yield (%)
1	1.1	2.0	60	49
2	1.1	2.0	15	52
3	2.0	2.2	15	80

[a] molar equivalents per position relative to compound **2.8**

Separation of the desired trialdehyde was achieved by simple column chromatography; while the majority of the product was isolated in excellent purities, there was some overlap between the elution of the dialdehyde and trialdehyde meaning some mixed fractions were recovered. These fractions were not further purified, leading to a slightly lower isolated yield than possible.

The trialdehyde was then converted to tricyano truxene (**5.2**) using iodine and ammonia. The general mechanism suggested by Shie and Fang is shown in Figure 5.1.[142] After initial reaction with ammonia, the tetrahedral intermediate will lose water to form the intermediate *N*-iodo aldimine; this subsequently loses a molecule of HI to form the cyano compound. Up to this point, reactions were performed under inert conditions with a constant positive pressure of nitrogen. However, in this case it was found that the iodine would sublime from the reaction vessel before complete conversion could occur. Therefore, after addition of the reagents was complete the flask was sealed, allowing the reaction to proceed in good yield, 68%.

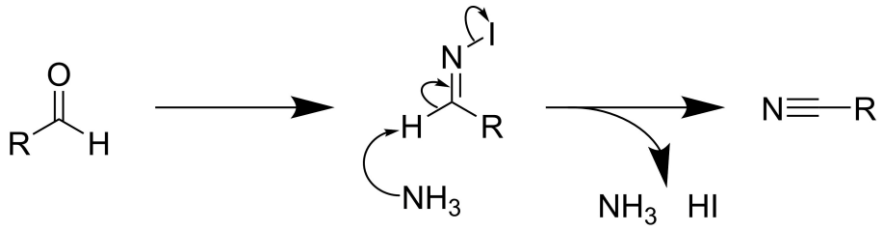

Figure 5.1 - Mechanism of cyano formation

Compound **5.3** was prepared from the same intermediate, **5.1**, by Knoevenagel condensation with malononitrile. Initially this was attempted with a few drops of the mild base piperidine, Table 5.2. No product was formed so the quantity of base was increased; magnesium sulfate was added to remove water, in an attempt to drive the equilibrium to the desired product. This modification also resulted in no product being formed, therefore the conditions were changed based on a procedure reported by Cariello *et al.*, attempt 3.[143] Though this formed some of the desired product the yield was low. Therefore an alternative method was employed whereby malononitrile and the trialdehyde (**5.1**) were heated in the presence of basic alumina.[144] This lead to a cleaner reaction, and **5.3** was isolated in 36% yield following recrystallisation.

Table 5.2 - Conditions trialled in the formation of compound **5.3**

Attempt	Solvent	Piperidine	$MgSO_4$	Other
1	Ethanol	3 drops	None	None
2	Ethanol	1.3 [a]	0.60 [a]	None
3	Toluene	0.21 [a]	0.21 [a]	Glacial acetic acid (0.60 [a])
4	Toluene	None	None	Basic alumina (1:1 weight per position)

[a] molar equivalents per position relative to compound **5.1**

In order to further decrease the HOMO-LUMO gap an attempt was made to incorporate tetracyanobutadiene (TCBD) acceptor units, as shown in Scheme 5.2. The first step was to form the truxene acetylene using a Negishi coupling between **2.8** and a zinc acetylene which is formed *in situ* from the corresponding dibromopropane.

Previous work within the Skabara group had shown that where R = H the resultant TCBD may be unstable, therefore R = Me was selected to improve both the stability and the solubility. Though the reaction to produce **5.4** occurred fairly cleanly and the conversion was high, the isolated yield for this step was low (22%) due to difficulties in removing residual triphenylphosphine oxide.

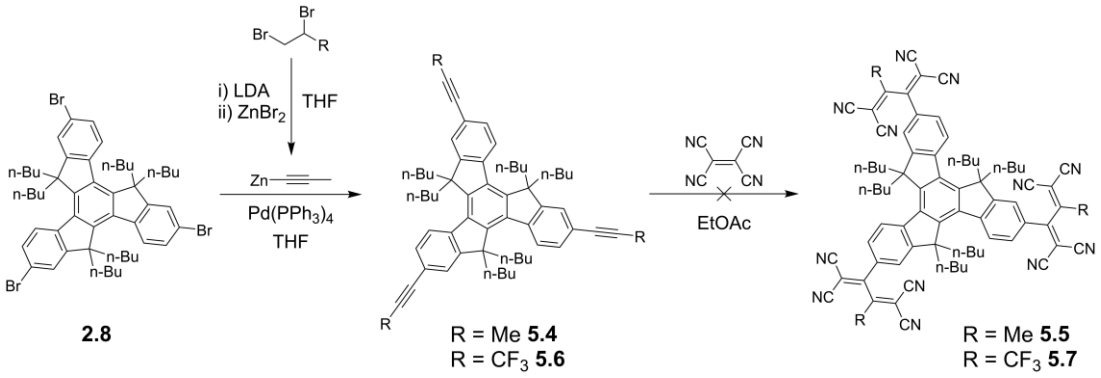

Scheme 5.2 - Attempted synthesis of tetracyano substituted truxenes **5.5** and **5.7**

The subsequent electrocyclisation to form **5.5** was unsuccessful, and a further literature search suggested that the acetylene needs to be polarised for the reaction with tetracyanoethylene (TCNE) to proceed.[145–147] Therefore compound **5.7** was chosen as a new target; the CF_3 group should sufficiently polarise the acetylene to aid the reaction with TCNE, in addition to increasing the acceptor strength in the final compound. Unfortunately attempts to form **5.6** were not successful, likely due to no formation of the acetylene required for the *in situ* coupling.

5.3 Results and discussion

5.3.1 Optical and electrochemical properties

The electrochemical properties of **5.2** and **5.3** were initially measured in acetonitrile, at concentrations of 10^{-3} molar. In both cases the oxidation was clearly defined, but the reduction was not; therefore to improve the resolution the reduction of each was run in DMF. The voltammograms for **5.2** and **5.3** are shown in Figure 5.2 and Figure 5.3 respectively. Both compounds show a pseudo-reversible oxidation, which occur at around the same potential, 1.52 V and 1.42 V, respectively. Compound **5.2** shows a pseudo-reversible reduction with a half-wave potential of −2.31 V, while the irreversible reduction for **5.3** occurs at a higher potential of −1.49 V.

The optical properties of both **5.2** and **5.3** were measured in acetonitrile and are shown in Figure 5.4 and Figure 5.5 respectively. Compound **5.2** has a more defined vibronic structure with a maximum absorbance at 321 nm and higher energy peaks at 294 nm and 309 nm, additionally there are two less intense peaks at 344 nm and 361 nm. The absorbance of **5.3** is more featureless, with a maximum at 399 nm, and a second peak at 305 nm. Both the absorption and emission are red shifted compared to **5.2** due to the increased electron withdrawing ability of the substituents.

These results and the associated HOMO-LUMO gaps are summarised in Table 5.3. Due to the greater electron withdrawing ability of the dicyanovinyl functionality, compound **5.3** has a smaller optical and electrochemical HOMO-LUMO gap, with only a small difference between the two. The optical HOMO-LUMO gap of **5.2** is significantly smaller than the electrochemical HOMO-LUMO gap, this is due to the presence of low intensity, low energy peaks in the absorption spectrum. The HOMO-LUMO gap calculated using the onset of the main peak is 3.6 eV which is more comparable with the electrochemical HOMO-LUMO gap.

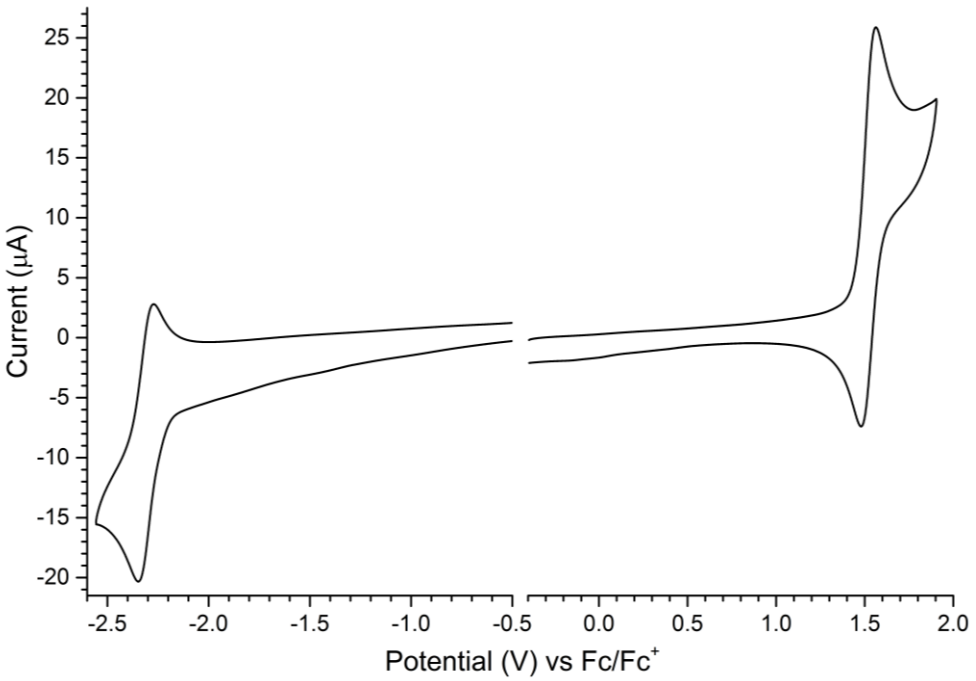

Figure 5.2 - Cyclic voltammogram of compound **5.2**, 10^{-3} M in acetonitrile (oxidation) and 10^{-3} M in DMF (reduction). Both obtained using a glassy carbon working electrode, platinum wire counter electrode and silver wire reference electrode, a scan rate of 100 mV s^{-1}, and 0.1 M *n*-Bu_4NPF_6 as the supporting electrolyte

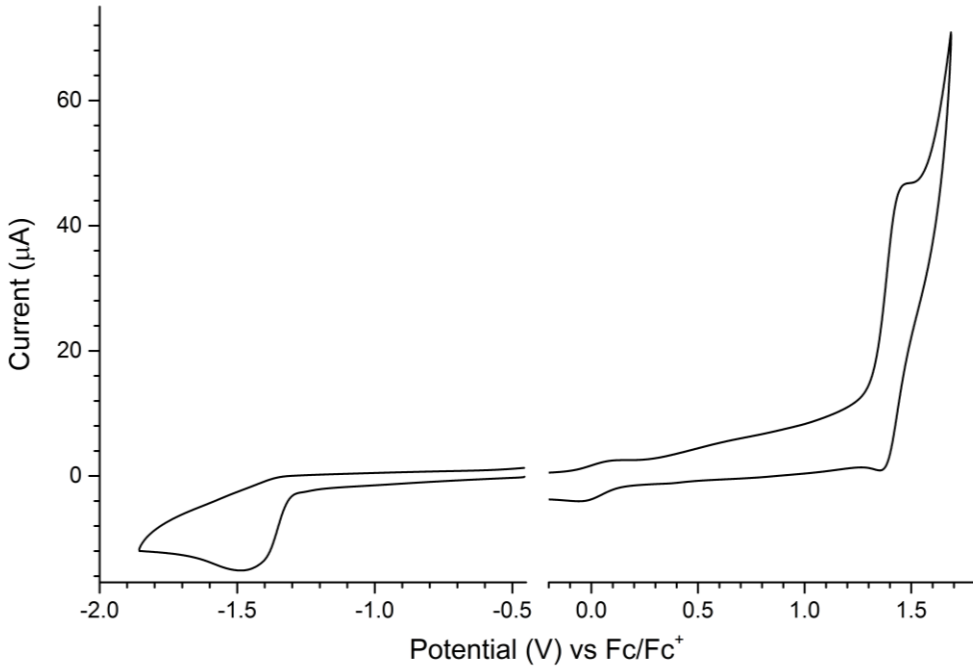

Figure 5.3 - Cyclic voltammogram of compound **5.3**, 10^{-3} M in acetonitrile (oxidation) and 10^{-3} M in DMF (reduction). Both obtained using a glassy carbon working electrode, platinum wire counter electrode and silver wire reference electrode, a scan rate of 100 mV s^{-1}, and 0.1 M *n*-Bu_4NPF_6 as the supporting electrolyte

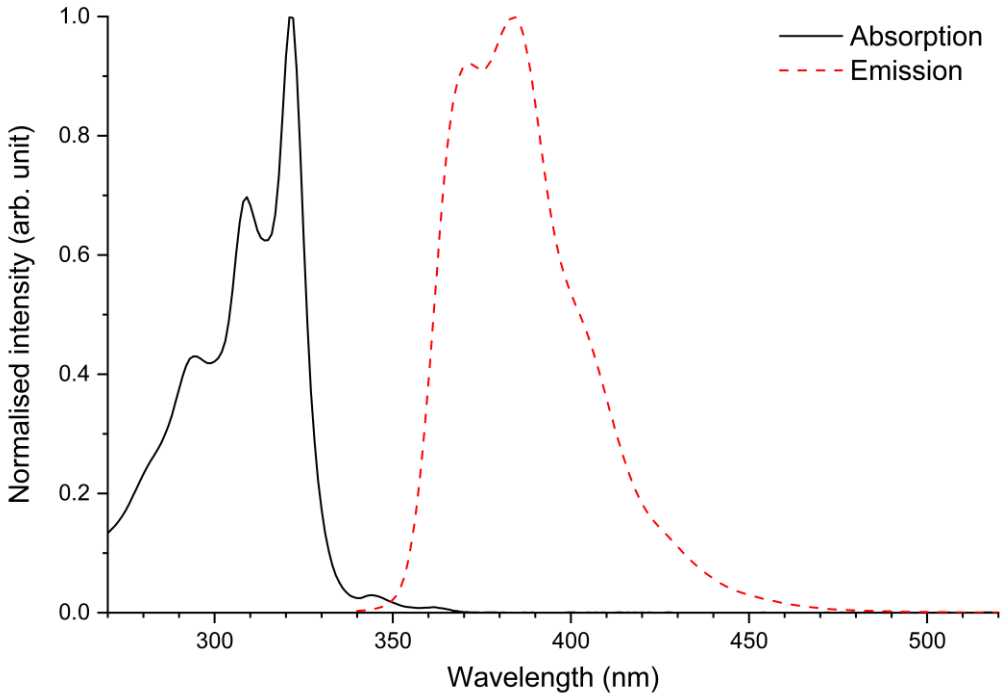

Figure 5.4 - Normalised absorption (10^{-5} M) and emission (10^{-6} M) spectra of compound **5.2** in acetonitrile

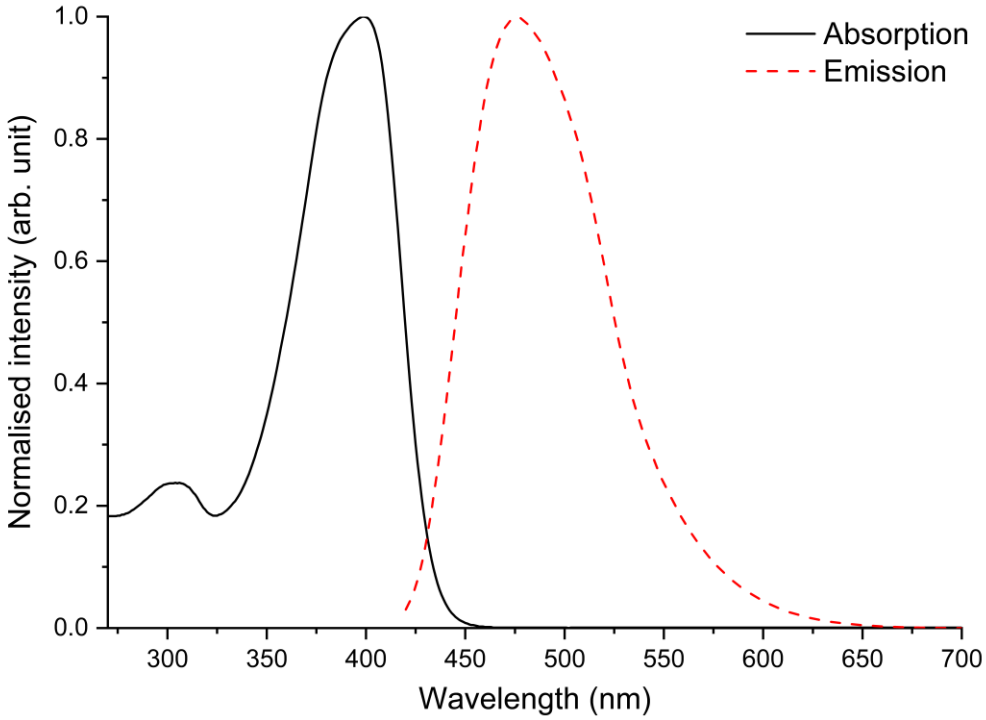

Figure 5.5 - Normalised absorption (10^{-5} M) and emission (10^{-5} M) spectra of compound **5.3** in acetonitrile

When compared to the carboxylic acids shown in Chapter 2 the electrochemical HOMO-LUMO gap of **5.2** is quite similar, but shows a pseudo-reversible reduction. The HOMO-LUMO gaps of **5.3** are much smaller than compounds **2.10**–**2.13** and **4.4** due to the inclusion of the strongly electron withdrawing group.

Table 5.3 - Optical and electrochemical properties of compounds **5.2** and **5.3**

Compound	**5.2**	**5.3**
λ_{abs} (nm)	294, 309, 321, 344, 361	399, 305
λ_{PL} (nm)	384, 371, 404 (sh)	476
$E_{1/2}^{ox}$ (V)	1.52	1.42
E^{red} (V)	−2.31 [a]	−1.49 [b]
E_g^{UV} (eV)	3.3 [c]	2.8
E_g^{CV} (eV)	3.8	2.9

[a] $E_{1/2}$; [b] E_p; [c] calculated using the onset of the longest wavelength of absorbance

5.3.2 Solvation effects

It was observed that compound **5.3** appeared a slightly different colour when dissolved in different solvents, this effect can be seen under ambient light and UV illumination as shown in Figure 5.6.

Therefore the absorption and emission spectra of **5.2** and **5.3** were measured in five solvents which were selected to cover a wide range of polarities. The wavelength of the maximum absorption and emission of both compounds in each solvent is shown below in Table 5.4, along with the dielectric constant of each solvent.

Table 5.4 - Solvent dependent optical properties of compounds **5.2** and **5.3**

Solvent	Toluene	CH_2Cl_2	Acetone	MeCN	DMSO
ε[148]	2.37	8.93	20.49	35.69	46.83
5.2 λ_{abs} (nm)	323	323	325	321	324
5.2 λ_{PL} (nm)	384	385	383	384	386
5.2 Stokes shift (nm)	61	62	58	63	62
5.3 λ_{abs} (nm)	408	412	399	399	401
5.3 λ_{PL} (nm)	435	458	466	476	485
5.3 Stokes shift (nm)	27	46	67	77	84

It can be seen that the optical properties of **5.2** do not depend on the solvent polarity; hence the Stokes shift does not show any dependency on solvent polarity. Compound **5.3** shows a slight change in the maximum wavelength of absorption but a large variation in the emission maximum, leading to a linear relationship between polarity and Stokes shift, illustrated in Figure 5.7. This positive solvatochromism suggests that the geometry of the excited state differs depending on the polarity of the solvent.[149]

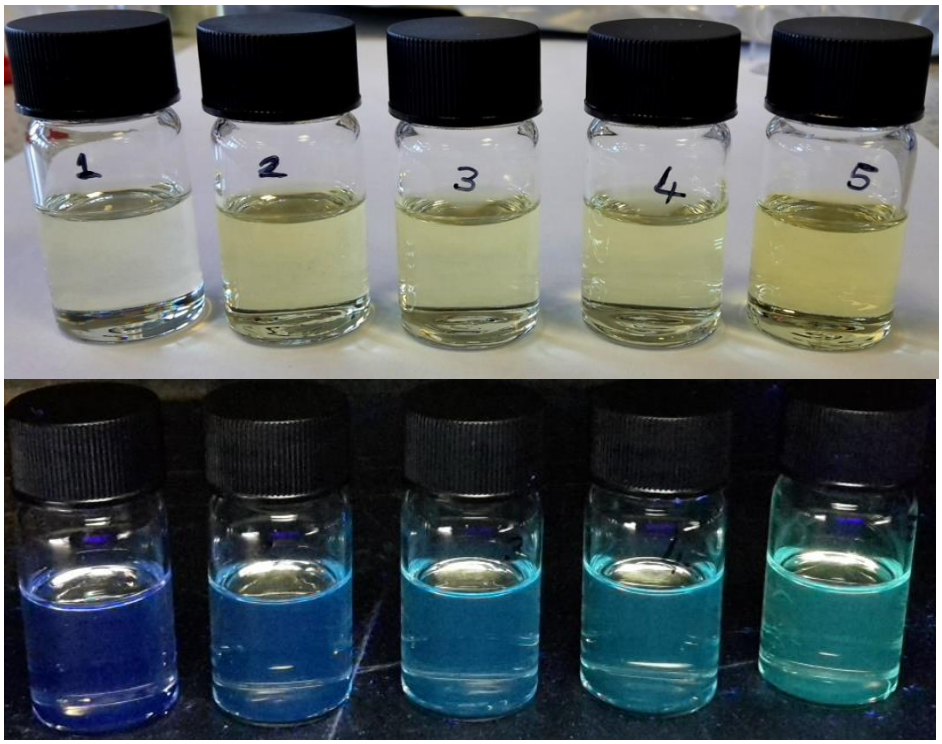

Figure 5.6 - Compound **5.3** under ambient light and UV illumination in various solvents: 1) toluene, 2) CH_2Cl_2, 3) acetone, 4) MeCN, and 5) DMSO

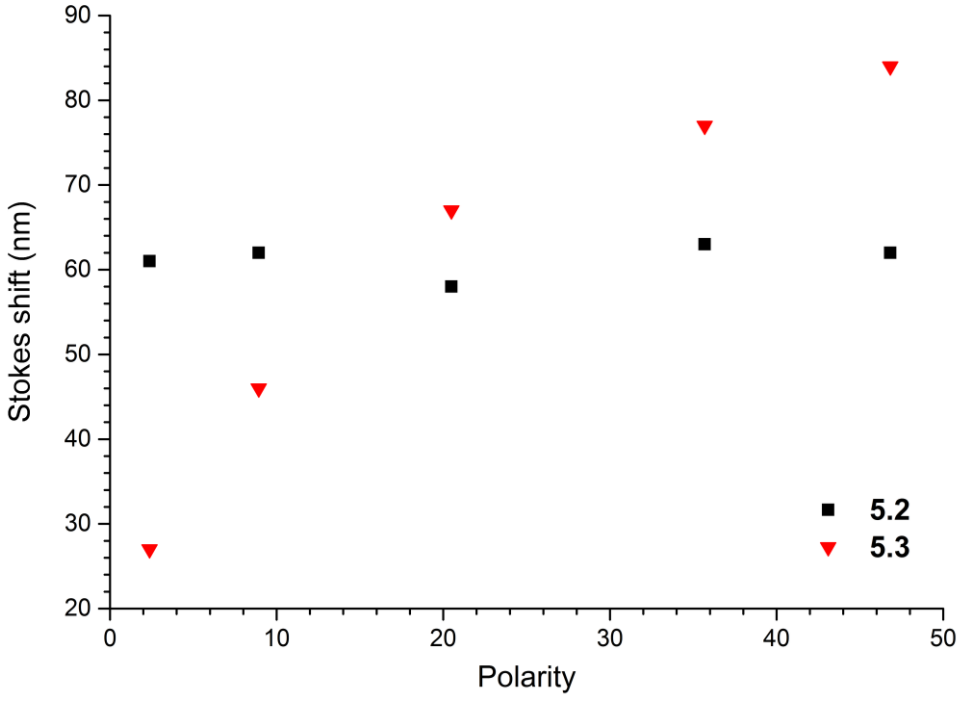

Figure 5.7 - Stokes shift of compounds **5.2** and **5.3** measured in different solvents

5.3.3 Thermal properties

The TGA plots of **5.2** and **5.3** are shown in Figure 5.8 and Figure 5.9 respectively. Two processes are visible for compound **5.2**, beginning around 350 °C there is a sharp drop in mass, with only 17.2% remaining at 440 °C. Immediately following this, there is a much shallower mass decrease leading to 9.9% of the original weight remaining at 540 °C. Compound **5.3** shows a single process beginning around 390 °C, with a gradient in-between that of the two processes seen for **5.2**. At 540 °C there is 61.2% of the original mass remaining. These results are summarised in Table 5.5.

In a heat-cool-heat DSC cycle no thermal processes were observed up to 250 °C for compound **5.2**, Figure 5.10. The heat-cool-heat DSC cycle for compound **5.3** is shown in Figure 5.11. The cooling cycle features a glass transition at 98 °C and an exothermic peak at 73.8 °C, while the second heat cycle has a glass transition at 115 °C. The morphological stability of films of compound **5.2** will not be altered by thermal annealing but films of compound **5.3** will be. Therefore heating up to, or above, the glass transition temperature will cause the packing of **5.3** to change. This may be beneficial or detrimental to the device performance, but is an important consideration for device fabrication and lifetimes.

Table 5.5 - Thermal properties of compounds **5.2** and **5.3**

Compound	**5.2**	**5.3**
Melting point [a] (°C)	308–309	188–190
5% mass loss (°C)	369	419
Mass remaining at 540 °C (%)	9.9	61.2
T_g (°C)	-	98/115

[a] Melting point determined on a melting point apparatus

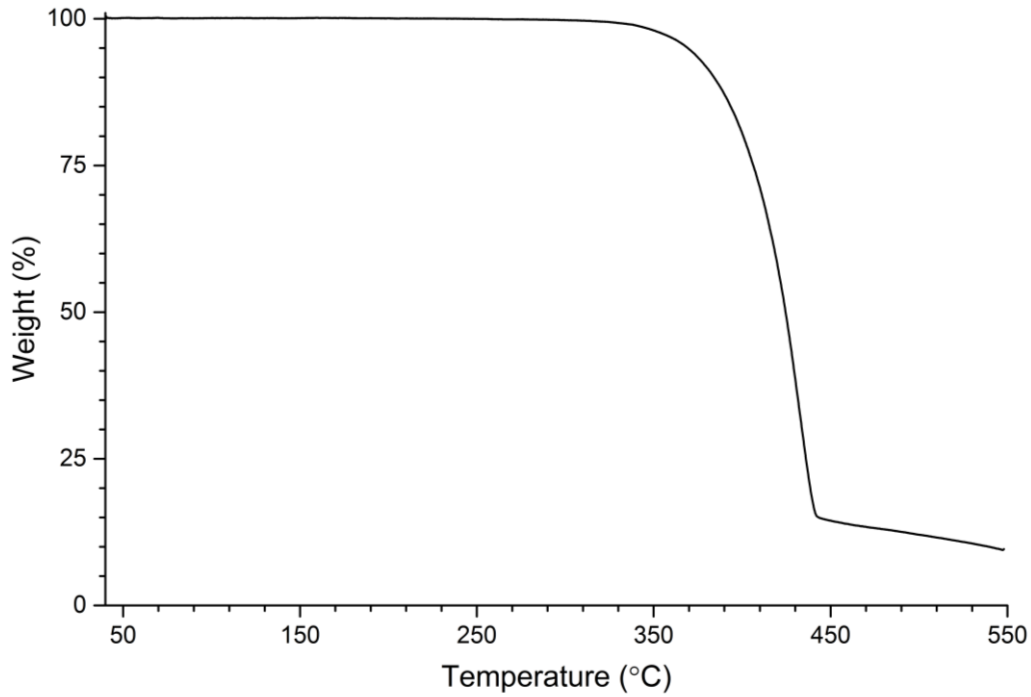

Figure 5.8 - TGA plot of compound **5.2**, heating at a rate of 10 °C min^{-1} under argon

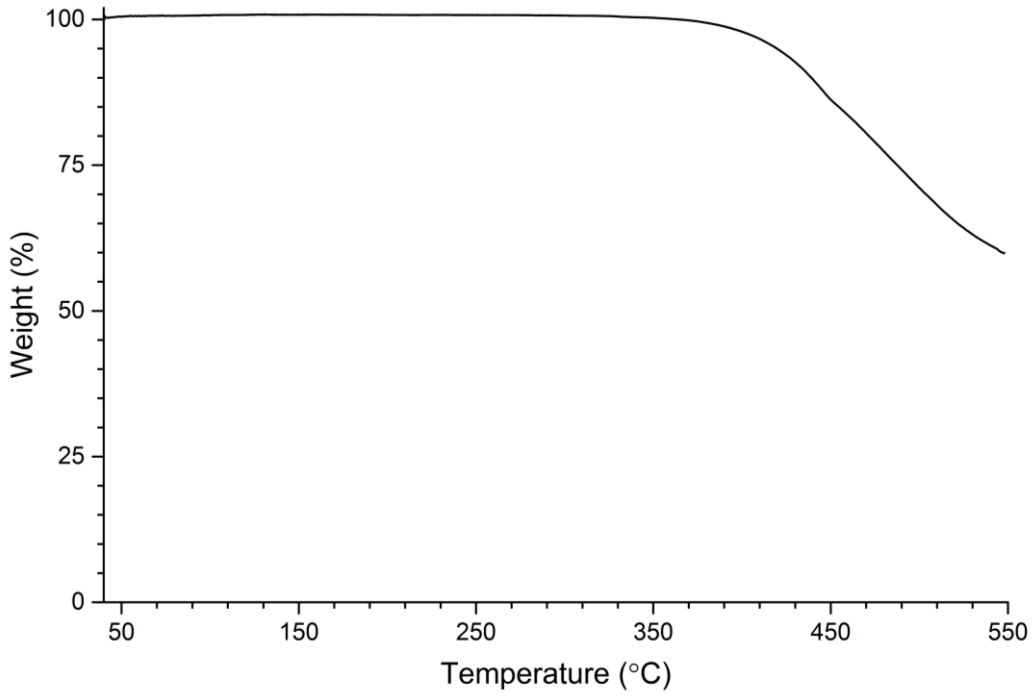

Figure 5.9 - TGA plot of compound **5.3**, heating at a rate of 10 °C min^{-1} under argon

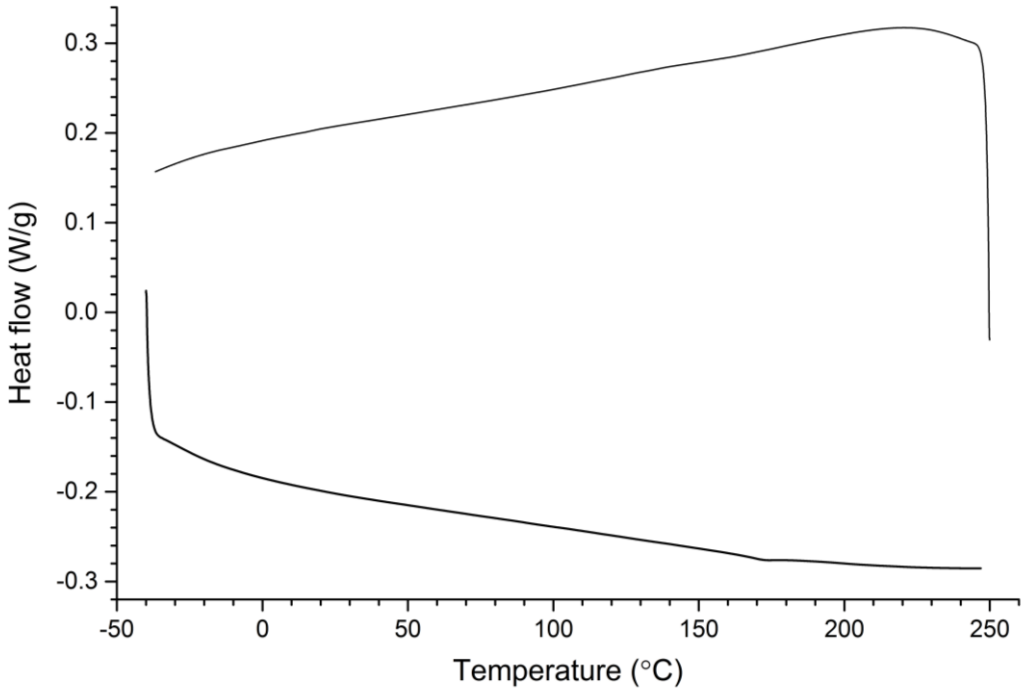

Figure 5.10 - DSC plot of compound **5.2** during a heat-cool-heat cycle, showing cooling from 250 °C to −40 °C, then heating from −40 °C to 250 °C at a rate of 10 °C min^{-1} under nitrogen

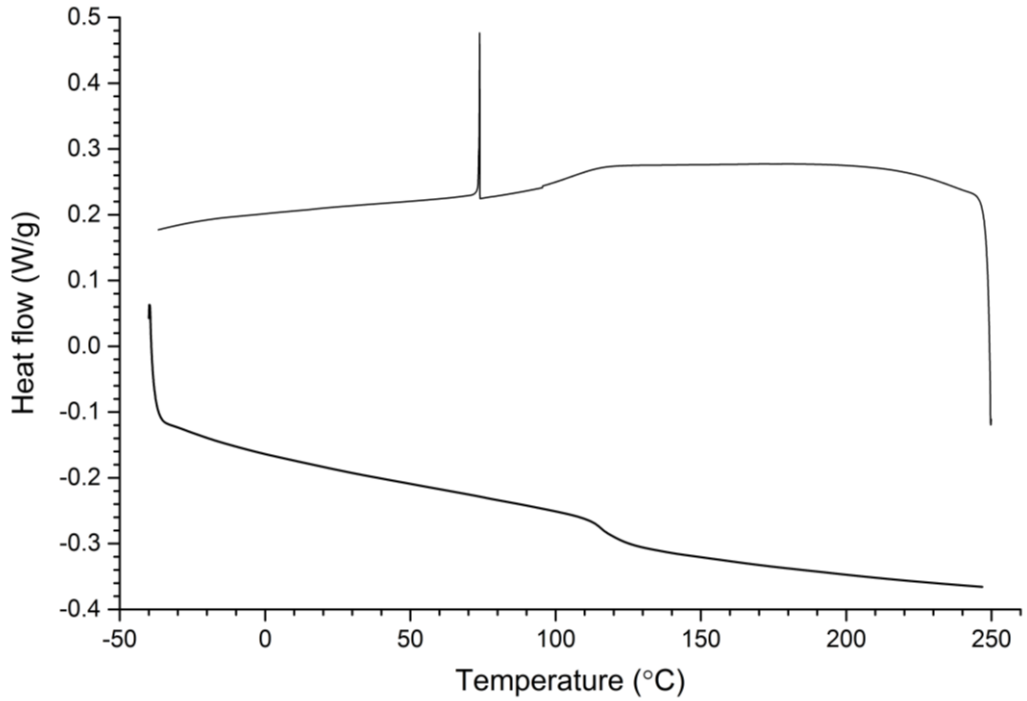

Figure 5.11 - DSC plot of compound **5.3** during a heat-cool-heat cycle, showing cooling from 250 °C to −40 °C, then heating from −40 °C to 250 °C at a rate of 10 °C min^{-1} under nitrogen

5.4 Conclusions and future work

Through a brief trial of conditions the yield of the trialdehyde truxene **5.1** was significantly improved to 80%. This common intermediate allowed the successful synthesis of compounds **5.2** and **5.3** to be completed.

Thermogravimetric analysis showed that 5% mass loss occurred at 369 °C and 419 °C for **5.2** and **5.3** respectively, therefore they are very unlikely to decompose during device processing. Compound **5.2** showed excellent thermal stability, with no events up to 250 °C. Although compound **5.3** has a glass transition at around 100 °C this would not prevent its inclusion in organic electronic devices, but may limit applicable annealing temperatures.

The smaller tricyano derivative **5.2** exhibited a pseudo-reversible oxidation and pseudo-reversible reduction and an electrochemical HOMO-LUMO gap of 3.8 eV. The oxidation of compound **5.3** was also pseudo-reversible and occurred at around the same potential, but the irreversible reduction occurred at a much higher potential. This is due to the greater electron withdrawing nature of the substituents, meaning that the electrochemical HOMO-LUMO gap was reduced to 2.9 eV.

The vibronic structure of compound **5.2** was more defined, and had an optical HOMO-LUMO gap of 3.3 eV, while that of **5.3** was 2.8 eV. Most notably compound **5.3** exhibited positive solvatochromism, with an increase in Stokes shift corresponding to the increasing solvent polarity. This effect was not observed for compound **5.2**.

Compound **5.4** was obtained through a one pot reaction, however conversion to the more strongly electron withdrawing **5.5** was not possible. This is most likely due to the low polarisation of the alkyne bond; therefore inclusion of a CF_3 group was proposed. The initial molecule **5.6** could not be formed by the attempted one pot synthesis, however if this molecule could be formed then the final reaction with TCNE is likely to be successful, producing the very electron deficient truxene **5.7**.

It is possible to synthesise the truxene TMS-acetylene (**5.8**) from **4.1** and ethynyltrimethylsilane using the Sonogashira conditions described in Chapter 4. This could then be converted to the CF_3 acetylene **5.6** using the reaction shown below in Scheme 5.3.[150,151]

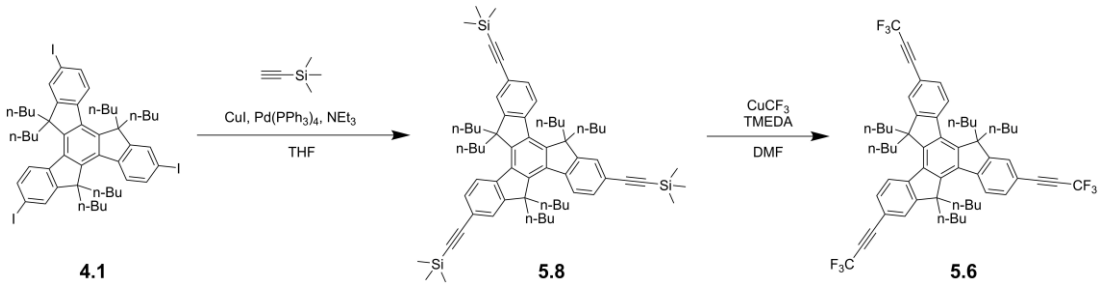

Scheme 5.3 - Potential route to compound **5.6**

Several groups have reported a cascade cycloaddition reaction using TCNE followed by tetrathiafulvalene (TTF).[147,152,153] Due to the different electronics, a cycloaddition with TTF may be possible with compounds **5.4** and **5.6**, producing the two new materials shown in Figure 5.12. The electronic nature of TTF suggests that the molecule on the left would be suited as a donor material, while the inclusion of the electronegative CF_3 furnishes a donor-acceptor material. The structures lend themselves to non-covalent interactions so should produce ordered films, meaning they could also be used as a templating layer.

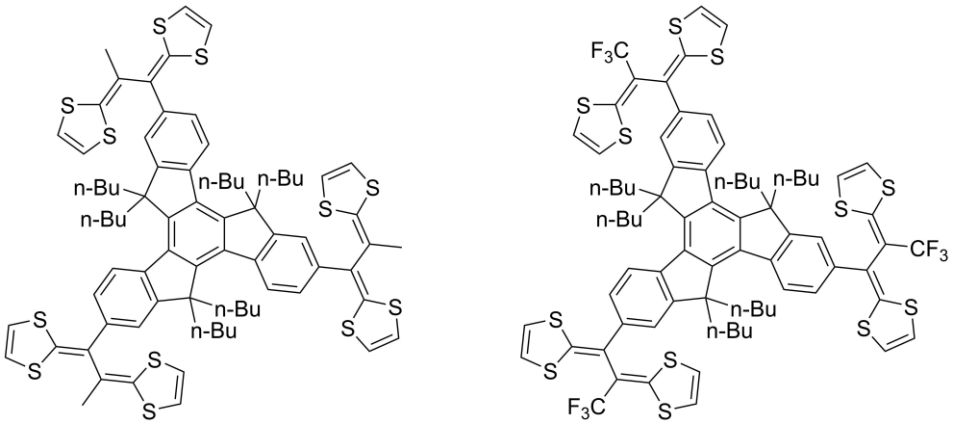

Figure 5.12 - Potential new materials from TTF cycloadditions

Copper catalysed click chemistry would be possible to further functionalise **5.4**, **5.6** or even **5.8** leading to several new materials, Scheme 5.4. These reactions could also be trialled on unsaturated compound **4.4**; although there is considerably more steric bulk around the alkyne bond, there is evidence which suggests that these reactions would successfully furnish the triazoles.[145]

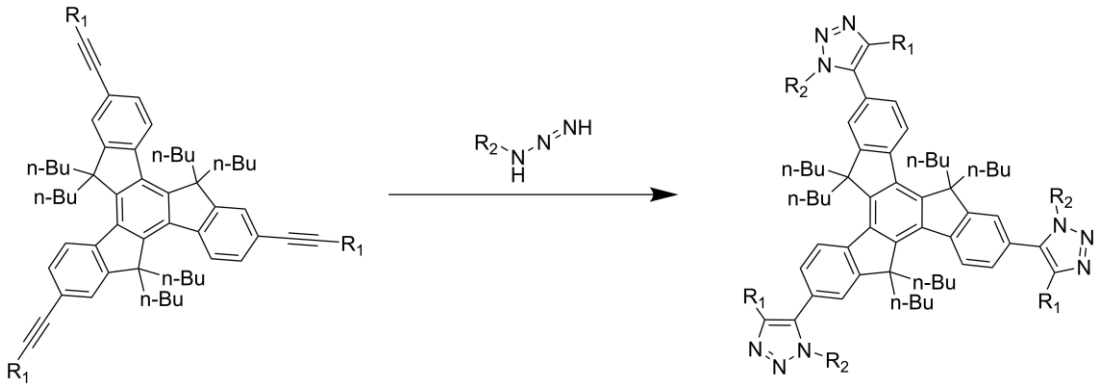

Scheme 5.4 - Potential click chemistry

Finally, the reaction of compound **5.2** with sodium azide would form the tetrazole as shown in Scheme 5.5.[154] These tri- and tetrazoles will not have the same electrochemical instability which is associated with the carboxylic acid functionality. However, they should exhibit hydrogen bonding and strong π-π interactions, making them strong candidates for application as a templating layer.

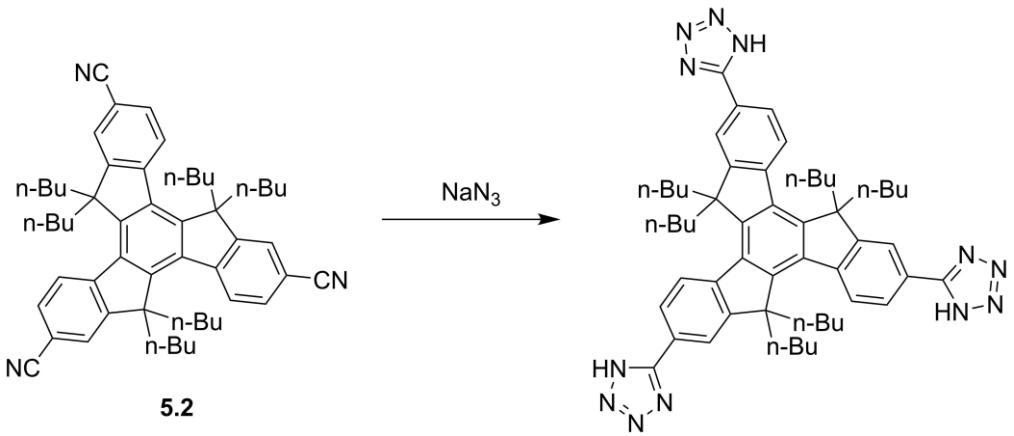

Scheme 5.5 - Potential formation of tetrazole

6 SUMMARY AND FUTURE WORK

6.1 Summary of work

Tricarboxylic acids were initially chosen to begin exploring truxene based interlayer materials; the hydrogen bonding ability of this functionality should produce an ordered layer. Four tricarboxylic acids were synthesised to examine the effect of alkyl chain length on the material properties. The planned synthetic route was *via* an ester, however the yields were low. By refining the methodology the proportion of undesired mono- and dicarboxylic acids was reduced, meaning the final materials could be obtained in isolated yields of 31–80%.

Using the slow vapour diffusion method to grow crystals, x-ray structures were obtained for two of the four tricarboxylic acids (**2.12** and **2.13**). Due to the strong hydrogen bonding ability of the carboxylic acids, molecules of THF were trapped in the lattice. While these could mostly be removed by precipitation this introduced water molecules instead. A further eight structures were acquired for the intermediate compounds (**2.1**–**2.8**). Changes in the packing motifs were observed due to the alteration of the length of alkyl chains. In general the longer alkyl chains resulted in less dense packing and an increasing twist angle in the truxene core.

These molecules showed little change in the optical and electrochemical properties on altering the length of the alkyl chains. The optical and electrochemical HOMO-LUMO gaps were around 3.8 eV, showing minor variation with alkyl chain length. In the solution state the peak position and vibronic structure of the absorption and emission spectra did not significantly change; in the solid state there was a concentration dependant variation in the vibronic structure.

Cyclic voltammetry showed a pseudo-reversible oxidation and irreversible reduction for compounds **2.10**–**2.13**. Square wave voltammetry experiments confirmed this finding, and also indicated a high overpotential for proton reduction when using a glassy carbon working electrode. Due to the electrochemical instability of the tricarboxylic acids, carboxylate salts of compound **2.13** were formed. When spin-coated from methanol these materials showed very poor wettability leading to an

uneven, cracked film. Despite this rough morphology, when the carboxylate salt **3.4** was applied in an OLED it functioned as an interlayer allowing light to be produced from the device.

The tricarboxylic acids displayed excellent thermal stability, with a slight dip observed for compounds **2.11** and **2.12**. The intermediate compounds **2.1**–**2.8** also exhibited a dip in thermal stability for the propyl derivatives, **2.3** and **2.7**. As it occurs across all three series, this dip is not dependent on the chemical structure but instead the molecular weight, indicating that the source of the decomposition is chain scission. Despite this thermal stability it was found that compound **2.12** was unstable to vacuum deposition. Though some material could be evaporated, the thickness seemed to be limited. ^{1}H NMR of the residual material confirmed that some decomposition had occurred.

Vacuum deposition was successful with the lighter intermediate **2.3**. When SubPc (**3.1**) is deposited on top of a layer of this compound there is a clear change in morphology. The thickness of the truxene layer strongly influences the growth behaviour of the subsequently deposited material.

Interlayers of **2.3** with varying thicknesses were included in a standard solar cell stack. It was found that the optimal interlayer thickness was 3.8 nm; above this the fill factor and PCE began to decline. Compared to reference devices with no interlayer, the J_{SC} and consequently the PCE increased from 2.54% to 3.09%, an improvement of 21%. The main reason for this performance enhancement is the increased absorption of the SubPc layer, most likely due to morphology changes caused by the inclusion of the interlayer. Additionally, this interlayer acts as an electron blocking layer, reducing exciton quenching which also contributes to the augmented efficiency.

Further electrochemistry experiments showed that the ester **2.9** exhibits a reversible reduction, therefore an extended truxene derivative with six carboxylic ester functionalities was synthesised. A small screen was carried out to find improved reaction conditions for the Sonogashira coupling of the arm, with isolated yields ranging from 46% to 88%. Applying the best conditions to the coupling between the arm and the iodinated core allowed the final compound (**4.4**) to be prepared in 87% yield on a multigram scale.

Cyclic voltammetry of this compound showed irreversible oxidation and reduction, with an electrochemical HOMO-LUMO gap of 3.6 eV. The absorption profile shows two main peaks, while the emission profile contains one peak with a shoulder; the optical HOMO-LUMO gap was found to be 3.2 eV. Due to the extended conjugation present in **4.4** this is lower than the tricarboxylic acids, and results in a highly emissive material. Though not quantified in the solid state, the relative PLQY was 0.94 in solution.

A crystal structure was also obtained for this molecule, the core was found to be planar while two of the arms were twisted. The hexaester showed some very interesting packing with strong π-π stacking.

Through a brief trial of conditions, the yield of the trialdehyde truxene **5.1** was significantly improved to 80%. This common intermediate allowed the successful synthesis of compounds **5.2** and **5.3** to be completed. Both compounds showed excellent thermal stability with a glass transition at around 100 °C observed for compound **5.3**.

The smaller tricyano derivative **5.2** exhibited a pseudo-reversible oxidation and pseudo-reversible reduction and an electrochemical HOMO-LUMO gap of 3.8 eV. The oxidation of compound **5.3** was also pseudo-reversible and occurred at around the same potential, but the irreversible reduction occurred at a much higher potential.

This is a result of the greater electron withdrawing nature of the substituents, and reduced the electrochemical HOMO-LUMO gap to 2.9 eV.

The vibronic structure of compound **5.2** was more defined, and had an optical HOMO-LUMO gap of 3.3 eV, while that of **5.3** was 2.8 eV. Most notably compound **5.3** exhibited positive solvatochromism, with an increase in Stokes shift corresponding to the increasing solvent polarity. This effect was not observed for compound **5.2**.

6.2 Future work

Further investigation into the ability of compound **2.3** to template other active layer materials is required. Some commonly reported materials include anthracene, P3HT and PTB7 so these would be a logical starting point, but there are many which could be explored. Additionally, the templating ability of other intermediate compounds discussed in this thesis should be evaluated. Furthermore, it would be worth trialling solution processed films of the tricarboxylic acids as interlayers in devices. Due to the strength of the hydrogen bonding interactions, the morphology control and templating effect should be more pronounced. Additionally, compounds **4.4**, **5.2**, and **5.3** should be applied in devices as both solution and vacuum deposited layers, although the molecular weight of the former may make it unsuitable for vacuum deposition.

The carboxylate salts have already been shown to function as a charge transport layer, but improving the morphology to produce an even film would allow full characterisation of a device. Spin-coating from a longer chained alcohol such as butanol will impact the film drying; this could prevent the cracking which was observed with methanol solutions of **3.4** and **3.5**. Other higher boiling point solvents like DMF (*N*,*N*-dimethylformamide) or DMSO will also slow the drying time of the films.

By forming salts of the tricarboxylic acids (**2.10**–**2.13**) with different cations such as calcium or anilinium, the morphology of spin-coated films could be greatly improved without significantly altering the transport properties of the interlayer. Furthermore, the ester **4.4** could be easily converted to a carboxylate salt, which could be incorporated into a solution processed device. The morphology may be improved due to the increased aromatic character of this material. Additionally, combining the hexaanion with multivalent cations such as calcium, copper or iron could be used to create a complex intermolecular network within the thin film.

Due to the highly emissive nature of **4.4** it should be trialled for lasing applications. If this proved successful, then different substituents on the phenyl groups could be explored as way of tuning the wavelength of the laser. Furthermore, the inclusion of more electronegative substituents would produce a more reversible electrochemical profile which is desirable for electrically pumped lasers.

Although compound **5.4** was obtained, attempts to form molecule **5.6** using the same method were unsuccessful. It is possible to synthesise the truxene TMS-acetylene (**5.8**) from **4.1** and ethynyltrimethylsilane using the Sonogashira conditions described in Chapter 4. This could then be converted to the CF_3 acetylene **5.6** using the reaction shown below in Scheme 6.1. Subsequent reaction with TCNE would produce the very electron deficient truxene **5.7**, which should demonstrate improved electrochemical properties.

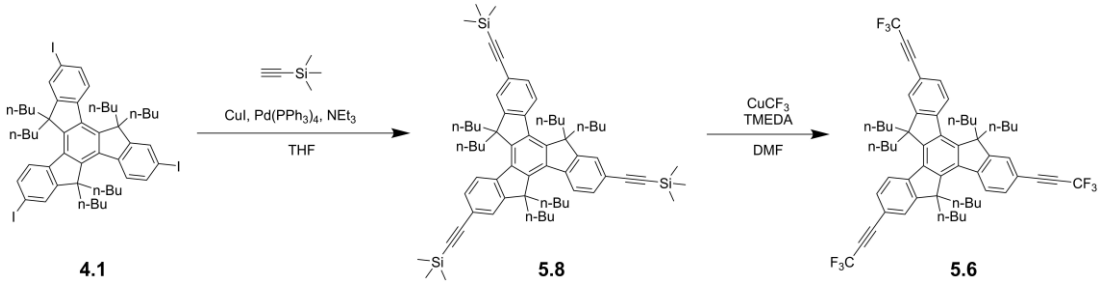

Scheme 6.1 - Potential route to compound **5.6**

Future work should also examine other functional groups which mitigate the instability associated with the acidic protons. For example, intermolecular interactions will be possible with the inclusion of amides, nitrile containing groups, sulfonamides, thioamides and various heterocycles (such as oxadiazoles, thiadiazoles, thiazolidine dione and pyrrolidine dione). Compounds **2.9** and **4.4** could be easily converted to an amide, as could the tricarboxylic acids though this may be more difficult. These materials would produce a complex hydrogen bonded network.

A cycloaddition with TTF may be possible with compounds **5.4** and **5.6**, producing the two new materials shown in Figure 6.1. The electronic nature of TTF suggests that the molecule on the left would be suited as a donor material, while the inclusion of the electronegative CF_3 furnishes a donor-acceptor material. The structures lend themselves to non-covalent interactions so should produce ordered films, meaning they could also be used as a templating layer.

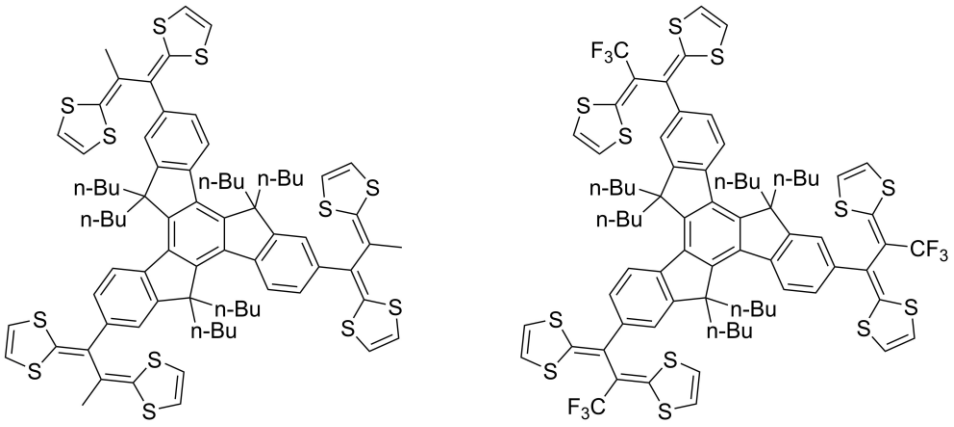

Figure 6.1 - Potential new materials from TTF cycloadditions

Copper catalysed click chemistry would be possible to further functionalise **5.4**, **5.6** or even **5.8** leading to several new materials, Scheme 6.2. These reactions could also be trialled on unsaturated compound **4.4**; although there is considerably more steric bulk around the alkyne bond, there is evidence which suggests that these reactions would successfully furnish the triazoles.[146]

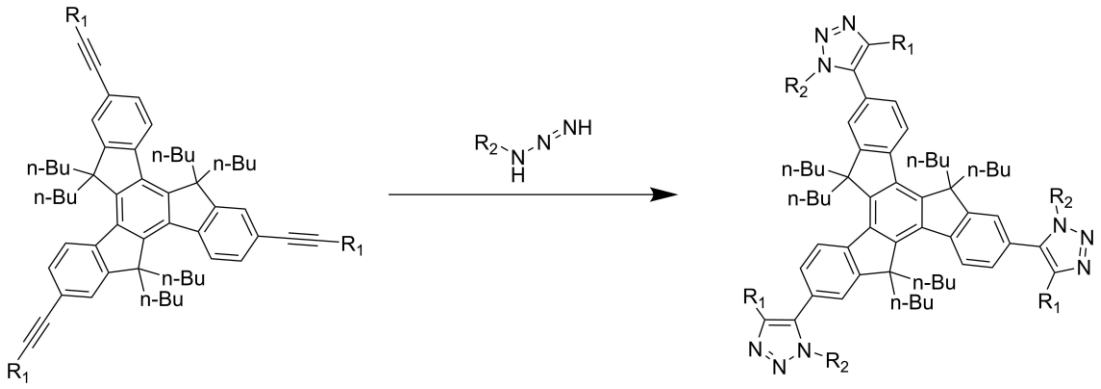

Scheme 6.2 - Potential click chemistry

The reaction of compound **5.2** with sodium azide would form the tetrazole as shown in Scheme 6.3. These tri- and tetrazoles will not have the same electrochemical instability which is associated with the carboxylic acid functionality. However, they should exhibit hydrogen bonding and strong π-π interactions, making them strong candidates for application as a templating layer.

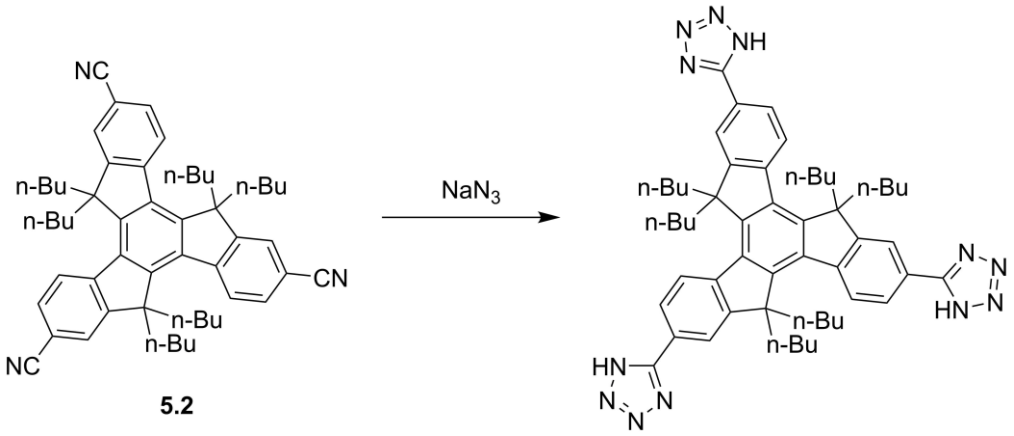

Scheme 6.3 - Potential formation of tetrazole

Once a suitable candidate with the desired optical and electrochemical profile has been identified, it would be prudent to rescreen the alkyl chain length. This will allow the desired processability and thermal properties of the material to be obtained, and by optimising these conditions the device performance can be improved. Many variations are possible beyond the simple alkyl chains, for example branched chains could be investigated. These chains will fill the space differently, impacting the molecular packing.

Alternatively, it may be advantageous to have different chains on each face of the molecule. By incorporating different functionalities on each face, multiple interactions would be available to these materials, giving rise to the possibility of face selective binding. This would provide asymmetric functionalization of the surface, while maintaining intermolecular interactions within the layer through the 2, 7 and 12 positions.

7 EXPERIMENTAL

7.1 General

All reagents were obtained from commercial suppliers and used without further purification unless stated. *n*-Butyllithium was titrated against diphenyl acetic acid before use, while lithium diisopropylamide was titrated against menthol using fluorene as an indicator. Solvents were purified using a Pure-Solv 400 solvent purification system (Innovative Technology, Inc.).

All glassware was oven dried to remove traces of moisture before use.

^{1}H NMR were run on either a Bruker DPX 400 or AV 500 spectrometer at 400 MHz or 500 MHz respectively, while ^{13}C NMR were run on either a Bruker DPX 400 or AV 500 at 100 MHz or 125 MHz respectively. Chemical shifts are in parts per million referenced to the solvent peak.[155] Spectra were generated using Topspin 3.5.

Commercial thin layer chromatography (TLC) plates (Merck Silica gel 60 F254) were used, column chromatography was carried out on silica gel Geduran® Si 60 (40–63 μm).

Microwave reactions were run in a Biotage Initiator+. Evaporations were carried out in a customised Edwards E306A Coating System, and an Esoteric Chemicals AB sublimer was used for thermal gradient sublimations.

MALDI-TOF spectra were recorded on a Shimadzu Axima-CFR spectrometer (mass range 1–150000 Da).

Elemental analyses were obtained on a Perkin Elmer 2400 elemental analyser.

Absorption spectra were recorded on a Shimadzu UV 2700 instrument, whilst emission spectra were recorded using a Perkin Elmer LS45 Luminescence Spectrometer.

Melting points were determined using a Stuart Scientific SMP1 and are uncorrected. TGA was carried out on a Perkin Elmer Thermogravimetric Analyzer TGA 7 under

argon, using a heating rate of 10 °C min^{-1}. DSC was carried out using a TA instruments DSC QC1000 Differential Scanning Calorimeter under nitrogen.

Cyclic voltammetry (CV) measurements were performed on a CH Instruments 660A electrochemical workstation with *iR* (internal resistance) compensation and a scan rate of 100 mV s^{-1}. The electrodes were glassy carbon, platinum wire and silver wire as the working, counter and reference electrodes respectively. All solutions contained *n*-Bu_4NPF_6 (0.1 M) as the supporting electrolyte and were degassed with argon prior to reduction measurements. All measurements are referenced against the $E_{1/2}$ of the Fc/Fc^+ redox couple as an external standard.

AFM measurements in Figures 3.7, 3.10 and 3.16 were run on a Dimension 3100 in tapping mode. Post-analysis was performed on WSxM 5.0 software.[156]

The device characterisation and AFM imaging in Section 3.2 were carried out at the University of Oxford.

The electrochemistry and OLED fabrication in Chapter 3 was performed by CDT.

Crystal structures were run at the UK National Crystallography Service in Southampton, at 100 K and a wavelength of 0.71075 Å. Images were created using Diamond 3.1.

Graphs were generated with OrginPro 2015, chemical structures were produced using ChemDraw Professional 16.0.

Tetrakis(triphenylphosphine)palladium(0)

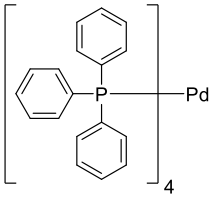

Palladium(II) chloride (1.0 g, 5.6 mmol) and triphenylphosphine (7.4 g, 28 mmol) were suspended in DMSO (80 mL) and heated to 160 °C until complete dissolution occurred. Hydrazine monohydrate (1.1 mL, 22 mmol) was rapidly added at this temperature, causing a vigorous reaction to occur. The solution was allowed to cool to room temperature and then stirred for 15 minutes, the precipitate was collected by filtration in inert conditions. The solid was washed with methanol (2 × 40 mL) then diethyl ether (2 × 40 mL), before being dried *in vacuo* for 30 minutes. The dry yellow crystals were transferred to a dry flask and stored in the freezer, 6.4 g (97% yield).

7.2 Chapter 2 synthesis

10,15-Dihydro-5*H*-diindeno[1,2-*a*:1',2'-*c*]fluorene (truxene, 1.25)

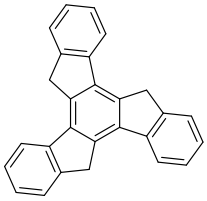

1-Indanone (25 g, 190 mmol) was dissolved in glacial acetic acid (120 mL) and concentrated hydrochloric acid (60 mL) was added. The resultant mixture was heated at reflux overnight. The reaction mixture was poured onto ice and the precipitate washed with water (1.0 L until pH 7), acetone (500 mL) and then CH_2Cl_2 (250 mL). The resulting light yellow solid was dried *in vacuo* to yield 18 g of the title compound (82% yield) which was used crude in the following steps.

^{1}H NMR (400 MHz, $CDCl_3$) δ_H 7.95 (3H, d, ^3J = 7.6 Hz), 7.70 (3H, d, ^3J = 7.2 Hz), 7.50 (3H, apparent t), 7.40 (3H, dt, ^3J = 7.4 Hz, ^4J = 1.2 Hz), 4.27 (6H, s). Consistent with previously published data.[157]

General procedure 1: Alkylation of truxene core

n-Butyllithium (3.8 molar equivalents) was added dropwise to a stirred suspension of 10,15-dihydro-5*H*-diindeno[1,2-*a*:1',2'-*c*]fluorene (**1.25**) in THF at 0 °C. After stirring for 30 minutes the alkyl halide (3.8 molar equivalents) was added dropwise at 0 °C. The reaction was allowed to warm to room temperature and stirred for 4 hours, before being cooled to 0 °C. *n*-Butyllithium (3.8 molar equivalents) was added dropwise, and the reaction mixture stirred for 30 minutes at 0 °C. The alkyl halide (3.8 molar equivalents) was then added dropwise at 0 °C, and the reaction allowed to warm to room temperature before being stirred overnight. The reaction was monitored by TLC and further additions made as required.

5,5,10,10,15,15-Hexamethyl-10,15-dihydro-5*H*-diindeno[1,2-*a*:1',2'-*c*]fluorene (2.1)

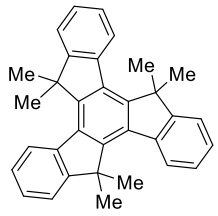

The title compound was prepared from 10,15-dihydro-5*H*-diindeno[1,2-*a*:1',2'-*c*]fluorene (**1.25**, 7.2 g, 21 mmol), *n*-butyllithium (2.4 M in hexanes, 2 × 33 mL, 2 × 79 mmol), iodomethane (2 × 5.0 mL, 2 × 81 mmol) and THF (100 mL) using general procedure 1. Starting material was still present by TLC so the reaction was cooled to 0 °C and an additional portion of *n*-butyllithium (2.4 M in hexanes, 33 mL, 79 mmol) added dropwise. After stirring for 30 minutes, iodomethane (5.0 mL, 81 mmol) was added dropwise at 0 °C. The reaction was allowed to slowly warm to room temperature then stirred for 3 days. The reaction was quenched by addition of saturated aqueous ammonium chloride solution and the aqueous phase was extracted three times with CH_2Cl_2. The organic phases were combined, dried with $MgSO_4$, filtered and concentrated *in vacuo*. The crude residue was purified by three recrystallisations from a 1:1 mixture of MeCN:CH_2Cl_2, then recrystallisation from a 2:1 mixture of methanol:CH_2Cl_2 to yield 0.71 g of the title compound (7.9% yield).

^{1}H NMR (400 MHz, $CDCl_3$) δ_H 8.32–8.30 (3H, m), 7.56–7.54 (3H, m), 7.45–7.39 (6H, m), 1.89 (18H, s); anal. calcd for $C_{33}H_{30}$: C, 92.91; H, 7.09%; found: C, 92.65; H, 7.29%; m.p. 322–324 °C. Consistent with previously published data.[158]

5,5,10,10,15,15-Hexaethyl-10,15-dihydro-5*H*-diindeno[1,2-*a*:1',2'-*c*]fluorene (2.2)

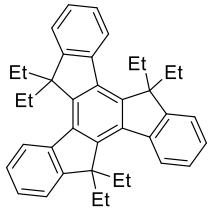

The title compound was prepared from 10,15-dihydro-5*H*-diindeno[1,2-*a*:1',2'-*c*]fluorene (**1.25**, 6.5 g, 19 mmol), *n*-butyllithium (2.4 M in hexanes, 2 × 29 mL, 2 × 71 mmol), bromoethane (2 × 5.4 mL, 2 × 72 mmol) and THF (100 mL) using general procedure 1. Starting material was still present by TLC so the reaction was cooled to 0 °C and *n*-butyllithium (2.5 M in hexanes, 14 mL, 36 mmol) added dropwise. After stirring for 30 minutes bromoethane (2.7 mL, 36 mmol) was added dropwise at 0 °C. The reaction was stirred for 3 hours then a further portion of *n*-butyllithium (2.5 M in hexanes, 2.8 mL, 7.1 mmol) added dropwise at 0 °C. After stirring for 30 minutes bromoethane (0.54 mL, 7.2 mmol) was added dropwise at 0 °C. The reaction was allowed to slowly warm to room temperature then stirred overnight. The reaction was cooled to 0 °C then a further portion of *n*-butyllithium (2.5 M in hexanes, 2.8 mL, 7.1 mmol) was added dropwise. After stirring for 30 minutes bromoethane (0.54 mL, 7.2 mmol) was added dropwise at 0 °C. The reaction was allowed to slowly warm to room temperature then stirred for 3 days. The reaction was quenched by addition of saturated aqueous ammonium chloride solution and the aqueous phase was extracted three times with petroleum ether. The organic phases were combined, dried with $MgSO_4$, filtered and concentrated *in vacuo*. The crude residue was purified by column chromatography (eluting with petroleum ether) then recrystallised from 2:1 mixture of methanol:CH_2Cl_2 to yield 7.6 g of the title compound (79% yield).

^{1}H NMR (400 MHz, $CDCl_3$) δ_H 8.37–8.35 (3H, m), 7.47–7.45 (3H, m), 7.40–7.37 (6H, m), 3.07–2.98 (6H, m), 2.20–2.11 (6H, m), 0.21 (18H, t, ^3J = 7.3 Hz); anal.

calcd for $C_{39}H_{42}$: C, 91.71; H, 8.29%; found: C, 91.96; H, 8.43%; m.p. 220–222 °C. Consistent with previously published data.[159]

5,5,10,10,15,15-Hexapropyl-10,15-dihydro-5*H*-diindeno[1,2-*a*:1',2'-*c*]fluorene (2.3)

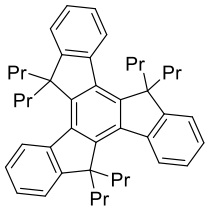

The title compound was prepared from 10,15-dihydro-5*H*-diindeno[1,2-*a*:1',2'-*c*]fluorene (**1.25**, 5.8 g, 17 mmol), *n*-butyllithium (2.5 M in hexanes, 2 × 26 mL, 2 × 64 mmol), 1-bromopropane (2 × 5.9 mL, 2 × 65 mmol) and THF (100 mL) using general procedure 1. Starting material was still present by TLC so the reaction was cooled to 0 °C and *n*-butyllithium (2.5 M in hexanes, 13 mL, 32 mmol) added dropwise. After stirring for 30 minutes 1-bromopropane (3.0 mL, 33 mmol) was added dropwise at 0 °C. The reaction was allowed to slowly warm to room temperature then stirred overnight. The reaction was cooled to 0 °C and a further portion of *n*-butyllithium (2.5 M in hexanes, 2.6 mL, 6.4 mmol) added dropwise. After stirring for 30 minutes 1-bromopropane (0.59 mL, 6.5 mmol) was added dropwise at 0 °C. The reaction was allowed to slowly warm to room temperature then stirred for 3 hours. Starting material was still present by TLC so the reaction was cooled to 0 °C and *n*-butyllithium (2.5 M in hexanes, 5.1 mL, 13 mmol) added dropwise. After stirring for 30 minutes 1-bromopropane (1.2 mL, 13 mmol) was added dropwise at 0 °C. The reaction was allowed to slowly warm to room temperature then stirred overnight. The reaction was quenched by addition of saturated aqueous ammonium chloride solution and the aqueous phase was extracted three times with petroleum ether. The organic phases were combined, dried with $MgSO_4$, filtered and concentrated *in vacuo*. The crude residue was pre-absorbed onto

silica and purified by column chromatography (eluting with petroleum ether) then recrystallised twice from MeCN to yield 7.9 g of the title compound (79% yield).

^{1}H NMR (400 MHz, $CDCl_3$) δ_H 8.37–8.35 (3H, m), 7.49–7.47 (3H, m), 7.42–7.36 (6H, m), 2.93–2.87 (6H, m), 2.10–2.05 (6H, m), 0.57–0.50 (30H, m); anal. calcd for $C_{45}H_{54}$: C, 90.85; H, 9.15%; found: C, 90.70; H, 9.32%; m.p. 157–159 °C.

5,5,10,10,15,15-Hexabutyl-10,15-dihydro-5*H*-diindeno[1,2-*a*:1',2'-*c*]fluorene (2.4)

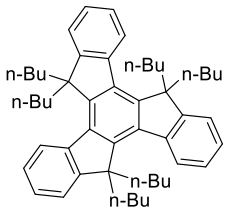

The title compound was prepared from 10,15-dihydro-5*H*-diindeno[1,2-*a*:1',2'-*c*]fluorene (**1.25**, 10 g, 29 mmol), *n*-butyllithium (2.2 M in hexanes, 2 × 50 mL, 2 × 110 mmol), 1-bromobutane (2 × 12 mL, 2 × 110 mmol) and THF (180 mL) using general procedure 1. The reaction was quenched by addition of saturated aqueous ammonium chloride solution and the aqueous phase was extracted three times with CH_2Cl_2. The organic phases were combined, dried with $MgSO_4$, filtered and concentrated *in vacuo*. The crude residue was recrystallised from MeCN to yield 17 g of the title compound (85% yield).

^{1}H NMR (500 MHz, $CDCl_3$) δ_H 8.38 (3H, d, ^3J = 7.5 Hz), 7.46 (3H, dd, ^3J = 7.5 Hz, ^4J = 1.5 Hz), 7.41–7.35 (6H, m), 3.01–2.95 (6H, m), 2.13–2.07 (6H, m), 0.95–0.83 (12H, m), 0.57–0.47 (12H, m), 0.44 (18H, t, ^3J = 7.5 Hz); anal. calcd for $C_{51}H_{66}$: C, 90.20; H, 9.80%; found: C, 89.91; H, 9.63%; m.p. 236–238 °C. Consistent with previously published data.[160]

General Procedure 2: Bromination

An excess of bromine (3.0–6.0 molar equivalents) was added dropwise to a stirred solution of the corresponding hexaalkylated truxene derivative in CH_2Cl_2. The resultant mixture was stirred overnight at room temperature, and free from light. The reaction was quenched with an aqueous solution of sodium sulfite and the aqueous phase extracted three times with CH_2Cl_2. The organic phases were combined and washed with a saturated aqueous sodium hydrogen carbonate solution, dried with $MgSO_4$, filtered and concentrated *in vacuo*.

2,7,12-Tribromo-5,5,10,10,15,15-hexamethyl-10,15-dihydro-5*H*-diindeno[1,2-*a*:1',2'-*c*]fluorene (2.5)

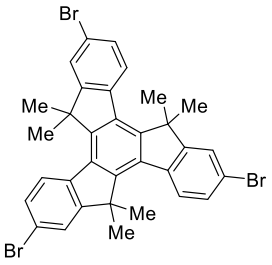

The title compound was prepared from 5,5,10,10,15,15-hexamethyl-10,15-dihydro-5*H*-diindeno[1,2-*a*:1',2'-*c*]fluorene (**2.1**, 0.55 g, 1.3 mmol), bromine (0.40 mL, 7.8 mmol) and CH_2Cl_2 (10 mL) using general procedure 2. The crude material was recrystallised from a 1:1 CH_2Cl_2:MeCN mixture to yield 0.69 g of the title compound (81% yield).

^{1}H NMR (400 MHz, $CDCl_3$) δ_H 8.10 (3H, d, ^3J = 8.4 Hz), 7.7 (3H, d, ^4J = 2.0 Hz), 7.54 (3H, dd, ^3J = 8.4 Hz, ^4J = 2.0 Hz), 1.83 (18H, s); anal. calcd for $C_{33}H_{27}Br_3$: C, 59.76; H, 4.10%; found: C, 59.42; H, 4.17%; m.p. > 350 °C. Consistent with previously published data.[158]

2,7,12-Tribromo-5,5,10,10,15,15-hexaethyl-10,15-dihydro-5*H*-diindeno[1,2-*a*:1',2'-*c*]fluorene (2.6)

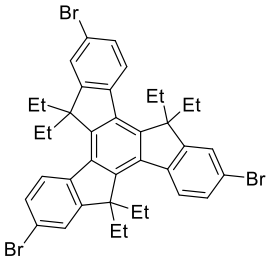

The title compound was prepared from 5,5,10,10,15,15-hexaethyl-10,15-dihydro-5*H*-diindeno[1,2-*a*:1',2'-*c*]fluorene (**2.2**, 3.0 g, 5.9 mmol), bromine (1.4 mL, 27 mmol) and CH_2Cl_2 (60 mL) using general procedure 2. The crude material was recrystallised from a 1:2 CH_2Cl_2:hexane mixture and then from a 1:1 CH_2Cl_2:MeCN mixture to yield 3.5 g of the title compound (80% yield).

^{1}H NMR (400 MHz, $CDCl_3$) δ_H 8.16 (3H, d, ^3J = 8.5 Hz), 7.57 (3H, d, ^4J = 1.9 Hz), 7.52 (3H, dd, ^3J = 8.5 Hz, ^4J = 1.8 Hz), 2.95–2.86 (6H, m), 2.15–2.06 (6H, m), 0.21 (18H, t, ^3J = 7.3 Hz); anal. calcd for $C_{39}H_{39}Br_3$: C, 62.67; H, 5.26%; found: C, 62.51; H, 5.11%; m.p. 345–348 °C. Consistent with previously published data.[159]

2,7,12-Tribromo-5,5,10,10,15,15-hexapropyl-10,15-dihydro-5*H*-diindeno[1,2-*a*:1',2'-*c*]fluorene (2.7)

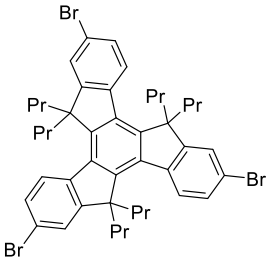

The title compound was prepared from 5,5,10,10,15,15-hexapropyl-10,15-dihydro-5*H*-diindeno[1,2-*a*:1',2'-*c*]fluorene (**2.3**, 2.0 g, 3.4 mmol), bromine (0.60 mL, 12 mmol) and CH_2Cl_2 (40 mL) using general procedure 2. The crude material was recrystallised from a 1:1 CH_2Cl_2:MeCN mixture to yield 2.7 g of the title compound (96% yield).

^{1}H NMR (400 MHz, $CDCl_3$) δ_H 8.16 (3H, d, ^3J = 8.8 Hz), 7.58 (3H, d, ^4J = 1.6 Hz), 7.53 (3H, dd, ^3J = 8.6, ^4J = 1.8 Hz), 2.81–2.75 (6H, m), 2.07–2.01 (6H, m), 0.60–0.47 (30H, m); anal. calcd for $C_{45}H_{51}Br_3$: C, 64.99; H, 6.18%; found: C, 64.86; H, 5.96%; m.p. 287–288 °C. Consistent with previously published data.[119]

2,7,12-Tribromo-5,5,10,10,15,15-hexabutyl-10,15-dihydro-5*H*-diindeno[1,2-*a*:1',2'-*c*]fluorene (2.8)

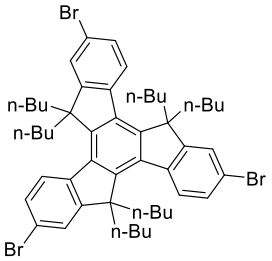

The title compound was prepared from 5,5,10,10,15,15-hexabutyl-10,15-dihydro-5*H*-diindeno[1,2-*a*:1',2'-*c*]fluorene (**2.4**, 2.0 g, 2.9 mmol), bromine (0.50 mL, 8.8 mmol) and CH_2Cl_2 (60 mL) using general procedure 2. The crude material was recrystallised from a 1:1 CH_2Cl_2:MeCN mixture to yield 2.6 g of the title compound (97% yield).

^{1}H NMR (400 MHz, $CDCl_3$) δ_H 8.19 (3H, d, ^3J = 8.4 Hz), 7.57 (3H, d, ^4J = 2.0 Hz), 7.52 (3H, dd, ^3J = 8.4 Hz, ^4J = 2.0 Hz), 2.90–2.83 (6H, m), 2.07–2.00 (6H, m), 0.99–0.80 (12H, m), 0.59–0.34 (30H, m); anal. calcd for $C_{51}H_{63}Br_3$: C, 66.89; H, 6.93%; found: C, 66.75; H, 6.72%; m.p. 321–324 °C. Consistent with previously published data.[161]

Triethyl 5,5,10,10,15,15-hexabutyl-10,15-dihydro-5*H*-diindeno[1,2-*a*:1',2'-*c*]fluorene-2,7,12-tricarboxylate (2.9)

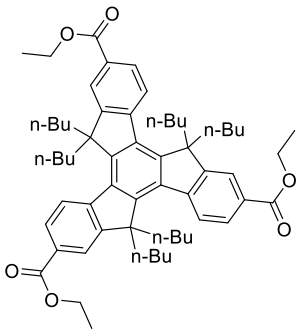

2,7,12-Tribromo-5,5,10,10,15,15-hexabutyl-10,15-dihydro-5*H*-diindeno[1,2-*a*:1',2'-*c*]fluorene (**2.8**, 400 mg, 0.47 mmol) was dissolved in THF (20 mL) and cooled to −80 °C. *n*-Butyllithium (2.5 M in hexanes, 0.68 mL, 1.7 mmol) was slowly added and the mixture stirred for 1 hour with the temperature maintained below −60 °C. The mixture was further cooled to −80 °C and ethyl chloroformate (0.67 mL, 7.1 mmol) added dropwise. The resultant mixture was stirred at −80 °C for 1 hour, −60 °C for 2 hours and then overnight at room temperature. The reaction mixture was quenched with water and the aqueous phase was extracted three times with CH_2Cl_2, the organic phases were combined, washed with brine, dried with $MgSO_4$, filtered and concentrated *in vacuo*. The crude material was purified by column chromatography (eluting with 0–10% ethyl acetate in hexane) then recrystallised from methanol to yield 150 mg of the title compound (36% yield).

^{1}H NMR (400 MHz, $CDCl_3$) δ_H 8.45 (3H, d, ^3J = 8.9 Hz), 8.15–8.12 (6H, m), 4.46 (6H, q, ^3J = 7.1 Hz), 3.00–2.93 (6H, m), 2.24–2.16 (6H, m), 1.47 (9H, t, ^3J = 7.1 Hz), 0.98–0.78 (12H, m), 0.59–0.34 (30H, m); ^{13}C NMR (100 MHz, $CDCl_3$) δ_C 167.1, 153.8, 148.1, 144.4, 138.1, 128.8, 128.1, 124.5, 123.6, 61.2, 56.1, 36.6, 26.7, 22.9, 14.6, 13.9; MALDI-TOF MS: *m/z* 894.32 [M^+]; anal. calcd for $C_{60}H_{78}O_6$: C, 80.50; H, 8.78%; found: C, 80.34; H, 8.91%; m.p. 208–210 °C.

General Procedure 3: Formation of carboxylic acid

n-Butyllithium (3.6 molar equivalents) was added dropwise to a stirred suspension of the corresponding tribromo truxene derivative in THF at −78 °C and the resultant yellow mixture was stirred at this temperature for 30 minutes. Dry ice was added to a separate flask and passed through a calcium chloride drying column before being bubbled through the reaction mixture. This set-up was maintained at −78 °C for 1 hour, then slowly warmed to room temperature and stirred for a further hour. The reaction, now containing a white precipitate, was quenched with water, at which point the precipitate dissolved. The reaction was then acidified to around pH 2 with concentrated HCl, producing further precipitate. The aqueous phase was extracted three times with ethyl acetate. The organic phases were combined and washed with brine, dried with $MgSO_4$, filtered and concentrated *in vacuo*. The crude material was then dissolved in the minimum volume of THF and recrystallised by vapour diffusion of hexane.

NMR samples were prepared by taking a portion of the compound and suspending it in water. Aqueous NaOH solution (1.0 mM, 3.3 molar equivalents) was added and the resultant solution stirred for 15 minutes. The salt was then precipitated by the addition of diethyl ether. After stirring for a further 15 minutes the solid was collected and redissolved in water. This solution was acidified to pH ~2 with concentrated HCl and the resulting precipitate collected and washed with diethyl ether.

5,5,10,10,15,15-Hexamethyl-10,15-dihydro-5*H*-diindeno[1,2-*a*:1',2'-*c*]fluorene-2,7,12-tricarboxylic acid (2.10)

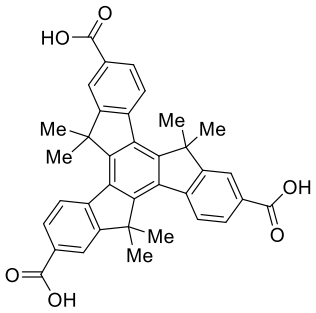

The title compound was prepared from 2,7,12-tribromo-5,5,10,10,15,15-hexamethyl-10,15-dihydro-5*H*-diindeno[1,2-*a*:1',2'-*c*]fluorene (**2.5**, 160 mg, 0.23 mmol), *n*-butyllithium (1.8 M in hexanes, 0.46 mL, 0.84 mmol), dry ice and THF (20 mL) using general procedure 3, to afford 100 mg (80% yield).

^{1}H NMR (400 MHz, DMSO-d$_6$) δ_H 13.03 (3H, br s), 8.40 (3H, d, ^{3}J = 8.4 Hz), 8.23 (3H, d, ^{4}J = 1.6 Hz), 8.11 (3H, dd, ^{3}J = 8.3 Hz, ^{4}J = 1.6 Hz), 1.86 (18H, s); ^{13}C NMR (100 MHz, DMSO-d$_6$) δ_C 167.3, 157.1, 150.6, 139.5, 134.6, 129.6, 128.3, 125.3, 123.5, 46.7, 23.4; MALDI-TOF MS: *m/z* 558.13 [M^{+}]; anal. calcd for $C_{36}H_{30}O_6$: C, 77.40; H, 5.41%; found: C, 74.72; H, 6.28%; m.p. > 350 °C. Consistent with previously published data.[158]

5,5,10,10,15,15-Hexaethyl-10,15-dihydro-5*H*-diindeno[1,2-*a*:1',2'-*c*]fluorene-2,7,12-tricarboxylic acid (2.11)

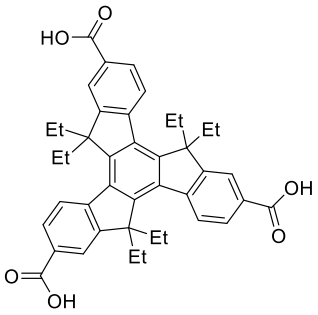

The title compound was prepared from 2,7,12-tribromo-5,5,10,10,15,15-hexaethyl-10,15-dihydro-5*H*-diindeno[1,2-*a*:1',2'-*c*]fluorene (**2.6**, 1.0 g, 1.4 mmol), *n*-butyllithium (2.4 M in hexanes, 2.1 mL, 5.0 mmol), dry ice and THF (80 mL) using general procedure 3, to afford 270 mg (31% yield).

^{1}H NMR (400 MHz, DMSO-d$_6$) δ_H 13.02 (3H, br s), 8.46 (3H, d, ^{3}J = 8.5 Hz), 8.12 (3H, d, ^{4}J = 1.6 Hz), 8.09 (3H, dd, ^{3}J = 8.3 Hz, ^{4}J = 1.5 Hz), 3.03–2.94 (6H, m), 2.31–2.22 (6H, m), 0.12 (18H, t, ^{3}J = 7.2 Hz); ^{13}C NMR (100 MHz, DMSO-d$_6$) δ_C 167.4, 152.3, 146.0, 143.5, 138.0, 129.4, 128.4, 124.2, 123.0, 56.6, 30.6, 28.6, 8.2; MALDI-TOF MS: *m/z* 642.13 [M$^+$]; anal. calcd for $C_{42}H_{42}O_6$: C, 78.48; H, 6.59%; found: C, 76.83; H, 6.67%; m.p. > 350 °C. Consistent with previously published data.[162]

5,5,10,10,15,15-Hexapropyl-10,15-dihydro-5*H*-diindeno[1,2-*a*:1',2'-*c*]fluorene-2,7,12-tricarboxylic acid (2.12)

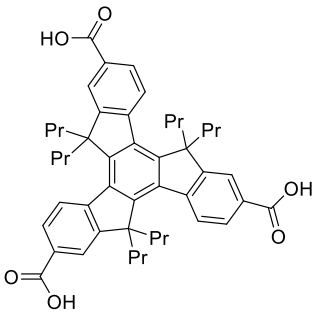

The title compound was prepared from 2,7,12-tribromo-5,5,10,10,15,15-hexapropyl-10,15-dihydro-5*H*-diindeno[1,2-*a*:1',2'-*c*]fluorene (**2.7**, 150 mg, 0.18 mmol), *n*-butyllithium (2.4 M in hexanes, 0.27 mL, 0.64 mmol), dry ice and THF (25 mL) using general procedure 3, to afford 54 mg (41% yield).

^{1}H NMR (400 MHz, DMSO-d$_6$) δ_H 13.03 (3H, br s), 8.46 (3H, d, ^{3}J = 8.4 Hz), 8.13 (3H, d, ^{4}J = 1.2 Hz), 8.09 (3H, dd, ^{3}J = 8.2 Hz, ^{4}J = 1.4 Hz), 2.90–2.85 (6H, m), 2.25–2.18 (6H, m), 0.48–0.40 (30H, m); ^{13}C NMR (100 MHz, DMSO-d$_6$) δ_C 167.4, 153.1, 147.1, 143.2, 137.5, 129.3, 128.3, 124.3, 123.1, 55.5, 38.3, 16.9, 14.1; MALDI-TOF MS: *m/z* 726.98 [M$^+$]; anal. calcd for $C_{48}H_{54}O_6$: C, 79.31; H, 7.49%; found: C, 76.26; H, 7.38%; m.p. > 350 °C.

5,5,10,10,15,15-Hexabutyl-10,15-dihydro-5*H*-diindeno[1,2-*a*:1',2'-*c*]fluorene-2,7,12-tricarboxylic acid (2.13)

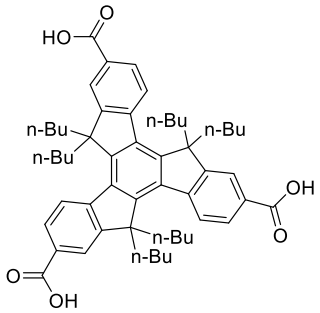

The title compound was prepared from 2,7,12-tribromo-5,5,10,10,15,15-hexabutyl-10,15-dihydro-5*H*-diindeno[1,2-*a*:1',2'-*c*]fluorene (**2.8**, 0.46 g, 0.51 mmol), *n*-butyllithium (2.4 M in hexanes, 0.75 mL, 1.8 mmol), dry ice and THF (40 mL) using general procedure 3, to afford 0.32 g (77% yield).

^{1}H NMR (400 MHz, DMSO-d$_6$) δ_H 13.03 (3H, br s), 8.50 (3H, d, ^{3}J = 8.4 Hz), 8.12 (3H, d, ^{4}J = 1.5 Hz), 8.08 (3H, dd, ^{3}J = 8.3 Hz, ^{4}J = 1.5 Hz), 3.03–2.96 (6H, m), 2.26–2.19 (6H, m), 0.91–0.70 (12H, m), 0.52–0.27 (30H, m); ^{13}C NMR (100 MHz, DMSO-d$_6$) δ_C 167.4, 153.1, 147.1, 143.3, 137.7, 129.3, 128.2, 124.4, 123.1, 55.5, 35.5, 26.3, 22.1, 13.6; MALDI-TOF MS: *m/z* 811.44 [M$^+$]; anal. calcd for $C_{54}H_{66}O_6$: C, 79.96; H, 8.20%; found: C, 80.16; H, 8.69%; m.p. > 350 °C. Consistent with previously published data.[160]

7.3 Chapter 3 synthesis

General procedure 4: Formation of tricarboxylic acid salt

The corresponding tricarboxylic acid was suspended in the minimum volume of methanol. To this, 3.3 equivalents (1.1 per position) of a methanol solution of the hydroxide salt were added. The mixture was stirred for 1 hour, diethyl ether was then added to precipitate the carboxylate salt. The suspension was stirred for a further 15 minutes. The precipitate was collected by filtration, washed with diethyl ether and dried *in vacuo*.

Trisodium 5,5,10,10,15,15-hexabutyl-10,15-dihydro-5*H*-diindeno[1,2-*a*:1',2'-*c*]fluorene-2,7,12-tricarboxylate

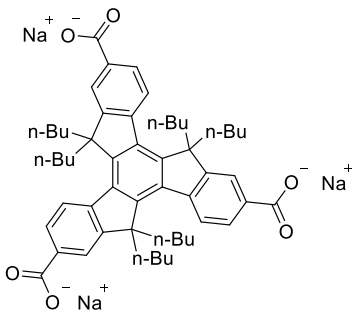

The title compound was prepared from 5,5,10,10,15,15-hexabutyl-10,15-dihydro-5*H*-diindeno[1,2-*a*:1',2'-*c*]fluorene-2,7,12-tricarboxylic acid (**2.13**, 20 mg, 0.025 mmol), sodium hydroxide solution (1 mM in methanol, 0.081 mL, 0.081 mmol), methanol and diethyl ether using general procedure 4 to afford 13.1 mg of precipitate.

Due to the low mass the product was used in devices without further purification or analysis.

Tripotassium 5,5,10,10,15,15-hexabutyl-10,15-dihydro-5*H*-diindeno[1,2-*a*:1',2'-*c*]fluorene-2,7,12-tricarboxylate

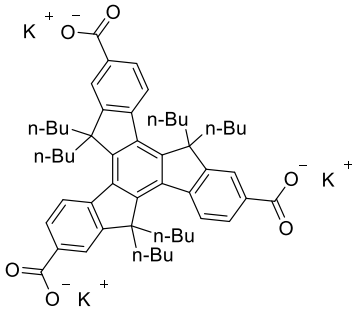

The title compound was prepared from 5,5,10,10,15,15-hexabutyl-10,15-dihydro-5*H*-diindeno[1,2-*a*:1',2'-*c*]fluorene-2,7,12-tricarboxylic acid (**2.13**, 20 mg, 0.025 mmol), potassium hydroxide solution (1 mM in methanol, 0.081 mL, 0.081 mmol), methanol and diethyl ether using general procedure 4 to afford 7.5 mg of precipitate.

Due to the low mass the product was used in devices without further purification or analysis.

Trisodium 5,5,10,10,15,15-hexabutyl-10,15-dihydro-5*H*-diindeno[1,2-*a*:1',2'-*c*]fluorene-2,7,12-tricarboxylate

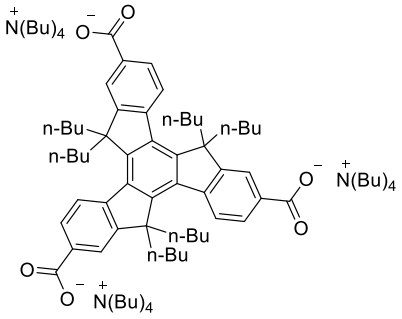

The title compound was prepared from 5,5,10,10,15,15-hexabutyl-10,15-dihydro-5*H*-diindeno[1,2-*a*:1',2'-*c*]fluorene-2,7,12-tricarboxylic acid (**2.13**, 20 mg, 0.025 mmol), tetrabutylammonium hydroxide solution (1 mM in methanol, 0.081 mL, 0.081 mmol), methanol and diethyl ether using general procedure 4 to afford 1.7 mg of precipitate.

Due to the low mass the product was used in devices without further purification or analysis.

7.4 Chapter 4 synthesis

5,5,10,10,15,15-Hexabutyl-2,7,12-triiodo-10,15-dihydro-5*H*-diindeno[1,2-*a*:1',2'-*c*]fluorene (4.1)

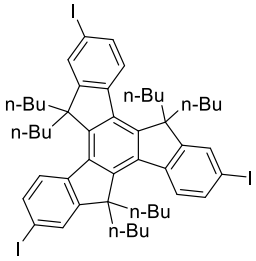

Attempt 1:

5,5,10,10,15,15-Hexabutyl-10,15-dihydro-5*H*-diindeno[1,2-*a*:1',2'-*c*]fluorene (**2.4**, 1.6 g, 2.3 mmol) was suspended in a mixture of glacial acetic acid (15 mL), concentrated sulfuric acid (3.0 mL) and water (0.45 mL). To this iodine (0.58 g, 2.3 mmol) and periodic acid (0.52 mg, 2.3 mmol) were added. The dark red mixture was stirred for 3 days at 60 °C, over which time it turned green. The mixture was cooled and filtered; the precipitate was washed with aqueous sodium hydrogen carbonate.

Analysis of the crude material showed no evidence of product.

Attempt 2:

n-Butyllithium (2.3 M in hexanes, 3.6 mL, 8.5 mmol) was added dropwise to a solution of 2,7,12-tribromo-5,5,10,10,15,15-hexabutyl-10,15-dihydro-5*H*-diindeno[1,2-*a*:1',2'-*c*]fluorene (**2.8**, 2.0 g, 2.2 mmol) dissolved in THF (80 mL) at −80 °C. After stirring for 15 minutes the solution was further cooled to −95 °C, and a solution of iodine (2.7 g, 10 mmol) in THF (20 mL) was added dropwise. The reaction was allowed to warm up to −15 °C and then quenched with an aqueous solution of sodium sulfite. The aqueous phase was extracted three times with CH_2Cl_2; the organic phases were combined, washed with brine, dried with $MgSO_4$,

filtered and concentrated *in vacuo*. The crude material was pre-absorbed onto silica and purified by column chromatography (eluting with hexane), to yield 2.1 g of the title compound (92% yield).

^{1}H NMR (400 MHz, $CDCl_3$) δ_H 8.07 (3H, d, ^{3}J = 8.4 Hz), 7.76 (3H, d, ^{4}J = 1.6 Hz), 7.71 (3H, dd, ^{3}J = 8.4 Hz, ^{4}J = 1.6 Hz), 2.88–2.81 (6H, m), 2.06–1.99 (6H, m), 0.99–0.79 (12H, m), 0.58–0.33 (30H, m); ^{13}C NMR (100 MHz, $CDCl_3$) δ_C 156.1, 145.3, 139.7, 137.8, 135.5, 131.7, 126.5, 92.8, 56.0, 36.6, 26.6, 22.9, 13.9; m.p. 332–336 °C. Consistent with previously published data.[163,164]

Dimethyl 5-((trimethylsilyl)ethynyl)isophthalate (4.2)

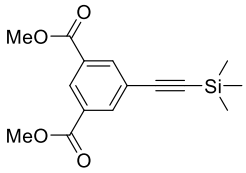

Attempt 1:

Dimethyl 5-bromoisophthalate (100 mg, 0.37 mmol), tetrakis(triphenylphosphine)palladium(0) (10 mg, 9.0 μmol) and copper iodide (21 mg, 0.11 mmol) were added to a microwave vial. Ethynyltrimethylsilane (0.10 mL, 0.72 mmol), triethylamine (0.25 mL) then DMF (1.8 mL) were added and the mixture degassed. The sealed vial was then heated in the microwave at 160 °C for 2 hours. No starting material was visible by TLC so the mixture was washed with aqueous ammonium chloride solution. The aqueous layer was extracted three times with ethyl acetate. The organic layers were then combined, dried with $MgSO_4$ and then filtered through Celite® to yield 38 mg of a crude mixture.

^{1}H NMR showed product formation but also impurities.

Attempt 2:

Dimethyl 5-bromoisophthalate (100 mg, 0.37 mmol) and copper iodide (25 mg, 0.13 mmol) were added to a microwave vial. DMF (1.8 mL), ethynyltrimethylsilane (0.20 mL, 1.4 mmol) then triethylamine (0.25 mL, freshly distilled over CaH_2) were added and the mixture degassed. Tetrakis(triphenylphosphine)palladium(0) (10 mg, 9.0 μmol) was then added at which point the mixture turned black; the resultant mixture was further degassed. The sealed vial was then heated in the microwave at 160 °C for 2 hours. No starting material was visible by TLC so the mixture was washed with aqueous ammonium chloride solution. The aqueous layer was extracted three times with ethyl acetate. The organic layers were then combined, washed with water, dried with $MgSO_4$ and then filtered through Celite® to yield 27 mg of a crude mixture.

^{1}H NMR showed product formation but also impurities.

Attempt 3:

Dimethyl 5-bromoisophthalate (100 mg, 0.37 mmol) and copper iodide (25 mg, 0.13 mmol) were added to a microwave vial. DMF (1.8 mL), ethynyltrimethylsilane (0.20 mL, 1.4 mmol) then triethylamine (0.25 mL, freshly distilled over CaH_2) were added and the mixture degassed. [1,1'-Bis(diphenylphosphino)ferrocene]dichloropalladium(II) (10 mg, 0.014 mmol) was then added at which point the mixture turned black; the resultant mixture was further degassed. The sealed vial was then heated in the microwave at 160 °C for 2 hours. No starting material was visible by TLC so the mixture was washed with aqueous ammonium chloride solution. The aqueous layer was extracted three times with ethyl acetate. The organic layers were then combined, washed with water, dried with $MgSO_4$ and then filtered through Celite® to yield 24 mg of a crude mixture.

^{1}H NMR showed product formation but also impurities.

Attempt 4:

Dimethyl 5-bromoisophthalate (100 mg, 0.37 mmol), copper iodide (70 mg, 0.37 mmol) and tetrakis(triphenylphosphine)palladium(0) (46 mg, 0.040 mmol) were added to a flask followed by ethynyltrimethylsilane (1.4 mL, 10 mmol) and triethylamine (15 mL, freshly distilled over CaH_2). The mixture was heated at reflux overnight, then cooled and filtered through Celite® to yield 120 mg of a crude mixture.

^{1}H NMR showed product formation but also impurities which mainly appeared to be triphenylphosphine oxide.

Attempt 5:

Dimethyl 5-bromoisophthalate (400 mg, 1.5 mmol), copper iodide (280 mg, 1.5 mmol) and tetrakis(triphenylphosphine)palladium(0) (180 mg, 0.15 mmol) were added to a flask followed by ethynyltrimethylsilane (4.2 mL, 30 mmol) and triethylamine (45 mL, freshly distilled over CaH_2). The brown mixture was heated at reflux overnight, then cooled and filtered through Celite®. The crude material was pre-absorbed onto silica and purified by column chromatography (eluting with 5–10% ethyl acetate in hexane) to yield 190 mg of the title compound, **4.2** (46% yield).

Attempt 6:

Dimethyl 5-bromoisophthalate (2.5 g, 9.2 mmol), copper iodide (1.9 g, 10 mmol) and tetrakis(triphenylphosphine)palladium(0) (0.59 g, 0.51 mmol) were added to a flask followed by ethynyltrimethylsilane (25 mL, 180 mmol) and triethylamine (200 mL, freshly distilled over CaH_2). The mixture was heated at reflux overnight. Excess triethylamine was removed by distillation; the residue was dissolved in THF and filtered through Celite®. ^{1}H NMR showed mainly unreacted starting material. The crude material was pre-absorbed onto silica and purified by column chromatography

(eluting with 0–10% ethyl acetate in hexane) to yield 2.3 g of the dimethyl 5-bromoisophthalate starting material.

^{1}H NMR (400 MHz, $CDCl_3$) δ_H 8.60 (1H, t, ^4J = 1.5 Hz), 8.35 (2H, d, ^4J = 1.5 Hz), 3.96 (6H, s). Consistent with starting material.

Attempt 7:

Triethylamine (200 mL, freshly distilled over CaH_2) was transferred to a flask containing dimethyl 5-bromoisophthalate (2.3 g, 8.3 mmol), ethynyltrimethylsilane (9.0 mL, 65 mmol) and copper iodide (1.7 g, 8.9 mmol). Tetrakis(triphenylphosphine)palladium(0) (1.0 g, 0.87 mmol) was then added and the resultant mixture heated at reflux overnight. An aliquot of the reaction mixture was analysed by ^{1}H NMR which showed partial conversion to product. More tetrakis(triphenylphosphine)palladium(0) (500 mg, 0.43 mmol) was added and the resultant mixture heated at reflux overnight. The solvent and base were removed by distillation, the residue dissolved and filtered through Celite®. The crude material was pre-absorbed onto silica and purified by column chromatography (eluting with 0–10% ethyl acetate in hexane) to yield 1.2 g of the title compound, **4.2** (52% yield).

Attempt 8:

Dimethyl 5-bromoisophthalate (3.0 g, 11 mmol), ethynyltrimethylsilane (5.8 mL, 42 mmol) and copper iodide (2.3 g, 12 mmol) were dissolved in THF (120 mL). Triethylamine (75 mL, freshly distilled over CaH_2) was added and the mixture degassed. Tetrakis(triphenylphosphine)palladium(0) (1.2 g, 1.0 mmol) was added and the resultant black mixture heated at reflux overnight. An aliquot of the reaction mixture was analysed by ^{1}H NMR which showed partial conversion to the product (~30%). Further tetrakis(triphenylphosphine)palladium(0) (300 mg, 0.26 mmol) and ethynyltrimethylsilane (2.0 mL, 14 mmol) were added; the resultant mixture was

heated at reflux overnight. Again ^{1}H NMR analysis of an aliquot showed ~90% conversion to the product; tetrakis(triphenylphosphine)palladium(0) (200 mg, 0.17 mmol) and ethynyltrimethylsilane (1.5 mL, 11 mmol) were added and the reaction heated at 45 °C for a further 2 days. The solvent and base were removed by distillation, the residue dissolved in CH_2Cl_2 and filtered through Celite®. The crude material was pre-absorbed onto silica and purified by column chromatography (eluting with 0–10% ethyl acetate in hexane) to yield 2.8 g of the title compound, **4.2** (88% yield).

^{1}H NMR (400 MHz, $CDCl_3$) δ_H 8.60 (1H, t, ^{4}J = 1.6 Hz), 8.29 (2H, d, ^{4}J = 1.6 Hz), 3.95 (6H, s), 0.26 (9H, s). Consistent with previously published data.[139,165]

Dimethyl 5-ethynylisophthalate (4.3)

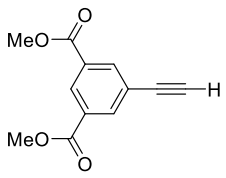

Tetrabutylammonium fluoride (1 M in THF, 0.85 mL, 0.85 mmol) was slowly added to a solution of dimethyl 5-((trimethylsilyl)ethynyl)isophthalate (**4.2**, 170 mg, 0.57 mmol) in THF (20 mL), and the resultant mixture stirred for 2 hours. Water and $CHCl_3$ were added; the aqueous phase was separated and washed with $CHCl_3$ three times. The organic phases were combined, washed with brine, dried with $MgSO_4$, filtered and concentrated *in vacuo*. The crude material was pre-absorbed onto silica and purified by column chromatography (eluting with 10% ethyl acetate in hexane) to yield 85 mg of the title compound (68% yield) as a white powder.

^{1}H NMR (400 MHz, $CDCl_3$) δ_H 8.64 (1H, t, ^{4}J = 1.6 Hz), 8.33 (2H, d, ^{4}J = 1.6 Hz), 3.96 (6H, s), 3.17 (1H, s). Consistent with previously published data.[139]

Hexamethyl 5,5',5''-((5,5,10,10,15,15-hexabutyl-10,15-dihydro-5*H*-diindeno[1,2-*a*:1',2'-*c*]fluorene-2,7,12-triyl)tris(ethyne-2,1-diyl))triisophthalate (4.4)

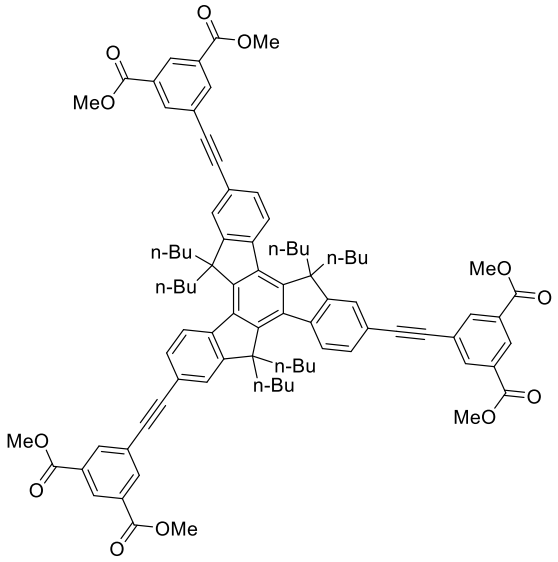

5,5,10,10,15,15-Hexabutyl-2,7,12-triiodo-10,15-dihydro-5*H*-diindeno[1,2-*a*:1',2'-*c*]fluorene (**4.1**, 2.0 g, 1.9 mmol), dimethyl 5-ethynylisophthalate (**4.3**, 1.6 g, 7.5 mmol) and copper iodide (1.2 g, 6.2 mmol) were dissolved in THF (100 mL). Triethylamine (50 mL, freshly distilled over CaH_2) was added and the mixture degassed. Tetrakis(triphenylphosphine)palladium(0) (0.66 g, 0.57 mmol) was added and the resultant mixture heated at reflux overnight. The solvent and base were removed by distillation, the residue dissolved in CH_2Cl_2 and filtered through Celite®. The crude material was pre-absorbed onto silica and purified twice by column chromatography (eluting with 20% ethyl acetate in hexane). Recrystallisation from a 1:1 mixture of CH_2Cl_2:MeCN gave 2.2 g of the title compound (87% yield).

^{1}H NMR (400 MHz, $CDCl_3$) δ_H 8.65 (3H, t, ^4J = 1.6 Hz), 8.45 (6H, d, ^4J = 1.5 Hz), 8.39 (3H, d, ^3J = 8.5 Hz), 7.67 (3H, d, ^4J = 1.5 Hz), 7.62 (3H, dd, ^3J = 8.2 Hz, ^4J = 1.4 Hz), 3.99 (18H, s), 3.01–2.94 (6H, m), 2.20–2.12 (6H, m), 1.03–0.84 (12H, m), 0.65–0.40 (30H, m); ^{13}C NMR (100 MHz, $CDCl_3$) δ_C 165.8, 153.9, 146.5, 140.9, 138.2, 136.7, 131.2, 130.2, 130.1, 125.7, 124.9, 124.7, 120.6, 92.3, 88.1, 56.0, 52.7, 36.8, 26.7, 23.0, 14.0; MALDI-TOF MS: *m/z* 1327.00 [M^+], 1269.97 [$M^+ - C_4H_9$];

anal. calcd for $C_{87}H_{90}O_{12}$: C, 78.71; H, 6.83%; found: C, 78.38; H, 6.59%; m.p. 280–282 °C.

7.5 Chapter 5 synthesis

5,5,10,10,15,15-Hexabutyl-10,15-dihydro-5*H*-diindeno[1,2-*a*:1',2'-*c*]fluorene-2,7,12-tricarbaldehyde (5.1)

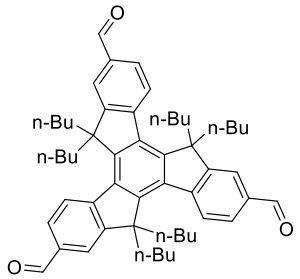

Attempt 1:

n-Butyllithium (2.2 M in hexanes, 2.0 mL, 4.4 mmol) was added drop wise to a stirred solution of 2,7,12-tribromo-5,5,10,10,15,15-hexabutyl-10,15-dihydro-5*H*-diindeno[1,2-*a*:1',2'-*c*]fluorene (**2.8**, 1.2 g, 1.3 mmol) in THF (60 mL) at −78 °C. After 1 hour, DMF (0.62 mL, 8.0 mmol) was slowly added at −78 °C. The reaction mixture was allowed to gradually warm to room temperature overnight. Water was added to quench the reaction; the aqueous layer was then separated and extracted three times with diethyl ether. The organic phases were combined and washed with brine, dried with $MgSO_4$, filtered and concentrated *in vacuo*. The crude material was pre-absorbed onto silica and purified by column chromatography (eluting with 0–10% ethyl acetate in petroleum ether). Subsequent recrystallisation from MeCN gave 490 mg of the title compound (49% yield).

Attempt 2:

n-Butyllithium (2.5 M in hexanes, 10 mL, 25 mmol) was added drop wise to a stirred solution of 2,7,12-tribromo-5,5,10,10,15,15-hexabutyl-10,15-dihydro-5*H*-diindeno[1,2-*a*:1',2'-*c*]fluorene (**2.8**, 7.0 g, 7.6 mmol) in THF (200 mL) at −78 °C. After 15 minutes, DMF (3.6 mL, 46 mmol) was slowly added at −78 °C. The

reaction mixture was allowed to gradually warm to room temperature overnight. Water was added to quench the reaction; the aqueous layer was then separated and extracted three times with CH_2Cl_2. The organic phases were combined and washed with brine, dried with $MgSO_4$, filtered and concentrated *in vacuo*. The crude material was pre-absorbed onto silica and purified by column chromatography (eluting with 0–10% ethyl acetate in petroleum ether) to give 3.0 g of the title compound as a white powder (52% yield).

Attempt 3:

n-Butyllithium (2.4 M in hexanes, 8.2 mL, 20 mmol) was added drop wise to a stirred solution of 2,7,12-tribromo-5,5,10,10,15,15-hexabutyl-10,15-dihydro-5*H*-diindeno[1,2-*a*:1',2'-*c*]fluorene (**2.8**, 3.0 g, 3.3 mmol) in THF (100 mL) at −78 °C. After 15 minutes, DMF (1.7 mL, 22 mmol) was slowly added at −78 °C. The reaction mixture was allowed to gradually warm to room temperature overnight. Water was added to quench the reaction; the aqueous layer was then separated and extracted three times with CH_2Cl_2. The organic phases were combined and washed with brine, dried with $MgSO_4$, filtered and concentrated *in vacuo*. The crude material was pre-absorbed onto silica and purified by column chromatography (eluting with 0–10% ethyl acetate in petroleum ether) to give 2.0 g of the title compound as a white powder (80% yield).

^{1}H NMR (400 MHz, $CDCl_3$) δ_H 10.16 (3H, s), 8.57 (3H, d, ^3J = 8.2 Hz), 8.03 (3H, d, ^4J = 1.4 Hz), 7.97 (3H, dd, ^3J = 8.2 Hz, ^4J = 1.5 Hz), 3.02–2.95 (6H, m), 2.28–2.21 (6H, m), 0.99–0.80 (12H, m), 0.61–0.35 (30H, m); ^{13}C NMR (100 MHz, $CDCl_3$) δ_C 192.3, 154.5, 149.2, 145.7, 138.1, 135.1, 129.7, 125.1, 122.5, 56.3, 36.7, 29.8, 26.7, 22.8, 13.9; MALDI-TOF MS: *m/z* 763.60 [M^+], 705.53 [$M^+ - C_4H_9$]; anal. calcd for $C_{54}H_{66}O_3$: C, 84.99; H, 8.72%; found: C, 84.61; H, 8.71%; m.p. decomposes above 280 °C.[166,167]

5,5,10,10,15,15-Hexabutyl-10,15-dihydro-5*H*-diindeno[1,2-*a*:1',2'-*c*]fluorene-2,7,12-tricarbonitrile (5.2)

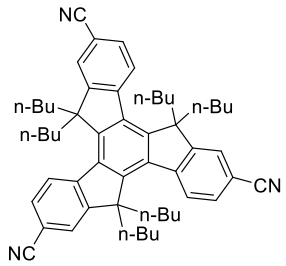

5,5,10,10,15,15-Hexabutyl-10,15-dihydro-5*H*-diindeno[1,2-*a*:1',2'-*c*]fluorene-2,7,12-tricarbaldehyde (**5.1**, 1.0 g, 1.3 mmol) was dissolved in THF (15 mL) then NH_3 (40 mL, 38% aqueous) was added followed by a solution of iodine (1.4 g, 5.5 mmol) in THF (10 mL). The resultant suspension was stirred overnight in a closed flask, at room temperature. The reaction was quenched with an aqueous solution of sodium thiosulfate; the aqueous layer was separated then extracted with CH_2Cl_2 three times. The organic layers were then combined, washed with brine and dried with $MgSO_4$. The crude material was purified by column chromatography (eluting with 80% CH_2Cl_2 in hexane) to yield 670 mg of the title material (68% yield).

^{1}H NMR (400 MHz, $CDCl_3$) δ_H 8.46 (3H, d, ^3J = 8.2 Hz), 7.77–7.74 (6H, m), 2.93–2.86 (6H, m), 2.19–2.11 (6H, m), 1.00–0.81 (12H, m), 0.55–0.28 (30H, m); ^{13}C NMR (100 MHz, $CDCl_3$) δ_C 154.3, 148.4, 143.7, 137.8, 130.9, 126.2, 125.2, 119.4, 110.7, 56.4, 36.6, 26.6, 22.8, 13.8; MALDI-TOF MS: *m/z* 754.40 [M^+], 696.34 [$M^+ - C_4H_9$]; anal. calcd for $C_{54}H_{63}N_3$: C, 86.01; H, 8.42; N, 5.57%; found: C, 85.72; H, 8.42; N, 5.30%; m.p. 308–309 °C.

2,2',2''-((5,5,10,10,15,15-Hexabutyl-10,15-dihydro-5*H*-diindeno[1,2-*a*:1',2'-*c*]fluorene-2,7,12-triyl)tris(methaneylylidene))trimalononitrile (5.3)

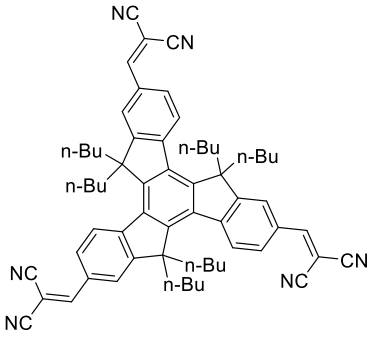

Attempt 1:

5,5,10,10,15,15-Hexabutyl-10,15-dihydro-5*H*-diindeno[1,2-*a*:1',2'-*c*]fluorene-2,7,12-tricarbaldehyde (**5.1**, 430 mg, 0.56 mmol), malononitrile (170 mg, 2.6 mmol) and piperidine (3 drops) were dissolved in ethanol (15 mL). The reaction mixture was heated at reflux overnight.

^{1}H NMR showed consumption of starting material but a complex mixture of peaks which could not be clearly identified. These peaks could not be separated by precipitation or column chromatography. No trace of the desired product could be identified by MALDI-TOF.

Attempt 2:

Piperidine (0.10 mL, 1.0 mmol) was added to a solution of 5,5,10,10,15,15-hexabutyl-10,15-dihydro-5*H*-diindeno[1,2-*a*:1',2'-*c*]fluorene-2,7,12-tricarbaldehyde (**5.1**, 200 mg, 0.26 mmol), malononitrile (67 mg, 1.0 mmol) and $MgSO_4$ (57 mg, 0.47 mmol) in THF (15 mL). The mixture was then heated at reflux overnight.

^{1}H NMR showed consumption of starting material but a complex mixture of peaks which could not be clearly identified. These peaks could not be separated by

precipitation or trituration. No trace of the desired product could be identified by MALDI-TOF.

Attempt 3:

5,5,10,10,15,15-Hexabutyl-10,15-dihydro-5*H*-diindeno[1,2-*a*:1',2'-*c*]fluorene-2,7,12-tricarbaldehyde (**5.1**, 200 mg, 0.26 mmol), malononitrile (68 mg, 1.0 mmol) and $MgSO_4$ (19 mg, 0.16 mmol) were suspended in toluene (20 mL). To this piperidine (0.020 mL, 0.16 mmol) and glacial acetic acid (0.030 mL, 0.47 mmol) were added; the resultant mixture was then heated at reflux overnight.

^{1}H NMR of the reaction mixture showed consumption of starting material with possible traces of product formation, but was very impure.

Attempt 4:

5,5,10,10,15,15-Hexabutyl-10,15-dihydro-5*H*-diindeno[1,2-*a*:1',2'-*c*]fluorene-2,7,12-tricarbaldehyde (**5.1**, 500 mg, 0.66 mmol), malononitrile (200 mg, 3.0 mmol) and basic alumina (1.5 g) were suspended in toluene (50 mL), then heated at reflux overnight. On cooling the reaction mixture was filtered and the solvent removed *in vacuo*. The crude material was then pre-absorbed onto silica and purified by column chromatography (eluting with 20% ethyl acetate in hexane). Recrystallisation from 1:1 CH_2Cl_2:hexane gave 220 mg of the title compound, **5.3** (36% yield).

^{1}H NMR (400 MHz, $CDCl_3$) δ_H 8.53 (3H, d, ^3J = 8.5 Hz), 8.08 (3H, d, ^4J = 1.6 Hz), 8.01 (3H, dd, ^3J = 8.4 Hz, ^4J = 1.6 Hz), 7.91 (3H, s), 2.97–2.90 (6H, m), 2.26–2.18 (6H, m), 1.01–0.82 (12H, m), 0.59–0.35 (30H, m); ^{13}C NMR (100 MHz, $CDCl_3$) δ_C 159.4, 154.8, 150.1, 145.7, 138.0, 130.1, 130.0, 125.6, 124.5, 114.1, 113.2, 82.3, 56.6, 36.7, 26.7, 22.8, 13.9; MALDI-TOF MS: *m/z* 849.43 [$M^- - C_4H_9$]; anal. calcd for $C_{63}H_{66}N_6$: C, 83.40; H, 7.33; N, 9.26%; found: C, 83.63; H, 7.41; N, 9.38%; m.p. 188–190 °C.

5,5,10,10,15,15-Hexabutyl-2,7,12-tri(prop-1-yn-1-yl)-10,15-dihydro-5*H*-diindeno[1,2-*a*:1',2'-*c*]fluorene (5.4)

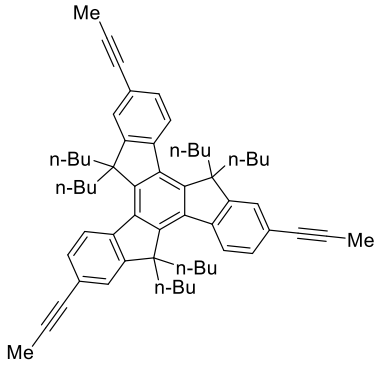

Lithium diisopropylamide (0.99 M in THF, 27 mL, 26 mmol) was added dropwise to a solution of 1,2-dibromopropane (0.91 mL, 8.7 mmol) in THF (15 mL), with the temperature maintained below −60 °C. After stirring at this temperature for 10 minutes the solution was moved to an ice bath and stirred for 20 minutes. The cold solution was then transferred by syringe to a solution of zinc (II) bromide (2.0 g, 8.7 mmol, dried *in vacuo* overnight) in THF (40 mL) at −78 °C. The resultant solution was then gradually warmed to room temperature. A solution of 2,7,12-tribromo-5,5,10,10,15,15-hexabutyl-10,15-dihydro-5*H*-diindeno[1,2-*a*:1',2'-*c*]fluorene (**2.8**, 2.0 g, 2.2 mmol) in THF (40 mL) was added to this mixture, followed by tetrakis(triphenylphosphine)palladium(0) (760 mg, 0.66 mmol). The reaction mixture was then refluxed overnight. Saturated aqueous ammonium chloride solution was added and the aqueous layer then extracted with ethyl acetate three times. The organic layers were then combined, washed with water, brine and dried with $MgSO_4$. The crude material was pre-absorbed onto silica and purified by column chromatography (eluting with 0–3% ethyl acetate in hexane). Further purification by column chromatography (eluting with diethyl ether) and recrystallisation from diethyl ether gave 390 mg of the title material (22% yield).

^{1}H NMR (400 MHz, $CDCl_3$) δ_H 8.26 (3H, d, ^{3}J = 8.3 Hz), 7.48 (3H, d, ^{4}J = 1.5 Hz), 7.42 (3H, dd, ^{3}J = 8.2 Hz, ^{4}J = 1.5 Hz), 2.93–2.86 (6H, m), 2.13 (9H, s), 2.08–2.01 (6H, m), 0.97–0.77 (12H, m), 0.60–0.33 (30H, m); ^{13}C NMR (100 MHz, $CDCl_3$) δ_C

153.7, 145.7, 139.8, 138.2, 129.8, 125.4, 124.6, 121.9, 86.3, 80.6, 55.7, 36.7, 26.6, 22.9, 13.9, 4.6; MALDI-TOF MS: *m/z* 792.19 [M^+]; anal. calcd for $C_{60}H_{72}$: C, 90.85; H, 9.15%; found: C, 90.55; H, 8.96%; m.p. 131–134 °C.

3,3',3''-(5,5,10,10,15,15-Hexabutyl-10,15-dihydro-5*H*-diindeno[1,2-*a*:1',2'-*c*]fluorene-2,7,12-triyl)tris(2-methylbuta-1,3-diene-1,1,4,4-tetracarbonitrile) (5.5)

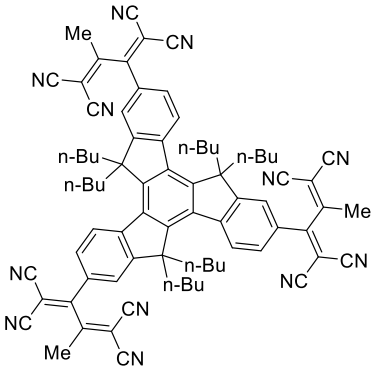

5,5,10,10,15,15-Hexabutyl-2,7,12-tri(prop-1-yn-1-yl)-10,15-dihydro-5H-diindeno[1,2-a:1',2'-c]fluorene (**5.4**, 200 mg, 0.25 mmol) and tetracyanoethylene (120 mg, 0.91 mmol) were dissolved in ethyl acetate (20 mL); the mixture was heated at 80 °C overnight.

Crude ^{1}H NMR showed the formation of some new peaks, but mainly starting material. MALDI-TOF showed no peaks corresponding to desired product.

5,5,10,10,15,15-Hexabutyl-2,7,12-tris(3,3,3-trifluoroprop-1-yn-1-yl)-10,15-dihydro-5*H*-diindeno[1,2-*a*:1',2'-*c*]fluorene (5.6)

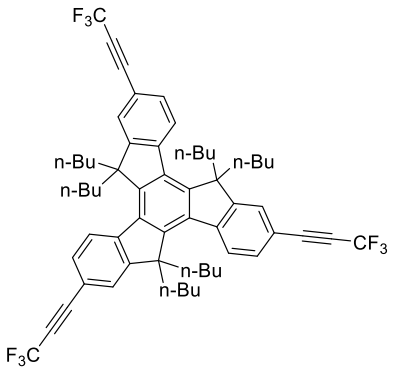

Lithium diisopropylamide (2.0 M in THF, 13 mL, 26 mmol) was added dropwise to a solution of 1,2-dibromo-3,3,3-trifluoropropane (1.1 mL, 8.7 mmol) in THF (15 mL), with the temperature maintained below −60 °C. After stirring at this temperature for 10 minutes the solution was moved to an ice bath and stirred for 20 minutes. The cold solution was then transferred by syringe to a solution of zinc (II) bromide (2.0 g, 8.7 mmol, dried *in vacuo* overnight) in THF (40 mL) at −78 °C. The resultant solution was then gradually warmed to room temperature. A solution of 2,7,12-tribromo-5,5,10,10,15,15-hexabutyl-10,15-dihydro-5*H*-diindeno[1,2-*a*:1',2'-*c*]fluorene (**2.8**, 2.0 g, 2.2 mmol) in THF (40 mL) was added to this mixture, followed by tetrakis(triphenylphosphine)palladium(0) (760 mg, 0.66 mmol). The reaction mixture was then refluxed overnight. TLC and ^{1}H NMR showed starting material still present so a further portion of tetrakis(triphenylphosphine)palladium(0) (720 mg, 0.62 mmol) was added and the mixture refluxed overnight.

Analysis of the crude material by ^{1}H NMR, ^{19}F NMR and MALDI-TOF showed no evidence of the desired product.

8 REFERENCES

1 P. Y. Bruice, *Organic Chemistry*, Pearson Prentice Hall, Upper Saddle River, NJ, 5th edn., 2007.

2 P. Atkins and J. De Paula, *Atkins' Physical Chemistry*, Oxford University Press, Oxford, 9th edn.

3 J.-L. Bredas, *Mater. Horizons*, 2014, **1**, 17.

4 B. Averill and P. Eldredge, *Chemistry: Principles, Patterns, and Applications*, Pearson Benjamin Cummings, San Francisco, CA, 2007.

5 H. Klauk, *Organic Electronics: Materials, Manufacturing and Applications*, Wiley-VCH, Weinheim, 2006.

6 J. Clayden, N. Greeves, S. Warren and P. Wothers, *Organic Chemistry*, Oxford University Press, 2001.

7 C. K. Chiang, M. A. Druy, S. C. Gau, A. J. Heeger, E. J. Louis, A. G. MacDiarmid, Y. W. Park and H. Shirakawa, *J. Am. Chem. Soc.*, 1978, **100**, 1013.

8 H. Shirakawa, E. J. Louis, A. G. MacDiarmid, C. K. Chiang and A. J. Heeger, *J. Chem. Soc. Chem. Commun.*, 1977, **16**, 578.

9 B. Norden and E. Krutmeijer, *The Nobel Prize in Chemistry, 2000 : Conductive polymers*, The Royal Swedish Acedemy of Sciences, 2000.

10 Nobelprize.org, The Nobel Prize in Chemistry 2000, http://www.nobelprize.org/nobel_prizes/chemistry/laureates/2000/, Accessed: 21 February 2018.

11 J. Roncali, *Chem. Rev.*, 1997, **97**, 173.

12 J. Roncali, *Macromol. Rapid Commun.*, 2007, **28**, 1761.

13 J.-L. Brédas, *J. Chem. Phys.*, 1985, **82**, 3808.

14 C. M. Cardona, W. Li, A. E. Kaifer, D. Stockdale and G. C. Bazan, *Adv. Mater.*, 2011, **23**, 2367.

15 J. Sworakowski and K. Janus, *Org. Electron.*, 2017, **48**, 46.

16 D. H. Williams and I. Fleming, *Spectroscopic Methods in Organic Chemistry*, McGraw-Hill, 4th editio., 1989.

17 J. C. De Mello, H. F. Wittmann and R. H. Friend, *Adv. Mater.*, 1997, **9**, 230.

18 *Methods for the determination of photoluminescence quantum yield*, Nanoco Technologies Limited, 2013.

19 *A Guide to Recording Fluorescence Quantum Yields*, Horiba UK Limited.

20 J.-F. Tremblay, *Chem. Eng. News*, 2016, **94**, 30.

21 P. Waide and S. Tanishima, *Light's Labour's Lost*, International Energy Agency, Paris, 2006.

22 C. J. Humphreys, *MRS Bull.*, 2008, **33**, 459.

23 T. Tsujimura, *OLED Display Fundamentals and Application*, John Wiley & Sons Inc, 2012.

24 B. Geffroy, P. le Roy and C. Prat, *Polym. Int.*, 2006, **55**, 572.

25 A. Kahn, *Mater. Horizons*, 2016, **3**, 7.

26 G. M. Farinola and R. Ragni, *Chem. Soc. Rev.*, 2011, **40**, 3467.

27 R. Friend, R. Gymer and A. Holmes, *Nature*, 1999, **397**, 121.

28 C. W. Tang and S. A. Van Slyke, *Appl. Phys. Lett.*, 1987, **51**, 913.

29 J. H. Burroughes, D. D. C. Bradley, A. R. Brown, R. N. Marks, K. Mackay, R. H. Friend, P. L. Burns and A. B. Holmes, *Nature*, 1990, **347**, 539.

30 Y. Ohmori, M. Uchida, K. Muro and K. Yoshino, *Jpn. J. Appl. Phys.*, 1991, **30**, L1941.

31 M. Leclerc, *J. Polym. Sci. Part A Polym. Chem.*, 2001, **39**, 2867.

32 M. T. Bernius, M. Inbasekaran, J. O'Brien and W. Wu, *Adv. Mater.*, 2000, **12**, 1737.

33 V. N. Bliznyuk, S. A. Carter, J. C. Scott, G. Klärner, R. D. Miller and D. C. Miller, *Macromolecules*, 1999, **32**, 361.

34 Y.-J. Pu, M. Higashidate, K. Nakayama and J. Kido, *J. Mater. Chem.*, 2008, **18**, 4183.

35 H. Wang, Y. Xu, T. Tsuboi, H. Xu, Y. Wu, Z. Zhang, Y. Miao, Y. Hao, X. Liu, B. Xu and W. Huang, *Org. Electron.*, 2013, **14**, 827.

36 Y.-W. Su, S. Lan and K.-H. Wei, *Mater. Today*, 2012, **15**, 554.

37 K. A. Mazzio and C. K. Luscombe, *Chem. Soc. Rev.*, 2015, **44**, 78.

38 K. M. Pelzer and S. B. Darling, *Mol. Syst. Des. Eng.*, 2016, **1**, 10.

39 S. Günes, H. Neugebauer and N. S. Sariciftci, *Chem. Rev.*, 2007, **107**, 1324.

40 A. A. A. Moliton and J.-M. Nunzi, *Polym. Int.*, 2006, **55**, 583.

41 B. Kippelen and J.-L. Brédas, *Energy Environ. Sci.*, 2009, **2**, 241.

42 Y. Lin, Y. Li and X. Zhan, *Chem. Soc. Rev.*, 2012, **41**, 4245.

43 F. Wudl, *Acc. Chem. Res.*, 1992, **25**, 157.

44 C. J. Brabec, S. Gowrisanker, J. J. M. Halls, D. Laird, S. Jia and S. P. Williams, *Adv. Mater.*, 2010, **22**, 3839.

45 R. Po and J. Roncali, *J. Mater. Chem. C*, 2016, **4**, 3677.

46 Q. Zhang, B. Kan, F. Liu, G. Long, X. Wan, X. Chen, Y. Zuo, W. Ni, H. Zhang, M. Li, Z. Hu, F. Huang, Y. Cao, Z. Liang, M. Zhang, T. P. Russell and Y. Chen, *Nat. Photonics*, 2015, **9**, 35.

47 Q. Shi, P. Cheng, Y. Li and X. Zhan, *Adv. Energy Mater.*, 2012, **2**, 63.

48 S. Park, J. Jeong, G. Hyun, M. Kim, H. Lee and Y. Yi, *Sci. Rep.*, 2016, **6**, 35262.

49 W. Chen and Q. Zhang, *J. Mater. Chem. C*, 2017, **5**, 1275.

50 H. Kang, W. Lee, J. Oh, T. Kim, C. Lee and B. J. Kim, *Acc. Chem. Res.*, 2016, **49**, 2424.

51 Y. Lin, J. Wang, Z.-G. Zhang, H. Bai, Y. Li, D. Zhu and X. Zhan, *Adv. Mater.*, 2015, **27**, 1170.

52 S. Li, L. Ye, W. Zhao, S. Zhang, S. Mukherjee, H. Ade and J. Hou, *Adv. Mater.*, 2016, **28**, 9423.

53 H. Bin, Y. Yang, Z. G. Zhang, L. Ye, M. Ghasemi, S. Chen, Y. Zhang, C. Zhang, C. Sun, L. Xue, C. Yang, H. Ade and Y. Li, *J. Am. Chem. Soc.*, 2017, **139**, 5085.

54 O. A. Abdulrazzaq, V. Saini, S. Bourdo, E. Dervishi and A. S. Biris, *Part. Sci. Technol.*, 2013, **31**, 427.

55 W. Wang, H. Wu, C. Yang, C. Luo, Y. Zhang, J. Chen and Y. Cao, *Appl. Phys. Lett.*, 2007, **90**, 183512.

56 S. Zhang, L. Ye and J. Hou, *Adv. Energy Mater.*, 2016, **6**, 1.

57 Y. Liang, Z. Xu, J. Xia, S.-T. Tsai, Y. Wu, G. Li, C. Ray and L. Yu, *Adv. Mater.*, 2010, **22**, E135.

58 W. Zhao, L. Ye, S. Zhang, M. Sun and J. Hou, *J. Mater. Chem. A*, 2015, **3**,

12723.

59 L. Huo, S. Zhang, X. Guo, F. Xu, Y. Li and J. Hou, *Angew. Chem. Int. Ed. Engl.*, 2011, **50**, 9697.

60 S. Zhang, L. Ye, W. Zhao, D. Liu, H. Yao and J. Hou, *Macromolecules*, 2014, **47**, 4653.

61 J. Huang, J. H. Carpenter, C. Z. Li, J. S. Yu, H. Ade and A. K. Y. Jen, *Adv. Mater.*, 2016, **28**, 967.

62 W. Zhao, L. Ye, S. Zhang, H. Yao, M. Sun and J. Hou, *J. Phys. Chem. C*, 2015, **119**, 27322.

63 L. Ye, S. Zhang, W. Zhao, H. Yao and J. Hou, *Chem. Mater.*, 2014, **26**, 3603.

64 Z. Li, G. He, X. Wan, Y. Liu, J. Zhou, G. Long, Y. Zuo, M. Zhang and Y. Chen, *Adv. Energy Mater.*, 2012, **2**, 74.

65 A. J. Moulé, M.-C. Jung, C. W. Rochester, W. Tress, D. LaGrange, I. E. Jacobs, J. Li, S. A. Mauger, M. D. Rail, O. Lin, D. J. Bilsky, Y. Qi, P. Stroeve, L. A. Berben and M. Riede, *J. Mater. Chem. C*, 2015, **3**, 2664.

66 Y. H. Kim, J. Lee, S. Hofmann, M. C. Gather, L. Müller-Meskamp and K. Leo, *Adv. Funct. Mater.*, 2013, **23**, 3763.

67 Y. Xia, K. Sun and J. Ouyang, *Adv. Mater.*, 2012, **24**, 2436.

68 H.-W. Chang, Y. H. Kim, J. Lee, S. Hofmann, B. Lüssem, L. Müller-Meskamp, M. C. Gather, K. Leo and C.-C. Wu, *Org. Electron.*, 2014, **15**, 1028.

69 C. Adachi, T. Tsutsui and S. Saito, *Appl. Phys. Lett.*, 1989, **55**, 1489.

70 S. A. Van Slyke, C. H. Chen and C. W. Tang, *Appl. Phys. Lett.*, 1996, **69**, 2160.

71 L. Duan, L. Hou, T.-W. Lee, J. Qiao, D. Zhang, G. Dong, L. Wang and Y. Qiu, *J. Mater. Chem.*, 2010, **20**, 6392.

72 C. Zhong, C. Duan, F. Huang, H. Wu and Y. Cao, *Chem. Mater.*, 2011, **23**, 326.

73 Y. Shirota, *J. Mater. Chem.*, 2000, **10**, 1.

74 Y. Shirota and H. Kageyama, *Chem. Rev.*, 2007, **107**, 953.

75 J. Salbeck, N. Yu, J. Bauer, F. Weissörtel and H. Bestgen, *Synth. Met.*, 1997, **91**, 209.

76 J. Lian, Y. Yuan, L. Cao, J. Zhang, H. Pang, Y. Zhou and X. Zhou, *J. Lumin.*, 2007, **122**–**123**, 660.

77 A. P. Kulkarni, C. J. Tonzola, A. Babel and S. A. Jenekhe, *Chem. Mater.*, 2004, **16**, 4556.

78 A. R. Brown, D. D. C. Bradley, J. H. Burroughes, R. H. Friend, N. C. Greenham, P. L. Burn, A. B. Holmes and A. Kraft, *Appl. Phys. Lett.*, 1992, **61**, 2793.

79 A. Kraft, A. C. Grimsdale and A. B. Holmes, *Angew. Chem. Int. Ed. Engl.*, 1998, **37**, 402.

80 D. O'Brien, M. S. Weaver, D. G. Lidzey and D. D. C. Bradley, *Appl. Phys. Lett.*, 1996, **69**, 881.

81 S. B. Heidenhain, Y. Sakamoto, T. Suzuki, A. Miura, H. Fujikawa, T. Mori, S. Tokito and Y. Taga, *J. Am. Chem. Soc.*, 2000, **122**, 10240.

82 M. Ikai, S. Tokito, Y. Sakamoto, T. Suzuki and Y. Taga, *Appl. Phys. Lett.*, 2001, **79**, 156.

83 S. Forrest, *Nature*, 2004, **428**, 911.

84 S. K. Park, T. N. Jackson, J. E. Anthony and D. A. Mourey, *Appl. Phys. Lett.*, 2007, **91**, 63514.

85 H. Sirringhaus, T. Kawase, R. H. Friend, T. Shimoda, M. Inbasekaran, W. Wu and E. P. Woo, *Science*, 2000, **290**, 2123.

86 R. Søndergaard, M. Hösel, D. Angmo, T. T. Larsen-Olsen and F. C. Krebs, *Mater. Today*, 2012, **15**, 36.

87 C. D. Müller, A. Falcou, N. Reckefuss, M. Rojahn, V. Wiederhirn, P. Rudati, H. Frohne, O. Nuyken, H. Becker and K. Meerholz, *Nature*, 2003, **421**, 829.

88 N. Thejo Kalyani and S. J. Dhoble, *Renew. Sustain. Energy Rev.*, 2015, **44**, 319.

89 J. Ahmad, K. Bazaka, L. J. Anderson, R. D. White and M. V. Jacob, *Renew. Sustain. Energy Rev.*, 2013, **27**, 104.

90 D. Yu, Y.-Q. Yang, Z. Chen, Y. Tao and Y.-F. Liu, *Opt. Commun.*, 2016, **362**, 43.

91 P. Le Rendu, T. P. Nguyen and L. Carrois, *Synth. Met.*, 2003, **138**, 285.

92 C. A. Gedelian, Y. Ou, H. Li and T.-M. Lu, *Thin Solid Films*, 2010, **518**, 4367.

93 A. L. Kanibolotsky, I. F. Perepichka and P. J. Skabara, *Chem. Soc. Rev.*, 2010, **39**, 2695.

94 M. M. Oliva, J. Casado, J. T. L. Navarrete, R. Berridge, P. J. Skabara, A. L. Kanibolotsky and I. F. Perepichka, *J. Phys. Chem. B*, 2007, **111**, 4026.

95 K. Shi, J.-Y. Wang and J. Pei, *Chem. Rec.*, 2015, **15**, 52.

96 B. Gómez-Lor, Ó. de Frutos and A. M. Echavarren, *Chem. Commun.*, 1999, **23**, 2431.

97 A. H. Abdourazak, Z. Marcinow, A. Sygula, R. Sygula and P. W. Rabideau, *J. Am. Chem. Soc.*, 1995, **117**, 6410.

98 E. V. Dehmlow and T. Kelle, *Synth. Commun.*, 1997, **27**, 2021.

99 H.-L. Ni, H. Monobe, P. Hu, B.-Q. Wang, Y. Shimizu and K.-Q. Zhao, *Liq. Cryst.*, 2013, **40**, 411.

100 F. Goubard and F. Dumur, *RSC Adv.*, 2015, **5**, 3521.

101 A. W. Amick and L. T. Scott, *J. Org. Chem.*, 2007, **72**, 3412.

102 X. Mao, Z. Ma, Y. Yang, S. Lei, C. Wang and W. Huang, *Front. Mater. Sci. China*, 2008, **2**, 26.

103 M.-T. Kao, J.-H. Chen, Y.-Y. Chu, K.-P. Tseng, C.-H. Hsu, K.-T. Wong, C.-W. Chang, C.-P. Hsu and Y.-H. Liu, *Org. Lett.*, 2011, **13**, 1714.

104 E. González-Cantalapiedra, M. Ruiz, B. Gómez-Lor, B. Alonso, D. García-Cuadrado, D. J. Cárdenas and A. M. Echavarren, *European J. Org. Chem.*, 2005, 4127.

105 X. Y. Cao, W. Zhang, H. Zi and J. Pei, *Org. Lett.*, 2004, **6**, 4845.

106 J. Pei, J.-L. Wang, X.-Y. Cao, X.-H. Zhou and W.-B. Zhang, *J. Am. Chem. Soc.*, 2003, **125**, 9944.

107 Y. M. Sun, K. Xiao, Y. Q. Liu, J. L. Wang, J. Pei, G. Yu and D. B. Zhu, *Adv. Funct. Mater.*, 2005, **15**, 818.

108 A. L. Kanibolotsky, R. R. Berridge, P. J. Skabara, I. F. Perepichka, D. D. C. Bradley and M. Koeberg, *J. Am. Chem. Soc.*, 2004, **126**, 13695.

109 G. Tsiminis, Y. Wang, P. E. Shaw, A. L. Kanibolotsky, I. F. Perepichka, M. D. Dawson, P. J. Skabara, G. A. Turnbull and I. D. W. Samuel, *Appl. Phys. Lett.*, 2009, **94**, 243304.

110 Y. Wang, G. Tsiminis, Y. Yang, A. Ruseckas, A. L. Kanibolotsky, I. F. Perepichka, P. J. Skabara, G. A. Turnbull and I. D. W. Samuel, *Synth. Met.*, 2010, **160**, 1397.

111 G. Heliotis, D. D. C. Bradley, G. A. Turnbull and I. D. W. Samuel, *Appl. Phys. Lett.*, 2002, **81**, 415.

112 G. Heliotis, R. Xia, G. A. Turnbull, P. Andrew, W. L. Barnes, I. D. W. Samuel and D. D. C. Bradley, *Adv. Funct. Mater.*, 2004, **14**, 91.

113 A.-M. Haughey, B. Guilhabert, A. L. Kanibolotsky, P. J. Skabara, M. D. Dawson, G. A. Burley and N. Laurand, *Biosens. Bioelectron.*, 2013, **54C**, 679.

114 C. R. Belton, A. L. Kanibolotsky, J. Kirkpatrick, C. Orofino, S. E. T. Elmasly, P. N. Stavrinou, P. J. Skabara and D. D. C. Bradley, *Adv. Funct. Mater.*, 2013, **23**, 2792.

115 S. Diring, F. Puntoriero, F. Nastasi, S. Campagna and R. Ziessel, *J. Am. Chem. Soc.*, 2009, **131**, 6108.

116 H.-J. Xu, A. Bonnot, P.-L. Karsenti, A. Langlois, M. Abdelhameed, J.-M. Barbe, C. P. Gros and P. D. Harvey, *Dalt. Trans.*, 2014, **43**, 8219.

117 C. Huang, W. Fu, C.-Z. Li, Z. Zhang, W. Qiu, M. Shi, P. Heremans, A. K.-Y. Jen and H. Chen, *J. Am. Chem. Soc.*, 2016, **138**, 2528.

118 K.-H. Lin, A. Prlj and C. Corminboeuf, *J. Phys. Chem. C*, 2017, **121**, 21729.

119 J. Wang, Y. Chen, M. Liang, G. Ge, R. Zhou, Z. Sun and S. Xue, *Dye. Pigment.*, 2016, **125**, 399.

120 M. Kimura, S. Kuwano, Y. Sawaki, H. Fujikawa, K. Noda, Y. Taga and K. Takagi, *J. Mater. Chem.*, 2005, **15**, 2393.

121 K.-P. Tseng, M.-T. Kao, T. W. T. Tsai, C.-H. Hsu, J. C. C. Chan, J.-J. Shyue, S.-S. Sun and K.-T. Wong, *Chem. Commun.*, 2012, **48**, 3515.

122 Ó. de Frutos, T. Granier, B. Gómez-Lor, J. Jiménez-Barbero, Á. Monge, E. Gutiérrez-Puebla and A. M. Echavarren, *Chem. - A Eur. J.*, 2002, **8**, 2879.

123 Ó. de Frutos, B. Gómez-Lor, T. Granier, M. Á. Monge, E. Gutiérrez-Puebla and A. M. Echavarren, *Angew. Chem. Int. Ed. Engl.*, 1999, **38**, 204.

124 B. Gómez-Lor, Ó. de Frutos, P. A. Ceballos, T. Granier and A. M. Echavarren, *European J. Org. Chem.*, 2001, 2107.

125 J. Luo, T. Lei, L. Wang, Y. Ma, Y. Cao, J. Wang and J. Pei, *J. Am. Chem. Soc.*, 2009, **131**, 2076.

126 T. Lei, C.-Y. Cheng, Z.-H. Guo, C. Zheng, Y. Zhou, D. Liang and J. Pei, *J. Mater. Chem.*, 2012, **22**, 4306.

127 J. Yang, D. Yan and T. S. Jones, *Chem. Rev.*, 2015, **115**, 5570.

128 H. Ishii, K. Kudo, T. Nakayama and N. Ueno, Eds., *Electronic Processes in Organic Electronics*, Springer Japan, Tokyo, 2014, vol. 209.

129 B. E. Lassiter, R. R. Lunt, C. K. Renshaw and S. R. Forrest, *Opt. Express*, 2010, **18**, A444.

130 A. Hinderhofer and F. Schreiber, *ChemPhysChem*, 2012, **13**, 628.

131 C. Orofino-Peña and P. J. Skabara, *Unpublished work*, University of McGill, 2012.

132 N. A. Wasio, R. C. Quardokus, R. P. Forrest, C. S. Lent, S. A. Corcelli, J. A. Christie, K. W. Henderson and S. A. Kandel, *Nature*, 2014, **507**, 86.

133 Y. Makoudi, M. Beyer, J. Jeannoutot, F. Picaud, F. Palmino and F. Chérioux, *Chem. Commun.*, 2014, **50**, 5714.

134 M. T. Nguyen, D. Sengupta, G. Raspoet and L. G. Vanquickenborne, *J. Phys. Chem.*, 1995, **99**, 11883.

135 W. Zhao, T. Cao and J. M. White, *Adv. Funct. Mater.*, 2004, **14**, 783.

136 R. Grisorio, G. Allegretta, P. Mastrorilli and G. P. Suranna, *Macromolecules*, 2011, **44**, 7977.

137 L. Rajput, N. Jana and K. Biradha, *Cryst. Growth Des.*, 2010, **10**, 4565.

138 S. Diring and R. Ziessel, *Tetrahedron Lett.*, 2009, **50**, 1203.

139 D. Wang, J. M. Schlegel and E. Galoppini, *Tetrahedron*, 2002, **58**, 6027.

140 B. Czako and L. Kurti, *Strategic Applications of Named Reactions in Organic Synthesis*, Elsevier Academic Press, Oxford, 1st edn., 2005.

141 I. D. W. Samuel and G. A. Turnbull, *Chem. Rev.*, 2007, **107**, 1272.

142 J. J. Shie and J. M. Fang, *J. Org. Chem.*, 2003, **68**, 1158.

143 M. Cariello, S. Ahn, K.-W. Park, S.-K. Chang, J. Hong and G. Cooke, *RSC Adv.*, 2016, **6**, 9132.

144 A. R. Morales, A. Frazer, A. W. Woodward, H. Y. Ahn-White, A. Fonari, P. Tongwa, T. Timofeeva and K. D. Belfield, *J. Org. Chem.*, 2013, **78**, 1014.

145 N. Kraußе, M. Kielmann, J. Ma and H. Butenschön, *European J. Org. Chem.*, 2015, 2622.

146 A. R. Lacy, A. Vogt, C. Boudon, J. P. Gisselbrecht, W. B. Schweizer and F. Diederich, *European J. Org. Chem.*, 2013, 869.

147 M. Kivala, C. Boudon, J. P. Gisselbrecht, P. Seiler, M. Gross and F. Diederich, *Angew. Chem. Int. Ed. Engl.*, 2007, **46**, 6357.

148 Solvent Polarity in Gaussian, http://wild.life.nctu.edu.tw/~jsyu/compchem/g09/g09ur/k_scrf.htm, Accessed: 7 June 2017.

149 G. V. Baryshnikov, S. V. Bondarchuk, V. A. Minaeva, H. Ågren and B. F. Minaev, *J. Mol. Model.*, 2017, **23**, 1.

150 C. Tresse, C. Guissart, S. Schweizer, Y. Bouhoute, A. C. Chany, M. L. Goddard, N. Blanchard and G. Evano, *Adv. Synth. Catal.*, 2014, **356**, 2051.

151 L. He and G. C. Tsui, *Org. Lett.*, 2016, **18**, 2800.

152 T. Shoji, S. Ito, T. Okujima and N. Morita, *Org. Biomol. Chem.*, 2012, **10**, 8308.

153 B. B. Frank, M. Kivala, B. Camafort Blanco, B. Breiten, W. B. Schweizer, P. R. Laporta, I. Biaggio, E. Jahnke, R. R. Tykwinski, C. Boudon, J.-P. Gisselbrecht and F. Diederich, *European J. Org. Chem.*, 2010, 2487.

154 F. I. Wu, D. S. Reddy, C. F. Shu, M. S. Liu and A. K. Y. Jen, *Chem. Mater.*, 2003, **15**, 269.

155 H. E. Gottlieb, V. Kotlyar and A. Nudelman, *J. Org. Chem.*, 1997, **62**, 7512.

156 I. Horcas, R. Fernández, J. M. Gómez-Rodríguez, J. Colchero, J. Gómez-Herrero, A. M. Baro, R. Fernandez, J. M. Gomez-Rodriguez, J. Colchero, J. Gomez-Herrero and A. M. Baro, *Rev. Sci. Instrum.*, 2007, **78**, 13705.

157 Y. N. Oded and I. Agranat, *Tetrahedron Lett.*, 2014, **55**, 636.

158 Y. Kim, S. Das, S. Bhattacharya, S. Hong, M. G. Kim, M. Yoon, S. Natarajan and K. Kim, *Chem. - A Eur. J.*, 2012, **18**, 16642.

159 M.-S. Yuan, Q. Fang, Z.-Q. Liu, J. Guo, H.-Y. Chen, W.-T. Yu, G. Xue and D.-S. Liu, *J. Org. Chem.*, 2006, **71**, 7858.

160 L. Liu and S. G. Telfer, *J. Am. Chem. Soc.*, 2015, **137**, 3901.

161 H. Zhou, X. Zhao, T. Huang, R. Lu, H. Zhang, X. Qi, P. Xue, X. Liu and X. Zhang, *Org. Biomol. Chem.*, 2011, **9**, 1600.

162 S. Das, H. Kim and K. Kim, *J. Am. Chem. Soc.*, 2009, **131**, 3814.

163 Q. Zheng, G. S. He and P. N. Prasad, *Chem. Mater*., 2005, **17**, 6004.

164 D. Raksasorn, S. Namuangruk, N. Prachumrak, T. Sudyoadsuk, V. Promarak, M. Sukwattanasinitt and P. Rashatasakhon, *RSC Adv.*, 2015, **5**, 72841.

165 G. J. Bodwell, D. O. Miller and R. J. Vermeij, *Org. Lett.*, 2001, **3**, 2093.

166 X. Wang, Y. Wang, H. Yang, H. Fang, R. Chen, Y. Sun, N. Zheng, K. Tan, X. Lu, Z. Tian and X. Cao, *Nat. Commun.*, 2016, **7**, 12469.

167 S. C. Yuan, H. B. Chen, Y. Zhang and J. Pei, *Org. Lett.*, 2006, **8**, 5701.

9 APPENDICES

9.1 NMRs of final compounds

Compound 2.10

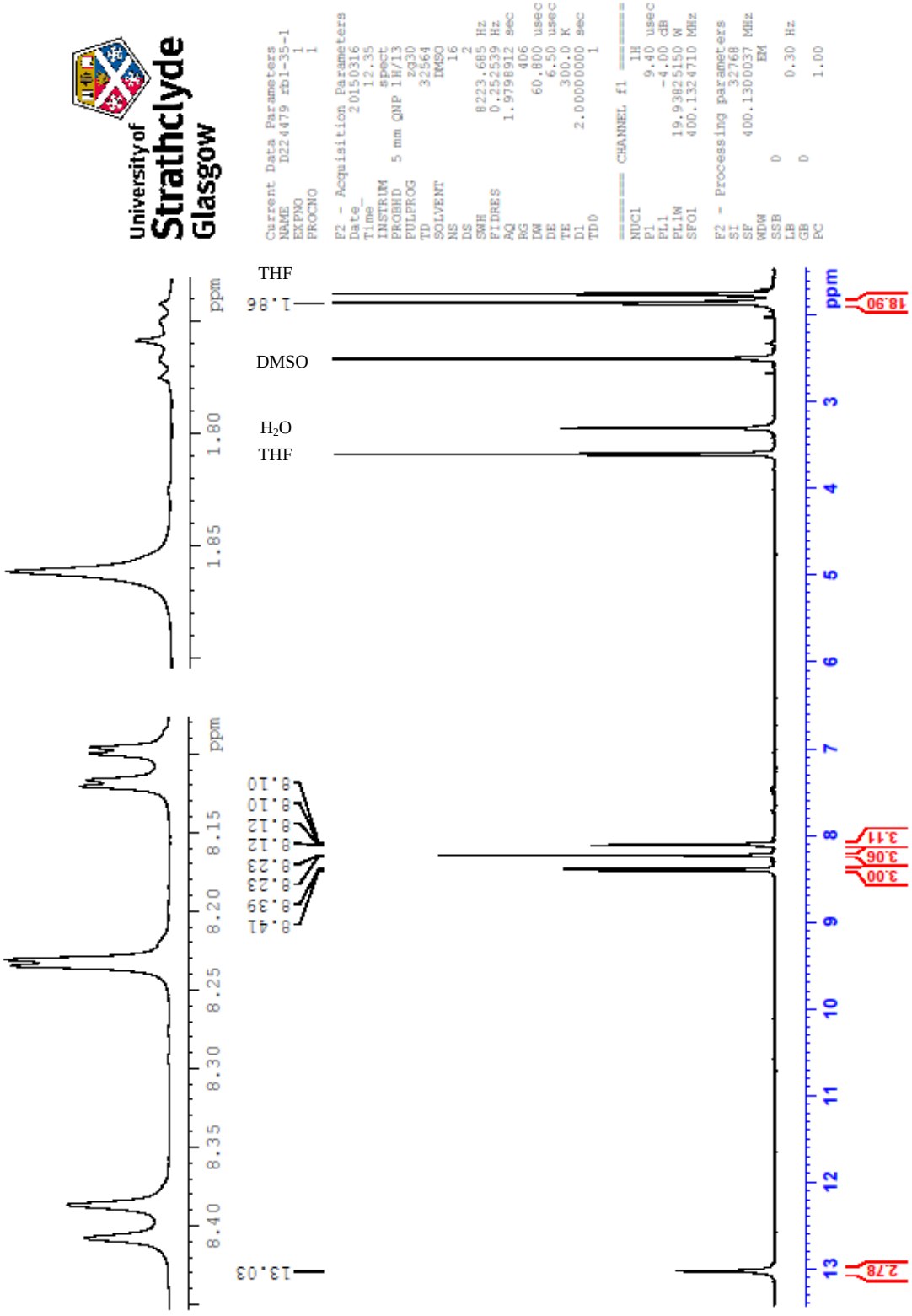

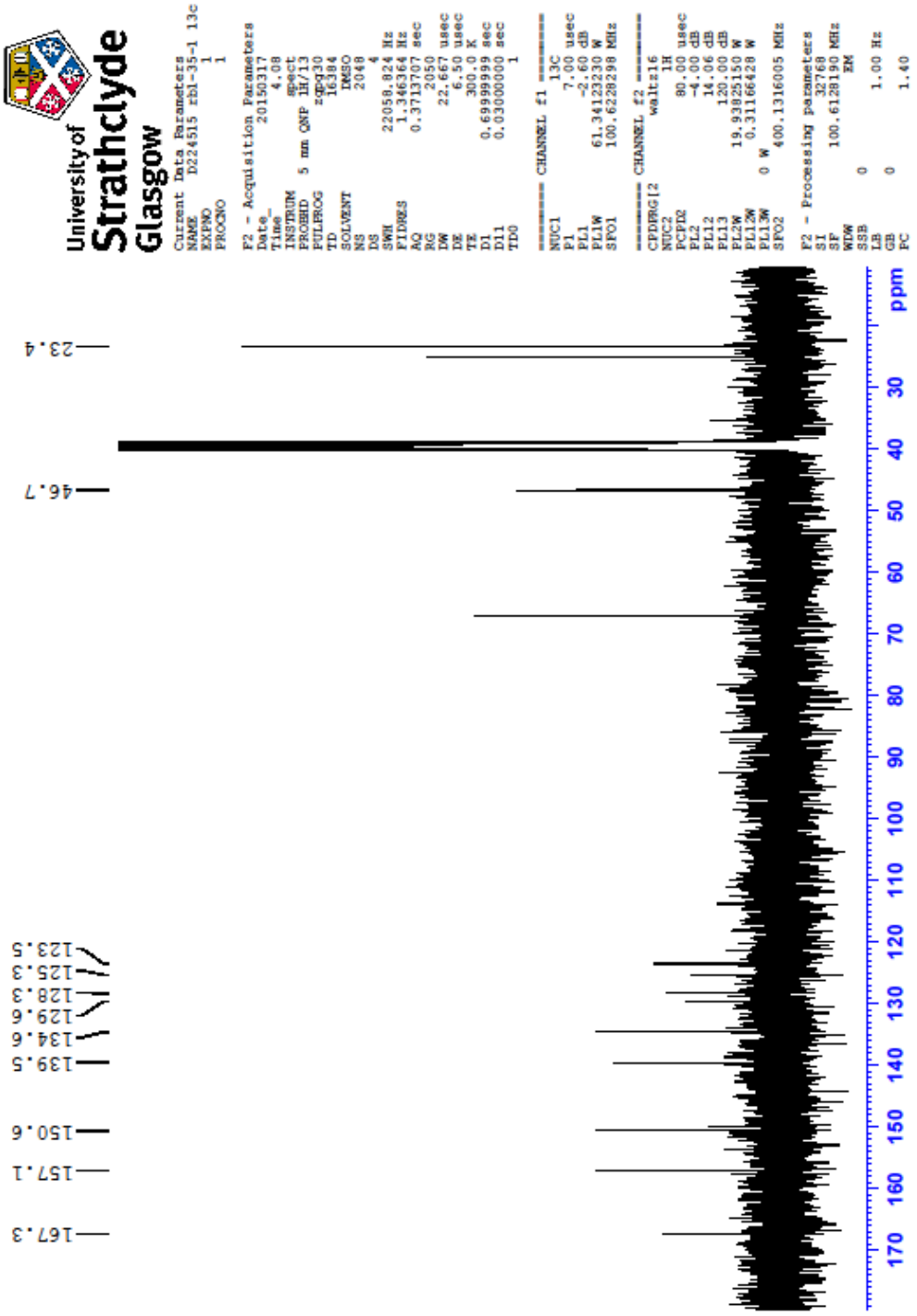
University of Strathclyde Glasgow
Current Data Parameters
NAME D224515 tbl-35-1 13c
EXPNO 1
PROCNO 1
F2 - Acquisition Parameters
Date_ 20150317
Time 4.08
INSTRUM spect
PROBHD 5 mm QNP 1H/13
PULPROG zgpg30
TD 16384
SOLVENT DMSO
NS 2048
DS 4
SWH 22058.824 Hz
FIDRES 1.346364 Hz
AQ 0.37137707 sec
RG 2050
DW 22.667 usec
DE 6.50 usec
TE 300.0 K
D1 0.69999999 sec
D11 0.03000000 sec
TD0 1
======== CHANNEL f1 ========
NUC1 13C
P1 7.00 usec
PL1 -2.60 dB
PL1W 61.34123230 W
SFO1 100.6228298 MHz
======== CHANNEL f2 ========
CPDPRG[2 waltz16
NUC2 1H
PCPD2 80.00 usec
PL2 -4.00 dB
PL12 14.06 dB
PL13 120.00 dB
PL2W 19.93825150 W
PL12W 0.31166428 W
PL13W 0 W
SFO2 400.1316005 MHz
F2 - Processing parameters
SI 32768
SF 100.6128190 MHz
WDW EM
SSB 0
LB 1.00 Hz
GB 0
PC 1.40
23.4
46.7
123.5
125.3
128.3
129.6
134.6
139.5
150.6
157.1
167.3
ppm
30
40
50
60
70
80
90
100
110
120
130
140
150
160
170

Compound 2.11

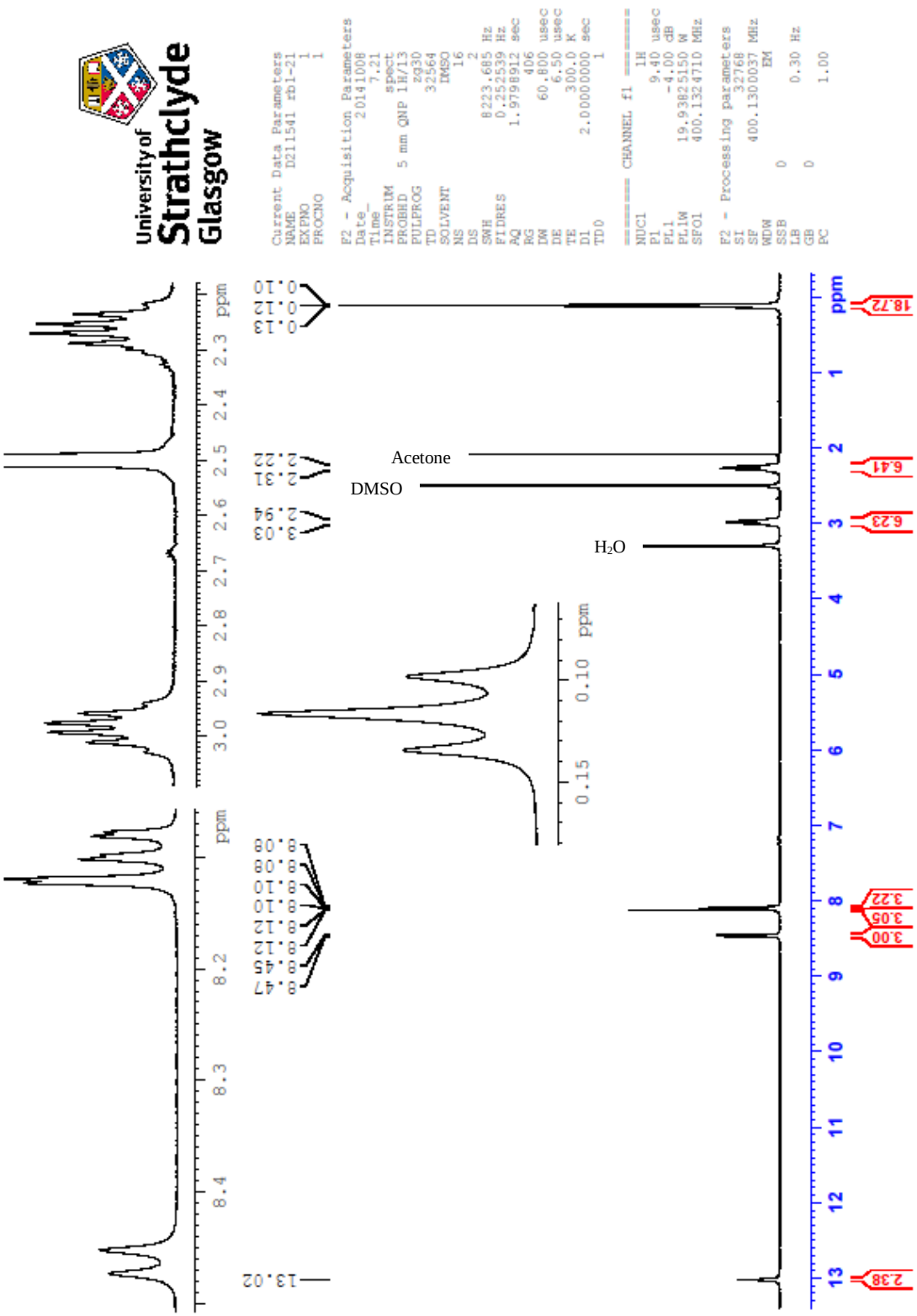

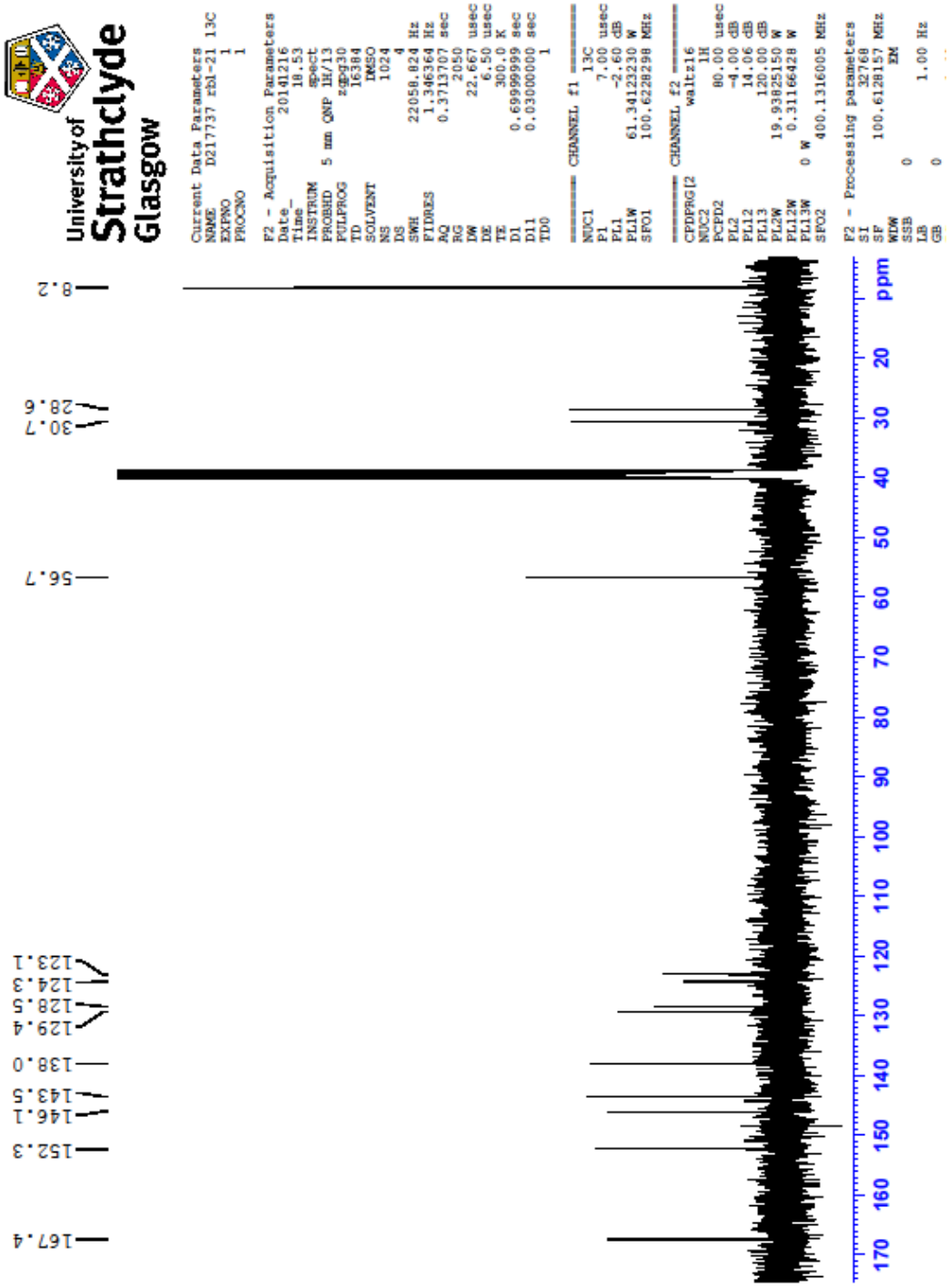
University of Strathclyde Glasgow
Current Data Parameters
NAME D217737 rbl-21 13C
EXPNO 1
PROCNO 1
F2 - Acquisition Parameters
Date_ 20141216
Time 18.53
INSTRUM spect
PROBHD 5 mm QNP 1H/13
PULPROG zgpg30
TD 16384
SOLVENT DMSO
NS 1024
DS 4
SWH 22058.824 Hz
FIDRES 1.346364 Hz
AQ 0.3713707 sec
RG 2050
DW 22.667 usec
DE 6.50 usec
TE 300.0 K
D1 0.69999999 sec
D11 0.03000000 sec
TD0 1
CHANNEL f1
NUC1 13C
P1 7.00 usec
PL1 -2.60 dB
PL1W 61.34123230 W
SFO1 100.6228298 MHz
CHANNEL f2
CPDPRG[2 waltz16
NUC2 1H
PCPD2 80.00 usec
PL2 -4.00 dB
PL12 14.06 dB
PL13 120.00 dB
PL2W 19.93825150 W
PL12W 0.31166428 W
PL13W 0 W
SFO2 400.1316005 MHz
F2 - Processing parameters
SI 32768
SF 100.6128157 MHz
WDW EM
SSB 0
LB 1.00 Hz
GB 0
8.2
28.6
30.7
56.7
123.1
124.3
128.5
129.4
138.0
143.5
146.1
152.3
167.4
ppm

Compound 2.12

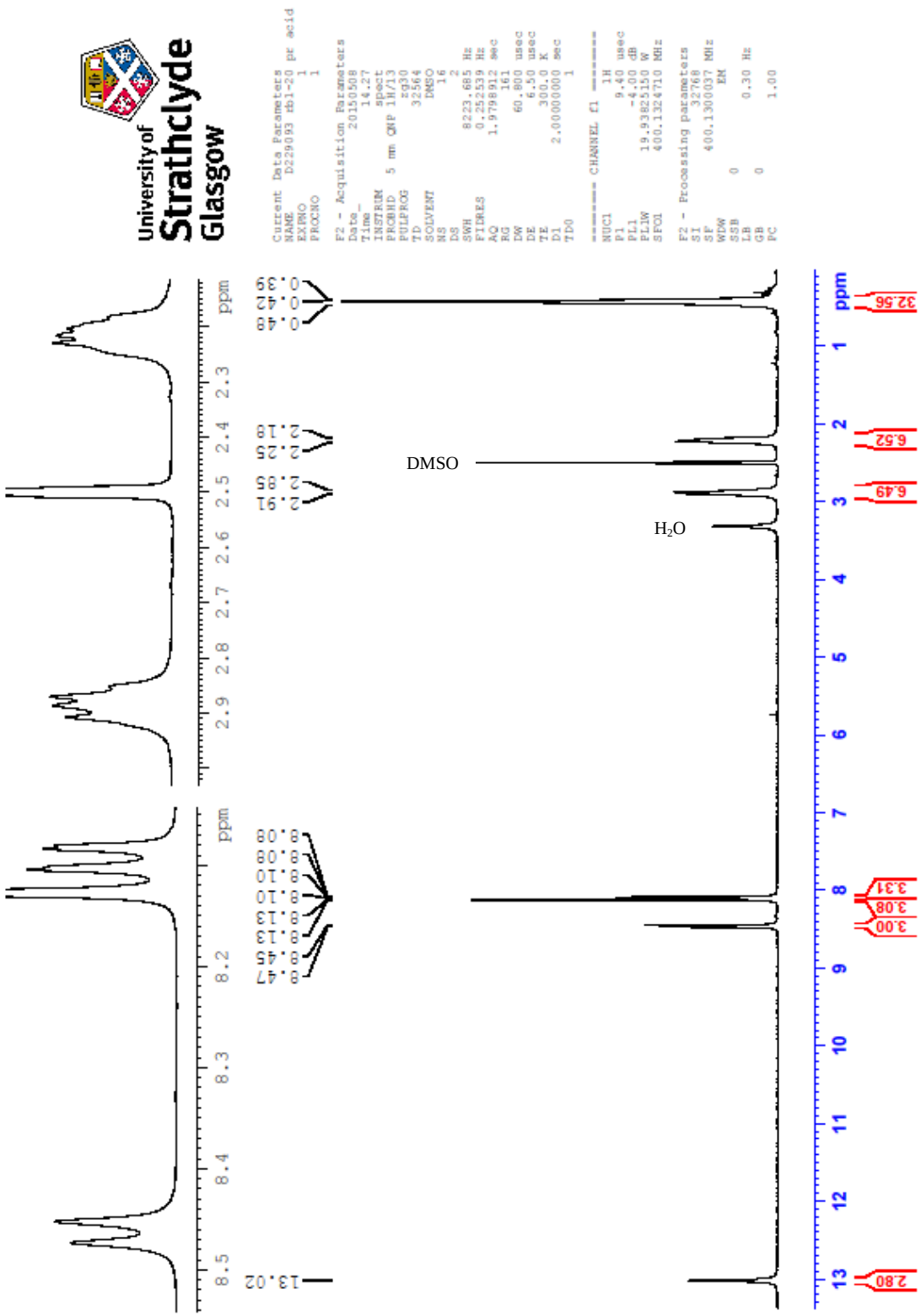

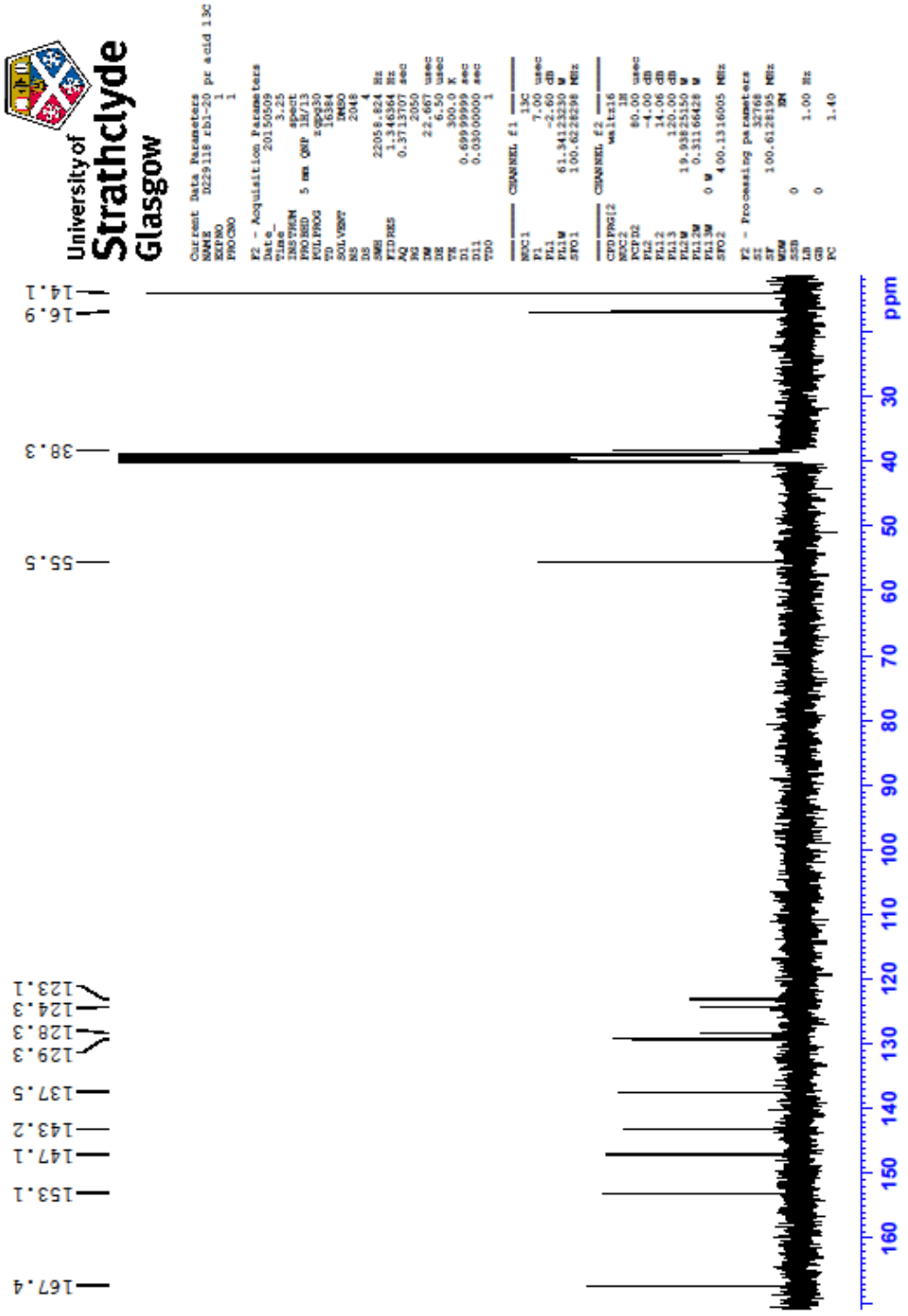
University of Strathclyde Glasgow
Current Data Parameters
F2 - Acquisition Parameters
F2 - Processing parameters
CHANNEL f1
CHANNEL f2
14.1
16.9
38.3
55.5
123.1
124.3
128.3
129.3
137.5
143.2
147.1
153.1
167.4
ppm

Compound 2.13

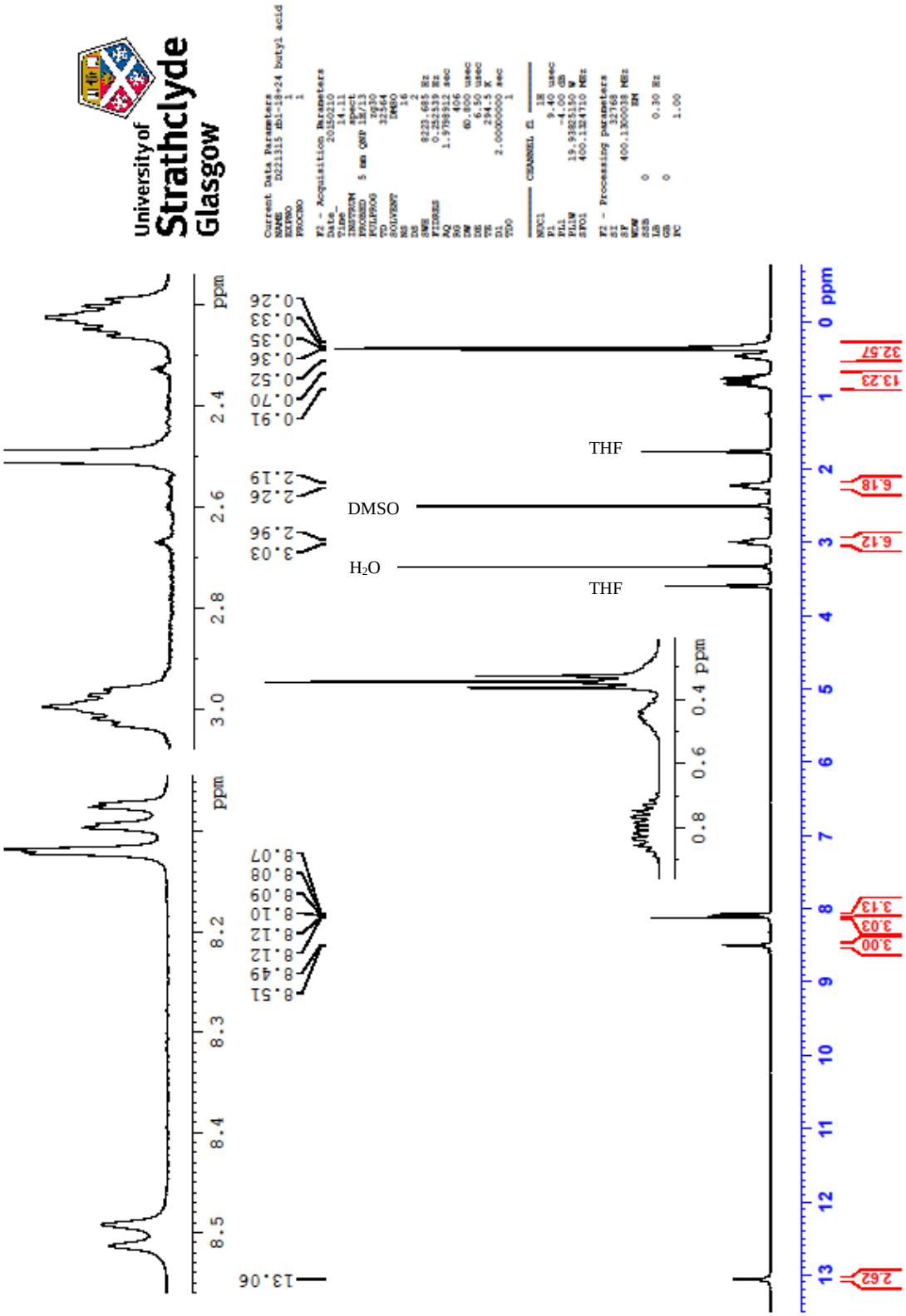

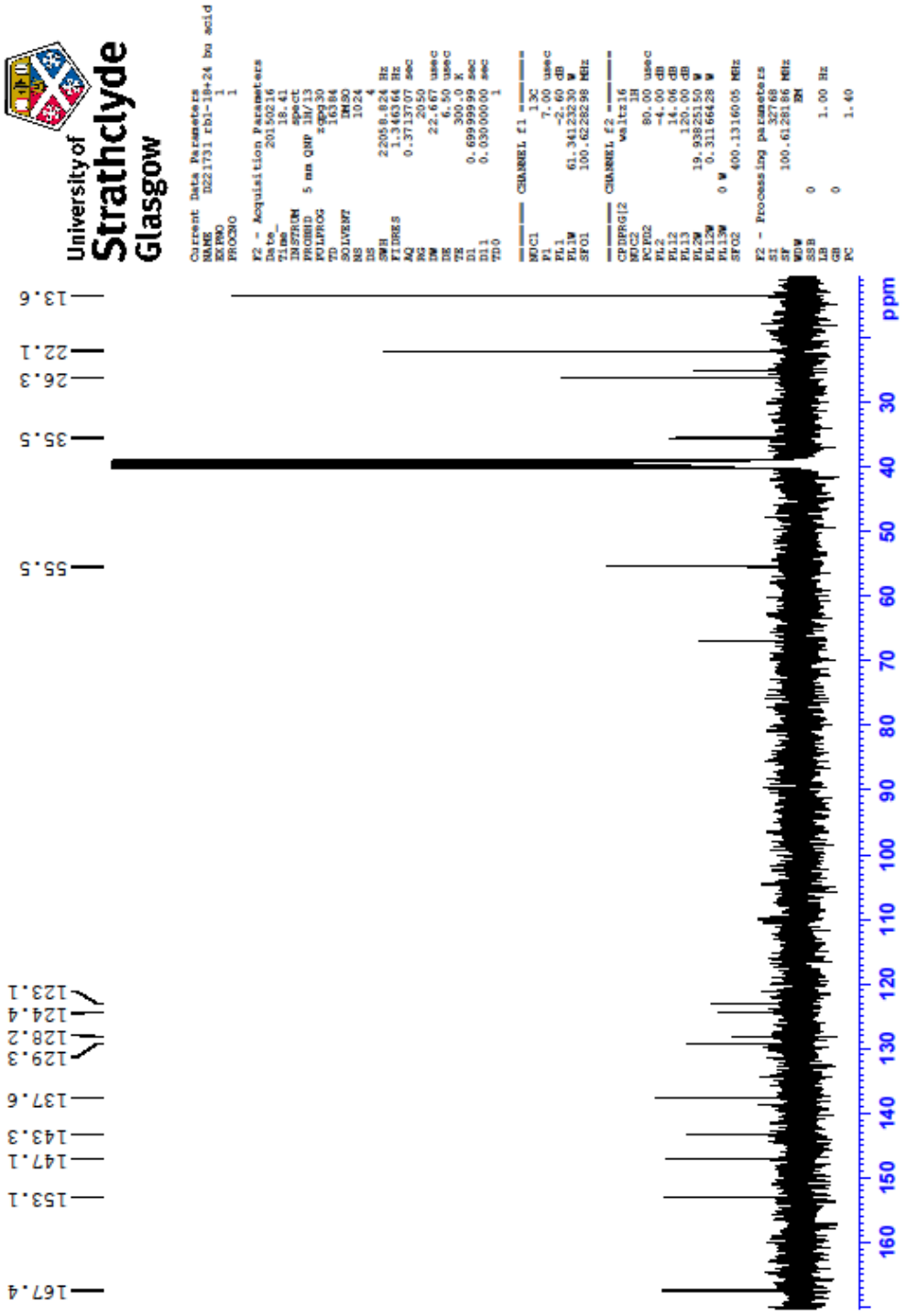
University of Strathclyde Glasgow
13.6
22.1
26.3
35.5
55.5
123.1
124.4
128.2
129.3
137.6
143.3
147.1
153.1
167.4
ppm

Compound 4.4

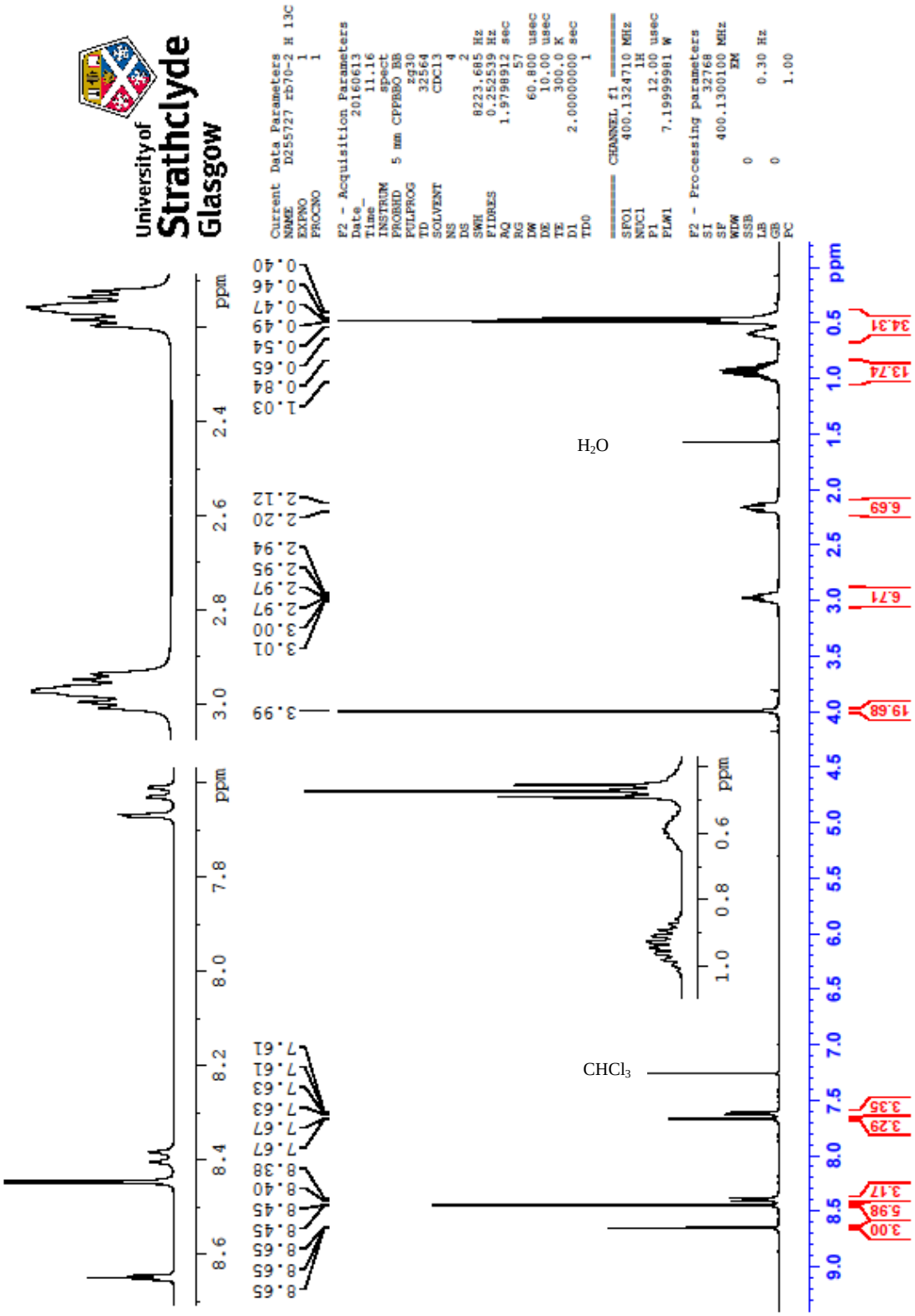

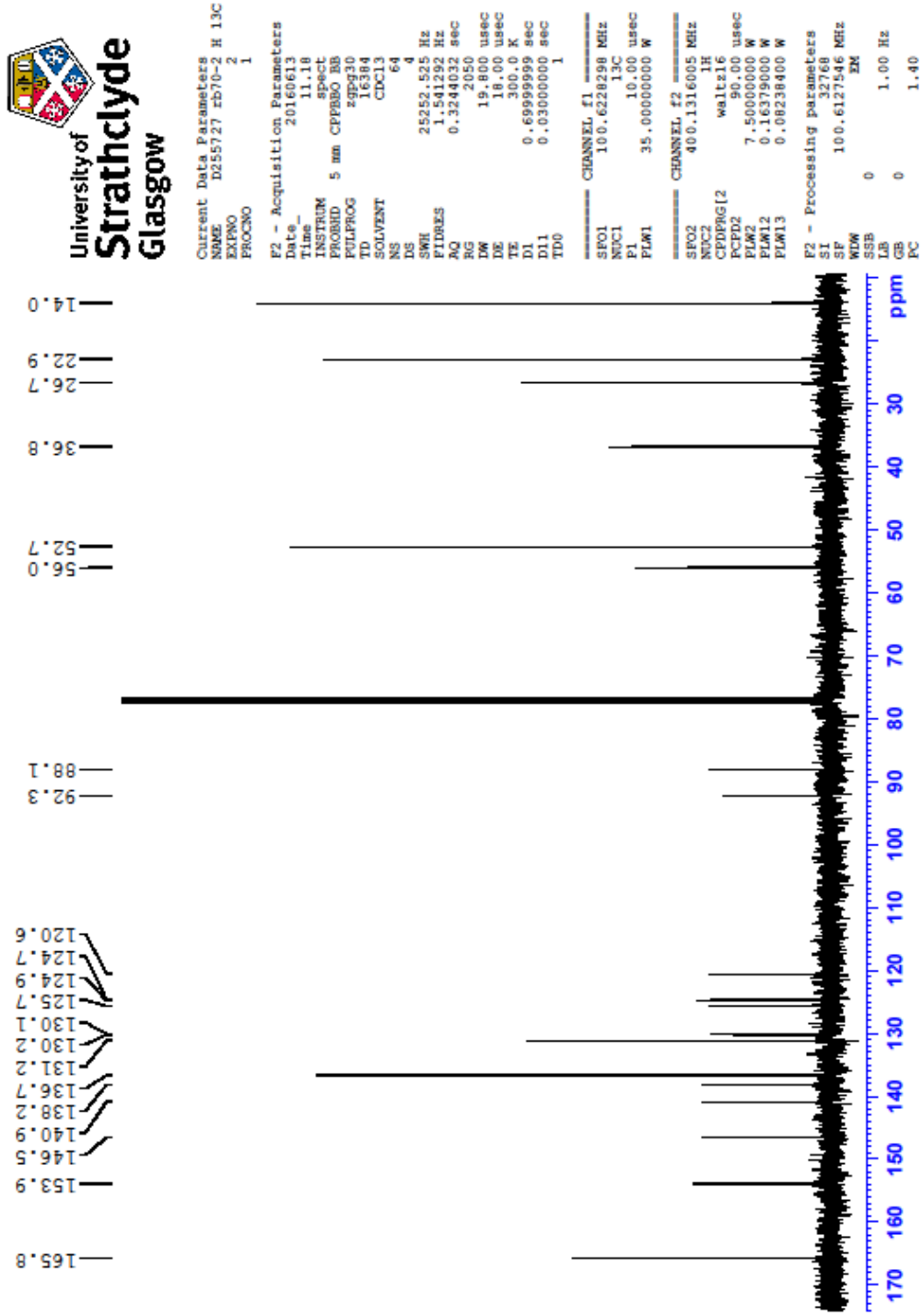
University of Strathclyde Glasgow
Current Data Parameters
NAME D255727 zb70-2 H 13C
EXPNO 2
PROCNO 1
F2 - Acquisition Parameters
Date_ 20160613
Time 11.18
INSTRUM spect
PROBHD 5 mm CPPBBO BB
PULPROG zgpg30
TD 16384
SOLVENT CDCl3
NS 64
DS 4
SWH 25252.525 Hz
FIDRES 1.541292 Hz
AQ 0.3244032 sec
RG 2050
DW 19.800 usec
DE 18.00 usec
TE 300.0 K
D1 0.69999999 sec
D11 0.03000000 sec
TD0 1
CHANNEL f1
SFO1 100.6228298 MHz
NUC1 13C
P1 10.00 usec
PLW1 35.00000000 W
CHANNEL f2
SFO2 400.1316005 MHz
NUC2 1H
CPDPRG[2 waltz16
PCPD2 90.00 usec
PLW2 7.50000000 W
PLW12 0.16379000 W
PLW13 0.08238400 W
F2 - Processing parameters
SI 32768
SF 100.6127546 MHz
WDW EM
SSB 0
LB 1.00 Hz
GB 0
PC 1.40
14.0
22.9
26.7
36.8
52.7
56.0
88.1
92.3
120.6
124.7
124.9
125.7
130.1
130.2
131.2
136.7
138.2
140.9
146.5
153.9
165.8
ppm
30
40
50
60
70
80
90
100
110
120
130
140
150
160
170

Compound 5.2

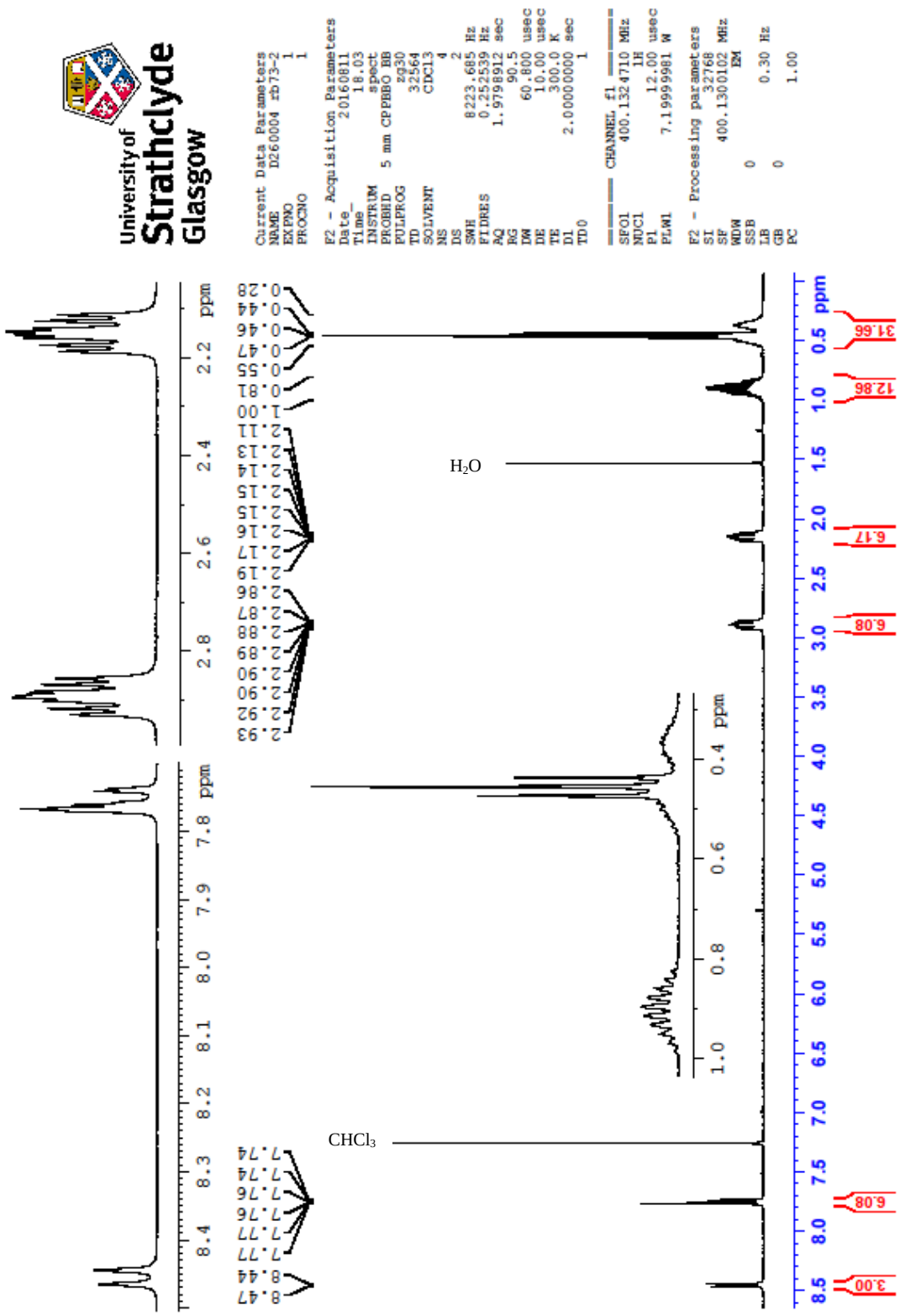
University of Strathclyde Glasgow
Current Data Parameters
NAME D260004 rb73-2
EXPNO 1
PROCNO 1
F2 - Acquisition Parameters
Date_ 20160811
Time 18.03
INSTRUM spect
PROBHD 5 mm CPPBBO BB
PULPROG zg30
TD 32564
SOLVENT CDCl3
NS 4
DS 2
SWH 8223.685 Hz
FIDRES 0.252539 Hz
AQ 1.9798912 sec
RG 90.5
DW 60.800 usec
DE 10.00 usec
TE 300.0 K
D1 2.00000000 sec
TD0 1
CHANNEL f1
SFO1 400.1324710 MHz
NUC1 1H
P1 12.00 usec
PLW1 7.19999981 W
F2 - Processing parameters
SI 32768
SF 400.1300102 MHz
WDW EM
SSB 0
LB 0.30 Hz
GB 0
PC 1.00
H2O
CHCl3
31.66
12.86
6.17
6.08
6.08
3.00
ppm

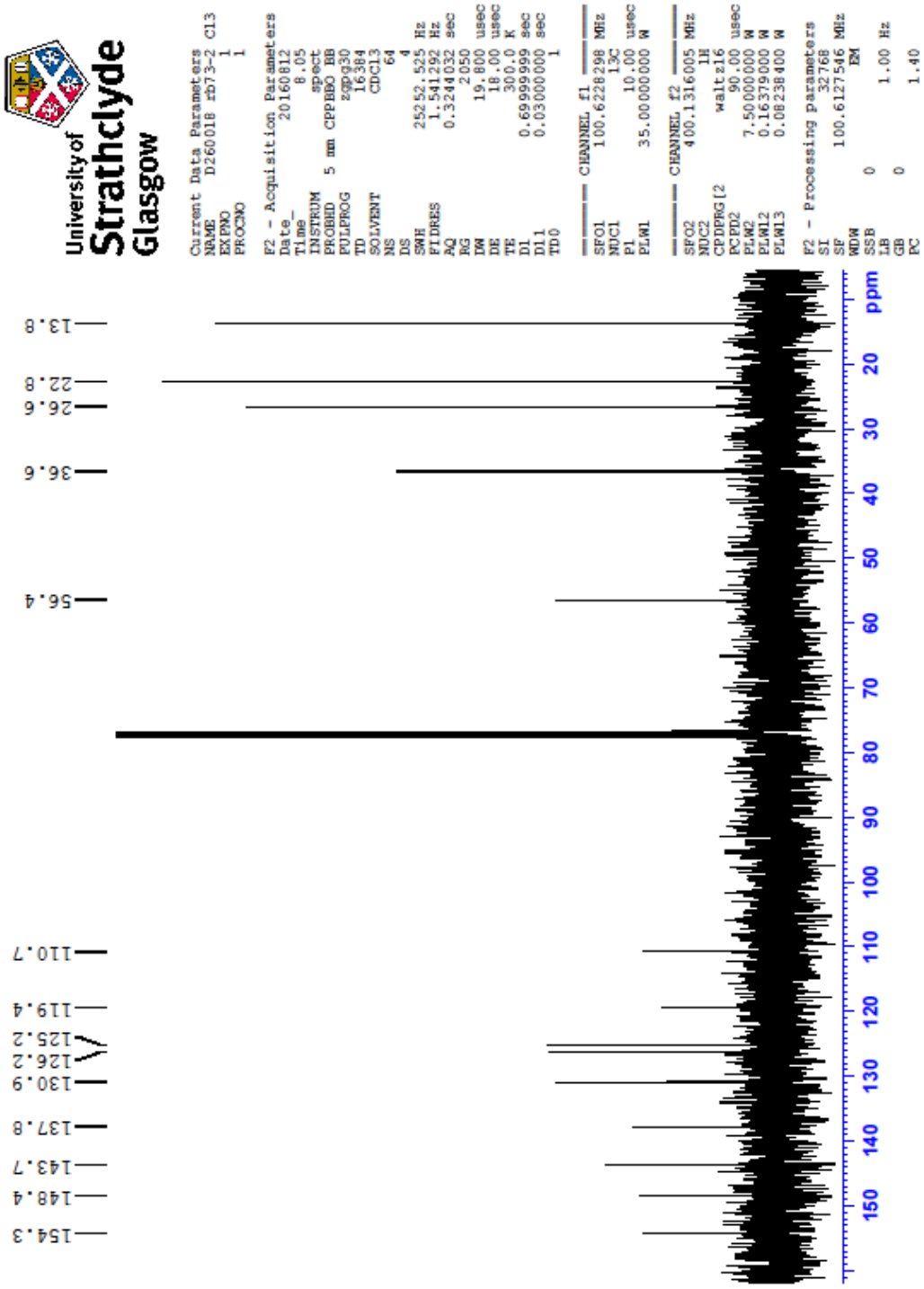
University of Strathclyde Glasgow
Current Data Parameters
NAME D260018 zb73-2 C13
EXPNO 1
PROCNO 1
F2 - Acquisition Parameters
Date_ 20160812
Time_ 8.05
INSTRUM spect
PROBHD 5 mm CPPBBO BB
PULPROG zgpg30
TD 16384
SOLVENT CDCl3
NS 64
DS 4
SWH 25252.525 Hz
FIDRES 1.541292 Hz
AQ 0.3244032 sec
RG 2050
DW 19.800 usec
DE 18.00 usec
TE 300.0 K
D1 0.69999999 sec
D11 0.03000000 sec
TD0 1
CHANNEL f1
SFO1 100.6228298 MHz
NUC1 13C
P1 10.00 usec
PLW1 35.00000000 W
CHANNEL f2
SFO2 400.1316005 MHz
NUC2 1H
CPDPRG[2 waltz16
PCPD2 90.00 usec
PLW2 7.50000000 W
PLW12 0.16379000 W
PLW13 0.08238400 W
F2 - Processing parameters
SI 32768
SF 100.6127546 MHz
WDW EM
SSB 0
LB 1.00 Hz
GB 0
PC 1.40
13.8
22.8
26.6
36.6
56.4
110.7
119.4
125.2
126.2
130.9
137.8
143.7
148.4
154.3
ppm
20
30
40
50
60
70
80
90
100
110
120
130
140
150

Compound 5.3

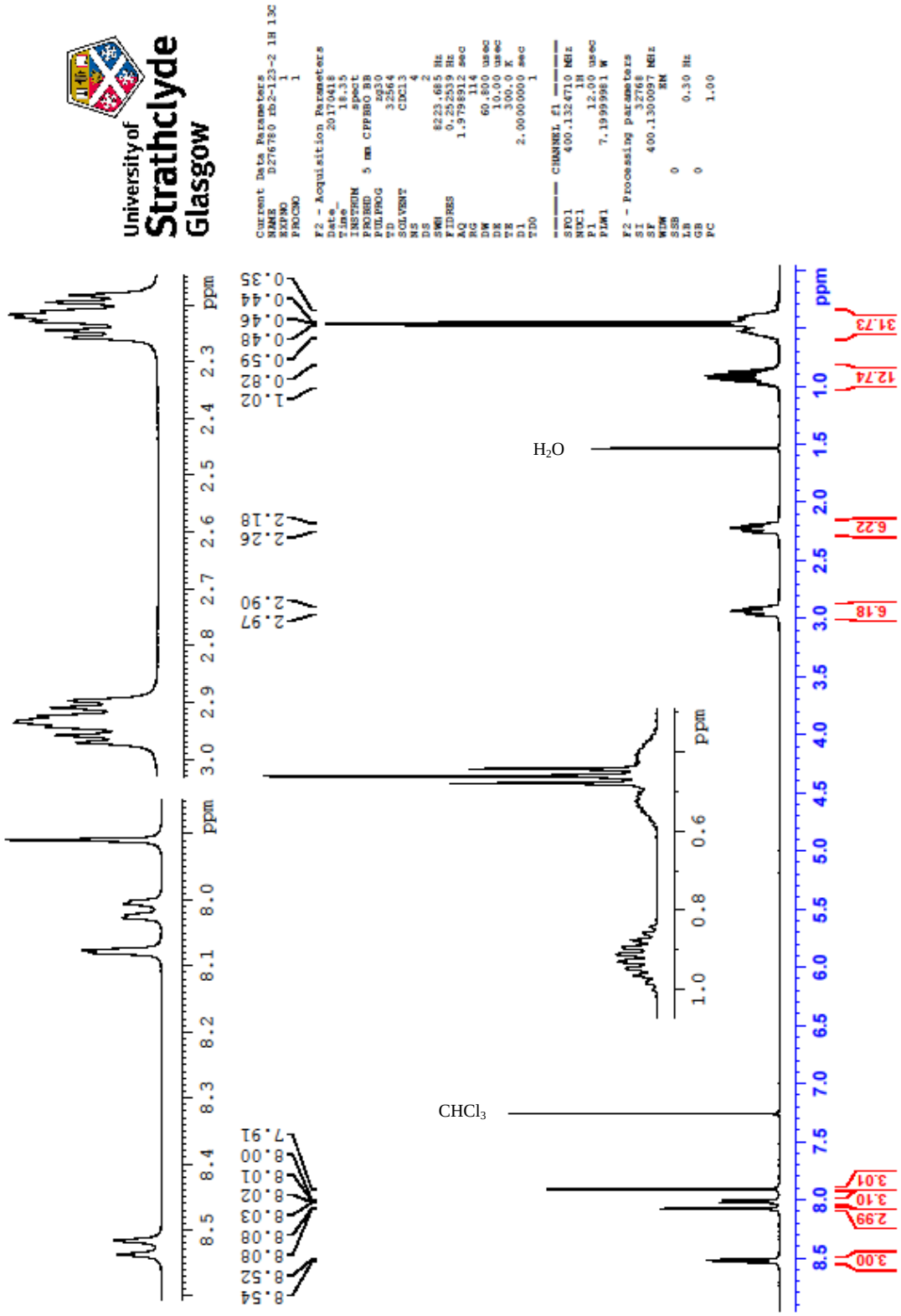

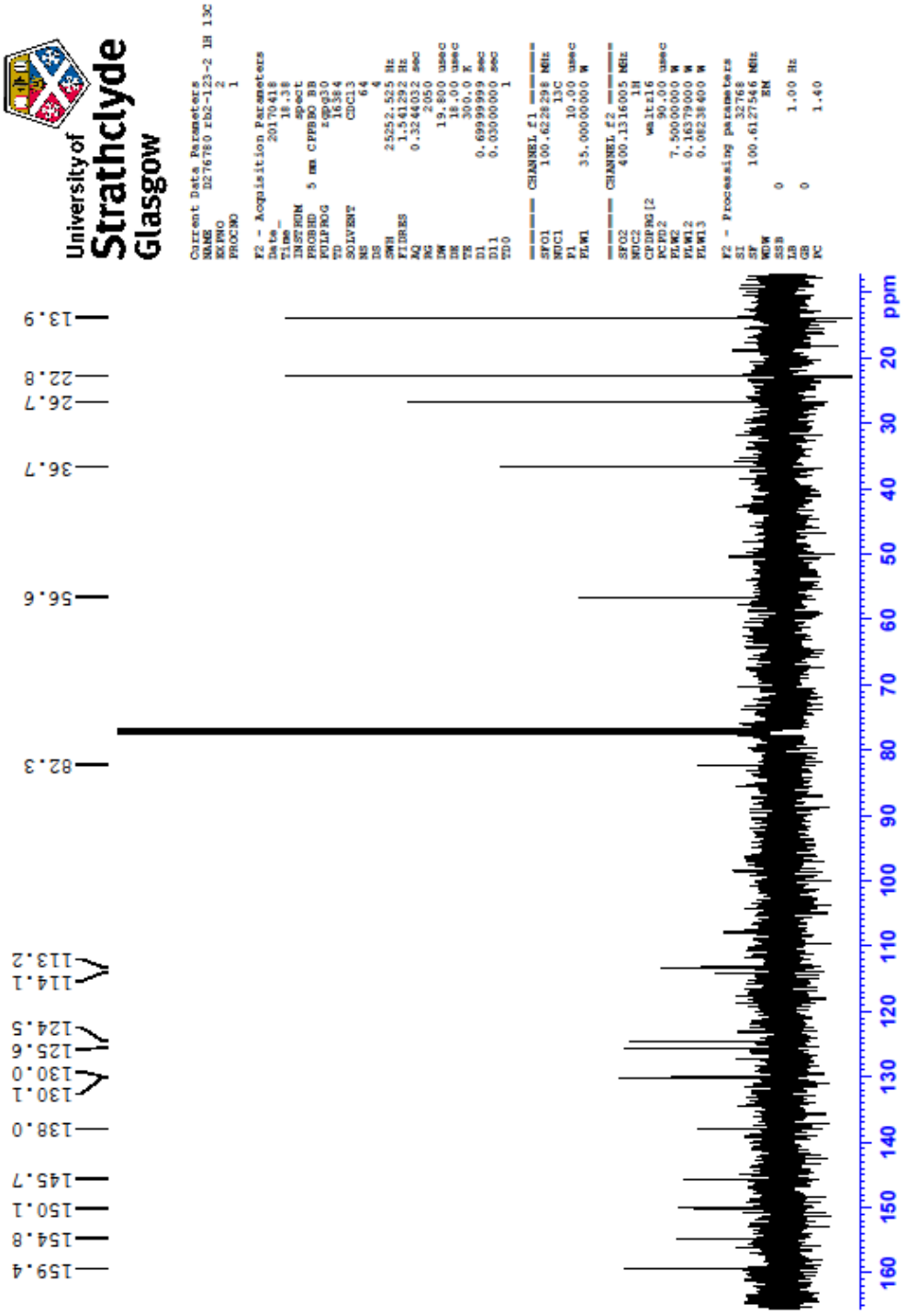
University of Strathclyde Glasgow
Current Data Parameters
NAME 1276780 rb2-123-2 1H 13C
EXPNO 2
PROCNO 1
F2 - Acquisition Parameters
Date_ 20170418
Time 18.38
INSTRUM spect
PROBHD 5 mm CPPBBO BB
PULPROG zgpg30
TD 16384
SOLVENT CDCl3
NS 64
DS 4
SWH 25252.525 Hz
FIDRES 1.541292 Hz
AQ 0.3244032 sec
RG 2050
DW 19.800 usec
DE 18.00 usec
TE 300.0 K
D1 0.69999999 sec
D11 0.03000000 sec
TD0 1
CHANNEL f1
SFO1 100.6228298 MHz
NUC1 13C
P1 10.00 usec
PLW1 35.00000000 W
CHANNEL f2
SFO2 400.1316005 MHz
NUC2 1H
CPDPRG[2 waltz16
PCPD2 90.00 usec
PLW2 7.50000000 W
PLW12 0.16379000 W
PLW13 0.08238400 W
F2 - Processing parameters
SI 32768
SF 100.6127546 MHz
WDW EM
SSB 0
LB 1.00 Hz
GB 0
PC 1.40
13.9
22.8
26.7
36.7
56.6
82.3
113.2
114.1
124.5
125.6
130.0
130.1
138.0
145.7
150.1
154.8
159.4
ppm

9.2 Crystallographic data

Compound 2.1

Empirical formula	$C_{33}H_{30}$
Formula weight	426.57
Temperature	100(2) K
Wavelength	0.71075 Å
Crystal system	Monoclinic
Space group	*P*121/*n*1
Unit cell dimensions	a = 9.5771(7) Å α = 90°
	b = 11.9821(8) Å β = 98.566(2)°
	c = 20.7151(15) Å γ = 90°
Volume	2350.6(3) Å^3
Z	4
ρ_{calcd}	1.205 Mg m^{-3}
μ	0.068 mm^{-1}
θ range	2.616–27.493°
Index ranges	$-12 \le h \le 12$, $-15 \le k \le 15$, $-23 \le l \le 26$
Measured reflections	17358
Independent reflections	5361 [R_{int} = 0.1301]
Completeness to θ = 25.242°	99.5%
Refinement method	Full-matrix least-squares on F^2
Data / restraints / parameters	5361 / 0 / 304
R indices [$F^2 > 2\sigma(F^2)$]	*R1* = 0.0484 *wR2* = 0.1336
R indices (all data)	*R1* = 0.0536 *wR2* = 0.1389
Goodness of fit	1.030
Largest diffraction peak and hole	0.440 and −0.248 e Å^{-3}

Compound 2.2

Empirical formula	$C_{39}H_{42}$
Formula weight	510.72
Temperature	100(2) K
Wavelength	0.71075 Å
Crystal system	Orthorhombic
Space group	*Pnma*
Unit cell dimensions	a = 14.151(4) Å α = 90°
	b = 52.301(16) Å β = 90°
	c = 12.140(4) Å γ = 90°
Volume	8985(5) Å^3
Z	12
ρ_{calcd}	1.133 Mg m^{-3}
μ	0.063 mm^{-1}
θ range	2.044–27.672°
Index ranges	$-18 \le h \le 14$, $-68 \le k \le 57$, $-15 \le l \le 15$
Measured reflections	55514
Independent reflections	10520 [R_{int} = 0.0784]
Completeness to θ = 26.000°	99.9%
Refinement method	Full-matrix least-squares on F^2 [a]
Data / restraints / parameters	10520 / 1500 / 655
R indices [$F^2 > 2\sigma(F^2)$]	*R1* = 0.1071 *wR2* = 0.2608
R indices (all data)	*R1* = 0.1205 *wR2* = 0.2724
Goodness of fit	1.150
Largest diffraction peak and hole	0.700 and −0.710 e Å^{-3}

[a] To maintain a sensible molecular geometry AFIX 66 restraints had to be used. A number of SIMU, DELU and RIGU restraints were applied to model atomic displacement parameters.

Compound 2.3

Empirical formula	$C_{45}H_{54}$	
Formula weight	594.92	
Temperature	100(2) K	
Wavelength	0.71075 Å	
Crystal system	Triclinic	
Space group	*P*–1	
Unit cell dimensions	a = 11.5947(6) Å	α = 98.316(7)°
	b = 12.4671(6) Å	β = 98.076(7)°
	c = 12.6790(8) Å	γ = 97.790(7)°
Volume	1772.65(18) Å^3	
Z	2	
ρ_{calcd}	1.115 Mg m^{-3}	
μ	0.062 mm^{-1}	
θ range	3.292–27.482°	
Index ranges	$-15 \le h \le 15$, $-16 \le k \le 16$, $-16 \le l \le 12$	
Measured reflections	23723	
Independent reflections	8106 [R_{int} = 0.0587]	
Completeness to θ = 25.242°	99.7%	
Refinement method	Full-matrix least-squares on F^2	
Data / restraints / parameters	8106 / 0 / 412	
R indices [$F^2 > 2\sigma(F^2)$]	*R1* = 0.0575	*wR2* = 0.1412
R indices (all data)	*R1* = 0.0938	*wR2* = 0.1560
Goodness of fit	1.040	
Largest diffraction peak and hole	0.335 and −0.233 e Å^{-3}	

Compound 2.4

Empirical formula	$C_{51}H_{66}$	
Formula weight	679.08	
Temperature	100(2) K	
Wavelength	0.71075 Å	
Crystal system	Monoclinic	
Space group	*P*121/*c*1	
Unit cell dimensions	a = 9.4388(4) Å	α = 90°
	b = 22.9218(11) Å	β = 95.297(7)°
	c = 18.8067(13) Å	γ = 90°
Volume	4051.5(4) Å^3	
Z	4	
ρ_{calcd}	1.113 Mg m^{-3}	
μ	0.062 mm^{-1}	
θ range	3.058–27.484°	
Index ranges	$-10 \le h \le 12$, $-28 \le k \le 29$, $-24 \le l \le 24$	
Measured reflections	53431	
Independent reflections	9286 [R_{int} = 0.1117]	
Completeness to θ = 25.242°	99.8%	
Refinement method	Full-matrix least-squares on F^2	
Data / restraints / parameters	9286 / 0 / 466	
R indices [$F^2 > 2\sigma(F^2)$]	*R1* = 0.0676	*wR2* = 0.1293
R indices (all data)	*R1* = 0.1352	*wR2* = 0.1526
Goodness of fit	1.021	
Largest diffraction peak and hole	0.272 and −0.217 e Å^{-3}	

Compound 2.5

Empirical formula	$C_{33}H_{27}Br_3$	
Formula weight	663.29	
Temperature	100(2) K	
Wavelength	0.71075 Å	
Crystal system	Monoclinic	
Space group	*P*121/*c*1	
Unit cell dimensions	a = 22.2188(18) Å	α = 90°
	b = 5.9618(4) Å	β = 106.572(8)°
	c = 21.3396(18) Å	γ = 90°
Volume	2709.3(4) Å^3	
Z	4	
ρ_{calcd}	1.626 Mg m^{-3}	
μ	4.488 mm^{-1}	
θ range	3.131–27.484°	
Index ranges	$-28 \le h \le 26$, $-7 \le k \le 6$, $-21 \le l \le 27$	
Measured reflections	22392	
Independent reflections	5791 [R_{int} = 0.1561]	
Completeness to θ = 25.242°	96.6%	
Refinement method	Full-matrix least-squares on F^2	
Data / restraints / parameters	5791 / 0 / 331	
R indices [$F^2 > 2\sigma(F^2)$]	*R1* = 0.0624	*wR2* = 0.0927
R indices (all data)	*R1* = 0.1605	*wR2* = 0.1144
Goodness of fit	0.880	
Largest diffraction peak and hole	0.867 and −0.584 e Å^{-3}	

Compound 2.6

Empirical formula	$C_{39}H_{39}Br_3$
Formula weight	747.43
Temperature	100(2) K
Wavelength	0.71075 Å
Crystal system	Monoclinic
Space group	$P2_1/c$
Unit cell dimensions	a = 10.7331(19) Å α = 90°
	b = 33.928(6) Å β = 114.5470(10)°
	c = 9.8325(17) Å γ = 90°
Volume	3256.9(10) $Å^3$
Z	4
ρ_{calcd}	1.524 Mg m^{-3}
μ	3.743 mm^{-1}
θ range	2.973–27.483°
Index ranges	$-13 \le h \le 13$, $-44 \le k \le 33$, $-12 \le l \le 12$
Measured reflections	55604
Independent reflections	7450 [R_{int} = 0.0312]
Completeness to θ = 25.242°	99.5%
Refinement method	Full-matrix least-squares on F^2
Data / restraints / parameters	7450 / 0 / 385
R indices [$F^2 > 2\sigma(F^2)$]	$R1$ = 0.0253 $wR2$ = 0.0635
R indices (all data)	$R1$ = 0.0258 $wR2$ = 0.0638
Goodness of fit	1.080
Largest diffraction peak and hole	0.473 and −0.533 e $Å^{-3}$

Compound 2.7

Empirical formula	$C_{45}H_{51}Br_3$
Formula weight	831.58
Temperature	100 K
Wavelength	0.71075 Å
Crystal system	Monoclinic
Space group	*P*121/*c*1
Unit cell dimensions	a = 16.9091(10) Å α = 90°
	b = 25.6844(14) Å β = 98.335(7)°
	c = 18.9364(13) Å γ = 90°
Volume	8137.2(9) Å^3
Z	8
ρ_{calcd}	1.358 Mg m^{-3}
μ	3.003 mm^{-1}
θ range	2.977–25.027°
Index ranges	$-20 \le h \le 18$, $-30 \le k \le 30$, $-22 \le l \le 22$
Measured reflections	77032
Independent reflections	14285 [R_{int} = 0.2132]
Completeness to θ = 25.242°	97.1%
Refinement method	Full-matrix least-squares on F^2
Data / restraints / parameters	14285 / 0 / 877
R indices [$F^2 > 2\sigma(F^2)$]	*R1* = 0.0671 *wR2* = 0.1269
R indices (all data)	*R1* = 0.2329 *wR2* = 0.1711
Goodness of fit	0.839
Largest diffraction peak and hole	0.573 and −0.452 e Å^{-3}

Compound 2.8

Empirical formula	$C_{51}H_{63}Br_3$
Formula weight	915.77
Temperature	100(2) K
Wavelength	0.71075 Å
Crystal system	Orthorhombic
Space group	*Pna*21
Unit cell dimensions	a = 16.3325(9) Å α = 90°
	b = 18.0221(12) Å β = 90°
	c = 15.2352(9) Å γ = 90°
Volume	4484.4(5) Å^3
Z	4
ρ_{calcd}	1.356 Mg m^{-3}
μ	2.732 mm^{-1}
θ range	3.048–27.472°
Index ranges	$-21 \le h \le 20$, $-18 \le k \le 23$, $-19 \le l \le 19$
Measured reflections	23477
Independent reflections	10212 [R_{int} = 0.0548]
Completeness to θ = 25.242°	99.7%
Refinement method	Full-matrix least-squares on F^2
Data / restraints / parameters	10212 / 1 / 493
R indices [$F^2 > 2\sigma(F^2)$]	$R1$ = 0.0479 $wR2$ = 0.0818
R indices (all data)	$R1$ = 0.0717 $wR2$ = 0.0897
Goodness of fit	1.024
Largest diffraction peak and hole	0.644 and −0.370 e Å^{-3}

Compound 2.12

Empirical formula	$C_{52}H_{62}O_7$
Formula weight	799.01
Temperature	100(2) K
Wavelength	0.71075 Å
Crystal system	Triclinic
Space group	*P*–1
Unit cell dimensions	a = 15.898(10) Å α = 89.53(7)°
	b = 16.561(13) Å β = 75.34(6)°
	c = 19.522(16) Å γ = 64.98(4)°
Volume	4477(6) $Å^3$
Z	4
ρ_{calcd}	1.185 Mg m^{-3}
μ	0.0077 mm^{-1}
θ range	2.939–25.028°
Index ranges	$-20 \le h \le 20$, $-21 \le k \le 21$, $-25 \le l \le 22$
Measured reflections	56878
Independent reflections	15749 [R_{int} = 0.0765]
Completeness to θ = 25.242°	97.2%
Refinement method	Full-matrix least-squares on F^2
Data / restraints / parameters	15749 / 12 / 1101
R indices [$F^2 > 2\sigma(F^2)$]	*R1* = 0.0873 *wR2* = 0.2382
R indices (all data)	*R1* = 0.1090 *wR2* = 0.2627
Goodness of fit	1.041
Largest diffraction peak and hole	0.782 and −0.325 e $Å^{-3}$

Compound 2.13

Empirical formula	$C_{58}H_{74}O_7$	
Formula weight	883.17	
Temperature	100(2) K	
Wavelength	0.71075 Å	
Crystal system	Triclinic	
Space group	*P*–1	
Unit cell dimensions	a = 9.279(3) Å	α = 99.276(5)°
	b = 14.510(4) Å	β = 101.689(5)°
	c = 19.415(6) Å	γ = 98.438(4)°
Volume	2482.4(13) Å^3	
Z	2	
ρ_{calcd}	1.182 Mg m^{-3}	
μ	0.076 mm^{-1}	
θ range	3.122–27.485°	
Index ranges	$-12 \le h \le 12$, $-18 \le k \le 18$, $-25 \le l \le 25$	
Measured reflections	33108	
Independent reflections	11305 [R_{int} = 0.0319]	
Completeness to θ = 25.242°	99.7%	
Refinement method	Full-matrix least-squares on F^2	
Data / restraints / parameters	11305 / 0 / 595	
R indices [$F^2 > 2\sigma(F^2)$]	*R1* = 0.0587	*wR2* = 0.1255
R indices (all data)	*R1* = 0.0684	*wR2* = 0.1304
Goodness of fit	1.100	
Largest diffraction peak and hole	0.541 and −0.309 e Å^{-3}	

Compound 4.4

Empirical formula	$C_{87}H_{90}O_{12}$	
Formula weight	1327.58	
Temperature	100(2) K	
Wavelength	0.71075 Å	
Crystal system	Triclinic	
Space group	*P*–1	
Unit cell dimensions	a = 12.0777(8) Å	α = 100.523(6)°
	b = 15.3754(11) Å	β = 92.271(6)°
	c = 20.5905(16) Å	γ = 3724.7(5)°
Volume	3724.7(5) Å^3	
Z	2	
ρ_{calcd}	1.184 Mg m^{-3}	
μ	0.078 mm^{-1}	
θ range	2.204–20.816°	
Index ranges	$-15 \le h \le 14$, $-19 \le k \le 19$, $-26 \le l \le 26$	
Measured reflections	53259	
Independent reflections	7785 [R_{int} = 0.1209]	
Completeness to θ = 20.816°	99.9%	
Refinement method	Full-matrix least-squares on F^2	
Data / restraints / parameters	6769 / 0 / 409	
R indices [$F^2 > 2\sigma(F^2)$]	$R1$ = 0.1733	$wR2$ = 0.4504
R indices (all data)	$R1$ = 0.1863	$wR2$ = 0.4618
Goodness of fit	1.129	
Largest diffraction peak and hole	1.435 and −0.650 e Å^{-3}	